

**X-ray studies of ultraluminous infrared
galaxies
observed with *XMM-Newton***

Dissertation
zur Erlangung des Doktorgrades
des Fachbereichs Physik
der Universität Hamburg

vorgelegt von

Ralf Keil

aus Elmshorn

Garching

2006

Gutachter der Dissertation:

Prof. Dr. D. Reimers

Prof. Dr. T. Boller

Gutachter der Disputation:

Prof. Dr. D. Reimers

Prof. Dr. J. H. M. M. Schmitt

Datum der Disputation:

13. 03. 2006

Vorsitzender des Prüfungsausschusses:

Prof. Dr. P. Hauschildt

Vorsitzender des Promotionsausschusses:

Prof. Dr. G. Huber

Dekan des Fachbereichs Physik:

Prof. Dr. G. Huber

Zusammenfassung

Umfangreiche Studien über ultra-leuchtkräftige Infrarot-Galaxien (ULIRGs) führen zu fundamentalen Fragen an die Astrophysik dieser Objekte: die Entflechtung der Emissionsprozesse zwischen AGN- und Sternentstehung sowie die Verbindung zu der Fe K Linienemission und anderen Emissionslinien. Die beste zur Verfügung stehende Technologie in Verbindung mit einem hohen Datendurchsatz erlaubt eine umfassendere und wesentlich genauere Analyse von Spektren als bei vorangegangenen Röntgenmissionen. In dieser Dissertation werden die Röntgeneigenschaften von zwei ULIRGs mit Hilfe des *XMM-Newton* Observatoriums untersucht.

Eine der bekanntesten ULIRGs ist NGC 6240. Das (0.3 – 10.0) keV-Spektrum lässt sich modellieren durch: (i) drei kollisions-ionisierte Plasmen mit Temperaturen von 0.7 keV (führt zu weichen Emissionslinien), 1.4 keV bzw. 5.5 keV (Fe XXV- und Fe XXVI-Linien); (ii) ein hoch-absorbiertes Potenzgesetz und (iii) eine neutrale Fe K α -Linie. Zudem wurde ein signifikanter neutrale-Säulendichte-Gradient detektiert, der mit der Temperatur der drei Plasmen korreliert ist. Eine Verknüpfung des *XMM-Newton*-Spektralmodells mit dem räumlich hoch-aufgelösten *Chandra*-Bild zeigt, dass die Temperaturen und die Säulendichten zur Zentralregion von NGC 6240 hin zunehmen. Die Emissionslinien werden durch Sternentstehung erzeugt, während das Potenzgesetz und die neutrale Fe K α -Linie auf eine AGN-Präsenz hinweisen.

Mit hoher Signifikanz wurde der Fe K Linienkomplex in drei voneinander getrennte schmale Linien aufgelöst: (i) die neutrale Fe K α -Linie bei 6.4 keV; (ii) eine ionisierte Linie bei 6.7 keV; und (iii) eine höher ionisierte Linie bei 7.0 keV (eine Überlagerung der Fe XXVI- und der Fe K β -Linie). Während die neutrale Fe K α Linie vermutlich auf Reflexion an optisch-dicker Materie zurückzuführen ist, entstehen die ionisierten Fe XXV- und Fe XXVI-Linien aus dem heißesten ionisierten Plasma.

Ein Vergleich der Plasma-Parameter bei NGC 6240 mit jenen, die in der lokalen Sternentstehungsgalaxie NGC 253 gefunden wurden, zeigt eine auffällige Ähnlichkeit in den Plasma-Temperaturen und den Säulendichte-Gradienten, welche einen gleichartigen zugrunde liegenden physikalischen Prozess in Galaxien mit hoher Sternentstehung und in ULIRGs nahelegt.

Die *XMM-Newton*-Daten von Mrk 1014 sind konsistent mit einem einfachen Potenzgesetz; ein Modell bestehend aus zwei Potenzgesetzen bzw. einem Potenzgesetz und einem kollisions-ionisierten Plasma ist ebenfalls akzeptabel. Daher ist es nicht sinnvoll, das Potenzgesetz gegenüber anderen Modellansätzen auf Grund der geringen Datenstatistik zu bevorzugen. Damit können keine physikalischen Aussagen über Mrk 1014 gemacht werden. Die Existenz eines weichen Überschusses konnte nicht bestätigt werden. Die harte überschüssige Emission ($E > 5$ keV) wurde mit grosser Sorgfalt analysiert, die geringe Photonenstatistik ließ eine Bestätigung dieser jedoch nicht zu. Zukünftige Röntgen-Missionen werden weiteres Licht auf diese Themen werfen.

Abstract

Extensive studies of ultraluminous infrared galaxies (ULIRGs) are leading to the fundamental issues about the astrophysics of these objects: the deconvolution of the AGN–Starburst emission processes and the link to the Fe line emission and other emission lines. The capability of the best available technology in combination with the high throughput of the satellite allows a comprehensive analysis of the spectra in much more detail than obtained from previous X–ray missions. In this thesis the X–ray properties of two ULIRGs are investigated with *XMM-Newton* data.

One of the most prominent extremely luminous infrared galaxies is NGC 6240. The spectrum within (0.3 – 10.0) keV can be modelled with: (i) three collisionally ionized plasma components with temperatures of about 0.7 keV (resulting in soft emission lines), 1.4 keV, and 5.5 keV (Fe XXV– and Fe XXVI lines); (ii) a highly absorbed power law component, and (iii) a neutral Fe-K α line. Furthermore, a significant neutral column density gradient has been detected and is correlated with the temperature of the three plasma components. Combining the *XMM-Newton* spectral model with the high spatial resolution *Chandra* image the temperatures and the column densities increase towards the central region of NGC 6240. The emission lines are produced by a Starburst, whereas the power law and the Fe-K α line points to an AGN–presence.

With high significance, the Fe K line complex is resolved into three distinct narrow lines: (i) the neutral Fe-K α line at 6.4 keV; (ii) an ionized line at about 6.7 keV; and (iii) a higher ionized line at 7.0 keV (a blend of the Fe XXVI and the Fe-K β line). While the neutral Fe K line is probably due to reflection from optically thick material, the ionized Fe XXV and Fe XXVI lines arise from the highest temperature ionized plasma component.

By comparing the plasma parameters of NGC 6240 with those found in the local Starburst galaxy NGC 253 a striking similarity has been found in the plasma temperatures and column density gradients, suggesting a similar underlying physical process at work in galaxies with an enhanced Starburst and in ULIRGs.

The *XMM-Newton* data of Mrk 1014 are consistent with a simple power law dominated spectrum. A model including two power laws or one power law and a collisionally–ionized plasma is also acceptable. Therefore, it is not reasonable to give preference to the power law compared to other attempts because of the low data statistics. For that reason, no statements about the physical conditions in Mrk 1014 can be made. The presence of a soft X–ray excess could not be confirmed. The published hard excess emission above 5 keV was analyzed with great accurateness, but could not be confirmed due to the low data quality. Future X–ray missions will shed more light on those issues.

The research described in this dissertation was performed at the Max–Planck–Institut für Extraterrestrische Physik (MPE), Garching near Munich between July 2000 and June 2003.

Contents

1	Introduction	1
1.1	The case of the ULIRGs	1
1.1.1	Definition	1
1.1.2	The luminosity function	3
1.1.3	The spectral energy distribution	5
1.1.4	The key issue: The relative fraction of X-ray and IR emission of ULIRGs	12
1.2	Active Galactic Nuclei as a power source	13
1.2.1	The central engine and the accretion disk	13
1.2.2	X-ray properties	14
1.2.3	Primary components of an AGN	20
1.2.4	The role of absorption	23
1.3	Starbursts as a power source	24
1.3.1	The hot diffuse plasma	25
1.3.2	Supernova Remnants	26
1.3.3	High- and low-Mass X-ray binaries	26
1.4	Disentangling the AGN-Starburst contributions	27
2	Data reduction with the <i>XMM-Newton</i> observatory	29
2.1	The scientific instrumentation	30
2.1.1	The X-ray mirror modules	31
2.1.2	The European Photon Imaging Camera (EPIC)	33
2.1.3	The Reflection Grating Spectrometer (RGS)	37
2.1.4	The Optical Monitor (OM)	37
2.2	The detailed reduction of <i>XMM-Newton</i> data files	38
2.2.1	The step-by-step analysis	38

3	The extremely luminous infrared galaxy NGC 6240 in the focus of <i>XMM-Newton</i>	41
3.1	The methodology of spectral analysis	43
3.1.1	General remarks	43
3.2	The object NGC 6240	47
3.2.1	Published results	47
3.2.2	The X-ray observation	52
3.2.3	Collisionally-ionized plasma emission	56
3.2.4	Spectral Analysis	58
3.2.4.1	The Fe-K emission line complex	58
3.2.4.2	The broad-band energy spectrum	66
3.2.4.3	Comparison with the nearby Starburst galaxy NGC 253	72
3.2.5	Comparison with the <i>Chandra</i> observation	73
3.2.6	Summary	76
3.3	Error handling in the spectral data analysis	77
3.3.1	Measurement errors	77
3.3.2	Uncertainties in modelling with XSPEC	81
4	Discussion	85
4.1	Overview	85
4.2	A detailed discussion of the Mrk 1014 data	86
4.2.1	Several earlier results	86
4.2.2	The X-ray observation	86
4.2.3	Spectral modelling	88
4.3	Properties of the hard components	95
4.3.1	Luminosities	95
4.3.2	The continuum slope	110
4.3.3	Fe-K line diagnostics	117
4.3.3.1	Equivalent widths	117
4.3.3.2	Ionized iron	121
4.4	The soft components	122
4.4.1	X-ray to IR flux ratios	122
4.4.2	Plasma properties	125
4.4.3	Emission lines at low energies	127
5	Conclusion and future prospects	129
5.1	Summary	129
5.2	Future prospects	130

References	135
Acronyms	153
Appendix	159
A Combining spectral files within XSPEC	159
Acknowledgement	163
Declaration	165

List of Figures

1.1	Examples of ultraluminous infrared galaxies (ULIRGs), observed with <i>HST</i> . . .	2
1.2	The luminosity function of infrared galaxies	4
1.3	The observed spectral energy distribution of NGC 6240 together with intensities of the background radiation in different energy bands	6
1.4	Nuclear emission classes for luminous infrared galaxies: relative fractions as a function of the IR luminosity	10
1.5	Schematic diagram of the X-ray and low γ -ray spectral features of a non-absorbed AGN	15
1.6	Simulated AGN reflection spectrum from an incident power law spectrum . . .	16
1.7	Iron $K\alpha$ line energies and Fluorescence yield of iron $K\alpha$ and $K\beta$ as a function of the ionization state	18
1.8	Overview of the diverse classes of active galaxies	22
1.9	The effect of X-ray-absorption by material of column densities $N_H = 10^{21}, 10^{22}, 10^{23}$ and 10^{24} atoms cm^{-2}	24
2.1	Arrangement of the instruments on the <i>XMM-Newton</i> satellite	30
2.2	The light path in a Wolter type I configuration of the <i>XMM-Newton</i> mirror modules with the EPIC and RGS detectors in the focus	31
2.3	Comparison of the focal plane layout of the EPIC MOS and EPIC pn cameras .	36
2.4	The steps of data reduction performed on each data set	39
3.1	Reduced χ^2 values as a function of the degrees of freedom for different confidence levels	46
3.2	The <i>ASCA-SIS</i> spectrum of NGC 6240 within (0.5 – 10.0) keV.	48
3.3	The best fitting model for NGC 6240, deconvolved from the responses of the <i>BeppoSAX</i> detectors	49
3.4	<i>Chandra</i> image of NGC 6240 in three different energy bands	51
3.5	<i>Chandra</i> spectrum of the X-ray brighter AGN in NGC 6240	51

3.6	The (0.3 – 10) keV source and background spectrum for the EPIC MOS1/2 data of NGC 6240	54
3.7	Source and background selection regions in the EPIC MOS1, MOS2, and pn detectors	55
3.8	Simulated spectra of an X-ray emitting plasma using the APEC, MEKAL, and RAYMOND model based on the Mrk 1014 fitting results	57
3.9	Spectral fits to the EPIC MOS1/2 data of NGC 6240 in the Fe-K line range (5.0 – 7.4) keV	59
3.10	Confidence contour plot for the high-energy part of the Fe line complex, using a single Gaussian line	60
3.11	Confidence contour plot for the Fe line complex, using three Gaussian lines	62
3.12	Spectral fit to the EPIC MOS1/2 data of NGC 6240 in the Fe-K line range, using four Gaussian lines	63
3.13	Spectral fit to the EPIC MOS1/2 data of NGC 6240 in the Fe-K line range, using APEC and two Gaussian lines	65
3.14	Spectral model components to the EPIC MOS1/2 data of NGC 6240 in the Fe-K line range	66
3.15	The EPIC MOS1/2 spectrum of NGC 6240 with identifications of the most prominent emission lines	67
3.16	Spectral fits to the EPIC MOS1/2 data in the (0.3 – 2.5) keV range	68
3.17	Spectral fit to the merged EPIC MOS1/2 data of NGC 6240 in the energy range (0.3 – 10.0) keV and around the Fe-K line complex	70
3.18	The radial intensity profile of the EPIC MOS2 data for NGC 6240	74
3.19	<i>Chandra</i> images of selected energy bands based on <i>XMM-Newton</i> data	75
3.20	Comparison of spectral parameters by three different backgrounds	79
4.1	Comparison of source spectra with background spectra of the Mrk 1014 data gained from all EPIC devices	88
4.2	The (0.3 – 8.0) keV EPIC pn spectrum of Mrk 1014 with the power law model component	90
4.3	Spectral power law fits to the EPIC MOS1/2 data of Mrk 1014 in the range (0.3 – 8.0) keV	93
4.4	The (observed) $L_{(2.0-10.0) \text{ keV}}/L_{\text{FIR}}$ -ratio as a function of $f_{25\mu\text{m}}/f_{60\mu\text{m}}$ for various classes of objects	102
4.5	Luminosities and luminosity ratios of some observables for various classes of objects	105

4.6	Estimations of the SFR deduced from the far-IR- and the hard X-ray emission by comparison	109
4.7	The EW of the Fe-K α line in dependence on the column density N_{H} of the X-ray intervening gas	119
4.8	The observed $L_{(0.5-2.0) \text{ keV}}/L_{\text{FIR}}$ -ratio as a function of the far-IR-luminosity L_{FIR} for NGC 6240 and Mrk 1014 and comparable samples	123
5.1	X-ray model spectrum with its components of a composite galaxy of a heavily absorbed AGN and a Starburst	132
5.2	Simulated X-ray spectrum of a composite galaxy at redshifts $z = 4$ and $z = 8$, as seen by <i>XEUS</i>	132

List of Tables

2.1	Parameters of the <i>XMM-Newton</i> observatory (Lumb et al. 1996)	32
2.2	Parameters of the EPIC pn- and the EPIC MOS–CCDs	34
2.3	Performance modes of the EPIC devices	35
3.1	NGC 6240 observed with <i>XMM-Newton</i> and analyzed in this thesis	42
3.2	Optical classification of NGC 6240 and some luminosities	42
3.3	Summary of the NGC 6240 observations	53
3.4	Fit results of Gaussian lines to the Fe-K line complex	61
3.5	Fit results of <i>four</i> Gaussian lines to the Fe-K line complex	63
3.6	Fit results of an APEC model plus two Gaussian lines to the Fe-K line complex	64
3.7	Spectral fit results to the <i>XMM-Newton</i> soft X–ray spectrum	68
3.8	Spectral fit components to the entire (0.3 – 10.0) keV energy band	71
3.9	Comparison of the spectral fitting parameters for three background regions	78
4.1	Summary of the Mrk 1014 observation	87
4.2	Fitting parameters of attempted spectral models for the EPIC pn	91
4.3	Fitting parameters of attempted spectral models for the EPIC MOS1/2 and the combined EPIC pn and EPIC MOS1/2 devices	94
4.4	<i>Observed</i> luminosities and flux ratios of Mrk 1014 and NGC 6240	96
4.5	Absorption–corrected fluxes and luminosities of Mrk 1014 and NGC 6240	97
4.6	<i>Observed</i> X–ray fluxes and luminosities of Mrk 1014 and NGC 6240	98
4.7	Measured and predicted soft and hard X–ray luminosities from Starbursts	107
4.8	Diverse model approaches to the hard X–ray spectrum of NGC 6240	111
4.9	Derived physical parameters of the hot X–ray emitting gas in NGC 6240	114
4.10	X–ray parameters of the lines in the Fe–K complex of NGC 6240	118
4.11	Derived physical parameters of the X–ray emitting gas	126
4.12	Selected emission lines in the soft X–ray spectrum of NGC 6240	128

1

Introduction

1.1 The case of the ULIRGs

In the same way the discovery of the quasars and their physical implications changed our mind of the evolution of the universe, the identification of a class of infrared luminous galaxies had and still has a big imprint on all current research fields dealing with galaxy astrophysics (from the formation of galaxies to their evolution in the universe and their cosmological consequences). Luminous infrared galaxies are often detected as interacting and/or merging objects (see Figure 1.1 on p. 2).

The large number of published papers on this class of objects bears a considerable witness of the importance of galaxy interaction and star formation (for a review see Sanders and Mirabel 1996; Soifer et al. 1987a; Telesco 1988; Mirabel 1992; Sanders 1992; Scoville et al. 1994).

1.1.1 Definition

The first notes of the existence of luminous infrared galaxies can be found in papers by Low and Kleinmann (1968), and Kleinmann and Low (1970a,1970b), in which the authors published the detection of 15 extragalactic sources of high IR luminosity. Rieke and Low (1972) found that four galaxies out of a sample of 57 investigated objects show "extraordinary high infrared luminosities" and were associated with interacting and merging galaxies. They defined these so-called "ultrahigh luminosity infrared galaxies" as the upper end of the scale of galactic luminosities and therefore, put them into the same category as the quasars in terms of being the brightest objects in the universe. According to the conventional nomenclature of "Luminous Infrared Galaxies" (LIGs), these objects have luminosities of $L_{\text{IR}} > 10^{11} L_{\odot}$ ($\approx 4 \cdot 10^{44} \text{ erg s}^{-1}$) in the $(8 - 1,000) \mu\text{m}$ wavelength range. Moreover, Joseph and Wright (1985) used the term

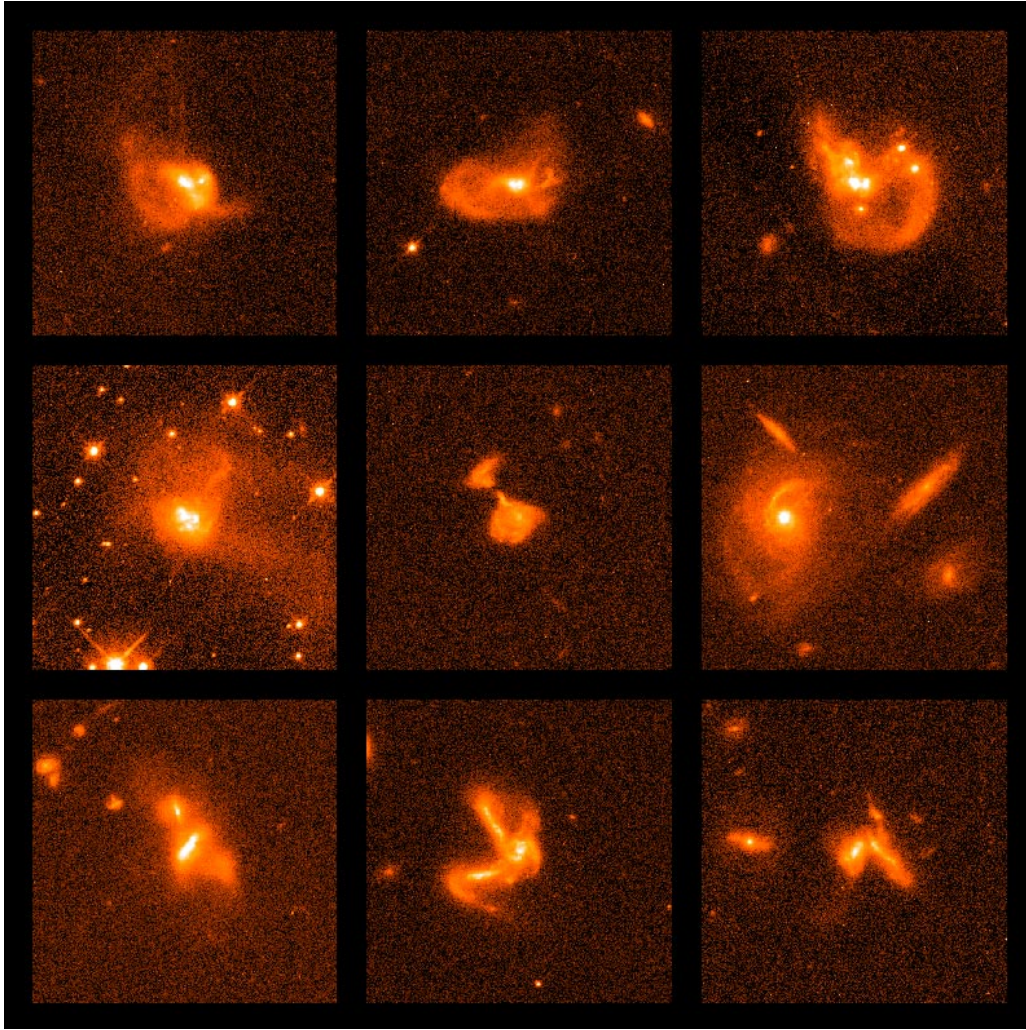


Figure 1.1: Examples of ultraluminous infrared galaxies (ULIRGs), showing the common occurrence of galaxy interactions and disturbances (observed with *HST*; STScI Public Archive, NASA release date: November 22, 1999, release number: STScI-1999-45). Due to the complexity of these systems, the task to disentangle the different emission processes is very sophisticated.

”Ultraluminous InfraRed Galaxies” (ULIRGs) for a class of advanced mergers, that have strong emission in the mid-IR. Their luminosities exceed the luminosities of the LIGs by one order of magnitude, *i.e.* $L_{\text{IR}} > 10^{12} L_{\odot}$ within the $(8 - 1,000) \mu\text{m}$ regime. Assuming that their energy is emitted mostly in the visible band, their absolute magnitude would be brighter than -25^{m} .

The realization of investigating the sky in the IR from space in form of the ”Infrared Astronomical Satellite” (*IRAS*) in 1983 (Neugebauer et al. 1984) pushed this field of research. This satellite was equipped with a telescope sensitive enough to detect large numbers of extragalactic sources at wavelengths in the mid-IR and far-IR. Within ten months of operation *IRAS* deeply

surveyed $\sim 96\%$ of the sky at wavelengths of $12 \mu\text{m}$, $25 \mu\text{m}$, $60 \mu\text{m}$, and $100 \mu\text{m}$ ¹, resulting in a point source catalogue of more than $\sim 30,000$ galaxies². This survey revealed a new class of objects consisting of luminous galaxies which emit most of their bolometric luminosity in the IR, having absolute luminosities in the range from those of normal galaxies to the most luminous optical quasars (Houck et al. 1984; Rowan-Robinson et al. 1984; Soifer et al. 1984). There is convincing evidence that the infrared is dominated by emission from other sources in the galaxy which is reprocessed by dust, but the nature of the nuclear source is still a current issue of lively debates.

The *IRAS* discovery of LIGS/ULIRGs triggered researchers to focus on the determination of the power source of such extremely high infrared luminosities. The importance of this distinct class of activity is not only because of its high luminosities and heavy extinction (see below), but also in the distribution of the interstellar gas and in terms of the Starburst processes. It is assumed that many *IRAS* galaxies appear to be powered by Starbursts whereas some of these sources seem to be powered by dust-enshrouded Active Galactic Nuclei (AGN), or a combination of both (see ch. 1.2 on p. 13 and ch. 1.3 on p. 24).

1.1.2 The luminosity function

Based on numerous redshift catalogues (see Saunders et al. 1990 for a reference on *IRAS* galaxy surveys) containing large unbiased samples of objects the properties of infrared galaxies could be studied in a comprehensive fashion. The combination of different compilations of deeper pointed observations with the *IRAS* All-Sky Survey (Soifer et al. 1987b) provided the opportunity to construct an accurate luminosity function of infrared bright galaxies. In comparison to the luminosity function of other classes of extragalactic sources the results are shown in Figure 1.2 (p. 4). The data were taken from the *IRAS* Bright Galaxy Survey (BGS; Sanders et al. 1995), *IRAS* 1-Jy Survey of ULIRGs (Kim 1995), Palomar-Green QSOs (Schmidt and Green 1983), Markarian Starburst and Seyfert galaxies (Huchra 1977), and normal galaxies (Schechter 1976). The bolometric luminosities for optical selected samples have been calculated accordingly to Soifer et al. (1986), apart from QSOs (Elvis et al. 1994). At low luminosities ($L_{\text{bol}} < 10^{11} L_{\odot}$) the IR luminosity function roughly obeys the slope of the optical function of normal galaxies, confirming that far-IR-emission of these galaxies is rather weak (e.g. Isobe and Feigelson 1992). Regarding the Markarian surveys both Starburst and Seyfert galaxies seem to be closer to IR-selected samples (in terms of the $L_{\text{IR}}/L_{\text{bol}}$ ratio) than to the

¹to calculate $L_{\text{IR}} = L(8 - 1,000 \mu\text{m}) = 4\pi \cdot D_L^2 \cdot [1.8 \cdot 10^{-11} (13.48 \cdot f_{12} + 5.16 \cdot f_{25} + 2.58 \cdot f_{60} + f_{100})]$ erg s⁻¹ (with f = flux densities, in Jy, at the given wavelength and D_L = luminosity distance of the source, in cm).

²an overview of the survey parameters and references to relevant *IRAS* databases is given in Soifer et al. (1984) and Sanders and Mirabel (1996).

optically selected interacting galaxies (e.g. Kennicutt et al. 1987; Sulentic 1989), in spite of the fact that only a few optically selected sources with $L_{\text{IR}} > 10^{11.5} L_{\odot}$ have been found.

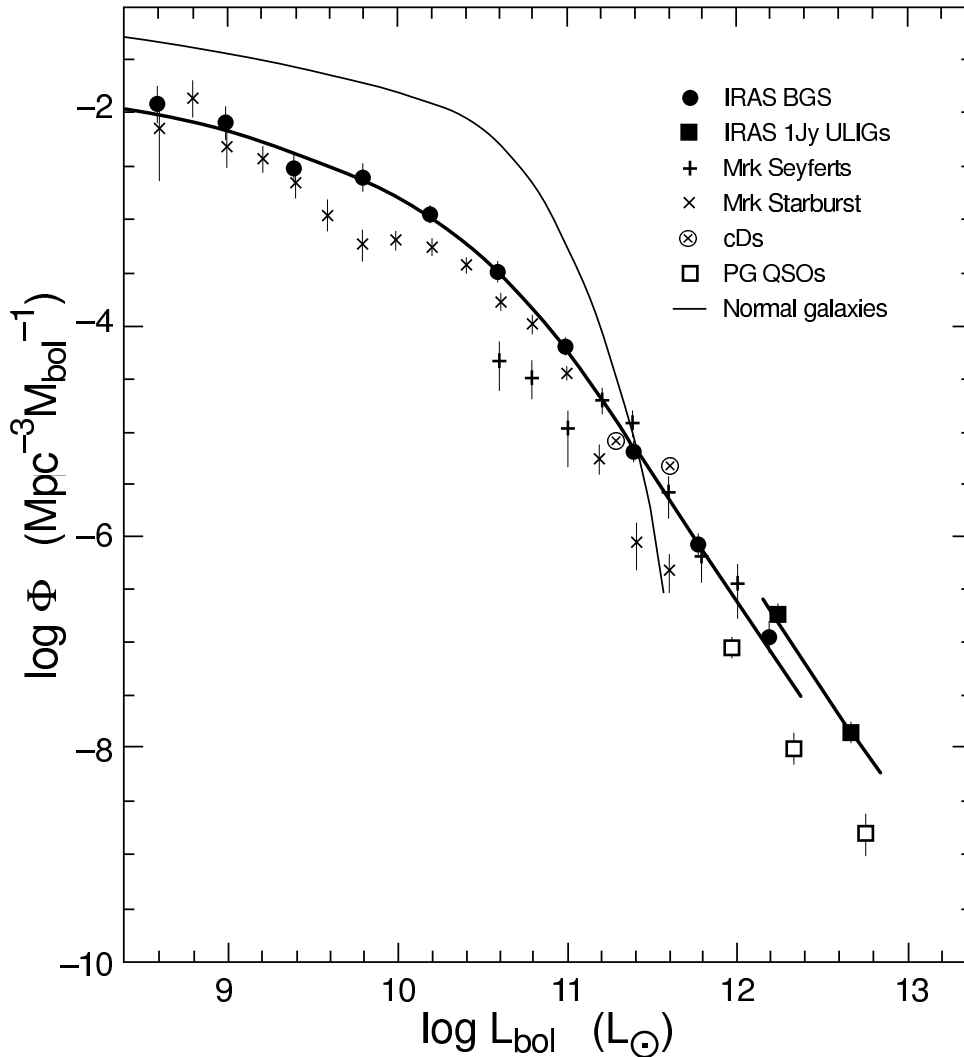


Figure 1.2: The luminosity function of infrared galaxies in comparison with other extragalactic sources (from Sanders and Mirabel 1996). The thick solid curve is a fit to the *IRAS*–BGS data points, whereas the thick line at the lower right connects the *IRAS* 1-Jy data points (for additional references see text).

Moreover, the luminosity function shows a strong steepening of the slope at luminosities above $L_{\text{bol}} \gtrsim 10^{10} L_{\odot}$. The very high luminosity tail exhibits a roughly parallel behaviour of the slopes of the IR luminosity function and the luminosity function of optically selected quasars. For a given luminosity the space density of *IRAS* galaxies is by a factor of a few higher than the density of the quasars (for $L_{\text{bol}} > 10^{12} L_{\odot}$). The observed excess of sources compared to the expected slope calculated from a simple Schechter function can be better fit by a combination of two power laws with slopes of $\lesssim -1$ at low luminosities and ~ -2.35 at $L_{\text{bol}} \gtrsim 10^{10.3} L_{\odot}$.

In addition, Figure 1.2 shows that *IRAS* galaxies exhibit an enormous range of luminosities. This variety can be also seen when looking at best-studied infrared galaxies like M 82 ($L_{\text{IR}} \approx 3 \cdot 10^{10} L_{\odot}$ and $L_{\text{IR}}/L_{\text{B}} = 10$) and Arp 220 ($L_{\text{IR}} \approx 1.6 \cdot 10^{12} L_{\odot}$ and $L_{\text{IR}}/L_{\text{B}} = 80$), with the tendency that the range of optical luminosities decreases with increasing IR luminosities.

ULIRGs appear to be more numerous (by a factor of $\sim 1.5 - 2$; Sanders et al. 1999) than optically selected quasars (with comparable bolometric luminosities; e.g. Sanders et al. 1988a, 1988b) and – besides of their high IR luminosities – they tend to be distinguished rather by their high IR/optical flux ratios. However, they are still relatively rare in terms of the different classes of extragalactic objects with $L_{\text{bol}} > 10^{11} L_{\odot}$. Following Figure 1.2 there is only one detection of an ULIRG expected within an (comoving) volume up to $z \sim 0.033$, in agreement with the observations (Arp 220 at $z = 0.0181$).

Finally, one has to keep in mind possible evolutionary effects in the luminosity function at the highest IR luminosities. This is suggested by comparing the space densities of ultraluminous infrared galaxies in the 1-Jy Survey with ultraluminous infrared galaxies of low redshift from the *IRAS*–BGS (see Sanders and Mirabel 1996 for details). They are informative of the kind of evolution, *i.e.* of pure number and/or of luminosity.

1.1.3 The spectral energy distribution

In the course of the large *IRAS* galaxy surveys first steps have been made to analyse the energy distribution of the luminous infrared galaxies by comparing their IR emission with radiation from other frequencies, aiming at a study of data covering the widest possible range of the electromagnetic spectrum.

The comparison between the spectral energy distribution (SED) of LIGs/ULIRGs and the related 'pure' AGN can be drawn when summarizing the spectral information known from different energy ranges of each type. Figure 1.3 shows the SED of the ULIRG NGC 6240. One remarkable result is the similarity of the emission from the radio band (for radio-quiet AGN) up to the IR part.

The best physical explanation of the spectrum so far is based on the synchrotron self-comptonization process, where relativistic electrons with a power-law distribution of energies produces a synchrotron power law spectrum over a wide range of energies under the influence of external magnetic fields. Even the high energy emission in the SED (up to hard X-rays) can be explained by this mechanism. This process gains in importance when the radiation density of the synchrotron emission becomes so high that the emitted photons are inverse-compton scattered off the electrons (which are the source of the synchrotron radiation).

Analyzing the SED can provide new insights into the origin of the emission. The first consequence is that the continuum is build up by multiple components - each component, *i.e.* physical

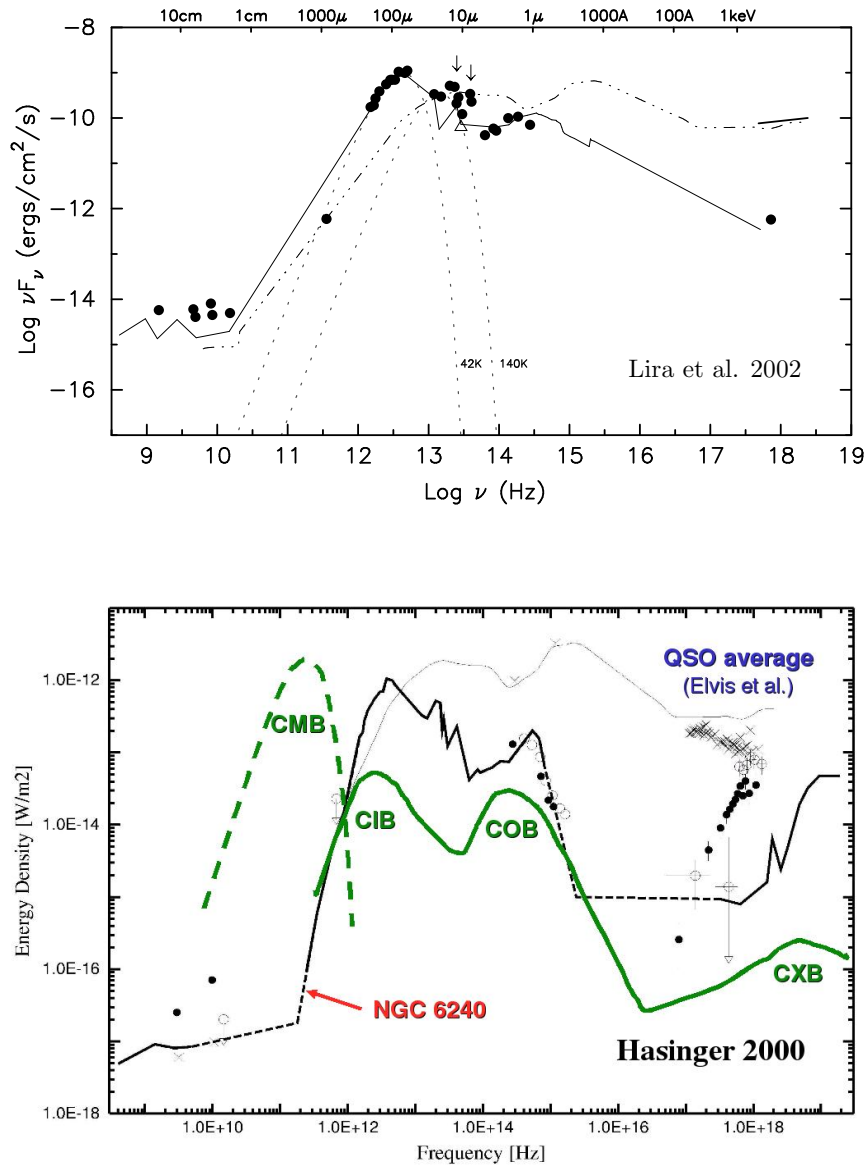


Figure 1.3: Upper plot: The spectral energy distribution of the obscured ULIRG NGC 6240 as observed by Colbert et al. (1994; *VLA*), Klaas et al. (1997; *ISO*), Lisenfeld et al. (2000; *SCUBA*), Scoville et al. (2000; *HST-NICMOS*), and Lira et al. (2002; *Chandra*) together with data extrapolated from Vignati et al. (1999; *BeppoSAX*) for the intrinsic (2.0 – 10.0) keV continuum (thick line). The continuous line marks the SED of “high-reddening” Starburst galaxies (Schmitt et al. 1997).

Lower plot: The intensity of the cosmic background radiation in different energy bands superposed by a scheme of the SED of NGC 6240. The black dashed regimes are not accessible to observations.

In both plots the average of an (unobscured) quasar template (Elvis et al. 1994) is overplotted; Lira et al. (2002): dash-dotted line, Hasinger (2000): thin line. These “ νF_ν – ν ”-plots are helpful since they show the total power per decade of energy, allowing to depict continuum shapes.

process, dominates the emission in a different range. The following parts give a summary of the most important features of the continuum emission.

Submillimeter- and Radio regime

Starting from the lowest energies the SED of LIGs/ULIRGs and of radio-quiet AGN are strongly decreased compared to higher energies. The starting point of this behaviour is called the "submillimeter break".

Continuum emission in the submillimeter (submm) regime, ($\sim 350 - 860$) μm , has been detected in a few of the brightest LIGs, in particular from Arp 220 (Emerson et al. 1984). Its submm emission (together with its far-IR radiation, see 1.1.3 on p. 8) can be explained by thermal emission from a single temperature dust model (with $T_{\text{dust}} \sim 60$ K). This interpretation has been confirmed by the work of Rigopoulou et al. (1996), where the authors analysed the submm emission of all ULIRGs in the *IRAS*-BGS. They claimed that their measurements are in very good agreement to the dust emission model. Moreover, Eales et al. (1989) and Clements et al. (1993) observed submm emission from numerous LIGs. In all sources the continuum of the far-IR/submm emission could be best fit by a dust model of a single temperature component ($T_{\text{dust}} \approx (30 - 50)$ K).

Since the early 1970s a tight correlation between the IR-flux and the radio continuum flux has been established across a wide range of galaxy types: normal, Starburst and Seyfert galaxies (van der Kruit 1971; Rieke and Low 1972; Dickey and Salpeter 1984; Helou et al. 1985; Sanders and Mirabel 1985; Wunderlich et al. 1987). Even for sources having IR luminosities different by several orders of magnitude this strong dependence appears to be valid. Nevertheless, the physical conditions to produce this correlation are still not fully understood, although there exist several models (e.g. Lisenfeld et al. 1996).

In order to explain the observations in the radio band (as well as in the IR) one has to propose that the nature of LIGs is based on ultra-compact Starbursts, possessing such high densities which the regions are optically thick to dust absorption for $\lambda \leq 25$ μm (*i.e.* with an extinction of $A_V > 1000$ m!). Another explanation favours a central AGN (presumably located inside a circumnuclear Starburst of 'little' extension) to produce the compact radio structure. According to Norris et al. (1990) compact cores (like in most of the ULIRGs) appear to be frequently associated with AGN and LIGs showing Seyfert-like optical spectra, but are rare among (optically selected) Starburst galaxies or LIGs with H II region-like spectra. This can lead to the assumption that Starbursts are the only heating source for the far-IR emission of the LIGs (having a strong radio component).

Infrared, optical and UV emission

Focusing on the IR emission (e.g. Sanders et al. 1988a; Soifer and Neugebauer 1991; van den Broek 1993) the emitted flux of LIGs/ULIRGs (per unit logarithmic interval) rises between $10 \mu\text{m}$ and $100 \mu\text{m}$ and reveal one strong peak at $\lambda \gtrsim (100 - 200) \mu\text{m}$ ("infrared bump"). It contains typically 30% of the total detected flux of the source (sometimes as high as 90%). A secondary peak around $1 \mu\text{m}$ (see Fig. 2 in Sanders and Mirabel 1996, p. 757; the "near-IR bump") forms the upper boundary of a local minimum at a few μm which carries $\lesssim 40\%$ of the $(2.5 - 10) \mu\text{m}$ luminosity. Both features are part of systematic variations of the shape of the spectral energy distribution in terms of the IR luminosity: the flux ratio f_{12}/f_{25} decreases whereas the ratio f_{60}/f_{100} increases with increasing IR luminosity. Several authors (e.g. Helou 1986; Rowan-Robinson and Efstathiou 1993) suggest that for low-luminous "normal" galaxies the secondary peak is a result of emission from dust near hot stars, in contrast to the stronger peak which is due to dust from a ring-like structure getting the energy from older stars. Going up in IR luminosity the combined emission of a Starburst component (with its peak at $\sim 60 \mu\text{m}$) and a warmer component (at roughly $25 \mu\text{m}$) becomes visible. The feature is often believed to represent warm dust, which is heated by an associated AGN and emission from mainly OB stars. According to the work of Sanders et al. (1988b) the mid-IR emission, *i.e.* ($\sim 5 - 40$) μm , of a small fraction of ULIRGs – the so-called 'warm' ULIRGs (with $f_{25}/f_{60} > 0.3$) – is at least one order of magnitude stronger than of the other ULIRGs. They are very useful to study evolutionary scenarios between ULIRGs and quasars (e.g. Sanders et al. 1988a, 1988b), since these 'warm' galaxies seem to include radio-loud galaxies as well as optically selected quasars. This assumption is supported by the analysis of the mean SED of AGN (see Elvis et al. 1994), but is in contrast to the SED of NGC 6240 (cf. Figure 1.3 on p. 6): the emission from the IR/submm bump, ($\sim 1 - 300$) μm – stronger than the neighbouring "big blue bump" (or "UV excess") at around $(0.05 - 1) \mu\text{m}$ – is presumably thermal emission coming from an extended disk of dust in a circumnuclear geometry surrounding an active nucleus. The big blue bump is assumed to be of thermal origin (with $T \simeq 10^{5 \pm 1}$ K; optically thick, *i.e.* blackbody emission). See the subsections 1.2.2 on p. 14ff and 1.2.3 on p. 20ff for detailed information on the physical nature of the various emission components.

Spectroscopic data of LIGs/ULIRGs (Lutz et al. 1996), gained with the *ISO*-SWS instrument (*ISO*-Short Wavelength Spectrometer), were combined to a diagnostic diagram. The strengths of low- and high-excitation fine structure lines and of the PAH feature are calculated for several fractions of an AGN contribution within a LIG/ULIRG. The "Polycyclic Aromatic Hydrocarbon" (PAH) feature at $7.7 \mu\text{m}$ originates in complex molecules built

up of benzene rings. According to this diagram the bolometric luminosity of NGC 6240 is mainly a result of star formation processes. The luminosity is dominated by dust emission in the far-IR. This is reflected in the SED: the energy output peaks in the dust band in the far-IR (as it is called above the "infrared bump"), in addition the PAH is present, as well as radio emission by synchrotron radiation characteristic for Starburst galaxies. Regarding the near-IR part the secondary peak is not as high as the strong dust emission peak, but it has a similarity to the overall energy distribution of extragalactic sources. Taking into account recent results from hard X-ray spectroscopic data performed by *BeppoSAX* (see section 3.2.1 on p. 47) a large fraction of the bolometric luminosity could be explained by an underlying very luminous, but heavily obscured AGN.

Although suffering from a large reddening in their optical spectra LIGs and ULIRGs show blue continua (e.g. Sanders et al. 1988a; Leech et al. 1994; Veilleux et al. 1995). By comparing the optical color index '41-50' (*i.e.* 4100 – 5000Å) of samples of mergers and normal galaxies with the equivalent width of the [O III]λ3727 line, Liu and Kennicutt (1995) found that 10 ULIRGs from the *IRAS*-BGS have – on average – a bluer color than normal galaxies. They supposed the presence of a (young) blue stellar population underlying the extinction-dominated spectra. This was confirmed by the analysis of the UV continua with its remarkable C IV and Si IV absorption lines (e.g. Sekiguchi and Anderson 1987).

Additional information about the underlying star formation and/or AGN activities can be obtained from emission-line spectra taken from LIGs (e.g. Armus et al. 1989; Veilleux et al. 1995). Kim (1995) and Veilleux et al. (1995) performed a comprehensive analysis of long-slit spectra of a complete subsample of sources in the *IRAS*-BGS, being added by a larger sample of ULIRGs one year later (Kim et al. 1996; cf. Veilleux et al. 1997). They took care that all three major classes of spectra (the low-excitation H II-region, the LINER, and the Seyfert) are represented in their compilation. The results are shown in Figure 1.4 (on p. 10). In low-luminosity galaxies, *i.e.* with $\log(L_{\text{IR}}/L_{\odot}) = 10 - 11$, these classes are represented similarly to normal spirals, where the H II-region nuclei are being the most frequent class ($\sim 65\%$) and the Seyfert galaxies comprising not more than $\sim 4\%$. By going up in IR luminosity, the fraction of Seyfert nuclei increases to $\sim 45\%$ for the ULIRGs at $\log(L_{\text{IR}}/L_{\odot}) > 12.3$, unlike the LINERs, because their fraction remains nearly constant ($\sim 33\%$) along IR luminosities with $\log(L_{\text{IR}}/L_{\odot}) > 10$.

The spectral information of near-IR data in comparison to the data of optical observations offers a powerful opportunity to probe the inner regions of these objects. For instance, analysing the shapes of the continuum can help to improve the diagnostics for disentan-

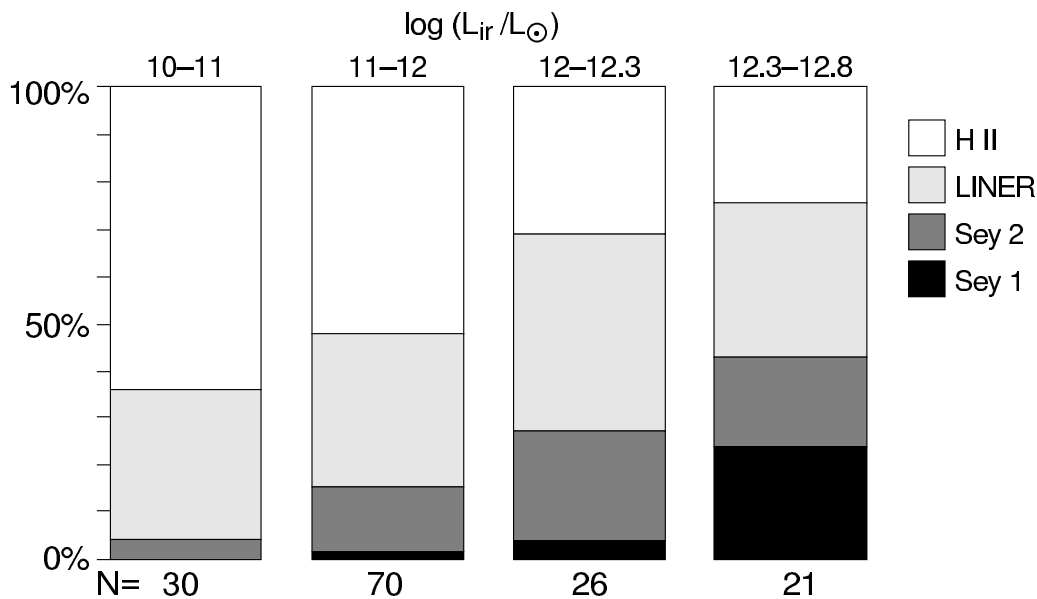


Figure 1.4: Nuclear emission classes for luminous infrared galaxies: relative fractions as a function of the IR luminosity (Kim 1995).

gling the AGN- from the Starburst-driven spectra (e.g. Armus et al. 1995a). A more detailed studies has been done by Rieke et al. (1985). They investigated relatively low-dispersion IR data for NGC 6240 and Arp 220 and claimed that the near-IR emission of NGC 6240 could be entirely related to a very powerful Starburst. On the other hand, in Arp 220 roughly half of the luminosity appears to be emitted from a Seyfert nucleus. In more recent papers, Armus et al. (1995a,1995b) could make use of high-quality data sets and analysed several IR lines in more details. Their works support the idea that at least 80 – 90% of the total IR luminosity result from an obscured AGN.

High-Energy radiation: X-ray emission and Superwinds

The first idea to use X-rays for investigating the class of luminous infrared galaxies came up when Rieke (1988) suggested that the presence of an (obscured) AGN in ULIRGs, suspected to be the dominant emission source (at least in the X-rays and the γ -rays), could be proven by analysing high energy emission.

Dust – associated with the molecular torus – is absorbing hard photons arising from the source, *i.e.* the disk or OB stars. Following the work of Tecza et al. 2000; Veilleux et al. 1995 and Iwasawa and Comastri 1998, the AGN in NGC 6240 is hidden by material absorbing the near-IR, optical, UV and X-rays (between $\sim 2 \mu\text{m}$ and 15 keV). The UV to soft X-ray continuum emission is completely obscured. Therefore, the only observable component in this range is the SED of a pure Starburst component together with a strong reprocessed Fe-K α line at 6.4 keV (e.g. Komossa et al. 2003, Boller et al. 2003).

The comparison between local ULIRGs and obscured AGN (of type 2, see 1.2.3 on p. 21) reveal a similarity of their SEDs. This gives evidence for hard X-ray sources (detected with *XMM-Newton*) being the high-redshift analogues of heavily obscured AGN similar to NGC 6240. Griffiths and Padovani (1990) proposed that LIGs could provide a significant contribution (up to 40%) to the X-ray background radiation.

In a recent publication Boller (1999) reported on 28 sources matching a cross-correlation analysis between a sample of ULIRGs from the *IRAS* 1.2 Jansky redshift catalogue (Fisher et al. 1995) and the *ROSAT* All-Sky Survey Bright Source Catalogue (the RASS-BSC; Voges et al. 1999) and from *ROSAT* (Trümper 1990) pointed observations. The ratio of X-ray- to far-IR-luminosity³, $L_{(0.1-2.4)\text{keV}}/L_{(40-120)\mu\text{m}}$, was calculated to be in the range between 10^{-1} and 10^{-4} , *i.e.* covering four orders of magnitude. Based on the paper by Boller and Bertoldi (1996) this ratio is roughly $10^{-2.5}$ for pure star-forming processes (with a time-averaged star formation rate SFR). For values above $\sim 10^{-2.5}$ galaxies should be predominantly powered by accretion processes. The L_X/L_{FIR} -ratio is in good agreement with the diagnostic diagram made from *ISO-SWS* measurements. Both show that *ROSAT*-selected sources are mainly powered by a Starburst, and that the AGN contribution is less than 50%. In 2001 Xia et al. correlated the *IRAS*-PSCz (a complete galaxy redshift survey adapted from the *IRAS* PSC; Saunders et al. 2000) with the RASS-BSC plus *ROSAT* *PSPC* and *HRI* archival data. The sample contains 35 ULIRGs; 20 sources are also included in the work of Boller (1999), as well as 15 new ULIRGs. The luminosity ratio $L_{(0.1-2.4)\text{keV}}/L_{(40-120)\mu\text{m}}$ spreads over five orders of magnitude, showing the diversity of the power source in ULIRGs (from strong accretion processes to a powerful Starburst activity, with comparable contributions from both energy sources in between for just a few of the objects).

Mapping campaigns using *ROSAT* have been performed on a few objects, in particular M 82 (e.g. Bregman et al. 1995) and Arp 220 (Heckman et al. 1996). Both sources show clear signatures of diffuse emission (with $T_{\text{kin}} \sim 10^7$ K), which extends into the galactic halos. They are assumed to be the outflow of gas, being ejected from the active nuclear region ("superwinds"). Evidence for these flows in the X-ray regime as well as in the optical range has been published by e.g. Heckman et al. (1990, 1996). They showed that the combination of the kinetic energy from supernovae and stellar winds from luminous nuclear Starbursts is responsible for the outflows on large scales. These flows are the source for (shock-)heating and accelerate the neighbouring gas in the circumnuclear

³Boller (1999) used the range of (40 – 120) μm as definition for the far-IR band, whereas this thesis makes use of the definition by Sanders and Mirabel (1996) with far – IR \equiv (40 – 500) μm :

$$L_{\text{FIR}} = L(40 - 500 \mu\text{m}) = 4\pi \cdot D_L^2 \cdot [1.8 \cdot 10^{-11} (2.58 \cdot f_{60} + f_{100})] \text{ erg s}^{-1}; [D_L] = \text{cm}, [f_{60}] = [f_{100}] = \text{Jy}$$

regions. "Superwinds" are supposed to play a major role in the process of enriching the interstellar medium. Applying a mass loss rate of

$$dM/dt = 4 \cdot L_{\text{far-IR}} / (10^{11} L_{\odot}) M_{\odot} \text{ yr}^{-1}$$

to Arp 220 leads to an injection mass of $\sim 5 \cdot 10^8 M_{\odot}$ in metals and an (mechanical) energy release of $(10^{58} - 10^{59}) \text{ erg s}^{-1}$ within a lifetime of $(10^7 - 10^8)$ yrs. According to Heckman et al. (1990), the total mass-injection rate is $\sim 2 \cdot 10^7 M_{\odot} \text{ Mpc}^{-3}$ (assuming no cosmological evolution and using a luminosity function similar to Figure 1.2 on p. 4), with 25% being metals.

1.1.4 The key issue:

The relative fraction of X-ray and IR emission of ULIRGs

One of the most crucial questions about the LIGs and ULIRGs is the nature of the underlying power source, responsible for the huge energy output: either an AGN, an extreme Starburst or the sum of both.

Sanders et al. (1988a) showed that the LIGs can be well described assuming an AGN as the central source, enshrouded by a huge amount of dust. In addition, several studies of LIGs have come to the result that the AGN phenomenon is the dominating process of powering luminous infrared galaxies (e.g. Lonsdale et al. 1993). When analysing broad emission lines in the near-IR and optical regime Veilleux et al. (1999) found that roughly 25 – 30% of the sources do show such lines, as they are indicative of an AGN activity (see Sanders 1999 for a support of the AGN-dominated idea and 1.1.3 on p. 8 for describing a diagnostic diagram for LIGs/ULIRGs according to Lutz et al. 1996).

But, for the majority of the low-luminous *IRAS* galaxies and most samples of ULIRGs (e.g. Goldader et al. 1995) they seem to be dominated by star formation processes (e.g. Veilleux et al. 1995). This impression is strengthened by measuring the far-IR as well as the radio properties of LIGs shows a clear sign of a compact Starburst residing in the central region (Condon et al. 1991, a Starburst-motivated discussion can be found in Joseph 1999).

Like in NGC 7679, there are a few cases known, where both parts play a significant role (Pogge and Eskridge 1993; Veilleux et al. 1995).

Finally, we are left with several issues of great importance. The following list should be considered as an overview of topics related to the field of galaxy interaction and thermal/non-thermal energy sources.

- **The physical properties of Starbursts in interacting galaxies,**
relating Starburst properties – like the star-formation rate (SFR) and efficiencies, ages,

and durations of starbursting – to the dynamical properties of the interaction processes, properties of the X–ray emitting gas (e.g. chemical composition),

- **The properties and physical nature of ultraluminous infrared galaxies,** identification of the nature of the power source and its properties (see above), relation to other Starburst galaxies and/or quasars in general,
- **The triggering mechanism of star formation in interacting galaxies,** important for all classes of galaxies, determine the time scale for star formation, explain the high efficiency of star formation, connection nuclear Starburst – AGN activity,
- **The cosmological implications of interaction/merging and AGN processes in galaxies** relation between local and high- z galaxies (ULIRGs as local sources of the high-luminosity tail of mergers), constraints on the production fraction of stars within interacting galaxies (as well as a function of the lookback time).

Answering this questions require many objects to study. There exist a lot of papers addressing particular problems of this list. In order to understand both mechanisms of activity the following two sections will give a summary about these phenomena in galaxies.

1.2 Active Galactic Nuclei as a power source

The fundamental work of Karl Seyfert (1943) opened the door for an incredible and tremendous progress in understanding galaxies and their physical properties and is the baseline for understanding the Seyfert phenomenon.

1.2.1 The central engine and the accretion disk

The name "Active Galactic Nucleus" (AGN) is a generic term for a lot of different objects, like quasars, Seyfert galaxies, Blazars, Low-Ionization Narrow Emission-line Regions (LINER) as well as radio- and X–ray-galaxies. Their common property is the non-thermal origin of the observed spectra, not describable by Starburst activity. The prevailing picture of an AGN assumes a black hole of a huge mass, $M_{\text{BH}} \approx (10^4 - 10^{10}) M_{\odot}$, accreting matter from its surroundings and producing bolometric luminosities of $L_{\text{bol}} \gtrsim 10^{10} L_{\odot}$. The efficiency of energy conversion (in terms of the rest energy) for fusion of hydrogen into helium ($\epsilon \sim 0.7\%$) is more than one order of magnitude less than the accretion process onto a compact object. Therefore, the fundamental physical process in AGN is the conversion of potential energy of infalling material into kinetic energy accompanied by its high acceleration rather than thermonuclear reactions.

It is assumed that many AGN emit radiation at a considerable fraction of their Eddington luminosities. Regarding the ULIRGs their high luminosities correspond to an accretion rate of the order of one $M_{\odot} \text{ yr}^{-1}$, implying black hole masses of $M_{\text{BH}} \gtrsim 10^7 M_{\odot}$ with time scales of doubling their masses of the order of 10^7 yrs (for an exponential growth; compared to the black hole masses of spiral galaxies with $10^6 M_{\odot}$ to a few $10^7 M_{\odot}$). Therefore, the AGN activity is most probably a temporary event in the evolution of a galaxy.

In order to conserve angular momentum and to consider interactions between particles the matter cannot fall into the black hole on direct paths but has to form a disk-like structure, called the "accretion disk"; geometrically thin (*i.e.* thickness/radius $\ll 1$) but optically thick (*i.e.* one mean scattering or absorption process of a photon moving across the disk). The matter is supposed to move according to Keplerian motion in general ($v_{\text{Kepler}} \sim (M_{\text{BH}}/R)^{1/2}$), as it is observed in the velocity gradients of NGC 4258 (Greenhill et al. 1995). The transporting mechanism of angular momentum outwards is probably due to turbulent effects (the differential rotation causes shear viscosity, parameterized by the α -mechanism; Shakura and Sunyaev 1973) and magnetic (rotational) instabilities (Balbus and Hawley 1991, review: Schramkowski and Torkelsson 1996). All heat energy produced in the disk is being released by radiation (without advection) and can be described by black body emission with an effective temperature $T_{\text{eff}} \propto R^{-3/4} \cdot M^{-1/4}$, where R is the radius of the disk and M is the mass of the central source. Important spectral features are Compton reflection and fluorescence processes, resulting in observable spectral features (see the next subsection 1.2.2).

1.2.2 X-ray properties

The following list summarizes the most important features of an AGN spectrum, with respect to the X-ray- and low γ -ray-regime (Figure 1.5).

The soft excess and the warm absorber

Due to frictional processes the inner regions of the disk are heated up to temperatures of $T > 10^5$ K. This leads to an immediate radiation of thermal (as a black body) and non-thermal emission (caused by inverse Compton scattering reactions and synchrotron emission) in the vicinity of the black hole. All of them are preferentially emerging in the optical, UV, EUV, and the X-ray regime (e.g. Blandford et al. 1990). A superposition of black bodies with different temperatures located in different regions of the disk may cause the optical-UV feature called the "big blue bump", whereas observations in the "soft" X-ray regime, (0.1 – 1.5) keV, reveal an excess in emission well above the power law. It is very likely that black body emission with $T \sim 10^{5\pm 1}$ K, as expected from an α -

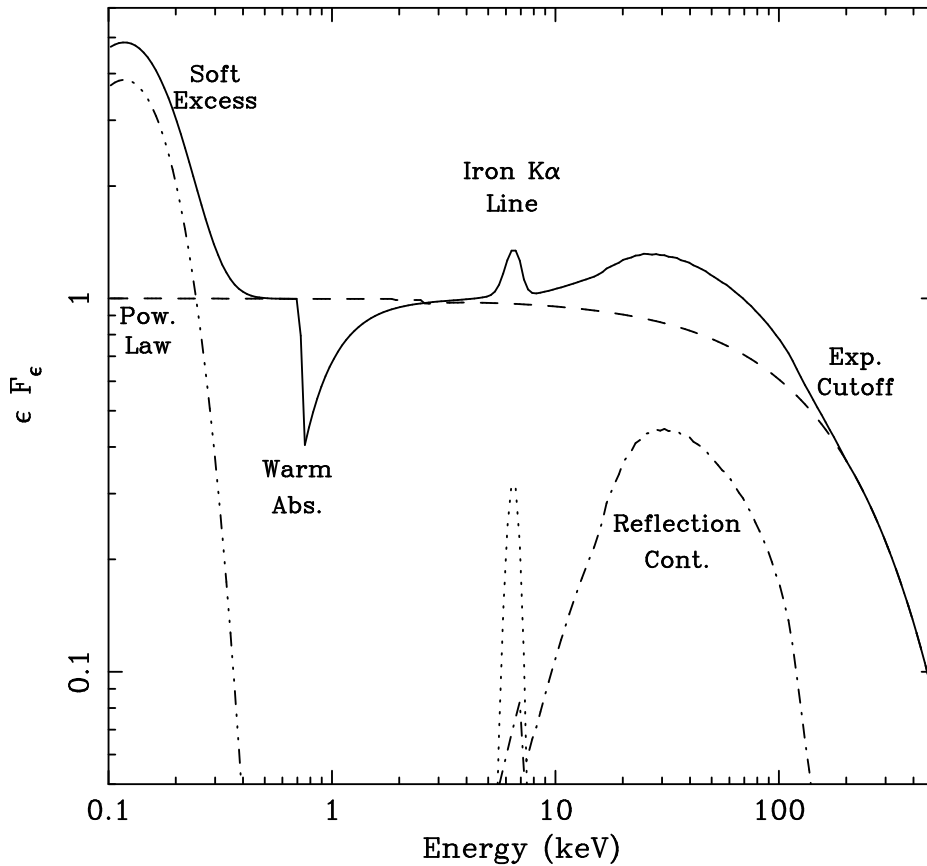


Figure 1.5: Schematic diagram of the X-ray and low γ -ray spectral features of an AGN, *i.e.* typical for a Seyfert 1 galaxy (Fabian 1998). All components are shown relative to the direct power law component.

parameterized disk, is the underlying mechanism to produce these features (e.g. Zhou et al. 1997).

Being the high energy tail of the "big blue bump", the so-called "soft excess" can be observed in the low energy X-ray band. Due to its inverse dependence on the mass of the black hole (see ch. 1.2.1 on p. 14; Kembhavi and Narlikar 1999) the disk temperature has a large effect on the soft X-ray emission of low-mass AGN, as Narrow-line Seyfert 1 galaxies (NLS1) are supposed to be.

In addition, the soft X-ray range is imprinted by several absorption features – spectral edges of oxygen (e.g. O VIII at 0.87 keV), carbon, and other ions, as well as resonant absorption lines and an unresolved transition array (UTA, a complex resonance absorption structure; Sako et al. 2001, Netzer 2004). This fact is likely due to the presence of a so-called "warm absorber", *i.e.* a variable ionization structure of matter in the line of sight (one or more gas clouds with $T_{\text{wa}} \gtrsim 10^6$ K).

The canonical power law spectrum

Assuming a power law of $f_\nu \sim \nu^{-\alpha}$ (in units of $\text{erg s}^{-1} \text{keV}^{-1}$) the best-fit energy index is $\alpha \sim 0.7 \pm 0.2$ (Mushotzky and Ferland 1984, confirmed later by Pounds et al. 1990 and Nandra and Pounds 1994): The amount of energy per decade ($\nu f_\nu = \epsilon F_\epsilon$) is nearly independent on X-ray energies below 10 keV and increases slightly with growing frequencies (Note: the power law in Figure 1.5 is normalized to unity at 0.1 keV). The power law originates via inverse-Compton scattering processes (IC) of radiation following a blackbody spectral shape from an accretion disk by a hot thermal electron gas. This gas is located in an "accretion disk corona" above the disk (Haardt and Maraschi 1991; Svensson and Zdziarski 1994; review: Kujipers 1995). This component can exceed up to a few hundreds keV, visible only in observations of highest energies. Moreover, IC scattering processes of a *non-thermal* momentum distribution of the electrons can result in a similar power law (e.g. Yaqoob 1992).

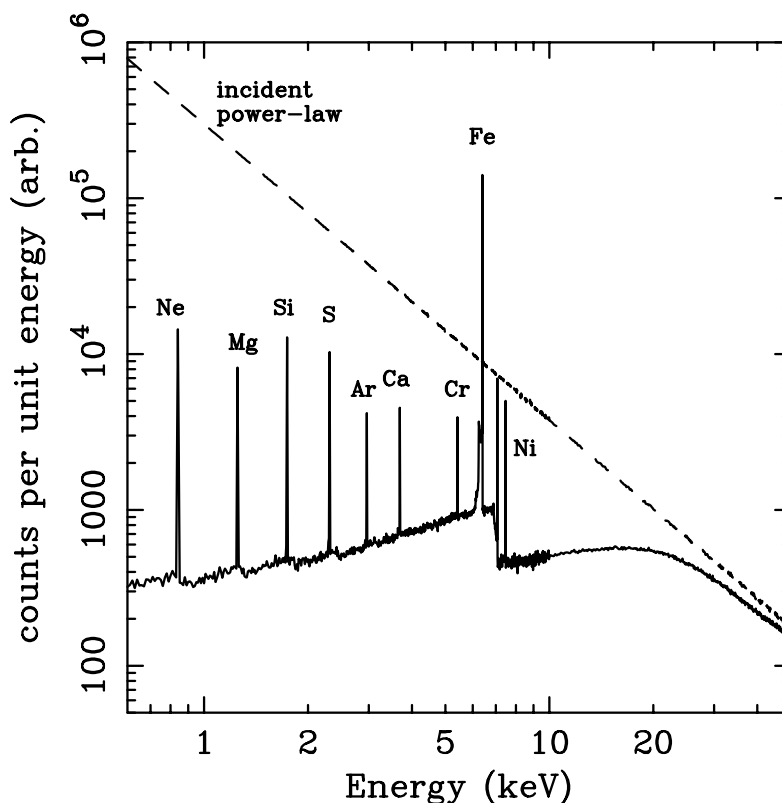


Figure 1.6: Reflection spectrum of an accretion disk caused by an incident power law. Based on a Monte Carlo algorithm the simulation assumes a cold and semi-infinite slab of gas (with cosmic abundances). An observation would contain the sum of the power law continuum and the reflection spectrum (Fabian et al. 2000).

The reflection hump (reflection continuum)

An important result of the Japanese *Ginga* mission (launched in 1987) was the discovery of a multicomponent structure of the emission in the (1 – 30) keV range; the incident power law emission is superimposed by an additional (reflection) continuum – a hump in energies up to some hundreds keV, which has been observed in many AGN spectra (Pounds et al. 1990; Matsuoka et al. 1990). This feature is assumed to originate via inelastic Compton scattering of high energy photons off low-energy electrons (“Compton reflection” off a cold gas, the accretion disk, e.g. Guilbert and Rees 1988; Zdziarski et al. 1990). As the photoelectric absorption cross section above 0.1 keV decreases with energy according to $\sim E^{-3}$ (regardless of the absorption edges, *i.e.* the binding energies of the various electron energy levels) the cross section of the electron Compton scattering remains almost constant up to a few tens of keV. Both cross sections are equal at ~ 10 keV (Lightman and White 1988; George and Fabian 1991) assuming the matter is completely neutral and the element abundances are close to the cosmic values. The reflection fraction may reach nearly 100% for very high ionization states of the disk.

The fluorescence emission

Fluorescence is a radiative emission process without any heat production occurring instantaneously, e.g. after a photoelectric absorption process. X-rays photoionize an atom by getting an electron out of the inner shell. The ionized atom - becoming excited - can de-excite either by radiative transitions (the vacancy is then filled by an electron from a higher energy level under the emission of a photon) or by the Auger effect (*i.e.* by a radiationless transition of an electron to the vacated state with a subsequent release of an outer-shell electron due to the energy difference). The energy of the absorption edges and the energy of the fluorescent photons depend on the state of ionization, as it is expected because of the shielding effect of the electrons in different shells to the nuclear charge.

The fluorescence yield $Y_Z^{K, L, M, \dots}$ (see Bambynek et al. 1972 for a review) represents the probability that the excited ion will de-excite via fluorescence rather than auto-ionization (*i.e.* ejection of Auger electrons). In a large ensemble of atoms this quantity gives the ratio of the photon number when the vacated state in the shell is filled to the number of vacancies in the shell due to ionization. It depends on the ionization state of the plasma (see Figure 1.7, right); in the case of neutral iron, the probability is $Y_{26}^K = 0.305$ and therefore the yield for $K\beta$ is roughly 9 times smaller because of the 150:17 relative intensity ratio between both lines (Matt et al. 1992).

The product of fluorescence yield and abundance of the chemical elements gives information about the radiative intensity of the K-shells of a particular element in a plasma.

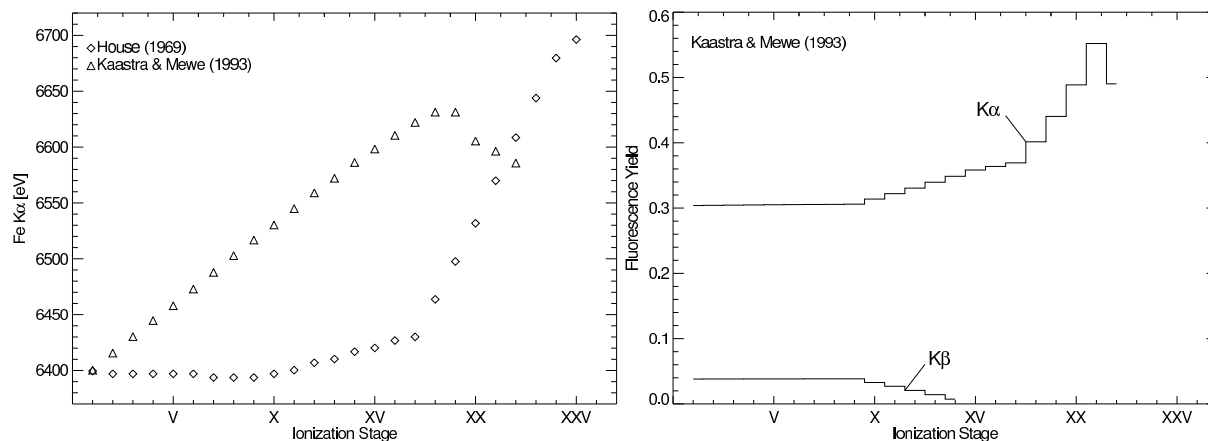


Figure 1.7: **Left plot:** Iron $K\alpha$ line energies as a function of the ionization stage. The data marked with diamonds are experimental values. The large energy change (at stage IX and XVII) are due to the removal of the last ($n=3, l=2$)- and ($n=3, l=0$)-electron. (The data point at $E_{\text{Fe},K\alpha} = 6.97$ keV for the XXVI stage is not shown.) **Right plot:** Fluorescence yield of iron $K\alpha$ and $K\beta$ as a function of the ionization state (after Kaastra and Mewe 1993). Both plots are taken from Wilms (1996).

Carrying out the calculations reveals that the most relevant element in the X-ray band in terms of the fluorescence emission is iron (see Fabian et al. 2000 and Reynolds and Nowak 2003 for reviews). The rest energy of the $K\alpha$ line⁴ is given by $E_{\text{FeI},K\alpha} = 6.4$ keV⁵ and of the $K\beta$ line $E_{\text{FeI},K\beta} \approx 7.06$ keV. The ionization threshold for iron is close to the $K\beta$ line at $E_{\text{FeI},K_{\text{edge}}} \approx 7.1$ keV (the Fe K edge). Proceeding to ionized states the number of outer electrons decreases and therefore are less effective in shielding the nuclear charge, leading to an increase in the energy gaps between the shells (Figure 1.7 on p. 18; left). For Fe XXVI – hydrogen-like or Ly α -like iron – the $K\alpha$ rest energy reaches $E_{\text{FeXXVI},K\alpha} \approx 6.97$ keV (not shown in Figure 1.7; see Makishima (1986), Krolik and Kallman (1987) and George and Fabian (1991) for data and references).

The Fe-K emission lines are produced by fluorescence (see Figure 1.6 on p. 16), whereas the Fe edge is made by (Compton scattered) reflection from the primary continuum (power law) source at cold matter, where the nature of the reflector is either the molecular torus (see ch. 1.2.3 on p. 20) or the cold outer regions of the accretion disk. In comparison to Galactic black hole candidates this interpretation seems to be very conceivable, since their accretion disk is supposed to be much hotter and therefore higher ionized.

⁴According to the nomenclature for multi-electron systems the $K\alpha$ line(s) arise(s) when an electron moves from the L shell (with the principal quantum number $n = 2$) to the K shell (with $n = 1$) due to fluorescence. In the same sense is the $K\beta$ line the fluorescent transition from the M shell ($n = 3$).

⁵Strictly speaking, this line is a doublet - comprising of the $K\alpha_2$ line (from the L_2 sub-shell) at $E = 6.391$ keV and the $K\alpha_1$ line (from the L_3 sub-shell) at $E = 6.404$ keV (with a line intensity ratio of 1:2), but not resolvable by the current detectors.

The illumination of a cold slab by incident X-ray photons with energies above the absorption threshold results in an iron line emission with an equivalent width (EW) of

$$EW = \frac{\int d\Omega \int_{E_{\text{threshold}}} dE F(E) Y_Z^K (1 - e^{-\tau_{\text{threshold}}})}{4\pi F_{\text{cont}, E=E_{\text{line}}}},$$

where the integration over the directions considers only photons which can be seen by the observer. The continuum flux is assumed to be the sum of the direct component and the Compton-reflected part. For the optical Thomson depth $\tau_{\text{threshold}} \leq 1$ and by using Y_Z^K for iron Blandford et al. (1990) calculated

$$EW(K\alpha) \simeq 300 \left(\frac{\Delta\Omega}{4\pi} \right) \cdot \left(\frac{Z}{Z_{\odot}} \right) \cdot \tau_{\text{threshold}} \text{ eV}.$$

With $\Delta\Omega \simeq 2\pi$, $Z = Z_{\odot}$ and $\tau_{\text{threshold}} \simeq 1$ an $EW(K\alpha) = 150 \text{ eV}$ can be expected (for a fixed geometry). This is in good agreement with the observations: Nandra and Pounds (1994) detected Fe-K emission lines in 25 of 27 Seyfert galaxies, having a mean EW of $(140 \pm 20) \text{ eV}$. However, absorbing material in the line-of-sight – instead of fluorescence processes – cannot account for such high EW values (Makishima 1986).

The first detection of Fe-K emission lines at energies of $\sim 6.4 \text{ keV}$ ⁶ dates from the late 1970s (Cen A; Mushotzky et al. 1978), but during the *Ginga* and *EXOSAT* missions in the 1980s there was growing evidence that this line feature is very common to all AGN (e.g. Mushotzky et al. 1993, Nandra and Pounds 1994, Tanaka et al. 1995, Yaqoob et al. 1995, Iwasawa et al. 1996a). The research on active galaxies became a subject of high interest, especially due to the *ASCA* detection of the unusual broad, two-pronged iron line profile in the Seyfert 1 galaxy MCG -6-30-15 (Tanaka et al. 1995). The prominent red (*i.e.* lower energetic) "wing" of the line is a clear signature of general-relativistic effects taking place at the inner-most regions of the accretion disk close to the event horizon of the black hole (Fabian et al. 1995, Iwasawa et al. 1996b, Fabian and Vaughan 2003).

Koyama (1992) investigated the X-ray emission of 30 narrow-line AGN (including *IRAS* selected Seyfert 2 galaxies) and found similar properties between Seyfert 1- and Seyfert 2 galaxies, pointing out that the latter shows strong absorption at low energies and an iron line emission. In particular, the intrinsic X-ray luminosities of Seyfert 2 galaxies are within the range of the Seyfert 1 luminosities, leading to the idea, Seyfert 2 galaxies are obscured Seyfert 1 galaxies (Antonucci 1993; e.g. Mrk 3: Awaki et al. 1990).

However, the X-ray spectrum of NGC 1068 has no indication of significant absorption ($N_{\text{H}} < 10^{22} \text{ atoms cm}^{-2}$). Its $(2 - 10) \text{ keV}$ luminosity of $\sim 10^{41} \text{ erg s}^{-1}$ is intrinsically

⁶The energy value is given in the rest frame of the source. The correction for the redshift is usually done during the model fitting procedure.

much fainter than that of a usual Seyfert 1 galaxy (Koyama et al. 1989) and the iron line at $E = (6.6 \pm 0.1)$ keV has an equivalent width of $EW = (1.3_{-0.3}^{+0.7})$ keV. The X-ray emission is only due to a scattering gas located spherically symmetric around the nucleus and is not due to the penetration of a torus (where $N_H \sim 10^{25}$ atoms cm^{-2} are assumed). The reflection efficiency is a few percent

1.2.3 Primary components of an AGN

AGN appear to be a rather inhomogeneous class of sources (in the different energy bands, see Figure 1.8 on p. 22). There is a common agreement that all observational facts are based on the simple assumption that the diversity of AGN is just an orientation effect (Antonucci 1993) and not because of distinctive intrinsic properties. In addition, it is now established that NLS1 and BLS1 (Broad-line Seyfert 1 galaxies) are connected through a continuum of physical properties. The dominant parameters are the mass and the accretion rate of the central black hole.

Both, observational properties and theoretical modelling of AGN (and also related objects; Weedman 1986), support the following components to be present in a "standard" AGN (relevant for the X-ray regime):

- **The super-massive black hole,**
sitting in the centre with a mass of $M_{\text{BH}} \approx (10^4 - 10^{10}) M_{\odot}$ to provide the required gravitational potential for accreting material. Studying its properties means to study the properties of matter in its vicinity, where general-relativistic effects have a strong impact on, for instance, line emission profiles (like the Fe-K α line), etc.,
- **The accretion disk,**
in order to thermalize the infalling matter and to produce the radiation in different energy bands, e.g. the "big blue bump" in the optical, UV and EUV bandpass; its size is roughly 1000 Schwarzschild radii. One of the models discussed explains the soft X-ray excess as the high energy tail of the radiation coming from the accretion disk,
- **The dusty (molecular) torus-like structure,**
geometric structure with an inner radius of \sim one pc. The composition is presumably dust and molecular gas of high optical opacity, which is heated by the central source and reradiates into the IR regime and in the Fe-K α line (at 6.4 keV) in reflection. Thus, it is responsible for the obscuration of the inner parts of an AGN and LIGs/ULIRGs,
- **The jet structure**
is a striking morphological property of AGN first observed in radio-loud sources. The radio emission is produced by synchrotron-emission of relativistic electrons, which is

also the source of the power law emission in the hard X-rays and γ -rays (via IC processes of radio-photons scattering at relativistic or thermal electrons, via synchrotron-self-comptonization or via pair-reprocessings). Jets are observed to be ejected perpendicular to the plane of the accretion disk and their length can exceed one Mpc (see e.g. M 87: Schreier et al. 1982; 3C 273: Marshall et al. 2001).

In the local universe the Seyfert galaxies represent the majority of AGN, with bright cores (usually spiral galaxies) with luminosities of $L_{\text{bol}} \approx (10^{43} - 10^{45}) \text{ erg s}^{-1}$. AGN are classified as Seyfert galaxies by the blue magnitude: $M_B > -21.5^{\text{m}} + 5^{\text{m}} \cdot \log(h_0)$, with $H_0 = 100 \cdot h_0 \text{ km s}^{-1} \text{ Mpc}^{-1}$ (Schmidt and Green 1983).

In general, all Seyfert galaxies show broad emission lines in their optical spectra, indicating the presence of a strong ionising source of radiation. Seyfert galaxies of type 1 exhibit permitted lines with a FWHM ranging from 500 to 10^4 km s^{-1} . The forbidden lines remain narrow (e.g. for [O III], FWHM: a few 10^2 km s^{-1}). Dense gas clouds are moving with high velocities (deduced from the line FWHM) around the centre (the "broad line region", BLR). In addition, Seyfert 1 galaxies are X-ray bright (up to a large fraction of the bolometric luminosity). In contrast to this, optical spectra of Seyfert galaxies of type 2 are characterized by narrow permitted and forbidden emission lines (Osterbrock 1989). The region of narrow lines (NLR) is much further away from the centre, resulting in lower velocities of the gas clouds (e.g. Peterson 1997). Seyfert 2 galaxies are in general less X-ray-luminous than the Type 1 Seyferts because of their heavy absorption by neutral matter.

Observations on Seyfert galaxies led to the conclusion that they can be divided into subclasses, from Seyfert 1.1 to Seyfert 1.9, where absorption is increasing. The idea of a torus-like structure came up when Antonucci and Miller (1985) and Miller and Goodrich (1990) published that the narrow lines of NGC 1068 (and other Seyfert 2 galaxies) are rather broad (*i.e.* Sy-1-like) when observed in linear polarized light. They argued that the broad lines in the spectrum are produced by reflection processes caused by a population of free electrons above a torus, maybe in a high-ionized medium. In the period following, "unified schemes" try to combine all observational facts of AGN by using an obscuring torus; they consider the different classes of AGN as a result of an orientation effect between the observer and the torus.

In this picture, a Seyfert 1 galaxy is believed to be an AGN where the observer can view the inner region within the opening angle of the torus (*i.e.* NLR and BLR; a "face-on" view), whereas in Seyfert 2 galaxies the BLR appears to be hidden by the torus ("edge-on" view). The latter are called *Compton-thick*, if the observed column density is higher than the value given by the inverse Thomson cross section ($N_{\text{H}} \geq \sigma_{\text{T}}^{-1} = 1.5 \cdot 10^{24} \text{ atoms cm}^{-2}$). Matt (2000) interprets *Compton-thick* Seyfert 2s as sources with high compact thick material (the torus) and *Compton-thin* and intermediate Seyferts as galaxies with lanes of dust at larger distances from the centre.

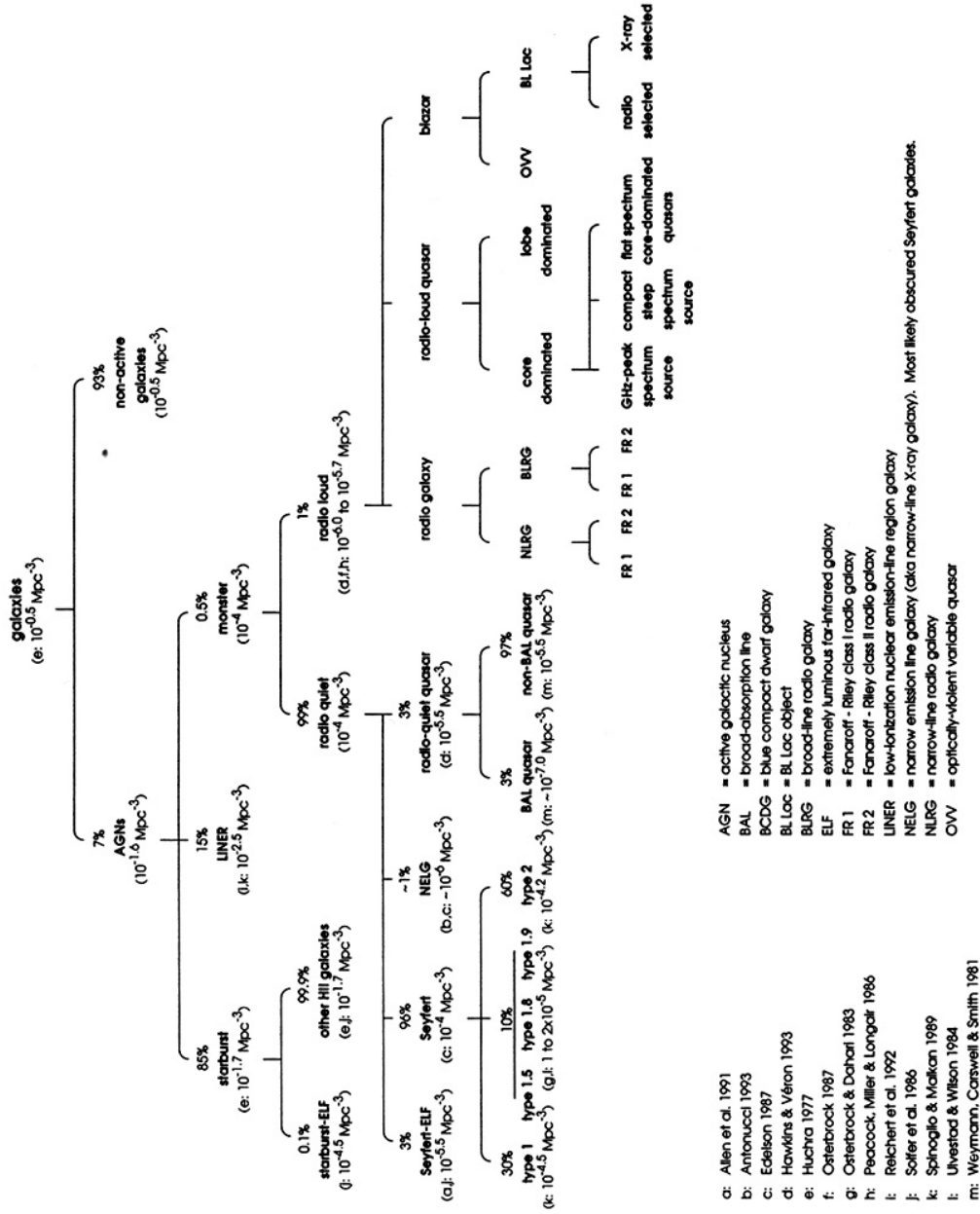


Figure 1.8: Overview of the diverse classes of active galaxies and rough estimates of their (comoving) space densities (Note: the abbreviation 'ELF' stands for the LIGs/ULIRGs in combination with the power source given and 'NELG' for the NLS1s; see the left side of the diagram; taken from Roy 1994)

It is generally accepted that local Seyfert 2 galaxies may often be obscured. However, Boller et al. (2000) have found a large absorption towards the radio-loud quasar GB 1428+4217 at soft X-rays. This source, with a redshift of $z = 4.72$, gives evidence for the idea that obscuration occurs for high-luminosity AGN at high redshifts. Recent results on the analysis of the cosmic X-ray background radiation give further evidence for the existence of a large population of heavily absorbed AGN as detected by deep *XMM-Newton* and *Chandra* surveys in the Lockman Hole (e.g. Fabian 2004; Hasinger 2002; Lehmann et al. 2002; Matt 2002; Hasinger 2001 and references therein).

1.2.4 The role of absorption

In the late 1990s it became clear (e.g. Turner et al. 1997a) that the X-ray spectra of most of the Seyfert 2 galaxies show a power law shape absorbed by large column densities of hydrogen matter (of the order of $N_{\text{H}} = 10^{22} - 10^{24}$ atoms cm^{-2}), several times larger than the value of $N_{\text{H}} < 10^{22}$ atoms cm^{-2} observed in many Seyfert 1 galaxies. Figure 1.9 shows the influence of photo-electric absorption on X-ray emission due to large column densities of obscuring matter. Applying different N_{H} values on an incident power law spectrum⁷ ($f_{\nu} \propto \nu^{-\alpha_x}$ with $\alpha_x = 1.0$) the observed X-ray spectrum in the soft band, (0.5 – 2.0) keV, is gradually becoming harder (i.e. α_x is decreasing) with increasing density up to the point where the transmitted flux is not detectable anymore. Once the column density exceeds values of $N_{\text{H}} \gtrsim 10^{23}$ atoms cm^{-2} the spectrum gets much harder. Photoelectric absorption makes it more and more difficult to detect an X-ray flux even in the hard part of the spectrum (unless the sources have high redshifts).

In order to check for the presence of an AGN in the centre of ULIRGs one can make use of X-ray observations in the hard band. According to Figure 1.9, large amounts of dust (with $N_{\text{H}} \gtrsim 10^{24}$ atoms cm^{-2}) are becoming transparent at energies above ~ 3 keV, allowing to investigate the inner parts of highly obscured sources (at least in sources with sufficiently high flux). From the observational point of view a considerable fraction of ULIRGs has been found to contain a hard X-ray source, highly absorbed by a molecular torus, which indicates the presence of a hidden AGN (Mitsuda 1995; Brandt et al. 1997; Kii et al. 1997; Braitto et al. 2003; Franceschini et al. 2003; Komossa et al. 2003; Ptak et al. 2003). This central AGN-like power source is imprinted on soft, (0.5 – 2.0) keV– sources in the nuclear region, which are supposed to be associated with a Starburst activity. Moreover, there are some sources known, having a relation between the strengths of IR emission lines (from highly ionized gas, most likely the NLR) and of the X-ray power law source. The AGN in ULIRGs is detectable in the X-ray range through the highly absorbed power law and the Fe-K α line at 6.4 keV, like in NGC 6240 (Netzer et al.

⁷By convention, the energy index α is defined by the proportionality given in the text; in the X-ray regime the often used photon index Γ is related to α according to $\Gamma = \alpha + 1$.

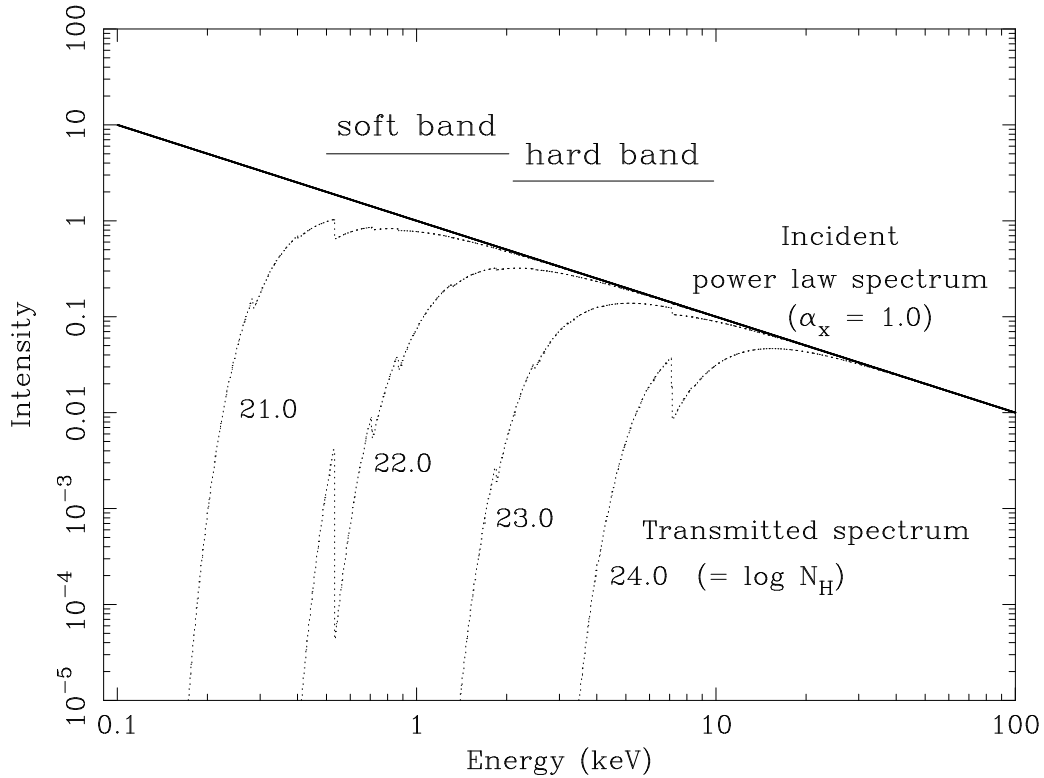


Figure 1.9: The impact of photoelectric absorption on X-ray fluxes. The dotted lines show the transmitted spectrum of an incident power law spectrum with $f_{\nu} \propto \nu^{-\alpha_x}$ (where $\alpha_x = 1.0$ and normalized to one photon $\text{keV}^{-1} \text{cm}^{-2} \text{s}^{-1}$ @ 1 keV; solid line), seen as a response of X-ray-absorption by material of column densities $N_{\text{H}} = 10^{21}, 10^{22}, 10^{23}$ and 10^{24} atoms cm^{-2} . This plot has been derived by using the XSPEC fitting software (Arnaud 1996) with the energy-dependent absorption cross-sections from Morrison and McCammon (1983).

1998; Vignati et al. 1999). In addition to the AGN activity emission from optically thin plasma is imprinted in the X-ray spectrum of ULIRGs.

1.3 Starbursts as a power source

The Starburst emission plays an important role in the energy budget of ULIRGs (e.g. Ptak et al. 2003, Franceschini et al. 2003, Risaliti et al. 2000). Considering the emission mechanism in ULIRGs, the expected X-ray spectrum of Starbursts-dominated ULIRGs are very different to that of AGN-dominated ULIRGs, helping to address the most recently debated question, *i.e.* the relative contribution of each emission mechanism to the total luminosity.

The term "Starburst" was first used by Weedman et al. (1981) in connection with interacting galaxies, after recognizing that a well-known simple model of stellar populations with "bursts" of star formation can be applied to these galaxies (Larson and Tinsley 1978). Pure Starburst ac-

tivity of high intensity (see Moorwood 1996 for an excellent review) can produce bolometric luminosities of $L_{\text{bol}} \sim 10^{11} - 10^{12} L_{\odot}$, compared to $L_{\text{bol}} < 10^{11} L_{\odot}$ of star formation in normal gas-rich spiral galaxies. It is thought to be a temporary event in a galaxy's life (lasting less than 10% of the Hubble time, *i.e.* with a time scale of $\lesssim 10^8$ yrs) in which a greatly increased star formation takes place, typically located within a radius of about one kpc from the centre of the galaxy, e.g. NGC 1068 (Wilson and Raymond 1999). In order to produce IR luminosities observed in ULIRGs, following the SFR – L_{IR} correlation of Kennicutt (1998a) requires a star formation rate of $\text{SFR} \sim 170 M_{\odot} \text{ yr}^{-1}$ and more. The enhanced SFR results in radiation also in the X-ray band. This is confirmed by the work of Schmitt et al. (1997), in which the authors pointed out that Starburst galaxies in the X-ray band (in parallel with other classes of AGN) are substantially brighter than normal galaxies, *i.e.* spiral and elliptical galaxies.

The typical X-ray spectrum of a Starburst galaxy in the (0.5 – 10.0) keV regime can be described by emission from collisionally-ionized plasma with different temperatures (Boller et al. 2003). A second effect is the interaction of supernovae ejecta with cool dense ISM clouds (Strickland et al. 2000). Imprinted on the continuum are several emission lines at low energies, as well as the Fe XXV and Fe XXVI lines. See Persic and Rephaeli (2002) for an identification and characterization of the main spectral components of Starbursts in X-rays.

The Starburst regions and their activity processes can be investigated due to four sources of large X-ray luminosities: hot gas (associated with the ambient interstellar medium), high- and low-mass X-ray binaries, the emission of young supernova explosions and the fast stellar winds (the "superwinds", see 1.1.3 on p. 12). All this processes can explain a large amount of X-ray flux, where the X-ray luminosity is $L_X \lesssim 10^{42} \text{ erg s}^{-1}$, though it is a small fraction of the total emission power.

1.3.1 The hot diffuse plasma

Emission from an *optically-thin* hot plasma ($kT \sim (0.3 - 2) \text{ keV}$), like it is present in stellar winds, shells from supernova remnants (SNR) and in the superwinds, can be expressed by the emissivity ϵ of the gas (in units of $\text{erg s}^{-1} \text{cm}^{-3}$, neglecting the frequency dependence). This quantity is a measure of the emitted power in a plasma volume element dV with a temperature T and number densities n_e and n_{ion} for electrons and ions according to $\epsilon = n_e \cdot n_{\text{ion}} \cdot \Lambda(T)$, where $\Lambda(T)$ is called the radiative cooling function of the gas (Dopita and Sutherland 2003). Therefore, the luminosity is given by

$$L = \int n_e \cdot n_{\text{ion}} \cdot \Lambda(T) dV$$

(Emerson 1996). Since the work of Raymond and Smith 1977 the calculations of the emissivity in X-rays for an optically-thin hot gas have been improved dramatically throughout the years

(Mewe et al. 1986, see also Kaastra et al. 1996). All of the recent models include both a continuum component as well as emission lines (such as He, C, N, O, Ne, Mg, Si, S, Ar, Ca, Fe, and Ni).

Whenever supernova explosions occur the interstellar environment and the gas in the galactic halo are heated by shocks to (virial) temperatures of $kT \lesssim 5.5 \text{ keV}$, thus visible in the X-rays (e.g. Della Ceca et al. 1999; Moran et al. 1999; Boller et al. 2003). In order to explain the soft X-ray emission of NGC 253 Pietsch et al. (2001) used two thin plasma components ($kT \sim 0.13 \text{ keV}$ and $\sim 0.4 \text{ keV}$) for the disk and three models ($kT \sim 0.6 \text{ keV}$, $\sim 0.9 \text{ keV}$ and $\sim 6 \text{ keV}$) for the nuclear region, consistent with results of simulations of Starburst-driven galactic winds.

1.3.2 Supernova Remnants

The ambient gas located around a supernova or around the ejected material from a SNR – mostly during phase one, *i.e.* in the free expansion and partly during phase two, the adiabatic expansion – can produce thermal X-ray emission in the range of 0.1 to several keV (with nearly solar abundances). Typically, the deduced X-ray luminosity of a (young) SNR is $\sim 10^{37} \text{ erg s}^{-1}$ (e.g. Burrows et al. 2000). The origin is assumed to be a heating process by three components: firstly, the blast wave shock of the supernova explosion, secondly, the reverse shocks from interaction processes of the ejected material with the surrounding shell (e.g. Borkowski et al. 2001; Decourchelle et al. 2000), and thirdly, the region between both shocks (called the "hot cavity"; Terlevich et al. 1992). Spatially resolved X-ray emitting shells around SNRs in the milky way have been detected with *ROSAT*, *ASCA* (e.g. Slane et al. 1999). This thermal radiation dominates the X-ray spectra of many SNR, although an additional non-thermal emission in the form of synchrotron radiation (due to the acceleration of electrons by SN-shocks) is expected to become more important at energies above a few keV (Reynolds 1998).

1.3.3 High- and low-Mass X-ray binaries

In general, black hole X-ray binaries (with a mean $L_{(2-10) \text{ keV}} \sim 10^{37} \text{ erg s}^{-1}$; e.g. White et al. 1983) exhibit two distinct components in their X-ray spectra: the ultrasoft component has a temperature of $kT \gtrsim 1 \text{ keV}$, arising from an optically thick, but geometrically thin accretion disk. At higher energies the ultrahard component (up to several hundred keV) has the shape of a power law with $\Gamma \sim 1.5$ to ~ 2.5 (Wilson and Rothschild 1983). Based on a quantitative model of synthetic X-ray spectra of Starburst galaxies, Persic and Rephaeli (2002) suggested that high- and low-mass X-ray binaries have the largest contribution to the (2 – 15) keV spectrum of all stellar components with the required spectral shape (assuming that an AGN is absent).

Each class shows a spectrum describable by various power laws with a cut-off (e.g. Christian and Swank 1997). Assuming a mixture of both classes with a variety of luminosities (resembling the galactic values) a cut-off power law of the form $E^{-\Gamma} \cdot e^{-E/kT}$ is a good approximation to the (2 – 10) keV emission, providing $\Gamma \sim 1.1$ and a cut-off energy of $kT \sim 8$ keV. In addition, a prominent Fe K emission with a central energy in the range of (6.4 – 6.7) keV and with $EW_{\text{FeK}} \sim 0.2 - 0.6$ keV is visible in the spectra of high-mass X-ray binaries. The origin is most probably due to the stellar wind of the companion star and/or in the magnetosphere of the neutron star (Ebisawa et al. 1996). *Chandra* data of M 82 and NGC 253 in the (2 – 10) keV band indicate that the emission comes mainly from point sources (Strickland et al. 2000; Griffiths et al. 2000).

1.4 Disentangling the AGN–Starburst contributions

About 20 years after their discovery and 15 years after a systematic sky survey with *IRAS* the nature and the energy source of ULIRGs is presently explained by a combination of Starburst and AGN activity. Studies of a sample of ULIRGs based on *ISO* data indicate the Starburst activity from 0 to 100 per cent in the bulk of the IR emission (e.g. Genzel et al. 1998; Lutz et al. 1996; and supported by diagnostic tools). On the other hand, the presence of energetically important obscured AGN in ULIRGs has been revealed not only by optical and near-IR spectroscopy (e.g. Veilleux et al. 1997) – and by evidence for completely buried AGN (e.g. Soifer et al. 2001) – but also due to their spectral properties in the X-rays (*i.e.* Iwasawa 1999).

X-ray studies of ULIRGs offer a fundamental tool to investigate the presence of buried AGN, and allow to obtain quantitative estimates of their contribution to the bolometric luminosity. This diagnostic method is based on the fundamentally different spectra and regimes of luminosities between Starburst galaxies and AGN in the X-ray band. Distinguishing features of hidden AGN are the hard continuum emission as well as prominent Fe-K α lines, which are able to penetrate large column densities of gas.

The purpose of this thesis is to present X-ray studies of the two ultraluminous infrared galaxies NGC 6240 and Mrk 1014. Recent publications on some of the brightest nearby ULIRGs, including NGC 6240, classify the majority as pure Starbursts based on optical and IR spectroscopy, but in the hard X-rays they show spectral properties typical of obscured AGN (Iwasawa 1999; Vignati et al. 1999; see also Franceschini et al. 2003, Komossa et al. 2003, Ptak et al. 2003). This work aims to identify signatures of an AGN in the (hard) X-ray spectrum of this two prominent ULIRGs, and to quantify separately the contributions of the hidden AGN from the Starburst emission to the overall X-ray spectra. The unique large collecting area in

combination with the hard X-ray response of *XMM-Newton* have been used to study the complex X-ray spectra of NGC 6240 and Mrk 1014 in unprecedented detail. This allows – by far much better than with previous missions – to perform a high-quality spectral analysis. This results in significantly better constraints of the real amount of the absorbing column density in the line-of-sight to the hidden AGN, and to obtain reliable estimates for the plasma temperatures, abundances of existing metals, etc. In the case of NGC 6240, the high spatial resolution of *Chandra* made it possible to separate *two* AGN being active in the hard X-rays (Komossa et al. 2003). X-rays coming from regions very close to the nuclei (of the order of a few hundred pc) can now be studied. This provides the direct verification of radiation being reflected on the molecular torus. However, a straightforward extrapolation of the X-ray properties into the bolometric luminosity is still very model dependent.

2

Data reduction with the *XMM-Newton* observatory

The *XMM-Newton* mission (X-ray Multi-Mirror; Barré et al. 1999, Jansen 1999, Jansen et al. 2001) had been proposed by the Science Programme Committee of the European Space Agency (ESA) in the year 1984 as one of the first cornerstone projects of the "horizon 2000"-program. In 1985 the ESA's Council of Ministers in Rome settled on to its realization. One year later the development of the satellite and its components started, both in close collaboration between several research institutes and an international industry syndicate of more than 46 companies (under the leadership of Dornier Satellitensysteme, Friedrichshafen, Germany). The arising costs and the work to be done have been distributed evenly under the multi-national teams of researchers and engineers (from Belgium, Germany, France, Great Britain, Italy, the Netherlands, Switzerland, and the USA).

After the lift-off of the Ariane-504 launcher rocket from the launch pad in Kourou (French-Guiana) on December 10th, 1999 at 14:32 GMT and the release of the satellite into a highly eccentric orbit *XMM-Newton* had been renamed to its final name in honour of Sir Isaac Newton (1643 – 1727).

Being the largest scientific satellite ever built in Europe, *XMM-Newton* is designed for a life time of ten years of operation.

2.1 The scientific instrumentation

The essential parts of the satellite are the three X-ray mirror modules which focus the collected radiation on five instruments (see Figure 2.1; for a review on X-ray telescopes see Gursky and Schwartz 1974 and Aschenbach 1985). The modules are aligned in parallel, constructed and designed equally according to the Wolter type I design for X-ray telescopes. The instruments are three imaging X-ray cameras – EPIC devices (European Photon Imaging Cameras) – and two reflection grating spectrometers (RGS). The EPIC have been developed in order to perform spectroscopic measurements as well as imaging of X-ray sources in the (0.1 – 15) keV band, whereas the RGS provide the best spectral resolution in the range of (0.35 – 2.5) keV. In addition, an optical monitor (OM) allows simultaneous observations in the optical/UV and in the X-ray regime.

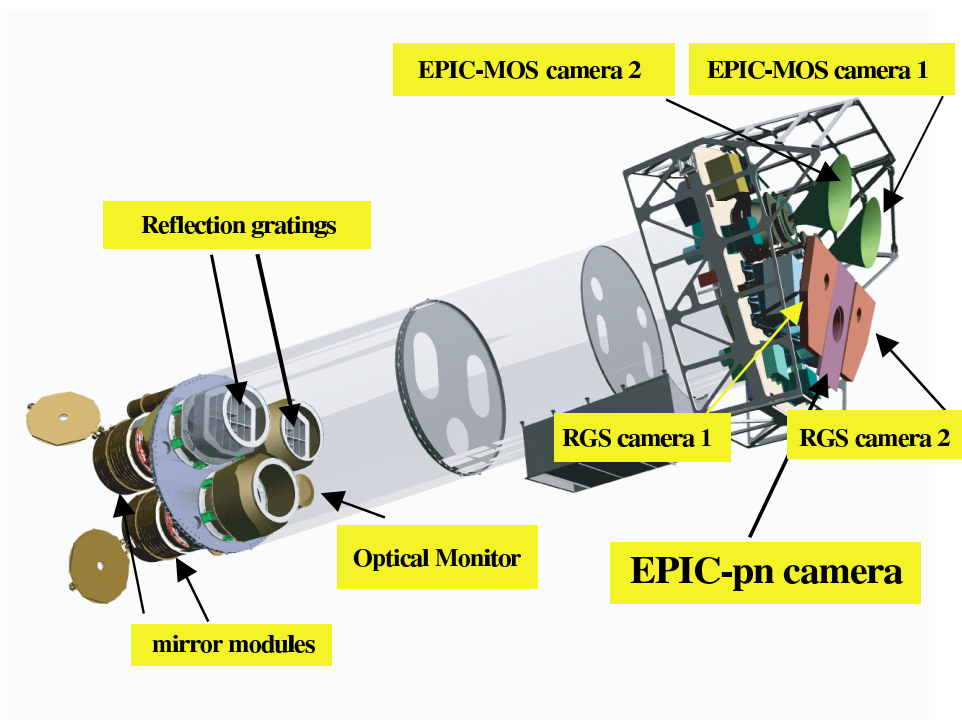


Figure 2.1: Arrangement of instruments on the *XMM-Newton* satellite. Two of the mirror modules include the Reflection Grating Arrays, the third one is related to the EPIC pn device, close to the optical monitor and the radiation monitor. The focal instruments on the right side of the payload are the two EPIC MOS cameras (with its green horns of the thermal radiators), the EPIC pn camera (behind the violet radiator) and the pink RGS detectors (*XMM-Newton Users' Handbook*, 2004; adapted from Kirsch 2003).

The following items describe the main instruments on board of *XMM-Newton* (see Bagnasco et al. 1999; more detailed information about the instrumentation can be found in the *XMM-Newton Users' Handbook*, Ehle et al. 2004, version 2.1).

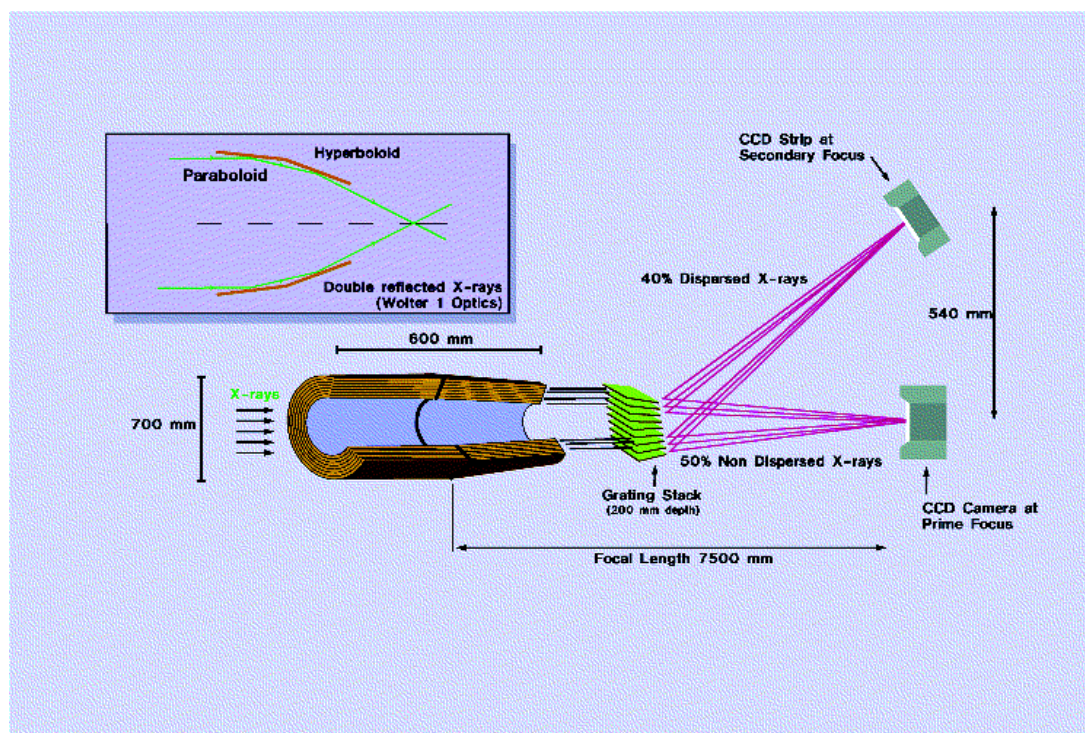


Figure 2.2: The light path in a Wolter type I configuration of the *XMM-Newton* mirror modules with the EPIC devices in the prime foci and the RGS detectors in the secondary foci (taken from de Chambure et al. 1999; *XMM-Newton* Users' Handbook, 2004).

2.1.1 The X-ray mirror modules

The *XMM-Newton* optics to focus X-rays consist of three identical, co-aligned (better than one arcmin) and tube-like telescopes with a focal length of $f = 7.5$ m and a field of view of $\sim 30'$ (see Table 2.1 on p. 32; de Chambure et al. 1999, Aschenbach 2002). Figure 2.2 shows the principal sketch of the modules, the heaviest masses of the satellite. Each of them contains 58 nested thin mirror shells made of nickel (thickness: ~ 1 mm). The inner side is coated with gold (with a surface roughness of ~ 3 Å). Gold is used to improve the reflectivity of the X-rays due to its high atomic number. The nesting method enables the effective collecting area to be maximized, because an X-ray photon sees only the projected area of the mirror surfaces (*i.e.* concentric annuli). The mirror shell with the smallest radius can reflect X-ray photons with energies up to 15 keV.

The mirror radii range from 15.9 cm to 35.0 cm with a distance of $\gtrsim 3$ mm between neighbouring shells. The geometry of the shells follows the Wolter type I design (Wolter 1952b, 1952a; Giacconi and Rossi 1960: Nobel prize for Giacconi in 2002) with a combination of a parabolic and a co-axial hyperbolic part (to reduce the focal length). The mirrors let X-rays – reflected at a shallow angle (the principle of "grazing incidence") – converge in the focus on the detectors. In order to be reflected efficiently the incident angle of X-ray photons has to be

Table 2.1: Parameters of the *XMM-Newton* observatory (Lumb et al. 1996)

Orbit		Operations	
Period	47.8 hr	Launch date	Dec 10 th , 1999
Apogee	114000 km	Minimum observation altitude	40000 km
Perigee	~ 830 km	Coverage	> 40 hr/orbit
Inclination	40°	Launcher	Ariane 504
Argument of perigee	300°	Nominal mission duration	2 years
Right ascension of ascending node	43°	Extended mission duration	10 years
Maximum eclipse duration	1.3 hr		
Telescope		Pointing	specified goal
Focal length	7.5 m	Solar aspect angle pitch/roll	20° 20°
Field of view (half cone)	15'	Absolute pointing error	60'' –
Number of mirror modules	3	Absolute pointing drift (16 h)	45'' 2'' (RGS)
Mirror shells per module	58	Absolute pointing drift (1 h)	5'' –
Carrier/effective surface	nickel/gold	Relative pointing error (2 min)	5'' 2''
Reflective area at 1.5/8 keV	4425/1740 cm ²	Relative pointing error (10 sec)	5'' 0.25''
Mirror shell thickness	(0.47 – 1.07) mm	Absolute measurement accuracy	10'' 1'' (EPIC)
Mass		Power	
Total spacecraft	3900 kg	Solar array BOL	1945 W
Experiments	600 kg	EOL	1600 W
Mirror modules	1420 kg	Batteries	18 Ah (each)
Hydrazine	485 kg	Experiments	360 W
Thermal control		Data management	
Mirror module heating	100 W (2x)	Telemetry rate (S-band)	70 kbps
Mirror support platform	72 W	Experiment allocation	64 kbps
Passive thermal control		Tele command rate (S-band)	2 kbps
with safeguard heaters		Transmitter power	5 W

the smaller, the more energetic they are. The ratio of the mirror diameter to the focal length has to be sufficiently small to allow photons to be reflected at typical grazing angles of $\sim 2^\circ$. The mean FWHM of the Point Spread Function¹ for the mirror assembly related to the EPIC pn device is $6.6''$ and the angular resolution of the Half Energy Width (HEW) is $15''$ in the detector plane.

When combining all three mirror telescopes *XMM-Newton* provides an effective area of $A_{\text{eff}} \approx 4300 \text{ cm}^2$ at the energy 1.5 keV and $A_{\text{eff}} \approx 1800 \text{ cm}^2$ at 8 keV. On the one hand, this is smaller than the geometrical projection of the mirror shells due to the correction from absorption at the entrance window, from the reflectivity of the mirrors, etc. But on the other hand, this collecting area is by far much larger compared to previous satellite missions. *XMM-Newton* can even collect roughly six times more X-ray photons than the *Chandra* mission; *i.e.* *XMM-*

¹PSF, *i.e.* the shape of the CCD image due to distortions when light from an ideal point (unresolved) source propagates through the telescope to the detector

Newton is ideally suited to discover and spectroscopically study faint sources, in particular in the (2.0 – 10.0) keV regime.

2.1.2 The European Photon Imaging Camera (EPIC)

The X-ray imaging detectors are the main parts of the scientific payload on board of *XMM-Newton*. They provide the instrumentation for the three Wolter telescopes to record X-ray photons in the focus of the mirror modules and gather information about the position, energy and time of a detection (an "event") simultaneously.

The complete EPIC device consists of three CCD cameras (one pn-CCD² and two identical MOS-CCDs³) and a radiation monitor (ERMS⁴). The pn camera has been developed in collaboration between the IAAT⁵ and the MPE, whereas the MOS cameras have been made available by french and british collaborators. Each camera position is in the focus of one of the three Wolter tubes, imaging the 30'-FOV of the telescopes onto the detector plane in a distance of the focal length. The MOS-CCDs share the incoming X-ray flux with the RGS devices because of the geometrical arrangement of the gratings (compare with Figure 2.2 on p. 31 and see subsection 2.1.3 on p. 37). The pn camera makes use of its own mirror module. The MOS-CCDs are modified optical CCDs adapted to register X-ray photons, but the pn-CCD is a completely new development of the semi-conductor laboratory (HLL) of the MPE and the MPI of physics (in Munich), being a device purely built for X-ray-astrophysical purposes. A summary of the main parameters of the pn-CCD and the MOS-CCDs can be found in Table 2.2 (next page).

In front of each EPIC detector aperture a filter wheel can be fixed to six different positions. Four positions are equipped with aluminized filters of different thickness (one "thin", two "medium", and one "thick" filter) which allow to filter out low-energy radiation (e.g. from the IR, visible, and UV), one is the fully opened position without any blocking filter and the last one is the fully closed position with a thick (~ 1 mm) aluminium layer blocking any radiation and thus protecting the detectors from being damaged by radiation mainly originating from the Van-Allen radiation belts. This low-energy radiation causes an enhanced shot noise, a shift in energy scaling (~ 3.6 eV) and a change in energy resolution, *i.e.* an increased charge transfer inefficiency (CTI). Moreover, all EPICs are well shielded with an aluminium coat of 3 cm thickness. All cameras are designed to work in different observational modes due to the scientific requirements. Table 2.3 (on p. 35) gives a summary of the possible modes.

The purpose of the radiation monitor is to measure the rate of particle radiation affecting the

²pn = p-type/n-type semi-conductor

³MOS = Metal Oxide Semi-conductor

⁴ERMS = EPIC Radiation Monitor System

⁵Institut für Astronomie und Astrophysik, Tübingen

Table 2.2: Parameters of the EPIC pn- and the EPIC MOS–CCDs
(as given by the *XMM-Newton* Users’ Handbook, 2001)

Parameter	EPIC pn	EPIC MOS
number of CCDs	twelve	seven
number of pixels	64×200	600×600
pixel size [μm]	150×150	40×40
pixel size [arcsec]	4.1×4.1	1.1×1.1
Field of view (FOV) [arcmin]	27.5	33.5 (max.)
PSF (FWHM/HEW) [arcsec]	6/15	5/14
Time resolution of the full field [s]	0.056 ^{a)}	3
Timing resolution [ms]	0.04	1
Bandpass [keV]	0.15 – 15.0	0.15 – 12.0
Sensitivity ^{b)} [$\text{erg cm}^{-2} \text{s}^{-1}$]	$\sim 10^{-14}$	$\sim 10^{-14}$
Energy resolution ^{c)} (@ 1 keV/6.4 keV) [eV]	80 / 140	70 / 135
Quantum efficiency (QE; @ 0.5/6.4/8.0 keV)	88% / 99% / 97%	45% / 87% / 65%
Operating temperature [$^{\circ}\text{C}$]	~ -120	~ -80

a) excluding integration time,

b) in an exposure of 10 ks, in (0.15 – 15) keV,

c) see subsection 3.1 on p. 43.

satellite. It also gives information about the particle background of the CCD detectors. At a high level of background (caused e.g. by solar flares) it serves as a warning device for the sensitive CCDs and can cause the filter wheel to move into the blocking position to avoid damages on the CCDs.

The EPIC MOS cameras

The two MOS cameras (Turner et al. 2001) work on the basis of the highly–developed Metal Oxide Semi-conductor technology. The structure of the 2×7 identical front–illuminated chips is taken from optical CCDs and gets 600×600 pixels of $40 \times 40 \mu\text{m}^2$ in size (per CCD) into the conducting material, resulting in a slightly better positional resolution than the pn–CCD (see Table 2.2). The arrangement of the individual CCDs (Figure 2.3 on p. 36) is adapted to the curved geometry of the focal surface determined by the Wolter telescopes. The created charge can be read out within 2.6 s (in the standard Full Frame mode, see Table 2.3). Its design is optimized for recording soft X–ray radia-

Table 2.3: Performance modes of the EPIC devices

EPIC–pn modes (pixels)	Description
Full Frame (378×384) (standard mode)	full FOV is read out (6.3% out-of-time events ^{a)}), low timing resolution (73.4 ms)
Extended Full Frame (378×384)	full FOV is read out (2.3% out-of-time events), low timing resolution (200 ms)
Partial Window Large Window (198×384) Small Window (63×64)	2-D frame storage of half of the area in all CCDs (45 ms) 2-D image of a part of CCD-No. 4 (6 ms)
Timing Timing Burst	collecting data of a part of one chip into an 1-D row, timing resolution of $30 \mu\text{s}$ special type of the timing mode, extremely high timing resolution ($7 \mu\text{s}$), low duty cycle (3% effective exposure time)
EPIC–MOS modes (pixels)	Description
Full Frame (600×600)	full FOV is read out (all seven CCDs), low timing resolution (2.6 s)
Partial Window Large Window (300×300) Small Window (100×100)	part of the central chip is read out (0.9 s) (same as for 'Large Window', within 0.3 s)
Timing	the data of the central chip are combined into a 1-D row (instead of a 2-D image) from a user-defined area to allow high-speed photometry (1.5 ms)

a) during the readout process the CCD continues to register photons. These are not desirable because they have a false position information with respect to the direction of the charge movement in the CCD.

tion due to its very good energy resolution in this range. However, the quantum efficiency (QE) of the MOS–CCDs is less than the QE of the pn–CCD in the higher X–ray regime, because its sensitive silicon layer is roughly seven times thinner ($40 \mu\text{m}$) than the layer depth of the EPIC pn device. However, in combination with its front–illuminating architecture the MOS–CCDs are more resistant to the hard X–ray radiation.

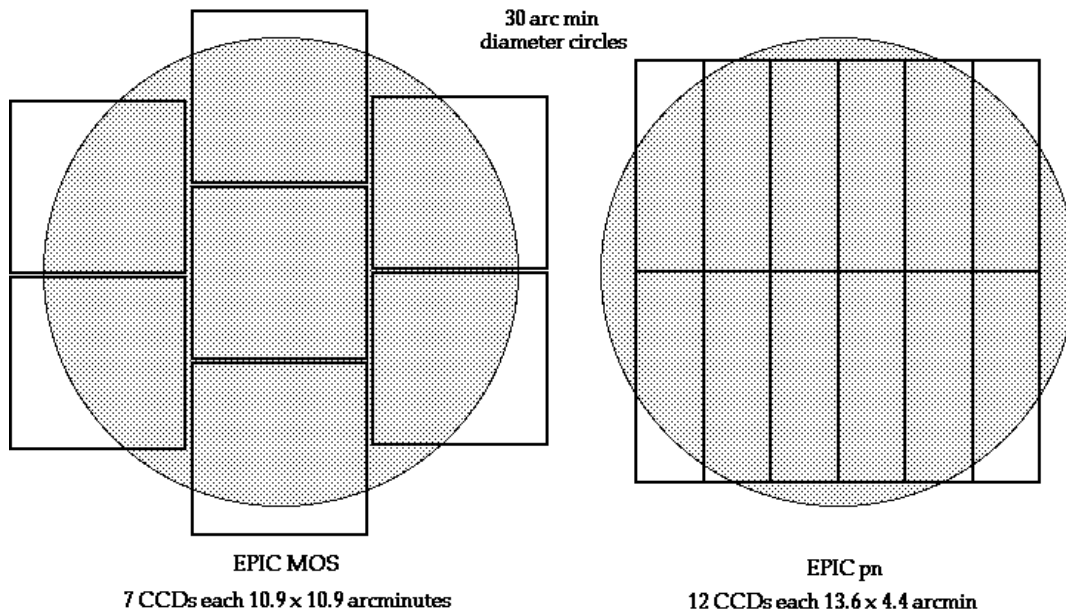


Figure 2.3: The focal plane arrangements of the EPIC-CCDs combined with the 30'-FOV

The EPIC pn camera

The pn-CCD as a whole (Strüder et al. 2000, 2001) is the heart of the focal unit of one mirror tube and its location is the centre of the camera head device (EPCH). This unit in the focal plane consists of an array of twelve pn-CCDs on a monolithically fabricated high-purity silicon-disc ("wafer"), divided into four quadrants of three pn-CCDs each (for safety reasons). Each quadrant can be controlled independently, having its own readout electronics (EPIC Control Electronics, EPCE) and voltage supply (EPIC Voltage Control, EPVC) to maintain the whole system even when individual CCDs or quadrants break down.

The approximately square shape of the total geometry can be achieved by the chosen design of the pn-CCDs with arrays of 64×200 pixels per chip and a pixel size of $150 \times 150 \mu\text{m}^2$ (see Table 2.2 on p. 34). Therefore, the whole pn-CCD provides a sensitive area of ca. $57.6 \times 60 \text{ mm}^2$, representing the largest X-ray CCD detector ever built. The angular resolution α of the pn-CCD (where $\alpha = \arctan[150 \cdot 10^{-6} \text{ m} / 7.5 \text{ m}] = 4.1''$) is even better than the resolution of the telescope. The pn-CCD is rear-side-illuminated by the X-ray radiation, *i.e.* all layers or coatings are responsive for detection, where the efficiency is extremely high and remarkably homogenous over the whole bandpass of the *XMM-Newton* instruments (over 88% QE from 0.5 keV to 10.0 keV). The other major advantage of this device is the very quick readout of the whole CCD area within $\sim 73 \text{ ms}$ (see Table 2.3 on p. 35). In addition, special observation modes improve the readout capabilities dramatically, both for spatial and timing analysis. The in-orbit calibration

source is a combined radioactive Fe-55– and Al-preparation of known energy and intensity to control the detection sensitivity, the amplification and the energy resolution of the pn–CCDs at any point of time during the mission.

In order to protect the EPCH from high-energetic protons of the cosmic radiation it is surrounded with an aluminium shielding. Moreover, it is possible to fully close the entrance window by moving a shutter into the light path to the camera head, independently of the filter wheel position.

2.1.3 The Reflection Grating Spectrometer (RGS)

Each of the two identical RGS (den Herder et al. 2001) is made of two parts, an array of reflection gratings and the detector, all are built in a dutch-american-swiss coproduction. Roughly 58 % of the X–rays propagating through the two mirror assemblies reach directly an arrangement of 182 reflection gratings with 645 lines per mm (the RGA – Reflection Grating Array; fabricated as "Blaze gratings" made of SiC). The dispersed X–rays interfere at the second focus of the corresponding grating at different points (due to the wavelength-dependence) on a Rowland circle geometry with a diameter of 6.7 m (to measure position and energy simultaneously).

The detector is built up of nine back–illuminated MOS–CCDs (The RGS Focal Cameras, RFC), arranged linearly along the dispersion direction of the spectrometer on the Rowland circle. The intrinsic energy resolution of the CCDs is used for discriminating between the different orders of the spectrum from each other. Each MOS–CCD contains 768×1024 pixels with a pixel size of $27 \times 27 \text{ cm}^2$. This size makes it possible to fit the spectrum of 253 mm in size completely into the array. The high energy resolution of the RGS devices between $E/\Delta E = 200$ and 800 allows detailed spectroscopy in the (0.35 – 2.5) keV regime (equivalent to 5 Å to 35 Å). In this band many emission lines of highly ionized elements due to hot plasma can be registered, e.g. the L-shell transitions of heavy elements like Fe and Ni and the K-shell transitions of lighter elements like N, O, Mg, S, Si, Na, Ca, Ar, and Ne. It allows to study the chemical composition of the emitting material and to develop several diagnostic tools and/or restrict existing ones. The RGS are sensitive to fluxes down to $3 \cdot 10^{-13} \text{ erg cm}^{-2} \text{ s}^{-1}$.

2.1.4 The Optical Monitor (OM)

In addition, a modified Ritchey–Chrétien telescope with an aperture of 30 cm (and 7 cm for the secondary mirror) allows observations in the optical/UV energy range (from 170 nm to 600 nm). Its focal length is $f_{\text{OM}} \approx 3.8 \text{ m}$, the field of view is $\text{FOV} = 17'$ at an angular resolution of one arcsec. The infalling light is amplified by micro-channel plates before it is registered in a CCD (MCPs to achieve a high sensitivity in order to detect objects up to 24^{m}). In combination with

several colour filters it is possible to receive optical broad-band spectra. The OM – built in Great Britain – is aligned to the X-ray telescopes and thus both can be used to observe sources in the X-ray and the optical/UV at the same time.

2.2 The detailed reduction of *XMM-Newton* data files

With each single observation the collected data from all devices are combined to the Observation Data Files (ODFs). Usually the data are stored in the FITS⁶ format and separated into the data of the different CCDs together with the relevant house keeping parameters of the instruments and the spacecraft information. The ODF data are organized according to their observation-ID, which is related to the submitted proposal.

The processing of the ODFs and the evaluation of the scientific data are easily made with the help of the *XMM-Newton* Science Analysis System, called the XMM-SAS software (Loiseau 2004). This analysis package has been developed by the *XMM-Newton* Science Operations Centre (SOC) in Villafranca near Madrid (Spain) and by the Science Survey Centre (SSC) in Leicester (Great Britain) and is still in a progressive phase. Their main duty is not only to provide the scientific community with the *XMM-Newton* data but also to simplify its handling. The XMM-SAS contains several routines (“tasks”) to process and explore the scientific exposures performed by the different instruments and to combine them, either by an interactive Graphical User Interface (GUI) or by a command-line script suitable for an automatic run of the reduction.

2.2.1 The step-by-step analysis

In order to take the advantage of setting the numerous options to the tasks individually the SAS makes it possible to let the user run the processing commands by himself, putting together the ODFs with the calibration information as the input for the SAS. In the best case it is only necessary to execute the pipeline processing routines on the ODFs (e.g. for the EPIC one needs the chain tasks “epchain” and “emchain” or the meta tasks “epproc” and “emproc”, respectively) to get scientifically usable data files. These processing programs include all ODF components without any interaction by the user and they are due to many kinds of known and required corrections to the raw data.

Carrying out the data reduction for each of the scientific devices is a multi-step procedure. By combining the resulting data files from the ODFs with the Current Calibration Files (CCF) – the files with all calibration information in the respective observation period – provide calibrated “event files”⁷. They are binary table files with one line per received event, recording numerous

⁶Flexible Image Transport System, the standard format for astronomical data (Hanisch et al. 2001)

⁷For a detailed description of the data files see Guainazzi and Santos-Lleó (2002)

attributes of the events such as the (X,Y)-position of the detection, the arrival time and the energy (see subsection 3.1.1 on p. 43). Building up an event file is the first step a user does before performing the analysis (see Figure 2.4).

The second step is to correct the observation from large flaring events caused mostly by soft protons. Therefore, only high-energy (> 10 keV) single pixel events (on just one CCD) have been selected and displayed in a light curve (using the meta tasks "xmmselect" in a GUI, and "evselect" in the command-line, respectively). The next step is to identify the times of high counts and filter them out from the original event file, remaining only intervals of good times (the GTI correction). The following step takes into account the different instruments and selects the data according to "good" events (*i.e.* single, double, triple and quadruple pixel events) within the energy range of (0.3 – 10.0) keV. After the creation of a new event file the GTI-corrected image of the observation has been visualized in order to extract the counts in the source and in the background region. For both areas a spectrum has been created. Standard astronomical tools like the FTOOLS⁸, XSPEC⁹, IDL¹⁰, etc. are able to handle the produced data files. For all extractions reported in this thesis I used a circular region for both the source and the background filtering.

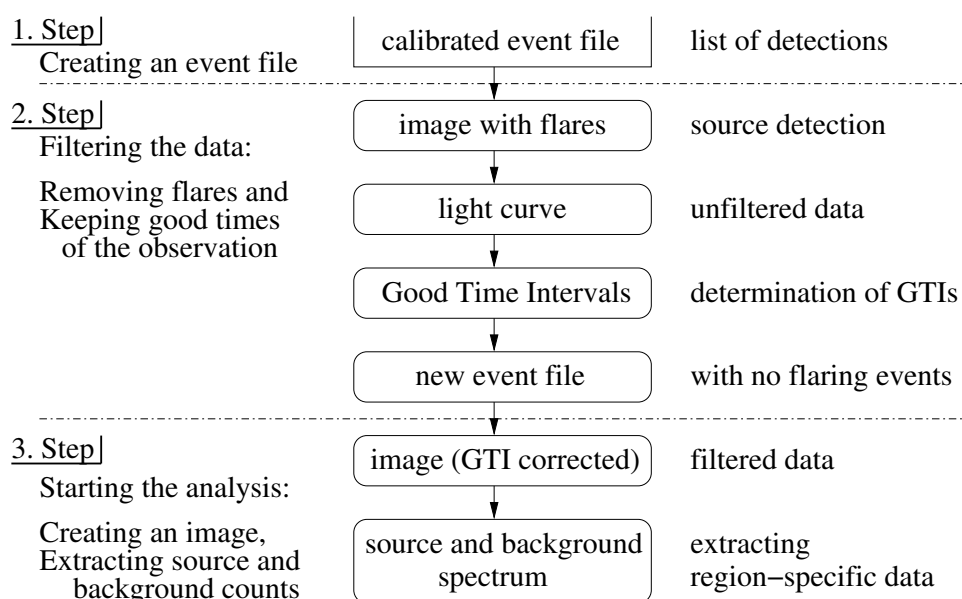


Figure 2.4: The steps of data reduction performed on each data set

⁸Blackburn (1995); <http://heasarc.gsfc.nasa.gov/ftools/>

⁹<http://heasarc.gsfc.nasa.gov/xanadu/xspec/index.html>

¹⁰<http://www.rsinc.com/>

3

The extremely luminous infrared galaxy NGC 6240 in the focus of *XMM-Newton*

The study of the (ultra-)luminous infrared galaxy NGC 6240 in the X-ray regime is the aim of this thesis. This source was on a list of objects proposed by my supervisor Prof. Dr. Thomas Boller et al. as a part of the guaranteed time observer program of the MPE on observations with *XMM-Newton*. In competition to other european institutes, involved substantially in the *XMM-Newton* mission, the MPE gained a significant amount of observing time within the first phase of the mission. A part of this time was dedicated to the research work on LIGs/ULIRGs.

To shed light on the topics of the emission mechanisms in LIGs and ULIRGs as well as on their (likely) AGN-Starburst connection at X-ray wavelengths, eight sources have been proposed and finally NGC 6240 has been observed by *XMM-Newton*. NGC 6240 was on top of the object list, as this source has been suggested to be an archetype for this class. During the following time another three sources have been added, but were too late to be part of this thesis.

The following Table 3.1 summarizes basic information about the selected target. NGC 6240 was taken because of its appearance in a sample of *ROSAT* detected sources (Boller 1999), in addition, marked in the *ISO-SWS* diagnostic diagram of AGN- and Starburst-dominated ULIRGs. The mid-IR spectra classify all of them as Starburst-dominated sources. However, X-ray observations show clear signs of non-thermal nuclear activity.

Table 3.1: NGC 6240 observed with *XMM-Newton* and analyzed in this thesis

Object name	Coordinates (J2000.0)		$N_{\text{H,gal}}$	Redshift
	R. A.	Dec.	$[10^{20} \text{ cm}^{-2}]$	z
NGC 6240	16 ^h 52 ^m 58 ^s .9	+02°24′03″.4	5.8 ± 0.2	0.02448 ± 0.00003

The position as well as the redshift of NGC 6240 are taken from the NASA/IPAC Extragalactic Database (NED)¹. The hydrogen column densities $N_{\text{H,gal}}$ of the Galactic absorption were calculated based on the source position by using the data from Dickey & Lockman (1990).

Table 3.2 lists the classification of the source due to optical observations taken from the NED. It is important to note that the optical classification of NGC 6240 is *not* unambiguous.

Table 3.2: Optical classification of NGC 6240 and some luminosities

Object name	Classification ^{a)}	$\log[L_{\text{FIR}}]$	$\log[L_{\text{X,ROSAT}}]$	$\log\left[\frac{L_{\text{X,ROSAT}}}{L_{\text{FIR}}}\right]$
		$[\text{erg s}^{-1}]$	$[\text{erg s}^{-1}]$	
NGC 6240	LINER/Sy-2	45.44	42.84	-2.61

a) as given in the NED

In addition, the luminosities in the far-IR and in the *ROSAT* X-ray band are given (according to Boller 1999). The *ROSAT* observation does not require an AGN contribution. The obscured AGN becomes visible in the *XMM-Newton* and *BeppoSAX* observations.

This study of ULIRGs in the X-ray regime pursues the following scientific goals.

- **Determination of the intrinsic column density in X-rays**

by measuring the amount of neutral hydrogen with high precision in the line-of-sight to the centre of the source,

- **Deconvolution of Starburst- and AGN-processes in ULIRGs**

by comparing the relative amounts of the Starburst and AGN spectral modelling,

- **Searching for iron line emission**

as seen in reflection from the molecular torus, and constraining some fundamental parameters like the ionization state (from the line energy) and the iron abundance (from the line strength).

¹<http://nedwww.ipac.caltech.edu>

3.1 The methodology of spectral analysis

Before going into the details of the X-ray observations, the following section describes the fundamental methodology of working with X-ray spectra and it summarizes the mathematical-statistical ideas behind the analysis.

The methods to obtain physical insights at X-rays are more complicated than, for instance, in the optical research field. The reason is the limited spectral resolution $\Delta E/E$ of the X-ray detectors in comparison with optical devices (ΔE gives the Full Width at Half Maximum (FWHM) of the energy distribution at the reference energy E). Over the whole high-energy range the spectral resolution obeys the proportionality $\Delta E/E \sim E^{-1/2}$. Instruments working in the (1 – 10) keV energy range have a typical energy resolution of $\Delta E/E \approx 15\%$ (@ 5.9 keV for proportional counters; Zombeck 1990, Thompson et al. 2001²) and *a few* percent for semiconductor devices (like Si(Li) or Ge; compare with Table 2.2 on p. 34). These values are more than two orders of magnitude higher than the values available for optical spectrographs (like prisms with $\Delta E/E < 0.01\%$).

3.1.1 General remarks

The event list data from an X-ray observation consist of a series of events (see 2.2.1 on p. 38f), with information of e.g. the position of the event on the detector (the DETX- and DETY-columns), the energy channel of the event (historically called PHA; Pulse Height Amplitude or Analyser), and the grade of the event (as the PATTERN of a single, double, triple or quadruple event; see Loiseau 2003, ch. 4.4.1 and 4.4.2). Moreover, the list stores computed numbers like the projected position of the source on the sky in the coordinate system of the detector (X- and Y-columns), the PI energy channel (Pulse height-Invariant; the PHA channel corrected for variations in the detector like spatial dependencies or gain non-linearities) and finally, an ENERGY channel column with estimates of the energy of the detected photon.

The measured X-ray spectrum in terms of the PHA values in the detectors is mathematically describable by a convolution of the true physical source spectrum (in photons per unit area, per unit time, and per unit energy interval; $[N_{\text{source}}(E)] = \text{photons cm}^{-2} \text{ s}^{-1} \text{ keV}^{-1}$) with a "technical" function containing all information about the characteristic properties of the detector. The latter is made up by the (matrix) product (called the "response matrix function", RMF) of the effective collecting area (see 2.1.1 on p. 31) and a "redistribution" function from which the probability is calculated that a registered photon has an energy in a range of a Gaussian distribution (to the first order) centered on the true energy of the photon and with a width equal to the energy resolution of the detecting instrument. In other words, the RMF gives the product of

²X-ray Data Booklet, Table 4-2, p. 4-33, <http://xdb.lbl.gov>

the effective area with the probability of the photon energy being in certain energy bins, when given the PHA (or PI) value of the event.

By multiplying the "response matrix function" with the true source spectrum the integration over all relevant energies gives the rate of photons (in counts s^{-1}) detected in each channel separately (and with an integration over the finite energy width of individual channels). The photon rate is a net rate, *i.e.* it is corrected for background effects like cosmic radiation events, radioactivity within the detector, the cosmic X-ray background, etc.

The effective collecting area and the redistribution exhibit complex forms. The deconvolution is non-unique and very sensitive to small changes in the number of counts within one channel. Therefore, the practical work on X-ray data begins with an assumption of a certain spectral form with a small number of free parameters (the "model" spectrum) for the observed object and then calculating the counts of the model spectrum expected in the various channels due to the known detector response. The "best fit" to the data is reached when the deviations between the predicted model spectrum and the measured spectrum is minimized. A typical minimization algorithm is the Levenberg-Marquardt method (e.g. in Bevington and Robinson 2003; a modified version using the CURFIT code is implemented in XSPEC). The χ^2 -test (e.g. Babu and Feigelson 1996, Wall 1996) allows a statistical quantification of the match of the model spectrum with the measured data. The calculated sum

$$\chi^2(\theta) = \sum_i \frac{[h(x_i) - N \cdot p(x_i, \theta)]^2}{\sigma_i^2(h(x_i))}$$

over all channels i gives an estimation of the correspondence between model and observational data with $n - k$ degrees of freedom (dof; n is the number of spectral channel bins and k the number of free model parameters). $h(x_i)$ is the observed (Gaussian) frequency distribution of the measured and binned counts x_i over the observation duration, whereas the x_i are background subtracted. N is the total number of measurements, and $p(x_i, \theta)$ represents the (theoretical) probability function of the measured values as predicted by the model. Finally, $\sigma_i(h(x_i))$ is the uncertainty in the frequency $h(x_i)$ of the data counts in the PHA channel i . Using statistical theorems it can be shown, that the best estimator for θ (as a single parameter or a vector of k parameters) is the best estimator that minimizes $\chi^2(\theta)$. As a consequence, $\chi^2(\theta_0)$ (where θ_0 is the "true" value) follows a χ^2 -distribution. If the number of detected photons is large and the measured events are statistically independent, the measured counts obey the Poissonian distribution and the variance $\sigma_i^2(h(x_i))$ is the sum of the measured source and background counts (in practice, σ_i could also be affected by systematic errors).

Fitting a model means to vary the free parameters of the spectrum in order to reduce the χ^2 value to a minimum. At that point the values of the parameters are considered to be the statistically best fitting parameters. Under ideal circumstances the measured data will be described by

only one particular functional form, with fitting parameters much better than in other models.

The confidence level (CL) for a given value of $\nu = n - k$ and a calculated χ^2 in the fit results is a test for the statistical significance of the correspondence according to

$$\text{CL} = \int_{\chi^2_{(\theta)}}^{\infty} p_{\chi^2}(\nu = n - k | x^2) dx^2$$

(taken from Zombeck 1990³), where $p_{\chi^2}(\nu = n - k | x^2)$ is the χ^2 -probability-distribution for $n - k$ degrees of freedom, given as

$$p_{\chi^2}(\nu = n - k | x^2) dx^2 = \frac{1}{2^{\nu/2} \cdot \Gamma(\nu/2)} (x^2)^{(\nu/2)-1} e^{-x^2/2} dx^2.$$

For a high confidence in a fitting result, one can prove that the relation $\chi^2/(n - k) \sim 1$ is valid (by using an asymptotic expansion of p_{χ^2}). The ratio defined by $\chi^2_{\text{red}} := \chi^2/(n - k)$ is called the "reduced χ^2 " (often written as " χ^2/dof " or " χ^2_{ν} "). Having found a set of parameters as a good description of the data, this value should be approximately unity (Bevington & Robinson 1992; see Figure 3.1). For $\chi^2/\nu \gg 1$ the results represent a poor fit, whereas in the opposite case ($\chi^2/\nu < 1$) the errors of the data have been over-estimated.

In order to use the fitting technique mentioned above it is appropriate to have at least 20 counts per spectral bin (Nandra et al. 1997b). If there are too few counts in each PI channel, it is common to rebin the data, *i.e.* to bin the PI channels with the neighbouring channel, so that the statistical error in each bin is Gaussian-like. Care has to be taken when computing the statistical uncertainties of the newly formed data bins due to the small number statistics (e.g. Gehrels 1986). The fitting results might be wrong. If the count rate is too low and rebinning is useless, it is only possible to determine the total flux in the detector corresponding to some assumed form.

The spectra presented in this thesis were initially binned to 20 counts per bin for the purpose of determining the goodness-of-fit. Where possible the binning of the photon statistics was reduced to reach a better comparison between the data and the shape of the different model components. All fitting results of spectral models to the data presented are based on the usage of the spectral fitting package XSPEC, version 11.2 (Arnaud 1996, 1999). The statistical uncertainties were calculated with the algorithms included in this program (see the XSPEC Manual for details). The uncertainty of a model parameter is computed by firstly, varying it around its best fit value, and secondly, for each value of the parameter range: fitting a new model (with the parameter fixed at its present value and letting the other parameters to vary) to obtain a new χ^2 value. As a result the probability of the "true" value of the parameter being in its varying

³<http://ads.harvard.edu/books/hxaa/toc.html>

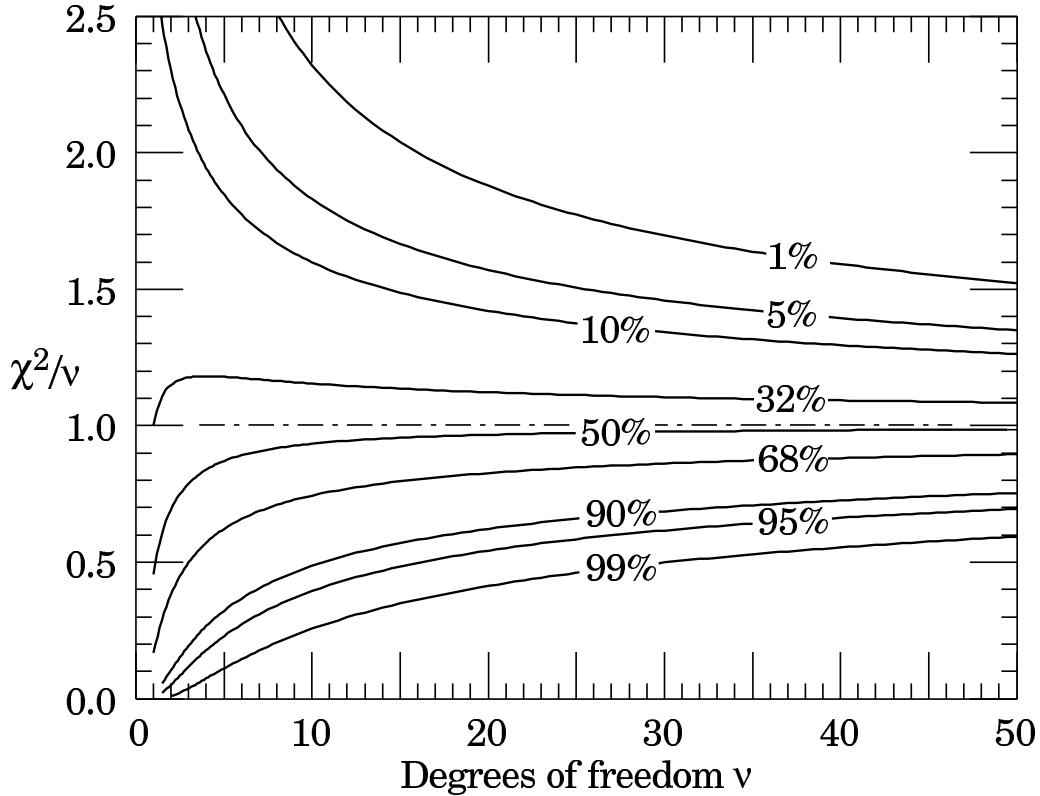


Figure 3.1: χ^2/v values as a function of the degrees of freedom v for different confidence levels. The labels at the curves indicate the probability of exceeding an χ^2/v value given on the ordinate. The larger v (*i.e.* the more free parameter a model has) the closer χ^2/v is to unity for a given level of confidence (Hagiwara et al. 2002).

range is $1 - \text{CL}$ (called the "confidence interval" of the parameter). The uncertainties given in the text are confidence intervals for one parameter ($k = 1$) at the 90% level ($\text{CL} = 0.1$) with $\chi_1^2(0.1) = 2.71$ (located slightly outside Figure 3.1 on the upper left).

The count rate of the background spectrum (BG; in counts s^{-1}) is automatically normalized when it is subtracted from the count rate of the spectrum in the region with the source (SRC)⁴ according to

$$\text{count rate (SRC - BG)} = \frac{\text{count rate (SRC)}}{\text{EXPOSURE (SRC)}} - \frac{\text{count rate (BG)}}{\text{EXPOSURE (BG)}} \cdot \frac{\text{BACKSCAL (SRC)}}{\text{BACKSCAL (BG)}},$$

where the exposure times of the source and the background region are stored in the FITS keyword "EXPOSURE" of each of the spectral data files. The ratio of the real number keywords "BACKSCAL" of both regions accounts for different selection areas.

⁴To be more precisely: the source region SRC contains counts from the source *and* the background, but is here called the source count rate.

3.2 The object NGC 6240

The results on the *XMM-Newton* observation of NGC 6240 presented in this section are based on the major analysis steps published by Boller, Keil, Hasinger et al. (2003, *A&A*, 411, 63). Using the same processed data files the quoted values originate from an own independent data analysis. Most of the results are consistent with the numbers in the paper (except for the Fe-K-EWs; see note of Table 3.8 on p. 71). Details of previous observations are given in the following subsection, with a separate part dedicated to the recent *Chandra* results.

3.2.1 Published results

NGC 6240 (= IRAS 16504+0228) is one of the most interesting and best studied objects in the class of LIGs/ULIRGs. Although it is slightly less luminous than the typical IR luminosity used to define an ULIRG (with $L_{\text{FIR}} \simeq 6 \cdot 10^{11} L_{\odot}$ for $H_0 = 75 \text{ km s}^{-1} \text{ Mpc}^{-1}$; Genzel et al. 1998), it exhibits all of the ULIRG characteristics, and it is thus studied as a prototype of AGN–Starburst composite galaxies. With a far–IR luminosity of some $0.9 L_{\text{bol}}$, NGC 6240 can be considered to be an extraordinary luminous infrared galaxy. Optical/IR observations show a complex system with a disturbed morphology consisting of two gravitationally interacting nuclei (separation $\sim 1.8''$; Fosbury & Wall 1979; Fried & Schulz 1983; Tacconi et al. 1999). This gives evidence for strong interactions, namely on–going merging processes such as the formation of double nuclei systems and/or tidal tails. An *ISO* observation of NGC 6240 (Genzel et al. 1998) favours a Starburst–power source, in which the high infrared emission arises from warm, absorbing dust, surrounding the inner parts of the galaxy. Spectroscopic results show evidence for a massive star formation without any strong high excitation lines typical for AGN.

The *ROSAT–PSPC* observation of NGC 6240 (Schulz et al. 1998) revealed an exceptionally high X–ray luminosity (with $L_{(0.1-2.4) \text{ keV}} \sim 10^{10} L_{\odot}$), which further confirmed the importance of NGC 6240 in understanding the AGN–Starburst connection. Therefore, considerable effort has been made to analyze the spectral and spatial properties using different X–ray satellites.

First *ROSAT* observations showed that a hot, diffuse gas model in combination with a power law component can give a good description of the (0.1 – 2.4) keV energy band spectrum (Schulz et al. 1998). The optically thin gas emits thermal radiation (with $T \simeq 0.63 \text{ keV}$) due to shocks arising in Starburst processes, whereas the power law component was attributed to the existence of an AGN–like source in NGC 6240, since it is interpreted as light upscattered from far–IR photons (via inverse-Compton processes) originating in a hidden powerful central engine. An extended and luminous soft X–ray component has been reported by Komossa et al. (1998) using *ROSAT–HRI* observations, which showed emission up to $\sim 25''$ from the centre.

This radiation should be responsible for at least 60% of the (0.1 – 2.4) keV luminosity (within a region of 5'' radius from the centre). The combination of the extent and the Raymond–Smith–like thermal spectrum led to the idea that the origin of the soft X–rays are strong thermal processes indicative of a powerful, X–ray luminous Starburst. In the author’s estimation each one of the power sources (either the AGN or the Starburst) can serve as the origin of the luminous far–IR emission, with a comparable contribution.

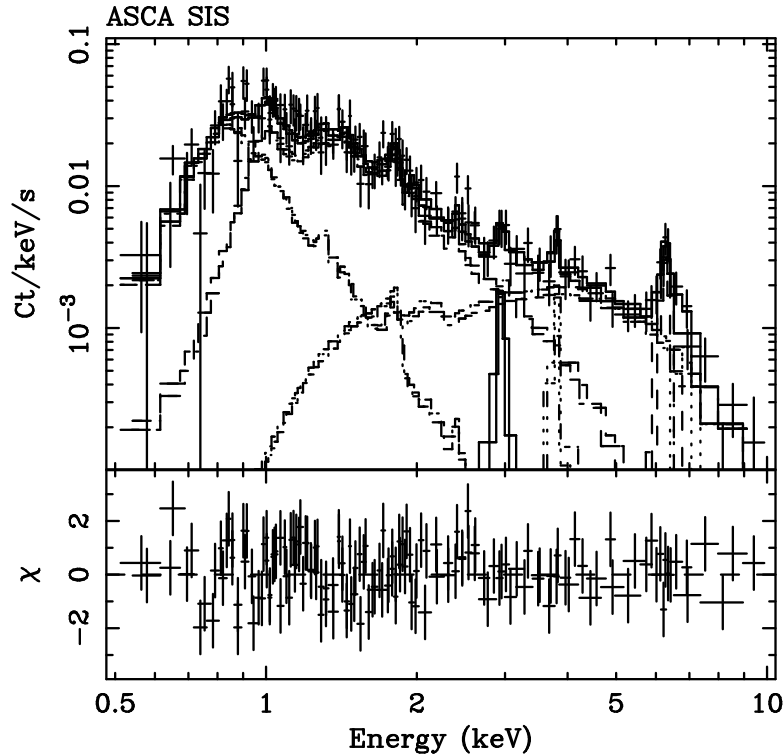


Figure 3.2: The *ASCA*–*SIS* spectrum of NGC 6240. As shown in the upper panel the model consists of two thermal components plus an absorbed (hard) power law with two significantly detected gaussian lines around (6 – 7) keV (Iwasawa & Comastri 1998; see the text for more details). The lower panel gives the deviations of the data from the model.

According to *ROSAT*–*PSPC* data Iwasawa and Comastri (1998) confirmed the detection of extended soft X–ray emission. This is indicated by the (0.5 – 2) keV spectrum from the *PSPC* and the *ASCA*–*SIS* data that can be best described by a superposition of two optically thin thermal plasmas having temperatures of $kT_1 \simeq (0.2 - 0.6)$ keV and $kT_2 \simeq 1$ keV and a N_H value roughly an order of magnitude higher than the Galactic value of $N_{H,gal} = 5.8 \cdot 10^{20}$ atoms cm^{-2} (Figure 3.2). At energies above 3 keV *ASCA* detected a highly absorbed hard X–ray source in NGC 6240, appearing via an extremely hard continuum slope ($\alpha \simeq -0.7$ to -1.0), typical for Seyfert 2 galaxies, as it has been previously supposed by Turner et al. (1997b) and Netzer et al. (1998). A column density of $N_H \sim 10^{24}$ atoms cm^{-2} measured an X–ray luminosity of $L_X \simeq 10^{44}$ erg s^{-1} . The continuum emission below 5 keV is scattered light, imprinted by emis-

sion lines of large EWs, namely from magnesium, silicon, sulphur and iron. Extrapolating the unobscured X-ray continuum to softer energies reveals that at least $0.5 L_{\text{bol}}$ is emitted in the hard band (assuming an AGN–“typical” SED). The presence of a strong Fe-K complex has been reported by Mitsuda 1995 and Iwasawa & Comastri 1998. This indicates the presence of a luminous AGN completely hidden by Compton-thick material. The emitted light is reflected into the line-of-sight (e.g. George, Fabian & Nandra 1990). Furthermore, the Fe emission line profile could be well explained by a superposition of two Gaussian lines at $E_1 = (6.44 \pm 0.04)$ keV and $E_2 = (6.87 \pm 0.05)$ keV. The authors interpret this as reflection from a highly ionized medium (with the complex being a blend of resonant lines). Later we will see that collisionally-ionized hot plasmas can provide a good explanation (3.2.3 on p. 56f and 3.2.4.2 on p. 69ff).

The idea of an AGN at the centre of NGC 6240 to account for a significant amount of the far-IR luminosity is supported by the X-ray spectroscopy. In order to search for a hidden AGN showing a strongly absorbed continuum emission above 10 keV, Vignati et al. (1999) as well as Ikebe et al. (2000) investigated NGC 6240 by using data from *BeppoSAX* and *RXTE*, respectively. Both authors conclude that NGC 6240 harbours an AGN. The results of their Starburst fit analyses are in agreement, regardless whether a direct nuclear X-ray emission component could be detected (Vignati) or not (Ikebe). Both find that the AGN component has an unabsorbed luminosity of $L_{(2.0-10.0) \text{ keV}} \simeq 10^{44} \text{ erg s}^{-1}$, directly related to a Compton-thick absorber (with $N_{\text{H}} \gtrsim 10^{24} \text{ atoms cm}^{-2}$; see Figure 3.3). This results in a ratio of $L_{(2.0-10.0) \text{ keV}}/L_{\text{IR}} = 0.01 - 0.1$. Compared to $L_{(2.0-10.0) \text{ keV}}/L_{\text{bol}} \sim 0.03$, which is typical for QSOs (Elvis et al. 1994), this value is consistent with usual values for AGN. Therefore, it implies that NGC 6240 is dominated by the AGN in the X-rays.

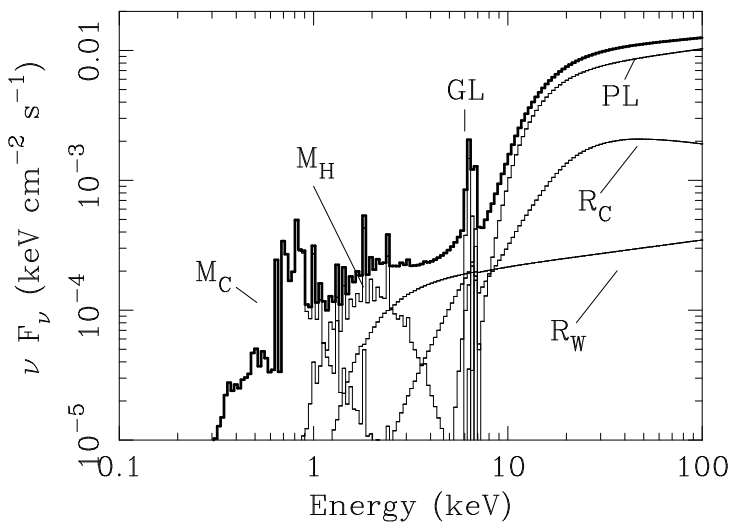


Figure 3.3: The best model fitting the NGC 6240 data, deconvolved from the responses of the *BeppoSAX* detectors (thick line: total model, thin lines: diverse model components). Gaussian lines (GL) as well as the reflection components R_{W} and (probably) R_{C} suggest the existence of an AGN hidden behind an absorber of $N_{\text{H}} \gtrsim 10^{24} \text{ atoms cm}^{-2}$, appearing above $\sim 9 \text{ keV}$. The AGN is modelled by a power law (PL) with $\Gamma = 1.8$ (Vignati et al. 1999).

The *Chandra* observation

In a recent paper on *Chandra*–*ACIS-S* data from NGC 6240 Komossa et al. (2003) report the discovery of a *binary* system of active galactic nuclei in the X–ray regime. The capability of high–resolution imaging spectroscopy available with the *Chandra* observatory led to this outstanding result. The positions of both nuclei are consistent with the measurements obtained from optical/IR observations. The detection of two strong neutral Fe–K α lines in each of the nuclei indicates the presence of a binary black hole.

Figure 3.4 (next page) displays the hard X–ray emission (blue colour–coded), surrounded by extended soft emission components, that show a filamentary morphological structure in NGC 6240 (in form of loops) with a clumpy concentration of emission (mainly ”knots”; see also the *Chandra*–*HRC-I* data in Lira et al. 2002). It is strongly dependent on the X–ray energy (Figure 1 of Komossa et al.) and is strikingly visible below 2.5 keV. Both the extent and the morphology of the X–ray emission are suggestive of an on–going Starburst, since the spectrum can be well described by a thermal plasma model with $kT = (0.81 \pm 0.05)$ keV and a moderate absorption of $N_H = (3.1 \pm 0.4) \cdot 10^{21}$ atoms cm^{-2} (and a hotter plasma for a blob–like structure, respectively). This interpretation is supported by considerations about ”superwinds” driven by Starburst processes as supposed by H α images (taken e.g. with the *HST*–*WFPC2*, Lira et al. 2002; Heckman et al. 1987); they ought to be responsible for the bulk of the extended X–ray emission.

Above 5 keV both *Chandra* observations have spatially resolved the emission from two compact sources, consistent with the optical positions and separated by 1.4”, corresponding to ~ 0.5 kpc at the distance of NGC 6240. The presence of the neutral Fe–K α lines (summed up to $2 \cdot 10^{-5}$ photons $\text{cm}^{-2} \text{s}^{-1}$) and the hard power law–like X–ray emission ($\alpha_1 = 0.2 \pm 0.3$ and $\alpha_2 = 0.9 \pm 0.2$) indicate that *both* nuclei of the galaxy harbour an AGN. In addition, they found residues in their spectral fits at energies above the neutral Fe–K line, which they interpreted as possible emission from H–like iron (or from the K β line) of the nuclear regions (Figure 3.5). However, the parameters of their spectral model are rather poorly constrained.

Ptak et al. (2003) published a more complex spectral model to the combined hard flux of the nuclei and the entire extended X–ray emission, *i.e.* within (0.5 – 8.0) keV, consisting mainly of two thermal components with $kT_1 \simeq (0.27 - 0.33)$ keV and $kT_2 \simeq (0.62 - 0.72)$ keV, an absorbed power law ($\Gamma \simeq 1.22 - 1.93$), representing scattered light from the AGN, an iron complex based on two Gaussian lines, $E_1 = (6.34 \pm 0.03)$ keV and $E_2 = (6.62 \pm 0.08)$ keV, and finally a Compton reflection component as proposed by Magdziarz and Zdziarski (1995). Following this model the deduced (absorption–corrected) luminosity of NGC 6240 in hard X–rays fit into the range of ULIRGs dominated energetically by an AGN (as defined in the sample of ULIRGs in Ptak et al.), giving $L_{(2.0-8.0) \text{ keV}} \approx 4 \cdot 10^{42}$ erg s^{-1} . Although a hard X–ray source

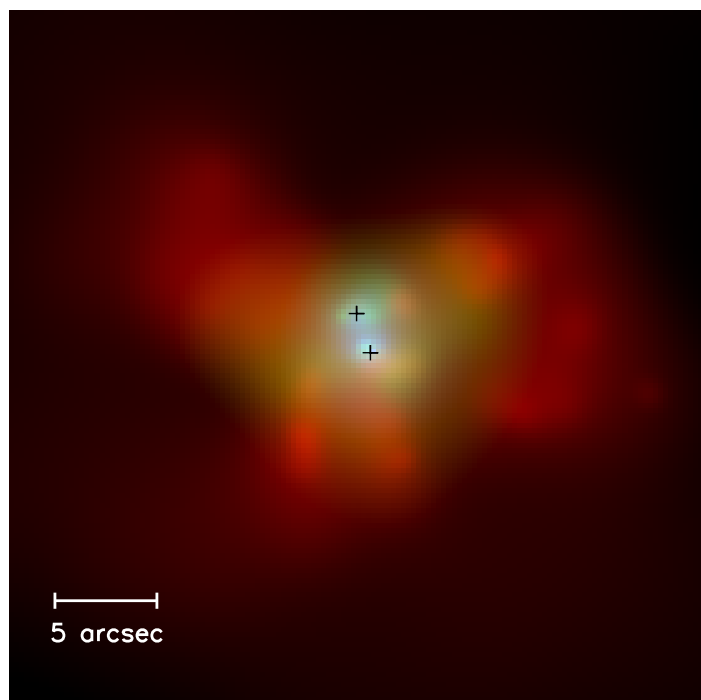


Figure 3.4: The *Chandra* image of NGC 6240 in the energy bands (0.5 – 1.5) keV (red colour-coded), (1.5 – 5.0) keV (green), and (5.0 – 8.0) keV (blue), respectively. The hardest X-ray emission is located in two compact sources (marked with the crosses for the optical sources) indicating the positions of the nuclei. 5'' correspond to 2.4 kpc at the distance of NGC 6240 (taken from Komossa et al. 2003).

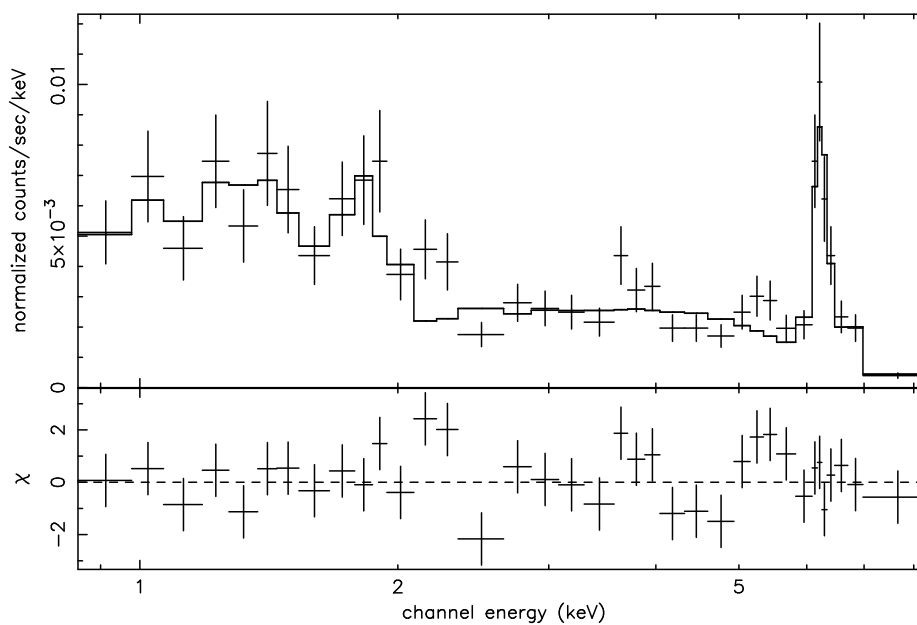


Figure 3.5: The *Chandra* spectrum of the X-ray brighter AGN in NGC 6240, (0.9 – 8.0) keV, together with the best fitting model (a thermal emission component, an absorbed power law and two Gaussian lines) as well as its deviations χ (lower panel; taken from Komossa et al. 2003).

is clearly detected below ~ 8 keV, this value is an explicit underestimation (if at all; compare with Figure 3.3 on p. 49) of the true luminosity of the nuclei. The ratio $L_{(2.0-8.0)\text{ keV}}/L_{\text{FIR}} = 1.7 \cdot 10^{-3}$ suggests that the nature of NGC 6240 is similar to a composite system of a Starburst and a Seyfert 2 galaxy (Levenson et al. 2001). There is no *direct* evidence for high absorbing columns in the *Chandra* data.

Taking into account these new results the data analysis based on *XMM-Newton* makes it possible to investigate the different spectral features with high photon statistics.

The following sections contain the analysis of the X-ray data of NGC 6240 taken with *XMM-Newton*. The data analysis and details of the *XMM-Newton* observations are described in the next section 3.2.2. In section 3.2.4 on p. 58ff the spectral fitting results are discussed. A comparison with the *Chandra* observation is given in section 3.2.5 on p. 73ff. Finally, a summary of the *XMM-Newton* results on NGC 6240 is presented in section 3.2.6 on p. 76ff. The luminosities and fluxes are calculated with a Hubble constant of $H_0 = 50 \text{ km s}^{-1} \text{ Mpc}^{-1}$ and $q_0 = 0.5$.

3.2.2 The X-ray observation

NGC 6240 was observed with *XMM-Newton* for the first time during orbit 0144 on the 22nd of September, 2000, with all instruments functioning except for the RGS. The EPIC pn camera was operated in full-frame mode and the EPIC MOS cameras were operated in large-window mode. Each of the detectors used the medium filter. The exposure times were 25,150 s and 24,349 s for the pn and MOS, respectively. The second observation, with a shorter exposure time of about 18 ks, was performed during orbit 0413 (12th of March, 2002), with all instruments working in the same mode and with the same filters as in the first exposure. In addition, the RGS was functional and operated in Spectro+Q mode, however the exposure time was too short to collect sufficient signal (raw exposure times: 18,917 s for each of the RGS devices).

Table 3.3 on p. 53 gives information about the basic parameters of the observations. The EPIC MOS1 and MOS2 data sets from each observation were combined for this analysis (see the appendix A on p. 159ff for more information on the combining procedure of spectral files and their handling under XSPEC). The resulting spectrum FITS file was grouped with a minimum of 20 counts per bin. For the spectral analysis single and double events have been selected. After correcting the MOS data for background flaring events, the GTI-corrected exposure times for MOS1 and MOS2 were 23,381 s and 23,601 s (first observation – orbit 0144) and 11,318 s and 11,601 s (second observation – orbit 0413), respectively; a total of about 35 ks worth of exposure time, which is used in the analysis. Examining each observation separately and comparing them

to the merged data set, no discrepancies are found in the spectral fitting parameters within the data uncertainties, hence justifying the compilation process. In addition, the EPIC pn data sets were merged in a similar fashion (orbit 0144: 16,255 s, orbit 0413: 9,750 s).

Table 3.3: Summary of the NGC 6240 observations
(revolutions 0144 & 0413)

Instrument	count rate	exposure time	Instrumental mode
	[counts/sec]	[sec]	
EPIC MOS1+2	0.352 ± 0.004	34,699 + 35,202	Large-Window
– MOS1	0.172 ± 0.003	23,381 + 11,318	— ” —
– MOS2	0.178 ± 0.003	23,601 + 11,601	— ” —
EPIC pn	1.190 ± 0.020	16,255 + 9,750	Full-Frame

The EPIC MOS energy resolution (FWHM) is slightly better than that of the EPIC pn. Comparing Fig. 25 and 26 of the XMM-Newton User’s Handbook (v2.1; Document number: XMM-PS-GM 14⁵) one gets an energy resolution for the EPIC MOS devices of about 150 eV in the energy range between 6 and 7 keV. In the same band the energy resolution for the EPIC pn ranges between (150 ± 10) eV for single events and (240 ± 10) eV for double events (upper curve of Fig. 26) and decreases for singles when considering on-axis sources. As the data reduction has made use of singles *and* doubles to increase the photon statistics, the exact value of the energy resolution for both EPIC devices ranges between 150 and 250 eV (depending on the ratio of the singles to doubles). In order to utilize many photons as possible the work has been concentrated on the EPIC MOS for subsequent spectral analyses (about twice as many photons than in the EPIC pn data). With the combined MOS1/2 photons from the two observations the $(0.3 - 10.0)$ keV energy range contains about $1.0 \cdot 10^{-3}$ photons $\text{cm}^{-2} \text{s}^{-1} \text{keV}^{-1}$ (compared to $5.0 \cdot 10^{-4}$ photons $\text{cm}^{-2} \text{s}^{-1} \text{keV}^{-1}$ for the EPIC pn). Nevertheless, the EPIC pn data served as an independent check to the EPIC MOS results for consistency.

⁵ftp://xmm.vilspa.esa.es/pub/A03/XMM_UHB.pdf

The X-ray data were processed using the standard procedures of the *XMM-Newton* Science Analysis System (XMM-SAS in version 20020413_2031-5.3.0) with default parameters for the EPIC chains. The event lists were calibrated with the latest available calibration files⁶.

The source counts in the 0144-observation were extracted from circular regions with radii of $\sim 44''$ (EPIC MOS1/2), and $\sim 53''$ (EPIC pn), respectively; the values for the 0413-observation are $\sim 25''$ (EPIC MOS1/2) and $\sim 30''$ (EPIC pn). The background photons were extracted from a source-free circular region with the following radii: $\sim 56''$ (EPIC MOS1/2) and $\sim 105''$ (EPIC pn) for revolution 0144, $\sim 51''$ (EPIC MOS1/2) and $\sim 97''$ (EPIC pn) for the revolution 0413 (see Figure 3.7, next page). The X-ray spectral analyses were done using the XSPEC package version 11.2 as well as the FTOOLS version 5.2.

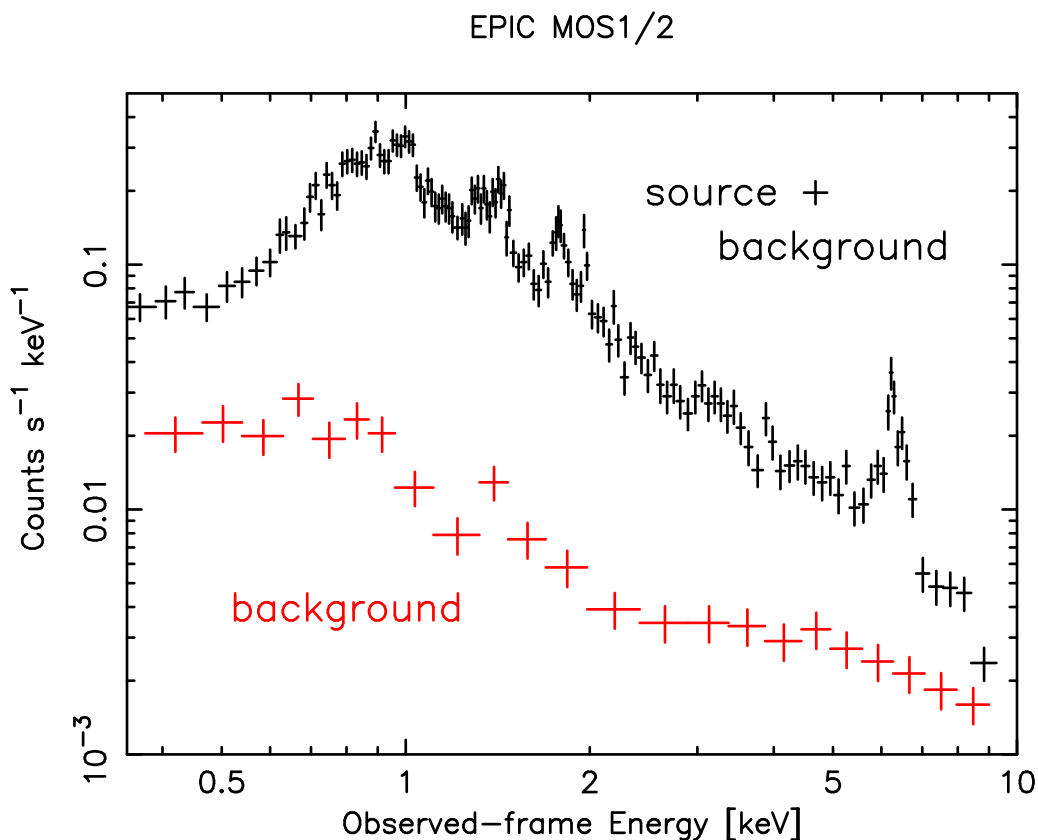


Figure 3.6: The (0.3 – 10) keV spectrum of the combined source *and* background counts (upper curve) and the background counts (lower curve) for the EPIC MOS1/2 data. The spectrum is not background dominated below 10 keV and the Fe-K emission line complex can be investigated with a high signal-to-noise ratio.

⁶<http://xmm.vilspa.esa.es/ccf/>

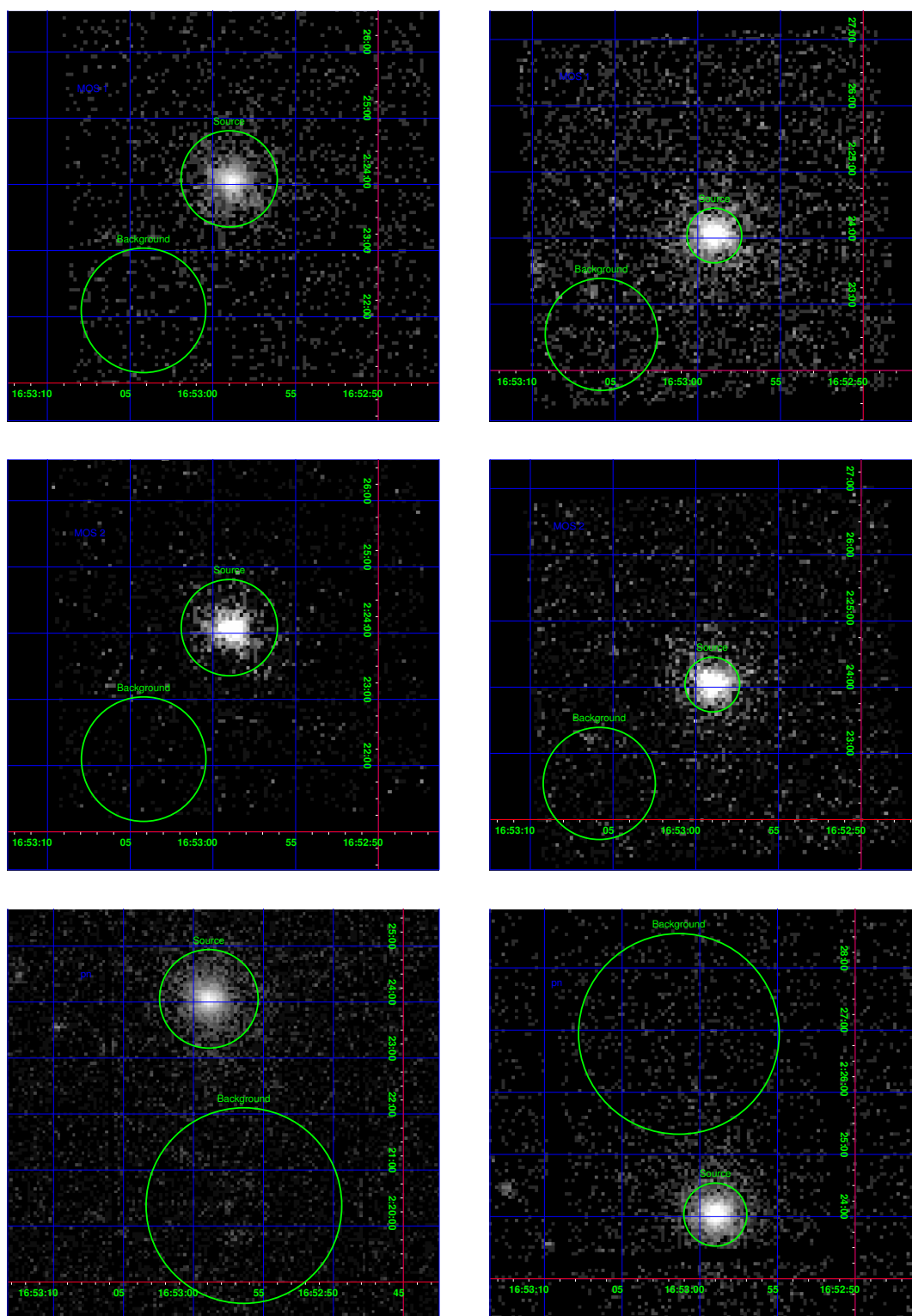


Figure 3.7: Selection regions (green circles) for the source and background counts in the energy band (0.3 – 10.0) keV of the EPIC MOS 1 (upper plot), EPIC MOS 2 (middle plot), and of the EPIC pn detector (lower plot), respectively. North is up and west to the right; a logarithmic scale of the count statistics was used for these images. The data are acquired in revolution 0144 (**left panel**) and 0413 (**right panel**).

3.2.3 Collisionally-ionized plasma emission

In order to model a putative Starburst component in NGC 6240 (see the next section for the application case), a Mewe–Kaastra model for the emission spectrum from a hot, diffuse gas of thin optical depth with solar abundance has been employed (a single phase plasma, *i.e.* with the same density, temperature and metallicity at all points). It is implemented as the "MEKAL" plasma emission code in the XSPEC package (Mewe et al. 1985,1986; Kaastra 1992; Mewe et al. 1995; with a modification by Liedahl, Osterheld & Goldstein 1995). This model is an advanced and sophisticated successor of the code developed by Raymond & Smith (1977, "RAYMOND"; cf. subsection 1.3.1 on p. 25). An updated version using atomic data from 1993 can be used in XSPEC. The main parameters of this model are the plasma temperature kT_{plasma} , the metallicity abundances Z (here the abundance ratios among the different elements are fixed to the solar values, according to Anders & Grevesse 1989) and the normalization $N_{\text{MEKAL}} := 10^{-14}/[4\pi(D_A \cdot (1+z))^2] \int n_e n_H dV$, where D_A is the angular size distance to the source ($[D_A] = \text{cm}$), n_e the electron number density ($[n_e] = \text{cm}^{-3}$), n_H the hydrogen density ($[n_H] = \text{cm}^{-3}$) and V the X-ray emitting volume.

Combined with a simple power law following

$$\begin{aligned} f_{\text{MEKAL+po}}(E) &= f_{\text{MEKAL}}(E) + f_{\text{po}}(E) \\ &= \text{MEKAL}(T_{\text{plasma}}, Z, N_{\text{MEKAL}}) + f_{\text{po}}(E) \end{aligned}$$

this model can provide crucial information about the physical conditions in a source with a thermal emission mechanism.

More recently Brickhouse et al. (2000) developed an independent model to calculate the emission spectrum of an optically-thin thermal X-ray plasma in collisional ionization equilibrium (CIE) with temperatures of $(10^{-2} - 10^2)$ keV (q.v. Smith et al. 2001). The "APEC" model (Astrophysical Plasma Emission Code) is a successor of the Raymond & Smith plasma code, and is based on a different atomic database than the MEKAL model. The output illustrates precalculated model spectra as a function of the plasma temperature and ionization state (the self-consistent ionization balance is provided by Mazzotta et al. 1998) according to

$$\begin{aligned} f_{\text{APEC+po}}(E) &= f_{\text{APEC}}(E) + f_{\text{po}}(E) \\ &= \text{APEC}(T_{\text{plasma}}, Z, N_{\text{APEC}}) + f_{\text{po}}(E) \end{aligned}$$

with exactly the same definition of the parameters as given for the MEKAL model parameters above. By combining the APEC results with calculations of individual line oscillator strengths, fits to the collisional excitation rate coefficients, etc. (stored within the Astrophysical Plasma

Emission Database "APED") result in both continuum spectra and emission line lists from an X-ray emitting plasma. Figure 3.8 shows the spectra predicted by the three different plasma spectral codes APEC, MEKAL, and RAYMOND, respectively. The model parameters used for this calculations are the values arising from the fitting process (including the Galactic absorption "PHABS" with $N_{\text{Gal. abs}} = 5.8 \cdot 10^{20}$ atoms cm^{-2}). The APEC description is the latest development from atomic physics, and is used three times in the spectral modelling (with varying elemental abundances for two of them):

$$\begin{aligned} f_{\text{APEC+po}}(E) &= f_{\text{vAPEC}(1)}(E) + f_{\text{vAPEC}(2)}(E) + f_{\text{APEC}(3)}(E) + f_{\text{po}}(E) \\ &= \text{vAPEC}(1)(T_{\text{plasma}}, Z, N_{\text{vAPEC}}) + \text{vAPEC}(2)(T_{\text{plasma}}, Z, N_{\text{vAPEC}}) \\ &\quad + \text{APEC}(3)(T_{\text{plasma}}, Z_{\odot}, N_{\text{APEC}}) \\ &\quad + f_{\text{po}}(E) \end{aligned}$$

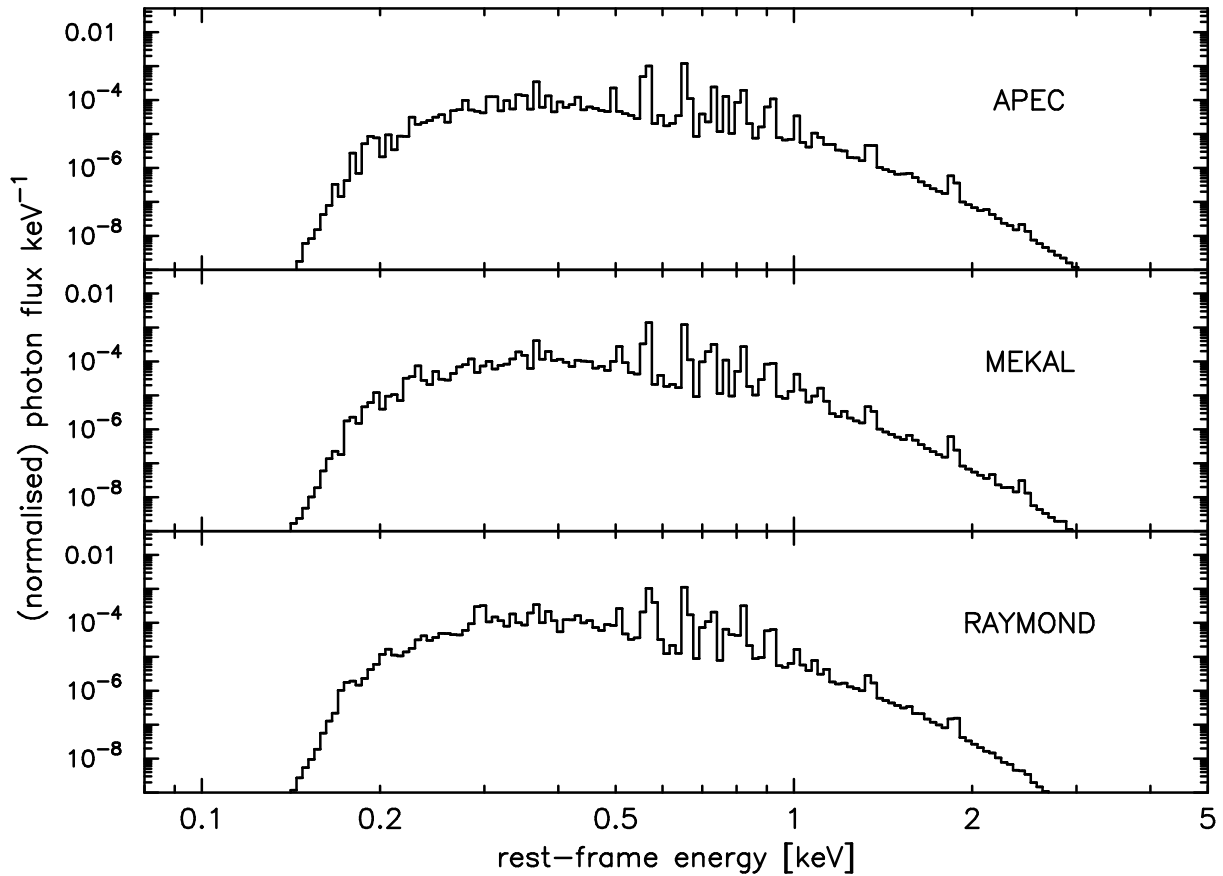


Figure 3.8: Simulated spectra of an optically thin thermal X-ray emitting plasma using the APEC (**top panel**), MEKAL (**middle panel**), and RAYMOND model (**lower panel**), respectively. To each of the models a PHABS component of $N_{\text{H,gal}} = 5.8 \cdot 10^{20}$ atoms cm^{-2} with solar metallicity abundance has been multiplied. The calculations are based on the output values of the fitting procedure and were performed using XSPEC version 11.1.

3.2.4 Spectral Analysis

The combined MOS1/2 spectrum of NGC 6240 is not background-dominated below 10 keV (cf. Figure 3.6 on p. 54). Therefore, the energy range (0.3 – 10.0) keV could be analyzed. A first look reveals typical characteristics of thermal emission in the soft part of the X-ray spectrum (below ~ 3.5 keV). Above ~ 6 keV a strong iron K line feature emerges.

3.2.4.1 The Fe-K emission line complex

The high throughput⁷ of *XMM-Newton* allows precise measurements of the Fe-K line complex in much more detail compared to previous X-ray missions. In this section it is demonstrated that the Fe-K line complex is resolved into *three* distinct lines with high significance.

XMM-Newton detection of three distinct Fe-K emission lines

As a simple first approach the (5.0 – 7.4) keV energy range was fitted with a power law model plus two narrow Gaussian lines (of physical width $\sigma = 0$ fixed; cf. Figure 3.9, upper plot). The centroid line energies are found at $E_{c,1} = (6.40 \pm 0.03)$ keV and $E_{c,2} = (6.67 \pm 0.02)$ keV in the rest frame of the source. Strong residuals remain at ~ 6.5 keV and around (6.8 – 6.9) keV, the fit appears to be barely acceptable ($\chi^2/\nu = 1.81$ for 21 dof). Moreover, the data poorly agree to the idea that the Fe line complex can be modelled by a narrow unresolved 6.4 keV line and a broad line at slightly higher energy, probably a close blend of higher ionized lines (see Figure 3.9, middle graph). The energies are given by $E_{c,1} = (6.40 \pm 0.03)$ keV and $E_{c,2} = (6.62 \pm 0.07)$ keV with $\sigma_2 = (0.3 \pm 0.1)$ keV and $EW_2 = (740 \pm 500)$ eV. The reduced χ^2 -value is $\chi^2/\nu = 1.71$ for 21 dof. The width of the second line is larger than the instrumental resolution at this energy according to $\sigma(\text{MOS}; E_{c,2}) = \text{FWHM}(\text{MOS}; E_{c,2})/2.35 \approx 150 \text{ eV}/2.35 \approx 60 \text{ eV}$. This favours a blending effect. To determine the uncertainties of this fit, the STEPPAR procedure in XSPEC provides confidence intervals of 68%, 90%, and 99% likelihood, where the χ^2 -statistics increases by no more than 2.3, 4.61, and 9.21. Figure 3.10 (on p. 60) plots the confidence contours for two line parameters, the centroid line energy in the observer's frame and the line width as measured by a fit with a Gaussian line profile. The best-fitting energy value is significantly higher than the expected energy from the Fe-K α line (by more than 3σ), thus the broadened line is likely a blend of iron lines of higher ionization level.

The strong residues at ~ 6.5 keV and around (6.8 – 6.9) keV (in the observer's frame) are clearly reduced by using a model of a power law plus three narrow unresolved Gaussian lines ($\chi^2/\nu = 1.08$ for 20 dof; Fig. 3.9, bottom plot). The fitting routine finds three lines at $E_{c,1} = (6.41 \pm$

⁷This engineering term describes the fraction of the input signal that is actually utilizable; having a high throughput an X-ray detector can register more X-ray photons at all attainable energies.

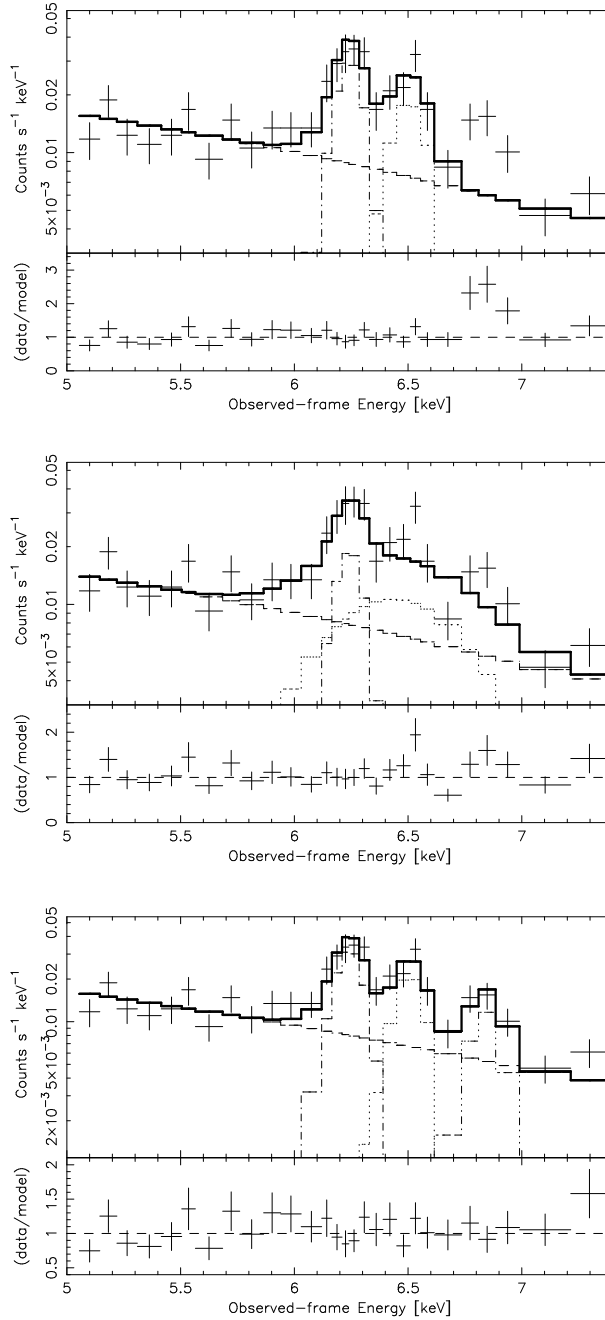


Figure 3.9: Fits to the EPIC MOS1/2 spectra of NGC 6240 in the Fe-K line range (5.0 – 7.4) keV, as seen in the frame of the source. In each plot the upper panel shows the data and the model (thick solid line) as well as the diverse model components (dash-dotted lines). The lower panel displays the ratio of the data to the model.

Upper plot: A model consisting of two narrow Gaussian lines and a power law continuum results in a barely acceptable fit ($\chi^2/\nu = 1.81$ for 21 dof).

Middle plot: Fitting the line complex with one narrow and one broad Gaussian line gives $\chi^2/\nu = 1.71$ for 21 dof, still improvable.

Bottom plot: An acceptable fit can be obtained by using an improved model with three Gaussian lines above a power law continuum. The line energies are $E_{c,1} = (6.41 \pm 0.01)$ keV, $E_{c,2} = (6.67 \pm 0.02)$ keV and $E_{c,3} = (7.01 \pm 0.03)$ keV in the observer’s frame. With high statistical significance ($\chi^2/\nu = 1.08$ for 20 dof), the *XMM-Newton* data reveal for the first time the presence of *three* distinct narrow Fe-K lines.

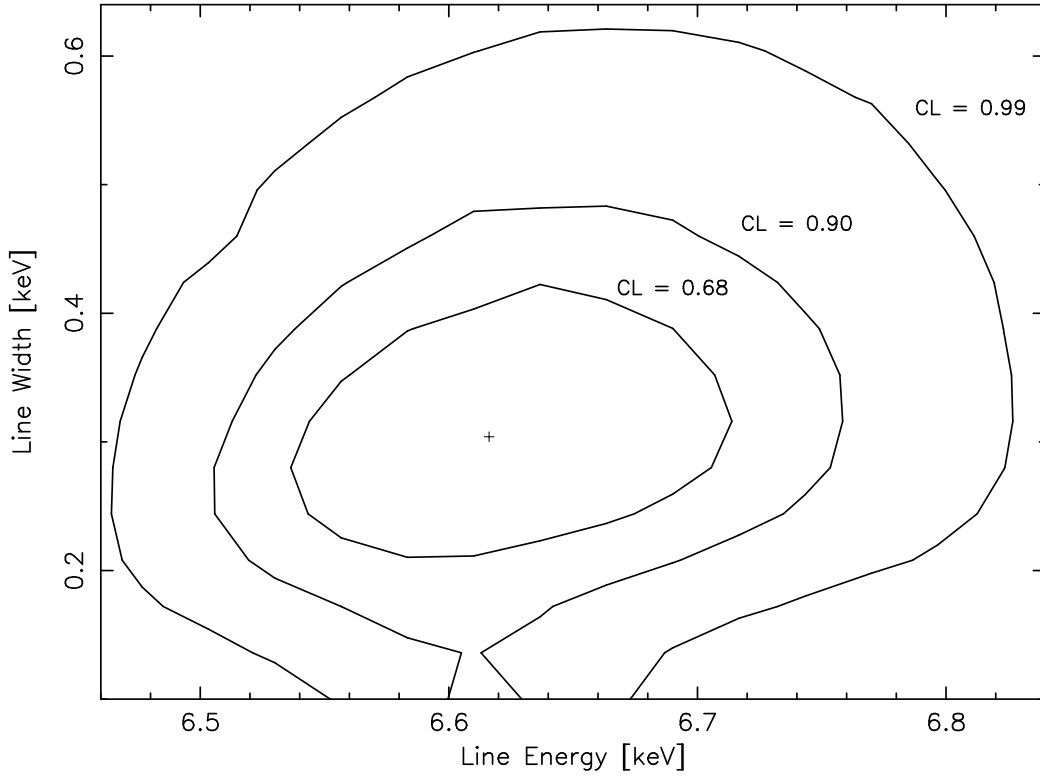


Figure 3.10: Confidence contour plot of the centroid line energy and the line width for the high-energy part of the Fe line complex, based on the EPIC MOS1/2 data of NGC 6240 within (5.0–7.4) keV. The line energy is redshift-corrected and the line width is determined by the fit of a Gaussian profile to the data. The confidence levels (CL) are 68%, 90%, and 99% for both parameters, respectively and labelled in the plot. The plus sign (+) marks the value of the parameters corresponding to the best fit. The 6.4-keV-line of neutral iron is clearly disentangled from this residual and is not shown.

0.01) keV, $E_{c,2} = (6.67 \pm 0.02)$ keV and $E_{c,3} = (7.01 \pm 0.03)$ keV with high significance and high stability against little deviations from the best-fitting parameter values. Table 3.4 gives an overview of all fit results concerning the Fe-K line complex, including the three line model (see also Table 3.8 on p. 71).

With high statistical significance, the XMM-Newton data reveal for the first time the presence of three narrow Fe-K lines.

In the former two of the fitting models the slope of the power law component is rather hard ($\Gamma \sim 0.7$), whereas the photon index of the best fitting model is $\Gamma \sim 1.2$. Nevertheless, these numbers should not be interpreted in terms of a physical explanation. They should merely provide the energy range with an acceptable representation of the continuum as a basis of measuring the parameters of the emission lines. In this case, the present absorbed power law for the modelling has not been taken into consideration.

Table 3.4: Fit results of Gaussian lines to the Fe-K line complex
(5.0 – 7.4) keV, EPIC MOS1/2, revolution 0144

Number of Gaussian lines	E_C [keV]	σ [keV]	EW [eV]	$I_{\text{Fe}}^{\text{a)}}$	$f_{\text{Fe}}^{\text{b)}}$	χ^2_{ν} (dof)
Two lines						1.81 (21)
Line 1	6.40 ± 0.03	0 (fixed)	570 ± 190	2.5 ± 0.8	2.5 ± 0.8	
Line 2	6.67 ± 0.02	0 (fixed)	520 ± 230	2.2 ± 1.0	2.3 ± 1.0	
Two lines						1.71 (21)
Line 1	6.40 ± 0.03	0 (fixed)	400 ± 260	1.6 ± 1.0	1.6 ± 1.0	
Line 2	6.62 ± 0.07	0.3 ± 0.1	1200 ± 820	5.0 ± 3.0	4.7 ± 3.2	
Three lines						1.08 (20)
Line 1	6.41 ± 0.01	0 (fixed)	660 ± 190	2.7 ± 0.8	2.6 ± 0.7	
Line 2	6.67 ± 0.02	0 (fixed)	550 ± 200	2.1 ± 0.7	2.2 ± 0.8	
Line 3	7.01 ± 0.03	0 (fixed)	400 ± 210	1.5 ± 0.7	1.6 ± 0.8	

a) the iron line intensity, in [10^{-5} photons $\text{cm}^{-2} \text{s}^{-1}$],

b) the iron (5.0 – 7.4) keV–flux, in [10^{-13} erg $\text{cm}^{-2} \text{s}^{-1}$].

The requirement to apply three lines to the data in order to resolve the (5.0 – 7.4) keV regime is supported quantitatively by the contour plot in Figure 3.11. It shows the line intensity as a function of the line energy for the EPIC MOS1/2 data within the (6.3 – 7.1) keV band. This plot gives evidence for the need of (at least) two emission lines representing the high–energy part of the Fe line complex in the spectral data. The emission around ~ 7 keV is supposed to be a superposition of the Fe XXVI and the Fe-K β lines (see 3.2.4.1 for details). The distinction of their emission amount is possible due to the high quality data, since the energy resolution of the EPIC detectors does allow to resolve an energy difference of $\Delta E \simeq 0.14$ keV as it can be seen in Figure 3.12 (on p. 63). The model including four Gaussian lines (incl. the Fe-K β line) does not provide significantly better constraints on the model parameters ($\chi^2/\nu = 1.09$ for 19 dof).

The physical origin of the ionized Fe-K lines

The line energies given in Table 3.4 suggest that – besides the emission line at 6.4 keV, which originates from neutral iron – ionized iron is present in NGC 6240 as well, since 6.67 keV would correspond to the K α –emission from Fe XXV and the 7.01 keV–line from Fe XXVI. However, a visible neutral Fe-K α line requires the neutral Fe-K β line to be present in the spectrum, though

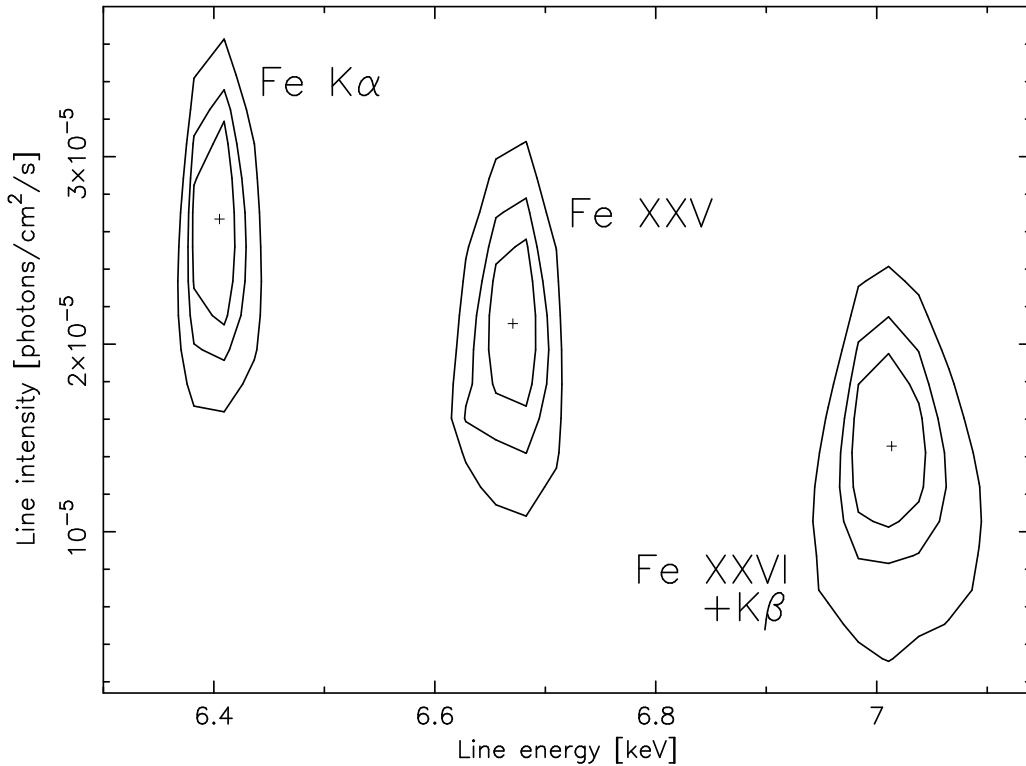


Figure 3.11: Confidence contour plot of the centroid line energy and the line intensity for the Fe line complex, based on the EPIC MOS1/2 data of NGC 6240 within the (5.0–7.4) keV range. The line energy is redshift–corrected and the line intensity is measured by the fit of a Gaussian profile to the data. The confidence levels are the same as for Figure 3.10 (on p. 60). The plot shows a clear evidence for a *third* emission component in the spectrum of the Fe line complex of NGC 6240.

with an intensity 8.8 times smaller than that of the $K\alpha$ line (see 1.2.2 on p. 17f). Therefore, the 7.01– keV–line intensity should be a superposition of the Fe XXVI line and the Fe- $K\beta$ line. In the spectral fitting procedure the model for the line complex includes the emission from the Fe- $K\alpha$ line at 6.4 keV and the Fe- $K\beta$ line at 7.058 keV as well as the components from the ionized material, the Fe XXV and Fe XXVI lines. For simplicity, all lines have been fitted as Gaussian lines in order to measure the parameters of each line individually. Table 3.5 shows the results of this model.

Figure 3.12 displays the EPIC MOS1/2 spectral fit of the Fe line complex in NGC 6240 within the (5.0 – 7.4) keV range. For illustration purposes the plot shows the detailed energy band (5.5 – 7.2) keV as well as each single line component. The continuum emission has been assumed to follow a simple power law slope ($\Gamma \sim 1.0$; not plotted) with the same restrictions as mentioned for the previous fitting models to the line complex.

A more physically motivated model to explain the appearance of ionized iron arises from the presence of a collisionally–ionized plasma (using the APEC model within XSPEC). A plasma

Table 3.5: Fit results of *four* Gaussian lines to the Fe-K line complex
(5.0 – 7.4) keV, EPIC MOS1/2, revolution 0144

Number of Gaussian lines	E_C [keV]	σ [keV]	EW [eV]	$I_{\text{Fe}}^{\text{a,c}}$	$f_{\text{Fe}}^{\text{b,c}}$	χ^2_{ν} (dof)
Four lines						1.09 (19)
Line 1	6.40 ± 0.01	0 (fixed)	680 ± 200	2.7 ± 0.8	2.6 ± 0.7	
Line 2	6.67 ± 0.02	0 (fixed)	550 ± 200	2.1 ± 0.7	2.2 ± 0.8	
Line 3	7.00 ± 0.03	0 (fixed)	360 ± 300	1.3 ± 1.1	1.4 ± 1.1	
Line 4	7.10 ± 0.20	0 (fixed)	90 ± 30	0.3 ± 0.1	0.3 ± 0.1	

a) the iron line intensity, in [10^{-5} photons $\text{cm}^{-2} \text{s}^{-1}$],

b) the iron (5.0 – 7.4) keV–flux, in [10^{-13} erg $\text{cm}^{-2} \text{s}^{-1}$],

c) $\text{Norm}_{\text{FeK}\beta} = \text{Norm}_{\text{FeK}\alpha}/8.8$.

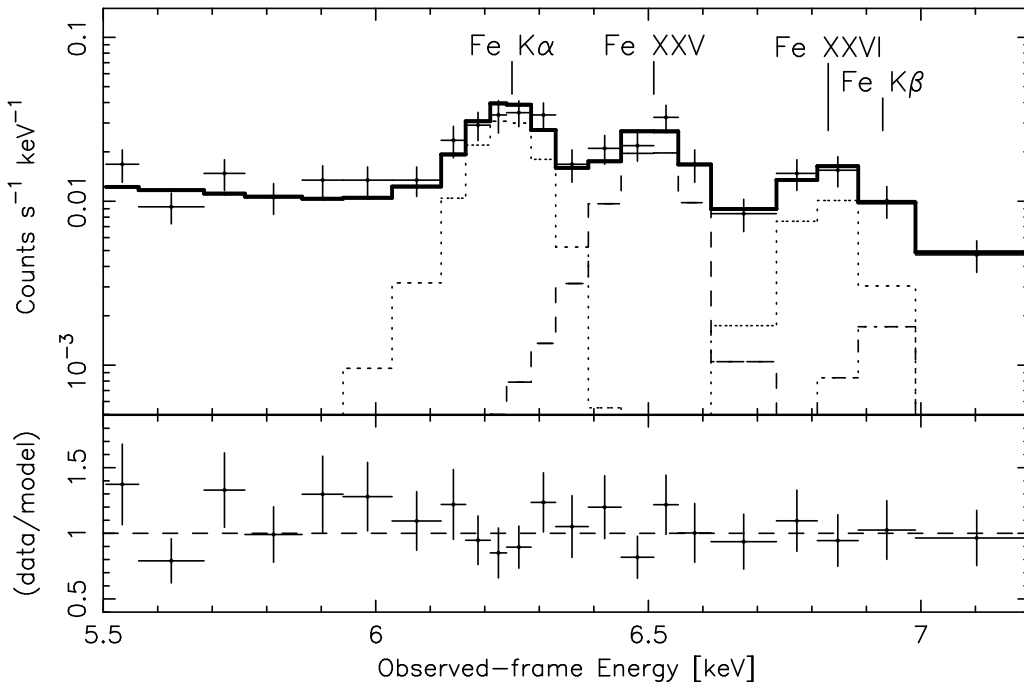


Figure 3.12: Spectral fit result to the EPIC MOS1/2 data of NGC 6240 in the (5.5 – 7.2) keV range, comprising the Fe line complex (with the identifications of the lines). The model used consists of four Gaussian lines for the neutral Fe-K α and K β lines as well as for the Fe XXV and Fe XXVI lines in order to measure the diverse parameters of each line individually. The continuum emission was assumed to obey a power law slope. The fitting was performed between 5.0 keV and 7.4 keV ($\chi^2_{\nu} = 1.09$ for 19 dof).

with a temperature of ~ 6.4 keV produces emission of the resonant lines Fe XXV at 6.68 keV and Fe XXVI at 6.93 keV, with a strength sufficient to match the observational data. Together with two Gaussian lines for the neutral Fe lines (fixing to $\sigma = 0$) the fitting procedure results in the parameters given in Table 3.6 (on p. 64). Although the temperature of the plasma seems to be extraordinary high compared to the plasmas usually assumed for thermal emission components in these objects, this value is not arbitrary, since it has been successfully applied to the nuclear spectrum of pure Starburst galaxies like the local NGC 253 (in addition to lower-temperature plasmas; see the subsection 3.2.4.3 on p. 72f). Its statistical significance is $\chi^2/\nu = 1.16$ for 25 dof, justifying this model to be considered as a physically description of the Fe-K line complex. Figure 3.13 shows the spectral fit results within the (5.5 – 7.2) keV range, based on the spectral model using APEC (see Figure 3.14 on p. 66 for all model components).

Table 3.6: Fit results of an APEC model plus two Gaussian lines to the Fe-K line complex (5.0 – 7.4) keV, EPIC MOS1/2, revolution 0144

Model Parameter	Value	Model Parameter	Value	Model Parameter	Value
APEC		Line 1		Line 2	
kT [keV]	6.40 ± 0.90	E_C [keV]	6.41 ± 0.01	E_C [keV]	7.10 ± 0.10
Norm ^{a)}	2.80 ± 0.30	Norm ^{b)}	2.80 ± 0.70	Norm ^{b)}	0.32 ± 0.08
flux ^{c)}	10.0 ± 1.0	flux ^{c)}	2.80 ± 0.70	flux ^{c)}	0.35 ± 0.09

a) $\times 10^{-3}$, for the unit see 3.2.3 on p. 56,

b) the iron line intensity, in [10^{-5} photons $\text{cm}^{-2} \text{s}^{-1}$]; $\text{Norm}_{\text{FeK}\beta} = \text{Norm}_{\text{FeK}\alpha}/8.8$,

c) in [10^{-13} erg $\text{cm}^{-2} \text{s}^{-1}$].

In addition, investigations were carried out into other model descriptions in order to understand the origin of the ionized line emission in NGC 6240. Firstly, the Fe-K line complex was modelled by helium- and hydrogen-like Fe emission originating from an accretion disk. The "ionised disk" model as described in Ross & Fabian (1993)⁸ and successfully applied on Narrow-line Seyfert 1 galaxies by Ballantyne et al. (2001), computes a reflection spectrum from an ionized slab of gas illuminated by an X-ray power law. Summing up the reflection spectrum (weighted with a parameter describing the fraction of reflection) and the illuminating spectrum results in a model of the observed spectrum. However, the fitting process did not result in a statistically acceptable fit. This is expected as *BeppoSAX* observations show that the direct AGN component is heavily absorbed and only dominates the spectrum above ~ 9 keV (cf. Figure 3.3

⁸<http://heasarc.gsfc.nasa.gov/docs/xanadu/xspec/models/iondisc.html>

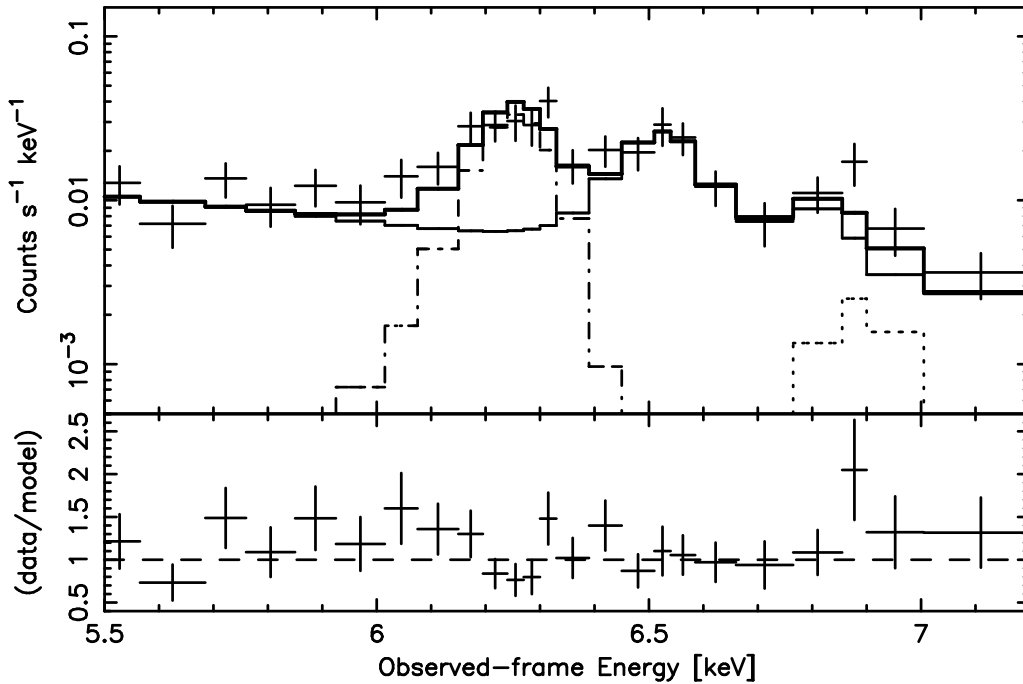


Figure 3.13: Spectral fit result to the EPIC MOS1/2 data of NGC 6240, as seen in the (5.5 – 7.2) keV range, comprising the Fe line complex (for the identifications of the lines see Figure 3.12). Emission from a collisionally-ionized plasma model has been applied to the ionized Fe-K lines, whereas the neutral Fe-K α and K β lines have been modelled by Gaussian lines. The Fe XXV and Fe XXVI lines originate from the 6.4 keV hot plasma component. The fitting was performed between 5.0 keV and 7.4 keV; $\chi^2_{\nu} = 1.16$ for 25 dof.

on p. 49; Vignati et al. 1999). Therefore, the putative helium- and hydrogen-like emission from the accretion disk should remain undetectable.

Other model assumptions try to match the observed spectrum by taking advantage of the complete (0.3 – 10.0) keV spectrum. As a second approach, the model includes an absorbed power law component plus three Gaussian lines instead of the APEC model. The fit to the spectrum is much poorer ($\chi^2_{\nu} = 1.8$) and thus the model appears to be unable to explain neither the broad-band spectral energy distribution nor the presence of the ionized Fe-K lines. Thirdly, using two APEC components to describe the broad-band spectrum can be excluded by the fitting statistics; a third APEC component is required by the data. The two lower temperature APEC components will be discussed in the subsection 3.2.4.2 (on p. 67f).

Colbert et al. (2002) have modelled the Fe-K features in NGC 1068 by emission from both optically thick and optically thin ionized reflection models. The PEXRIV code in XSPEC to simulate a reflection spectrum of ionized discs (Magdziarz & Zdziarski 1995) has been used to model the optically thick case, whereas the optically thin case was represented by a simple power law plus edge model. The fitting procedure reveals that the Compton reflection compo-

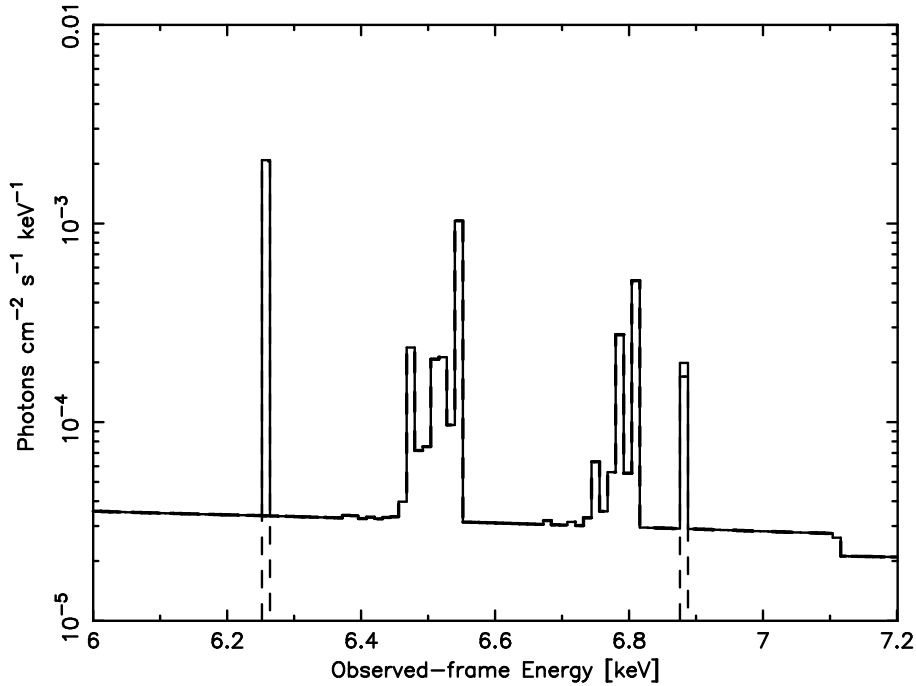


Figure 3.14: Spectral model components for the Fe-K line complex. Two unresolved Fe lines ($K\alpha$ and $K\beta$; dashed) and a collisionally-ionized plasma with $kT \simeq (6.4 \pm 0.9)$ keV can explain the emission (solid line) from the Fe-K line complex in NGC 6240. For line identification see Fig. 3.12.

ment provided by the optically thick model gives a better fit than the optically-thin reflection model. Therefore, the next step to match the EPIC MOS1/2 spectrum with a model specification was to substitute the APEC component with the PEXRIV description (in addition to the two Gaussian lines for the ionized Fe-K lines). Nevertheless, this model fails for being an adequate fit to the data ($\chi^2/\nu = 4.6$). The same holds for the power law plus edge model for an optically thin warm reflector. The *XMM-Newton* data do not require – within the limits of the available statistics – an additional ionized edge which is expected from that model.

The collisionally-ionized plasma provides the best spectral fitting results and appears to be the most likely explanation for these EPIC MOS1/2 observations of NGC 6240 (see Table 3.8 on p. 71 for the best fitting parameters).

3.2.4.2 The broad-band energy spectrum

Line identification

The soft spectral region within (0.3 – 3.5) keV shows diverse prominent emission line features. Figure 3.15 displays the EPIC MOS1/2 source spectrum and several identified chemical elements associated with the lines, like neon, magnesium, silicon, etc. For comparison a 1-keV-model spectrum of a diffuse collisionally-ionized plasma has been included, calculated on the

basis of the APEC algorithm (Astrophysical Plasma Emission Code⁹; Smith et al. 2001) with variable abundances as provided by the vAPEC model in XSPEC (solid line).

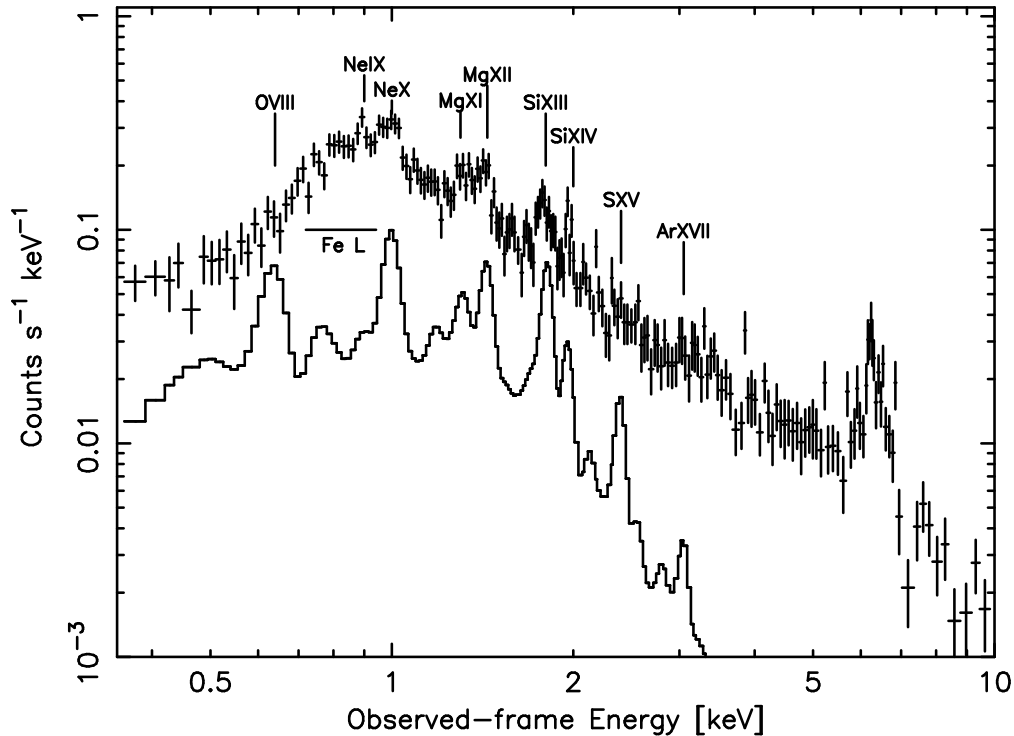


Figure 3.15: The EPIC MOS1/2 spectrum of NGC 6240 (upper curve) with identifications of the most prominent emission lines. For comparison a single vAPEC model with a temperature of 1 keV has been included (lower solid line; assumed abundances of the elements are given in the text).

The abundances of O, Ne, Mg, Si, S, and Ar were fixed to 10 times solar and the abundance of Fe was fixed to 0.01 times solar (the others were fixed to solar abundances). These values provided the most reliable fit parameters. Pairs of emission lines, which are in different ionization states, can be resolved in the EPIC pn spectrum. Moreover, emission lines at higher energies, such as S XV and Ar XVII, are also clearly detected. The flux ratio of the emission line pairs and the higher-energy emission lines, like Fe XXV and Fe XXVI, enable us to determine how many thermal plasma components are required to fit the soft energy spectrum.

The presence of two distinct plasmas at soft X-rays

Applying only one vAPEC model to the EPIC MOS1/2 data with free abundances for O, Ne, Mg, Si, S, the other α -elements¹⁰ and Fe–Ni, it appears to be acceptable ($\chi^2/\nu = 2.14$ for 119 dof), but can be significantly improved. Residues remain in the Fe L emission line region around 0.8 keV, as well as in the (1.0 – 1.5) keV range (Figure 3.16, left plot). The fitting results are

⁹<http://cxc.harvard.edu/atomdb/>

¹⁰The α (-process)-elements are isotopes formed by combining alpha particles, such as C-12, O-16, Ne-20, Mg-24, Si-28, S-32, Ca-40, Ti-48, etc.; they are likely built in Supernova type II explosions.

given in Table 3.7. The observed Fe L bump, the flux ratio of two emission lines in different ionization states and the fit residuals all suggest the presence of a second thermal component.

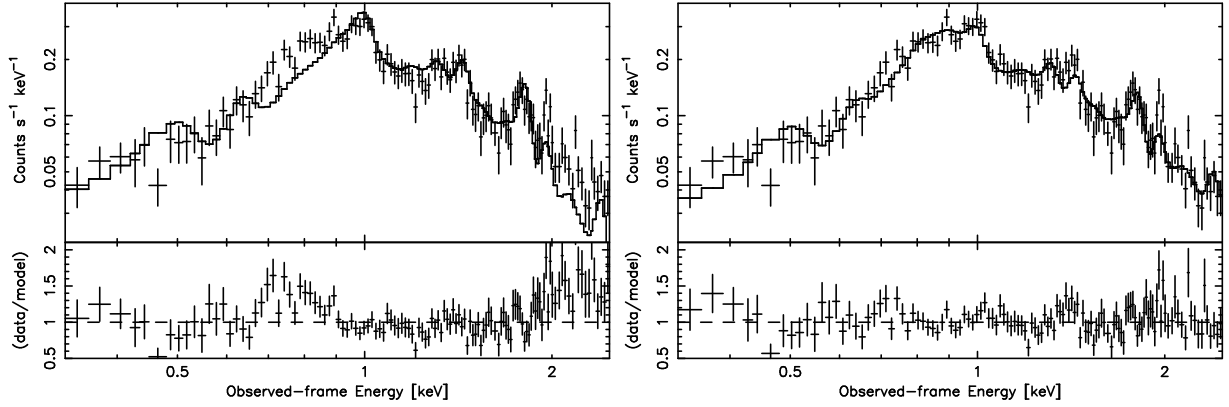


Figure 3.16: Spectral fits to the EPIC MOS1/2 data in the (0.3 – 2.5) keV range.

Left plot: absorbed vAPEC model; Fitting only one vAPEC model, where O, Ne, Mg, Si, S, the other α -elements and Fe–Ni abundances have been left free, results in $\chi^2/\nu = 2.14$ for 119 dof.

Right plot: two absorbed vAPEC models; the fit is significantly improved ($\chi^2/\nu = 1.23$ for 118 dof).

Table 3.7: Spectral fit results to the *XMM-Newton* soft X-ray spectrum (0.3 – 2.5) keV, EPIC MOS1/2

Model parameters	Model	
	vAPEC (1)	vAPEC (2)
$N_{H,1}(\text{fit})[10^{22} \text{ atoms cm}^{-2}]$	0.21	–
$kT_1[\text{keV}]$	0.97	–
$Z_{\text{He},1}[Z_{\odot}]^{\text{a)}$	0.40	–
$Z_{\text{Fe},1}[Z_{\odot}]^{\text{b)}$	0.07	–
χ^2_{ν}	255.3/119	–
$N_{H,1+2}(\text{fit})[10^{22} \text{ atoms cm}^{-2}]$	0.25 \pm 0.05	
$N_{H,2}(\text{fit})[10^{22} \text{ atoms cm}^{-2}]^{\text{c)}$	–	2.90 \pm 0.50
$kT_{(1 2)}[\text{keV}]$	0.72 \pm 0.02	2.10 \pm 0.30
$Z_{\text{He},(1 2)}[Z_{\odot}]^{\text{a)}$	1 (fixed)	0.14 (fixed)
$Z_{\text{Fe},(1 2)}[Z_{\odot}]^{\text{b)}$	1 (fixed)	0.04 (fixed)
$\chi^2_{\nu(1 2)}$	145.7/118	

a) $Z_{\text{He},i} = Z_{(\text{C}|\text{N}|\text{O}|\text{Ne}|\text{Mg}|\text{Al}|\text{Si}|\text{S}|\text{Ar}|\text{Ca}),i}$ for $i = 1, 2$,

b) $Z_{\text{Fe},i} = Z_{\text{Ni},i}$ for $i = 1, 2$,

c) additional (intrinsic) absorption component to the vAPEC (2) model.

By adding a second vAPEC component to the first model the fit becomes statistically acceptable ($\chi^2/\nu = 1.2$). The significance of this new component was verified using the F -test. It follows that the second component is required with a significance better than 5σ . The EPIC pn data explicitly confirm the MOS1/2 results. The best fit parameters of the two components are reported in Table 3.7.

The total X-ray spectrum

The best fit to the (0.3 – 10.0) keV EPIC MOS1/2 spectrum of NGC 6240 is obtained when using three major components: (i) a plasma component containing plasmas of three different temperatures; (ii) a highly absorbed power law component, and (iii) emission lines from the neutral Fe-K α and K β lines (see Table 3.8 and Figure 3.17). Combining all these parameters to a model and applying it to the data the approximation results in an acceptable fit ($\chi^2/\nu = 0.94$ for 190 dof). For soft energies the sum of a cold, $kT_{\text{cold}} = (0.66 \pm 0.03)$ keV, and a medium, $kT_{\text{med}} = (1.4 \pm 0.2)$ keV, plasma component dominates the spectrum. The medium component is intrinsically absorbed by a column density of $N_{\text{H,med}} = (3.6 \pm 0.3) \cdot 10^{21}$ atoms cm^{-2} , the cooler plasma component with $N_{\text{H,cold}} = (2.0 \pm 0.3) \cdot 10^{21}$ atoms cm^{-2} . The abundances of the α -elements are $Z_{\alpha} = (0.15 \pm 0.08) Z_{\odot}$ (where Z_{\odot} = solar values) and the iron/nickel abundances are determined to $Z_{\text{Fe,Ni}} = (0.05 \pm 0.01) Z_{\odot}$, thus lower compared to that of the α -elements. However, checks for the stability of the abundances against deviations have been performed. By varying the abundance values and comparing the fit results with each other, it can be clearly seen that all element abundances are rather uncertain due to the available photon statistics. In particular, it does not allow to constrain the element abundances for the cooler plasma component; therefore, both the α - as well as the iron/nickel abundances were fixed to that of the hotter plasma component, which results in a statistically acceptable fit for the soft energy region. Finally, including a third hot plasma component and an absorbed power law component is able to explain the origin of the ionized Fe-K lines. The temperature is $kT_{\text{hot}} = (5.5 \pm 1.5)$ keV and the intrinsic absorption is $N_{\text{H,hot}} = (4.1 \pm 1.3) \cdot 10^{22}$ atoms cm^{-2} . The APEC components provide a physical description of Starburst activity.¹¹

The *XMM-Newton* data require the presence of a power law in combination with a huge amount of absorbing material in order to fit the high-energy part of the spectrum. If neglected, significant residues remain above ~ 7 keV and the model becomes less significant. Moreover, the *XMM-Newton* data confirm the requirement for a power law at a 4σ significance level as proposed by Vignati et al. (1999) using *BeppoSAX* data (according to an F -test; $\Delta\chi^2 = 20.1$).

¹¹Additionally, the EPIC MOS1/2 fitting results indicate no significant difference when using the corresponding MEKAL component. The same holds for the comparison between the results of the combined EPIC MOS1/2 data with the data of the EPIC pn.

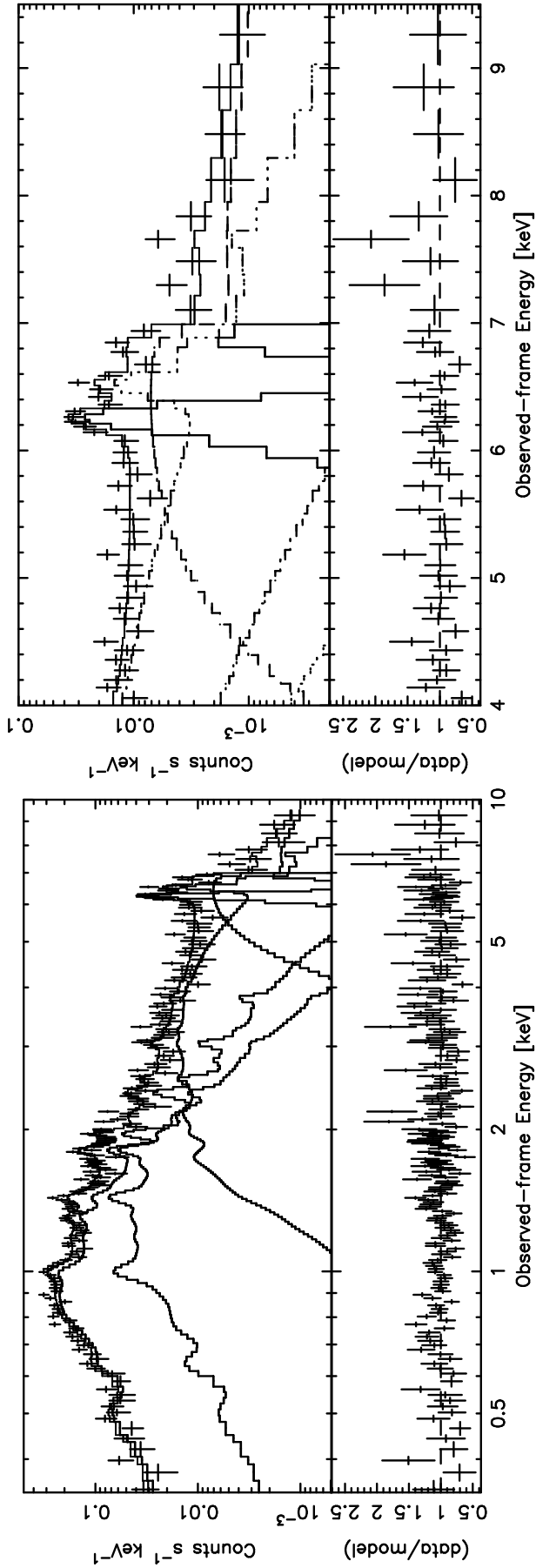


Figure 3.17: Spectral fit to the merged EPIC MOS1/2 data of NGC 6240 in the (0.3 – 10.0) keV energy range (**left plot**) and in the (4.0 – 9.5) keV regime (**right plot**). In the soft energy band, a statistically acceptable fit is obtained by using a cool and medium temperature plasma component, where the α - and Fe/Ni abundances have been left free. In addition, the emission from a third, hot plasma component is required to reproduce the line ratio of the ionized line emission of the Fe-K complex. Narrow, unresolved Fe-K α and Fe-K β lines, with a relative ratio of 1:8.8 as expected from atomic physics, have been added to the model. A highly absorbed power law component ($N_{\text{H}} = (1.0 \pm 0.2) \cdot 10^{24}$ atoms cm^{-2}) with a fixed photon index of $\Gamma = 1.8$ improves the fit significantly above ~ 7 keV. The fit to the (0.3 – 10.0) keV band is statistically acceptable with the above mentioned components as can be seen in the plots ($\chi^2/\nu = 0.94$ for 190 dof). Table 3.8 on the next page summarizes the values of the diverse spectral model parameters together with the calculated flux and luminosities. For a discussion about the element abundances see the text.

Table 3.8: Spectral fit components to the entire (0.3 – 10.0) keV energy band
gained with *XMM-Newton* (EPIC MOS1/2) on NGC 6240 in revolution 0144

Column (1) lists the different parameters of each model component used. All absorption-related model components have been left free and were approximated by the fitting procedure, except for the foreground absorption (fixed to the Galactic value). The individual columns (2) to (9) refer to the spectral components applied in the fit. The rows specify the measured values and their 1σ errors. The broad-band spectral energy distribution determined from these components is shown in Figure 3.17. The fluxes f and luminosities L are absorption corrected.

(1)	(2)	(3)	(4)	(5)	(6)	(7)	(8)	(9)
$\chi^2_{\nu}(\text{dof}) = 0.94(190)$	vAPEC (1)	vAPEC (2)	APEC (3)	power law	Fe-K α	Fe XXV	Fe XXVI	Fe-K β
$N_{\text{H}}(\text{fit}) [10^{22} \text{ cm}^{-2}]$	0.20 ± 0.03	0.36 ± 0.03	4.1 ± 1.3	100 ± 20	–	–	–	–
Temperature kT [keV]	0.66 ± 0.03	1.4 ± 0.2	5.5 ± 1.5	–	–	–	–	–
Norm ^{a)}	4.8 ± 1.2	2.5 ± 1.5	3.7 ± 1.3	6.0 ± 3.0	2.6 ± 0.8	1.8 ± 0.7	0.9 ± 0.7	0.3 ± 0.1
$f [10^{-12} \text{ erg cm}^{-2} \text{ s}^{-1}]$	1.5 ± 0.4	0.7 ± 0.4	1.4 ± 0.5	40 ± 20	0.25 ± 0.08	0.19 ± 0.07	0.10 ± 0.08	0.03 ± 0.01
$L [10^{42} \text{ erg s}^{-1}]$	3.9 ± 1.0	1.9 ± 1.1	3.6 ± 1.3	100 ± 50	0.60 ± 0.20	0.50 ± 0.20	0.30 ± 0.20	0.08 ± 0.02
Equivalent width [eV] ^{b)}	–	–	–	–	600 ± 200	550 ± 200	360 ± 300	100 ± 40

^{a)} NOTE: For the first three components the normalization is given in units of $[10^{-17}/(4\pi(D_{\text{A}} \cdot (1+z))^2) \int n_{\text{e}} n_{\text{H}} dV]$, where D_{A} is the angular size distance to the source (in cm), n_{e} is the electron density (cm^{-3}), and n_{H} is the hydrogen density (cm^{-3}). The integral is computed over the total X-ray emitting gas volume. The normalization of the power law component is $[10^{-3} \text{ photons cm}^{-2} \text{ s}^{-1} \text{ keV}^{-1}]$ at one keV. For the last four components the normalization is given in units of $[10^{-5} \text{ photons cm}^{-2} \text{ s}^{-1} \text{ keV}^{-1}]$,

^{b)} the values presented here deviate from the values published in Boller et al. (2003) due to a different assumption of the continuum emission (vAPEC instead of a power law slope). The EWs for the ionized Fe lines are taken from the Table 3.5 on p. 63.

The absorbing column density of $N_{\text{H}} = (1.0 \pm 0.3) \cdot 10^{24}$ atoms cm^{-2} is within a factor of two comparable with that found by *BeppoSAX*. Due to the fact that the photon index can be measured more reliably by *BeppoSAX* – when taking into account the larger energy range over which it was determined – the power law photon index in the own fitting procedures was fixed to $\Gamma = 1.8$. The absorbed power law is indicative of the direct emission from the accretion disk (corona).

3.2.4.3 Comparison with the nearby Starburst galaxy NGC 253

A striking similarity in the parameters of the plasma and absorbing columns is found between NGC 6240 and the prototype local Starburst galaxy NGC 253. Spectral data between 0.3 keV and 10.0 keV obtained with *BBXRT* can be well explained by two Raymond–Smith–like plasma models, having temperatures of ~ 0.6 and 6 keV (Petre 1992). Using higher spectral resolution provided by *ASCA*, Ptak et al. (1997) modelled the complex nuclear spectrum of NGC 253 by a combination of a soft thermal component ($kT \sim 0.8$ keV) and a hard absorbed component, either of thermal ($kT \sim 7$ keV) or non–thermal origin (power law with $\Gamma \sim 2$). In addition, the data show strong emission lines of a wide variety of elements (e.g. Si, S, and Fe L/Ni; confirmed by Cappi et al. (1999) with *BeppoSAX* data). However, the former authors found no narrow iron line emission ($EW < 180$ eV), whereas the latter detected Fe-K α lines at 6.4 keV and $6.69_{-0.06}^{+0.07}$ keV with an intensity of $I_{\text{FeK}\alpha} = (1.6 \pm 0.3) \cdot 10^{-5}$ photons $\text{cm}^{-2} \text{s}^{-1}$, and an $EW = 400_{-75}^{+125}$ eV. In 1998 Persic et al. reported the detection of a narrow Fe-K α line at (6.69 ± 0.07) keV with $EW = 329_{-109}^{+89}$ eV (most probable the Fe XXV line) in the *BeppoSAX* spectrum of NGC 253 together with a hot thermal model component of $kT_{\text{hard}} \sim 6$ keV apart from a soft thermal component ($kT_{\text{soft}} \sim 0.9$ keV). In connection with the continuum slope above 2 keV the authors assumed that the hard X–ray emission of NGC 253 is dominated by thermal processes. They discuss the underlying mechanism to produce a 6–keV–plasma in terms of a massive presence of SNRs and alternative concepts including magnetic confinement effects.

In a more recent observation Pietsch et al. (2001) have analyzed the emission of the nucleus of NGC 253 with *XMM-Newton*. The authors modelled the nuclear spectrum by a plasma composite of *three* different temperatures with the higher temperatures increasingly absorbed. The derived temperatures for the nuclear region are 0.56, 0.92 and 6.3 keV with the corresponding absorbing column densities of $N_{\text{H}} = (0.34, 1.78, 13.2) \cdot 10^{22}$ atoms cm^{-2} . These temperatures and absorbing column densities are remarkably similar to those found in NGC 6240. In addition, Pietsch et al. detected He–like Fe-K emission at (6.67 ± 0.05) keV, again similar to the detection in NGC 6240, but with a higher equivalent width of $EW = (930 \pm 300)$ eV. On the other hand, the weaker H–like Fe line is not detected. The authors attribute the presence of the

high temperature component to emission from type Ib and type IIa SNRs. Moreover, similar soft X-ray emission lines from the two cooler plasma components are detected in NGC 253, e.g. emission from Mg XI, Mg XII, Si XIII, Si XIV, Ar XVI (cf. section 4.1 of Pietsch et al.). The presence of different plasma components in the prototype local Starburst galaxy NGC 253 supports our spectral modelling, and further suggests that there may be a common underlying physical mechanism, which appears to be dominated by emission from young type Ib and type IIa SNRs.

3.2.5 Comparison with the *Chandra* observation

The following subsection presents a short overview of a comparative study of NGC 6240 when combining the high throughput of *XMM-Newton* with the high spatial resolution of *Chandra*. While *Chandra* has resolved the nuclear region into two isolated active nuclei embedded in diffuse extended emission components (Komossa et al. 2003; see subsection 3.2.1 on p. 50), *XMM-Newton* allows for detailed X-ray spectroscopy with high statistics.

Concerning a spatial analysis, the inner 30'' remain unresolved with the detectors on board *XMM-Newton* as obtained from the PSF. The PSF was calculated by simulating a point source at the same position on the detector as NGC 6240, and at an energy centered at 6.5 keV, using the XMM science simulator software *SciSim*¹². This reference energy has been chosen due to the correspondence to the mean energy of the Fe K line complex. Serendipitous sources, localized through the XMM-SAS task "emldetect", and out of time events were removed from the data. Each photon in the profile was corrected for vignetting and divided by the exposure map in order to remove chip gaps and hot pixels. Since neither the simulated source nor NGC 6240 show any pile-up effect, the sources were normalized to the maximum flux. Using such a PSF will allow to further investigate the spectral components around the two nuclei. The data were accumulated in the (5.5 – 7.5) keV energy range for the EPIC MOS2 data, representative of the other detectors and providing the best spatial information. The radial intensity profile of the emission is shown in Figure 3.18 overlaid with the PSF. Due to the large width of the PSF, the (PSF-uncorrected) extended emission seems to appear at a distance larger than 30'' from the X-ray centroid position. The spectral analysis of this diffuse emission extended out to a distance of $\sim 70''$. Beyond this distance the number of counts is too small to make a significant contribution to the statistics.

The spectral analysis of the inner 30'' was performed independently of the results obtained from the total emission (up to 70''). Interestingly, the spectral fit to the inner 30'' is consistent with the spectral fit components and parameters obtained for the total emission (cf. Figure 3.17

¹²<http://xmm.vilspa.esa.es/scisim/>

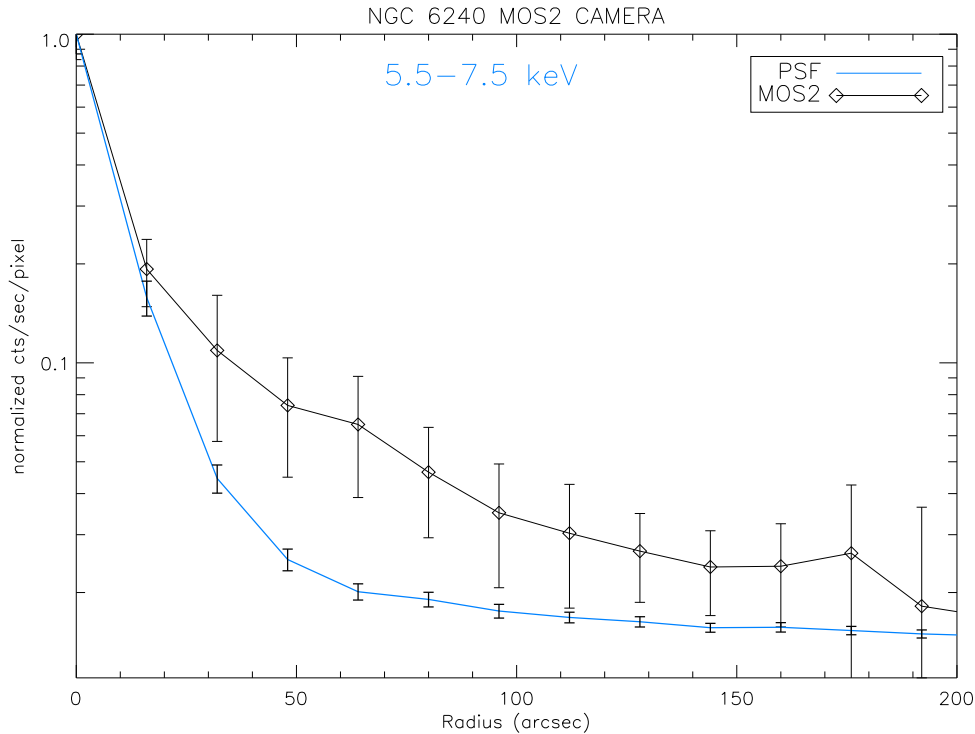


Figure 3.18: The radial intensity profile of the EPIC MOS2 data (upper line) compared to the instrumental point spread function (PSF, normalized to the maximum flux; lower line). The EPIC MOS PSF were calculated at the reference energy of 6.5 keV (incl. estimates for the count errors) and photons have been selected in the (5.5 – 7.5) keV range to match the emission from the Fe line complex. Extended emission is detected at distances of more than about 30'' from the X-ray centroid position.

on p. 70) except for the flux emitted by the cold APEC component. The inner core region is emitting almost 98% of the (0.3 – 10.0) keV flux. The derived temperatures for the plasma components confirm the existence of different plasma contributions in the core region. In the following the *XMM-Newton* plasma components are confronted with the energy bands used in the high resolution *Chandra* image (Figure 3 of Komossa et al. 2003). In the softest energy band (red coloured; from 0.5 keV to 1.5 keV) the emission from the 0.7-keV- plasma component dominates the spectral energy distribution, with a contamination level of about 10 per cent from the 1.4-keV- component. In the (1.5 – 5.0) keV band (yellow and green colour-coded), a mixture of all three plasma components is present and thus it is not possible to uniquely attribute a single temperature to the spatial location. Above 5 keV the hot 5.5-keV- plasma component dominates the spectrum and is responsible for the emission from Fe XXV and Fe XXVI. This is confirmed by the *Chandra* observation; Komossa et al. (2003) pointed out that the neutral Fe-K line dominates the spectrum between 6 keV and 7 keV, but some residues remain in their spectra which can be attributed to ionized Fe-K emission (see below). The three plasma components are found at different locations in the *Chandra* image, indicating that the temperature is

increasing towards the centre of NGC 6240. In addition, the *XMM-Newton* data reveal a strong column density gradient for the different plasma components for the inner region, decreasing from about $N_{\text{H}} = 4.1 \cdot 10^{22}$ atoms cm^{-2} (for $kT_{\text{hot}} = 5.5$ keV) over $N_{\text{H}} = 0.4 \cdot 10^{22}$ atoms cm^{-2} (with $kT_{\text{med}} = 1.4$ keV) down to $N_{\text{H}} = 0.2 \cdot 10^{22}$ atoms cm^{-2} (where $kT_{\text{cold}} = 0.7$ keV).

The *Chandra* data allow a detailed investigation of the two nuclei as well as of the north–east and south–west extended emission. While the temperature of the soft X–ray emission, projected on the nuclei, is $kT_{\text{soft,N}} = (0.9 \pm 0.2)$ keV (after subtracting the nuclei emission), no temperatures of the emission of the two nuclei could be measured. Absorption column densities of $N_{\text{H,N}} \lesssim 10^{22}$ atoms cm^{-2} in the direction of the nuclei are calculated from A_{V} –values based on IR observations. Both numbers are in agreement with the values of the cold and medium–temperature plasma when treating them together. Moreover, the derived plasma temperatures and column densities of the *extended* emission are consistent with the *XMM-Newton* findings for the low–energy thermal emission components. The temperature of (2.8 ± 0.8) keV for the south–west emission is – again – most probably a combination of the two hotter plasma temperature components found in our analysis.

In the discussion of the spectra emitted from both nuclei as seen with *Chandra*, Komossa et al. note the dominant role of the neutral Fe–K emission line in the $(6.0 - 7.0)$ keV range as well as the residues remaining in the spectra which can be attributed to H–like emission. This can be confirmed in two different ways. A statistically acceptable fit to the *Chandra* data of both nuclei includes two Gaussian lines. The higher energy line contains about half of the flux emitted by the neutral Fe–K line. Binning the *Chandra* spectrum in the light of the ionized lines, as detected with *XMM-Newton*, the number of photons (80) is also about half of that compared to the image selected for the neutral Fe–K line (see the left and middle plot of Figure 3.19).

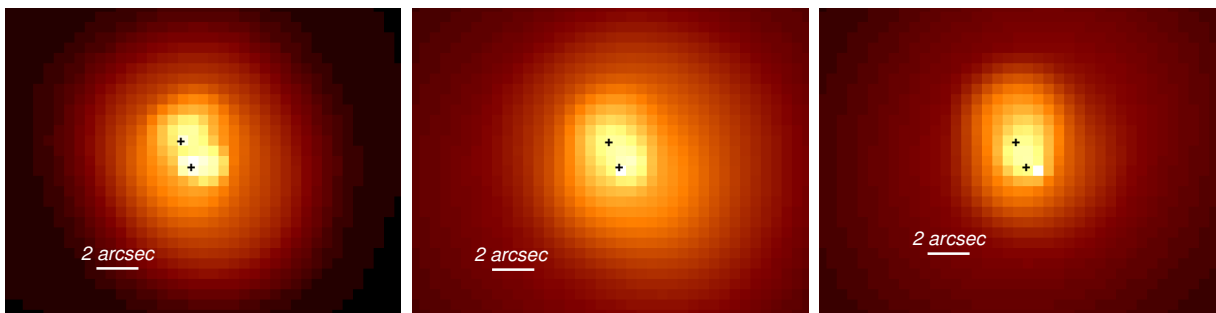


Figure 3.19: *Chandra* images binned in three different energy bands as obtained from the *XMM-Newton* spectrum. The crosses mark the position of the two nuclei detected with *Chandra*.

Left plot: The light of the neutral Fe–K line within $(6.10 - 6.35)$ keV (in the observer’s frame),

Middle plot: The ionized line emission $(6.4 - 7.0)$ keV,

Right plot: Energies between 7 keV and 10 keV from the highly absorbed power law component.

This supports the *Chandra* results of ionized line emission from the two nuclei, which can be attributed to a hot plasma component. Finally, the *Chandra* image above 7 keV (Figure 3.19; right plot) points to emission from both nuclei. The *XMM-Newton* data suggest that the highly-absorbed power law dominates that energy range, indicating the presence of emission from putative accretion disk coronae.

3.2.6 Summary

The *XMM-Newton* observations of the ULIRG NGC 6240 reveal

- For the first time, the presence of *three* distinct Fe-K lines located at (6.41 ± 0.01) keV and identified as the Fe-K α line, (6.67 ± 0.02) keV (likely Fe XXV) and (7.01 ± 0.03) keV (Fe XXVI with a contribution from the Fe-K β line; all energies in the rest frame of the source);
- The broad-band X-ray spectrum, (0.3 – 10.0) keV, is successfully described by thermal emission from *three* different plasma components with temperatures of (0.66 ± 0.03) keV, (1.4 ± 0.2) keV, and (5.5 ± 1.5) keV. The ionized lines can be explained by emission from the highest temperature plasma components resulting in emission from Fe XXV and Fe XXVI. The three plasma components are found at different locations in the *Chandra* image, indicating that the temperature and the column density are increasing towards the centre of NGC 6240. These components are supposed to be related to Starburst activities;
- A strong column density gradient for the diverse plasma components increasing with the temperature from $N_{\text{H}} = (0.20 \pm 0.03) \cdot 10^{22}$ atoms cm^{-2} , over $N_{\text{H}} = (0.36 \pm 0.03) \cdot 10^{22}$ atoms cm^{-2} up to $N_{\text{H}} = (4.1 \pm 1.3) \cdot 10^{22}$ atoms cm^{-2} ;
- The presence of several emission lines in the soft energy band, like Ne, Mg, Si, S, etc. which is in agreement with previous *ASCA* measurements;
- A direct power law component of $L_{\text{po}} = (1.0 \pm 0.5) \cdot 10^{44}$ erg s^{-1} , highly absorbed by $N_{\text{H}} = (1.0 \pm 0.2) \cdot 10^{24}$ atoms cm^{-2} and with $L_{\text{po}} \simeq 10 \cdot L_{\text{plasmas}}$; strongly indicating the presence of a buried AGN in NGC 6240 and confirming previous *BeppoSAX* results;
- A striking similarity to the prototype nearby Starburst galaxy NGC 253. In both, NGC 253 and NGC 6240, three plasma components are required, and their temperatures as well as their column density gradients are remarkably similar; hence, suggesting a similar underlying physical process at work in both galaxies.

It is shown that the spectral capabilities of *XMM-Newton* in combination with the high spatial resolution of the *Chandra* telescope give us a more precise understanding of the nuclear region in NGC 6240 than ever before (cf. Figure 3.17 on p. 70 and Figure 3.19). The chapter 4 on p. 85ff will discuss the implications for NGC 6240 in particular and ULIRGs in general based on these results together with a detailed consideration of other findings in the context of this work.

3.3 Error handling in the spectral data analysis

This section considers two major sources of error – namely, measurement errors and uncertainties due to the modelling itself. The third major source of uncertainty is that due to the small size of the data set, limiting the number and depth of argumentations in order to receive a favoured interpretation.

Considering the events, various forms of noise can be quoted. They include photon events from the X–ray background caused predominantly by other sources in the observed field, either resolved or unresolved, but also possibly including regions of diffuse X–ray emission. Other sources of interest are particle events due to cosmic rays and charged particles impinging up on the detectors, as well as dark events arise in the instruments themselves. All of them were taken into account during the reduction work as far as they are known and quantifiable.

3.3.1 Measurement errors

The automatic data pipeline for processing *XMM-Newton* data (see subsection 2.2.1 on p. 38f) saves a lot of time and effort, but is not thought to provide the user insights into the handling of errors and uncertainties of quantities accompanying and/or arising from the signals of interest due to the complexity of this task. This implies that a usual error treatment is required when the pipeline releases the data files, including the event list in order to work out the scientific data.

In practice, the measured quantities in the frame of an observation are erroneous due to numerous error sources, from which the most important are included in the following list:

- **Uncertainties both in the source and background selection regions,**
the selection of the size of the source’s region is important in order to maximize the number of X–ray photons receiving and thus, allowing to make use of all available information. The objects are usually imaged close to the read–out electronics of the detectors to minimize the noise arising in the read–out process. The background selection region should be taken from the same CCD (that with the lowest internal background) to ensure identical detection characteristics as for the source’s region to extract the counts.

- **Uncertainties in the background subtraction,**

The choice of a large background extraction region guarantees good statistics for the modelling procedures of the source's spectra and allow to average the small scale spatial fluctuations of the background. In order to estimate uncertainties in the spectral analysis due to systematic errors in the background estimation, three different background regions from the Mrk 1014 data sets have been extracted and compared spatially and spectrally. The first region was used for the detailed spectral analysis (cf. subsection 4.2 on p. 86ff), the second is little further away from the source region, and the last region grazes the gap to a neighbouring CCD. Mrk 1014 was chosen due to the higher count rate of the observation compared to the NGC 6240 observation, allowing to show possible deviations with higher significance.

In all cases the background was stable without any appreciable variability within the statistical errors. This was verified according to a simultaneous spectral fit to the EPIC data within (0.3 – 8.0) keV – performed by using the combination of an APEC (cf. subsection 3.2.3 on p. 56) and a power law model instead of the double power law model described in subsection 4.2.3 (on p. 90) because of the insufficient model stability of the latter. The APEC temperature and the photon index of the power law are constrained within their parameter range. Table 3.9 lists the relevant parameter sets of the models, subdivided into the three background regions. In addition, the calculated (0.3 – 8.0) keV–fluxes for the three backgrounds are presented and compared in the table.

Table 3.9: Comparison of the spectral fitting parameters for three background regions using the APEC plus power law model description (Mrk 1014 data)

<i>Simultaneous Fit [EPIC pn + EPIC MOS1/2]</i>					
Background region	temperature kT [eV]	power law Γ	(0.3 – 8.0) keV–flux [10^{-12} erg cm $^{-2}$ s $^{-1}$]		χ^2/ν
			[temperature]	[power law]	
No. 1	230 ± 30	$2.36^{+0.04}_{-0.03}$	0.10 ± 0.04	2.2 ± 0.2	1.21
No. 2	230 ± 30	$2.36^{+0.02}_{-0.03}$	0.09 ± 0.03	2.0 ± 0.1	1.22
No. 3	230 ± 30	$2.36^{+0.03}_{-0.04}$	0.11 ± 0.05	2.3 ± 0.2	1.22

It can be seen that the parameters do not show any dependency on the selection region of the background. The fluxes are consistent with each other within more than 99% confidence statistical errors (the table shows rounded numbers).

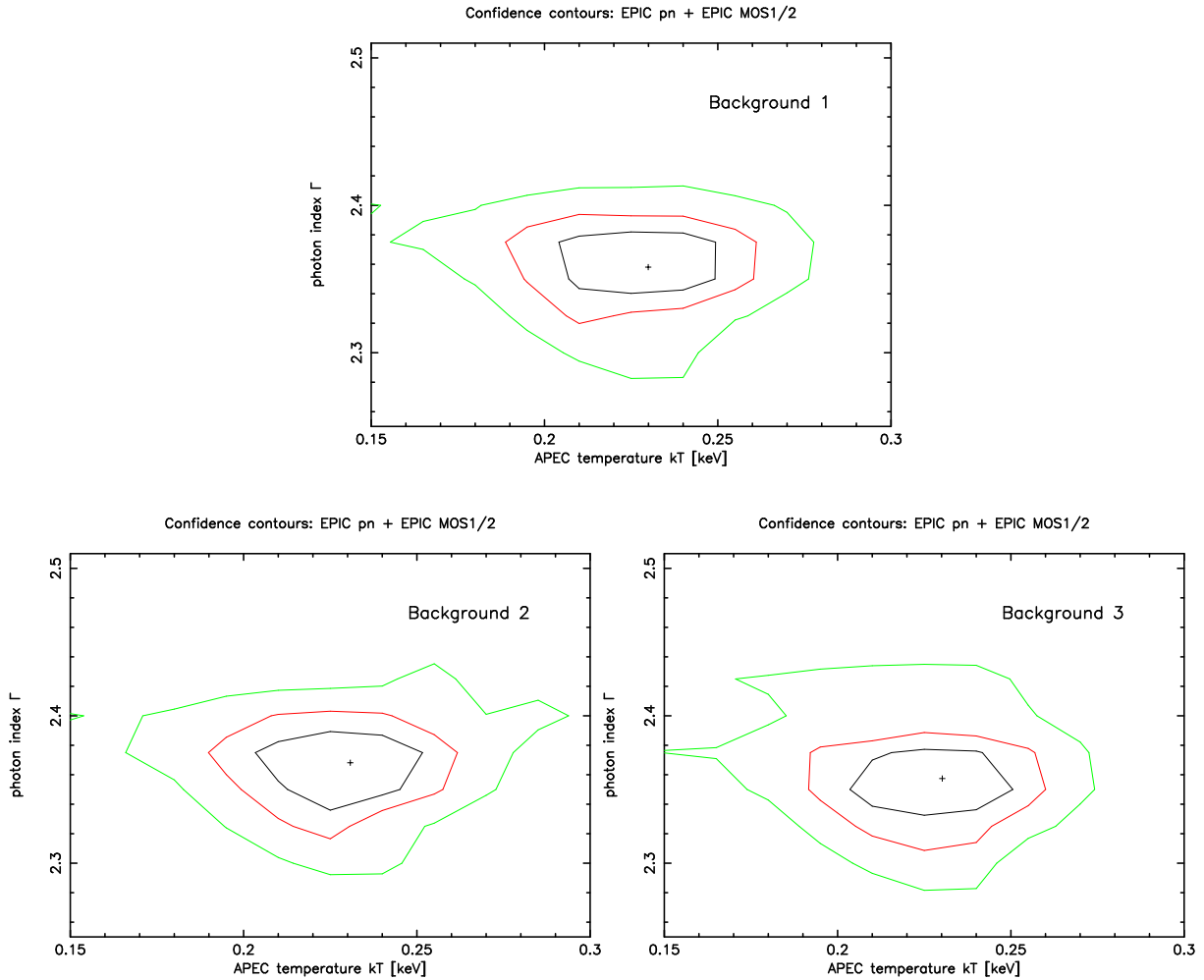


Figure 3.20: Confidence contours for an APEC plus power law model with three different selections of background regions (Background No. 1,2 and 3).

The **upper plot** shows the contours of the background region used for the detailed spectral analysis, the **lower left plot** is based on a background region a little further away from the source region, and the **lower right plot** represents the confidence contours of a background region grazing the gap to a neighbouring CCD, respectively.

The confidence contours of both main parameters – determined from the three fitting runs – are shown in Figure 3.20. The contours with the three background regions are in agreement with each other. Again, the stability of the derived model parameters is not at risk when choosing a rather unusual background region; in particular, for the more complex models.

In conclusion, the systematic errors in the spectral analysis, due to uncertainties in the background estimation, are negligible compared to other errors (see below).

- **Errors in the count rate of the spectrum of the source and of the background,**

The uncertainties in the source and background selection regions based on the spatial fluctuations of the count numbers lead to an error-affected count rate of the source's and background's spectra in dependence which detector is used. Concerning the Mrk 1014 and both NGC 6240 observations independently the source's count rate has a relative error of 0.9 – 2.7%, whereas the larger errors are associated with the NGC 6240 observations. The background's count rate is significantly larger and accounts for $\sim 14\%$ (Mrk 1014), and exceeds 20% for the NGC 6240 observations. However, the relative error of the background-subtracted count rate ranges between 1.0 and 2.9% (Mrk 1014: 1.0 – 1.8%; NGC 6240: 1.7 – 2.9%).

For both objects, in all observations using the EPIC instruments, more than 91% of the registered counts were used for the spectral studies.

- **Errors in the calibration,**

A major concern in the reduction and use of *XMM-Newton* data is the determination of reliable calibration information of the EPIC instruments. This task is subject to an intense elaboration and includes the X-ray mirror response, filter transmissions as well as detector responses as functions of flight-time, temperature, photon energy, etc. As a result, much effort is undertaken to understand the detector background of the EPIC devices. Apart from a cosmic X-ray background, it comprises of the instrumental noise (important at low energies, *i.e.* $\lesssim 0.2$ keV) and of particle interactions with the detectors and their mountings (important above a few keV). Since both energy regions are of significant scientific importance, it is advisable to use the most recent calibration files available. These files are permanently updated and allow the user the handling of the complex EPIC responses. However, the information in the files – such as the telescope effective area (including vignetting corrections for the EPIC devices), the EPIC filter transmissions, the EPIC CCD quantum efficiency, the smearing of out-of-time events¹³, etc. – are erroneous and/or need to be redefined with time. For example, a measured astrometrical offset of $\sim 1'$ from the nominal value in the telescope axis has likely implications for the cross-calibration of the fluxes measured between EPIC pn and EPIC MOS1/2. Another example is the difference in the low-energy calibration of the EPIC MOS cameras when comparing data of calibration targets with respect to the time of observation. With increasing revolution number the energy resolution decreases from ~ 200 eV (before orbit 200), over ~ 350 eV (between 200 and about 450) to $\lesssim 500$ eV, requiring to produce adapted response files.

¹³Events registered during the read-out of the CCD and which have to be removed from the images and spectra

3.3.2 Uncertainties in modelling with XSPEC

The fitting procedure provides an estimation of the goodness of a model description to the data, as well as the associated uncertainties of the fit parameters. The uncertainties on the derived quantities – using the χ^2 -statistics – strongly depend on the number and quality of the data points.

The results of the XSPEC fitting algorithms can fall into a *local* minimum in χ^2 -space instead of finding the *true* best fitting parameters. In this regard the word *local* means that the fitting methods use information around the current parameters to guess a new set of model parameters. Hence, they are liable to be bound in a local minimum. This behaviour is enhanced with increasing complexity of the model and with the number of correlations between the parameters. A major consequence of this problem is that the model parameters can sometimes replace their values with each other; they produce a fit which is statistically comparable to the true best fit, but physically unlikely. An example of this can be seen in the Mrk 1014 data set when the double power law model is applied to the modest photon statistics, in particular at high energies. Letting the values of the photon indices free without specific limitations, the fitting process finds several pairs of parameters. The corresponding confidence contours clearly show that the fit result is not stable against small deviations from the current fit parameter value.

The consequence of this behaviour is to minimize the probability of being trapped into such non-physical local χ^2 -minima. This is achieved by performing several fits within the XSPEC process. The first approach is to fit a model of highest simplicity to the data. As a new component is added, the parameters are chosen with the best fit values found in the previous, simpler model. This is carried out under the assumption that the previous best fit is a reasonable approximation of the parameter values appropriate for applying to the current model and therefore it provides a starting point that is close to the final set of best-fitting values. Moreover, the parameters are constrained to be within the bounds of an upper and lower limit in order to keep them from deviating too far from the expected values (but with the limits large enough to avoid any bad influence on the results).

In some situations, a fit does not converge on its *best* fit values, although all statistical parameters would suggest this parameter set as the best in χ^2 -space. In order to probe this eventuality, the ERROR command¹⁴ has been used to look for a new and better χ^2 -minimum. If successful, this new minimum is refined (after a new fit) and the associated parameter set represents a new candidate for the best fit. Therefore, reiterations of the fitting procedure – after checking the error ranges of the model parameters – provide the best way to adjust the

¹⁴The ERROR command within XSPEC determines confidence intervals for model parameters by stepping through the parameter space trying to find the values which correspond to the specified change in the fit statistics (e.g. the default $\Delta\chi^2 = 2.71$ is equivalent to the 90% confidence interval for a single interesting parameter).

candidate best fit values to the data. In addition, the XSPEC command STEPPAR¹⁵ performs a more sophisticated check of the χ^2 -space, e.g. for the Γ -temperature-parameter pair (cf. Figure 3.20 on p. 79) STEPPAR is executed to evaluate χ^2 -values across a 2-dimensional plane in the parameter space, resulting in confidence contours which reveals possible correlations between the parameters.

In addition to its physical description, the APEC model contains several sources of error and limitations. The APEC algorithm and the atomic data are strictly separated from each other, allowing to perform checks for the convergence of the APEC models and to compare atomic data from different sources. In contrast to the MEKAL model, one of the most vital features of the APEC is the ability to do an error analysis by itself, meaning that this code provides three different methods calculating the errors of a model due to errors in the underlying atomic physics (see below):

- **Data comparison,**

The APED contains atomic data from several investigations. Therefore, it is possible to run the APEC with different data sets and to compare them with each other;

- **Check for sensitivity,**

Estimates of the data errors due to numerical limitations are included in the APED. This results in a 1σ confidence level for a particular ion or line parameter;

- **Comparing Monte-Carlo-modelling,**

Computing atomic rates suffers from systematic errors of (theoretical) calculations. APEC is capable of varying the rates within given error ranges and therefore, deriving the best possible estimate of the error on the emissivity and (selected) line ratios.

Due to computing requirements the APED includes pre-calculated errors for every parameter, value, or fit, as deduced from uncertainties in the atomic physics data. The APEC algorithm processes this results into error estimations of both the wavelength and emission intensities of the desired ion or line.

However, the APEC/APED approach to provide a new tool for analyzing high- to highest-resolution X-ray spectra is limited due to the early stage of its development. Although plasma codes like the MEKAL model include only the strongest emission lines from each ion (and

¹⁵The XSPEC command STEPPAR probes the parameter space in order to measure its effect on the fit statistics. In contrast to the ERROR command, STEPPAR varies a parameter in steps of evenly space across a specified range of values in order to test the relation of this parameter to the fit statistics in a more uniform way. Moreover, STEPPAR allows two parameters to vary at the same time, mapping the values of the fit statistics across a grid in the 2-dimensional parameter space.

”bundled” nearby lines), it is sufficient to apply it to data showing a moderate number of line features. In the case of NGC 6240 the complex iron emission together with the huge number of soft X-ray lines of different ionization state require to make use of the best database of atomic physical information currently available; thus, applying the APEC model to the data.

In practice, collisionally-ionized models like the MEKAL code and APEC are an approximation to the observables. This is based on the assumptions made by the modelling code, which will restrict its ability to simulate real plasmas. In order of decreasing importance, one can list the following limitations of these kind of models,

- **Physical assumptions,**

Codes for plasma emission arise from solving physical problems within the scope of ionization equilibrium, thermal balance, and radiation transfer calculations. In particular, computing the ionization balance (*i.e.* the abundances of each ionization state for all interesting ions) and stating its accuracy are demanding tasks, being reflected in the fact that the APED does not yet contain all the necessary ionization/recombination rates. It has to rely on tabulated values for the ionization balance in thermal CIE¹⁶. Authors have included different physical and numerical approximations, assumptions and complexity in their plasma emission codes. Several approaches (e.g. Monte-Carlo-methods, the Bethe approximation) are pursued to help defining an error term in the line and continuum emission model. In order to compare model predictions and to identify possible causes of differences (like methods, assumptions, or atomic data) several workshops/conferences were held (like the “Joint Discussion on Atomic Data for X-ray Astronomy”, Sydney, 2003) where different codes were applied to diverse spectral features, e.g. the iron K complex seen in several extragalactic sources to study the underlying physical conditions and to obtain reliable diagnostics for line ratios. According to the latest findings an overall agreement in the spectroscopic data approaches 10% for the line strength of most of the elements and up to 1% for the line wavelengths. In conclusion, atomic data accuracy seems to be a more important limiting factor than the physical and numerical assumptions.

- **Atomic data,**

Further developments in the range of theoretical and experimental techniques have significantly improved the presence and quality of atomic data within the last decades. Several projects have been initiated in order to compute precise atomic data, e.g. for the Iron group elements (the “IRON Project”, Hummer et al. (1993); see Pradhan (1995, 2000) for reviews). Nevertheless, the mentioned accuracy on current data gives way to further

¹⁶Collisional Ionization Equilibrium

improvements. For instance, a relative 1% accuracy in the line wavelengths converts into an uncertainty of 0.07 keV at an energy of 6.97 keV, slightly above the limit of the spectral resolution of the *XMM-Newton* detectors. Although the fitting results for the Fe-K line complex in NGC 6240 agree with a superposed emission of the Fe XXVI– and the Fe-K β line (cf. subsections 3.2.4.1 and 3.2.4.1 on p. 61ff).

- **Element abundances,**

By default, the most interesting parameters of the MEKAL and APEC models are the plasma temperature and the emission measure. If the fitting results are poor ($\chi^2/\nu \gg 1$), a varying elemental abundance as an (additional) independent parameter to the model description can improve the approximation. If this step is without the anticipated effect on the fit, the model can be refined by taking into consideration individual abundance values for the elements used. An example shows the choice of a separate handling of the α -element and the Fe/Ni abundances for the (v)APEC model components (see the fitting results of NGC 6240 in the subsection 3.2.4.2 on p. 69ff and in Figure 3.17 on p. 70). The drawback of this improved fit result is to work with line strengths of individual elements/ions, cumulating the uncertainties from each transition calculation/measure in the model code. However, these limitations are defined by the bounds coming from the quality of the data, which are mostly not sufficient to give strong constraints to the abundance parameters.

This subsection is far from being complete in aiming at a list of all possible errors. Since the error inspections within the APEC models are vital for the analysis, e.g. of the Fe-K complex in NGC 6240, they have been discussed in more detail. Moreover, they are necessary for other models or other sources.

4

Discussion

This chapter discusses the findings of this thesis. After a short overview of the general spectral properties of NGC 6240 the results of the analyses will be interpreted and confronted with published results of previous observations in the context of an AGN- and Starburst activity.

A separate section is dedicated to the analysis of the *XMM-Newton* data of Mrk 1014 and contrasts the results based on an independent processing and interpretation of the data set with the findings of Boller et al. (2002). They reveal a different estimation of its spectral content. The total flux and luminosity can be used for further investigations as presented in the remaining part.

4.1 Overview

The data of NGC 6240 show the following general properties:

- The (0.3 – 10.0) keV spectrum has been modelled with three APEC components of different temperature, a highly absorbed power law and three Gaussian lines that resolve the Fe-K line complex;
- The SED does not require a cold or warm reflection component; a realistic physical interpretation was found by applying the collisionally-ionized, optically-thin plasma (APEC);
- At soft X-rays a *thermal* model description provides the best fitting results, most probably in form of several optically-thin hot plasmas, exhibiting low to moderate temperatures;
- The intrinsic luminosity of the power law component in the (0.3 – 10.0) keV energy band tends to be of the order of $L_{\text{po}} \approx 10^{44} \text{ erg s}^{-1}$ and is highly absorbed;

- The intrinsic Starburst luminosity in the (0.3 – 10.0) keV bandpass is derived to be no more than a tenth of the luminosity of the hard component, $L_{\text{Starburst}} \lesssim 10^{43} \text{ erg s}^{-1}$.

Given this outcome, the implications of the results on AGN– and Starburst activities are the topic of the remaining chapter, starting with section 4.3 on p. 95.

4.2 A detailed discussion of the Mrk 1014 data

This section deals with the outcome of a self–contained X–ray study of Mrk 1014 observed by *XMM-Newton* based on a detailed data reduction. It describes the fundamental differences that show up between my own subsequent and independent analysis work and the published results of Boller et al. (2002).

4.2.1 Several earlier results

Mrk 1014 (known as IRAS 01572+0009 in the *IRAS*–PSC; $z = 0.163$) produces a far–IR–luminosity of more than $10^{12} L_{\odot}$ (Yun et al. 2001) and thus it is one of the brightest members of the class of ”warm” ultraluminous infrared galaxies (see subsection 1.1.3 on p. 8; Sanders et al. 1988b) which is supposed to harbour a powerful AGN in its centre (according to its *IRAS*–25 μm /60 μm colours and optical spectrum).

Wilkes et al. (1994) presented first results of the X–ray–flux and luminosity within the framework of the *Einstein* database of optically– and radio–selected quasars (assuming a power law model with $\alpha = 0.5$). More recently, X–ray data were accumulated during the *ROSAT*–mission phase of pointed observations. Wang et al. (1996) and Brunner et al. (1997) modelled the soft X–ray spectrum successfully with a single power law component ($\Gamma_{(0.1-2.4) \text{ keV}} = 2.8 \pm 0.3$) absorbed by Galactic interstellar material ($N_{\text{H,gal}} = (2.6 \pm 0.9) \cdot 10^{20} \text{ atoms cm}^{-2}$). Based on a *ROSAT* All–Sky–Survey observation, Brinkmann et al. (2000) deduced a power law description of the X–ray emission of Mrk 1014 (= RXS J0159.8+0023) with $\Gamma_{(0.1-2.4) \text{ keV}} = 3.0 \pm 0.2$. Correcting for Galactic absorption, the source flux is determined to $f_{(0.1-2.4) \text{ keV}} = (3.8 \pm 0.5) \cdot 10^{-12} \text{ erg cm}^{-2} \text{ s}^{-1}$ (calculated from the measured count rate and its error and assuming $\Gamma = 2.2$ for the underlying X–ray continuum emission). This results into a luminosity of $L_{(0.1-2.4) \text{ keV}} = (4.8 \pm 0.6) \cdot 10^{44} \text{ erg s}^{-1}$.

4.2.2 The X–ray observation

The visibility of features in a spectrum always depend on the chosen binning of the channels. For that reason it has to be guaranteed that putative features are real and not just a consequence

of an unfavourable binning. Following this principle the *XMM-Newton* data of Mrk 1014 have been treated with great care. In order to allow a comparison the reduction and processing procedure has been performed with the same parameter values (e.g. position, regions of count extraction, etc.) and calibration files (see Boller et al. for more details), whereas the effective exposure times are slightly lower than given in the paper (Table 4.1).

Table 4.1: Summary of the Mrk 1014 observation
(revolution 0117)

Instrument	count rate	exposure time	Instrumental mode
	[counts/sec]	[sec]	
EPIC pn	1.30 ± 0.01	10,114	Full-Frame
EPIC MOS1+2	0.691 ± 0.008	10,427+10,428	Large-Window
– MOS1	0.336 ± 0.006	10,427	— ” —
– MOS2	0.355 ± 0.006	10,428	— ” —

Concerning the EPIC pn data set, the produced source and background spectra are in an excellent agreement with that published by Boller et al. (for a given bin size of $\gtrsim 60$ counts per energy bin). Figure 4.1 displays the EPIC pn, MOS1 and MOS2 spectra in the energy range of (0.3 – 10.0) keV. In each plot the black line represents the source spectrum (not background-corrected) and the background spectrum is indicated in red. The background spectrum includes the instrumental background, the background due to charged particles, and the cosmic X-ray background. One can see that the background spectrum accounts for a significant portion of the spectrum at energies higher than 8 keV, though it is not negligible below. However, the plot of the EPIC pn background spectrum (as published by Boller et al. in Figure 1) remains questionable, since it has been binned with the same bin size (for illustration purposes only), but for other channels than binned in the source spectrum.

In the case of the EPIC MOS 1/2 data sets the verification of their spectral accordance has been investigated. A comparison between MOS 1 and MOS 2 data (with 20 counts bin size) shows an undoubted discrepancy in the source spectra. One immediately notices that the slopes of the source spectra are different among each other, pretending line emission (mostly soft) on top of the continuum which is more marked in the EPIC MOS1 data. However, the EPIC pn spectrum does not show any convincing line emission across the total energy range, despite of the lower energy resolution particularly at soft X-rays.

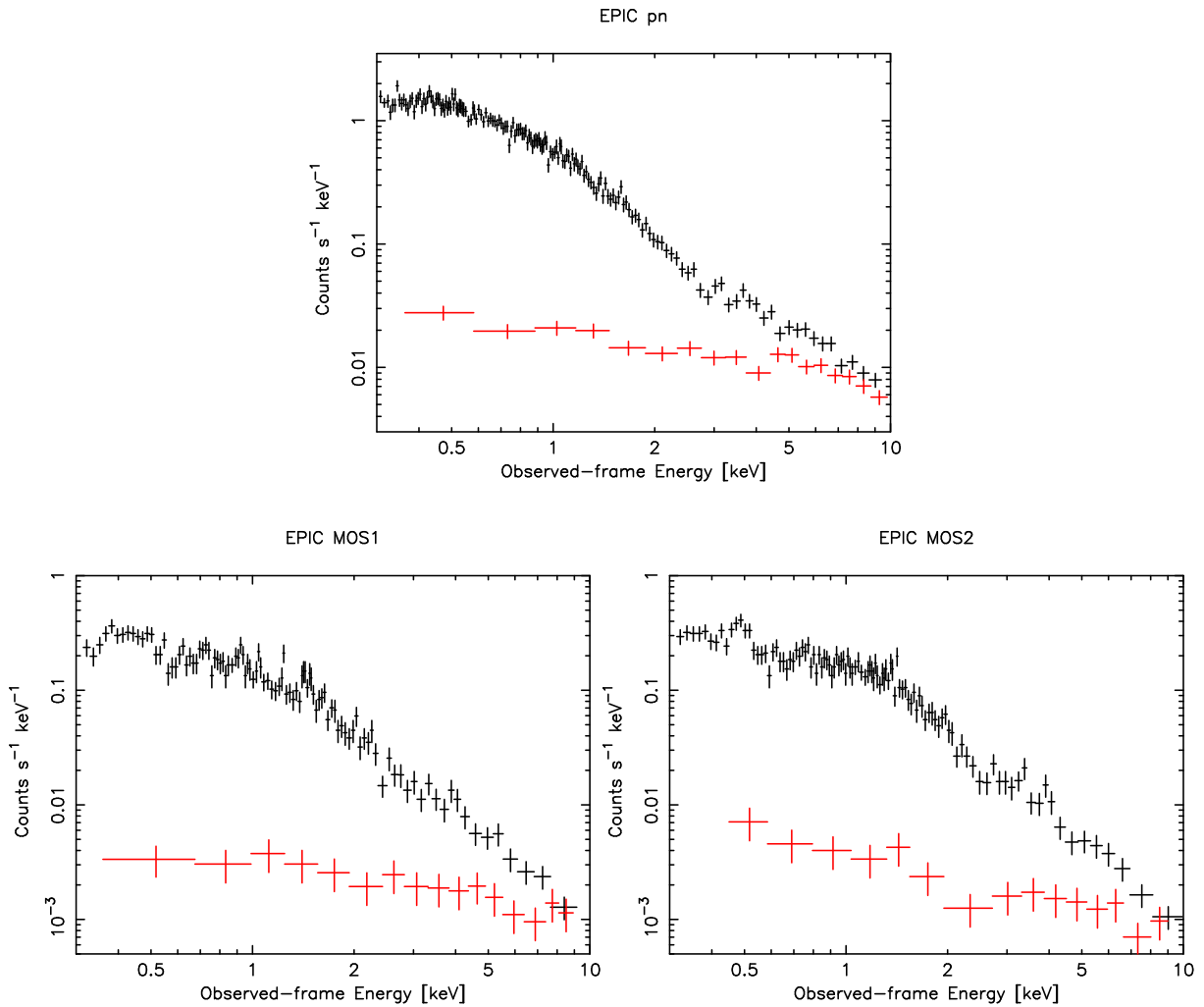


Figure 4.1: Comparison of source spectra with background spectra in the (0.3 – 10.0) keV energy range. **The upper plot** shows the EPIC pn spectrum and **the two lower** the EPIC MOS1 and MOS2 data. In each plot a spectrum in the source region is indicated by the black line with *no* background subtraction and a spectrum of the blank sky in the background region is indicated by the red color. The background spectrum becomes just as significant as the source spectrum at energies higher than ~ 8 keV.

4.2.3 Spectral modelling

The analysis of the EPIC pn spectrum of Mrk 1014 is based on a bin size of (at least) 60 counts per energy bin as stated by Boller et al.. By contrasting the source and the background spectra, the spectral range to be considered is between (0.3 – 8.0) keV for generating models to the X-ray data. In order to examine the significance and reliability of the spectral results this conclusion has been checked and confirmed by the EPIC pn data. Due to the higher statistics of the EPIC pn compared to the MOS1/2 devices the results of the fitting procedures are primarily checked against the data of the former device, whereas the fit results from the EPIC MOS1/2 were used for cross-checking.

Beginning with the easiest model the photoelectric absorption was treated as a free parameter. As a first result, absorption above the Galactic column density value $N_{\text{H,gal}}$ was not found in any spectral model ($N_{\text{H,gal}}$ has been calculated with the FTOOL `nh`). For the rest of the analysis the absorption parameter has been fixed to $N_{\text{H,gal}} = 2.6 \cdot 10^{20}$ atoms cm^{-2} (Dickey and Lockman 1990).

In order to get a first insight into the overall characteristics of the spectrum a power law model spectrum (f_{po}) multiplied by Galactic absorption ($f_{\text{Gal. abs}}$), *i.e.*

$$f_{\text{po+Gal. abs}}(E) = \underbrace{N_{\text{po}} \cdot E^{-\Gamma}}_{f_{\text{po}}(E)} \cdot \underbrace{e^{-(\sigma_{\text{photo}} \cdot N_{\text{H,gal}})}}_{f_{\text{Gal. abs}}(E)},$$

has been applied to the data. The (monochromatic) photon flux f_{po} (normalized at one keV; in photons $\text{cm}^{-2} \text{s}^{-1} \text{keV}^{-1}$) is described by the X-ray energy E , the photon index Γ , the photoelectric absorption cross-section σ_{photo} (Morrison and McCammon 1983) with $N_{\text{H,gal}}$, and by N_{po} as a normalization factor. By using the PHABS model within XSPEC (Balucinska-Church and McCammon 1992) all models described later in this section are multiplied with the exponential decay representing the radiative absorption within our galaxy, but are not explicitly written.

The two-parameter model was fit to the EPIC pn spectrum with the result of $\chi^2 = 113.5$ for 96 dof ($\chi^2/\nu = 113.5/96 = 1.2$). The photon index was computed to $\Gamma = 2.51 \pm 0.03$ (see Table 4.2 on p. 91). Figure 4.2 illustrates the quality of this model. One immediately notices the residuals of the model prediction to the data points above ~ 2.2 keV. This requires a further investigation, as to decide if the determined χ^2 -value is consistent with the model expectation of the data distribution. This step is performed by estimating the probability that a random set of data points taken from the assumed probability distribution would give a χ^2 -value as large as or larger than the calculated value from the measurements. If this value is close to unity, then the distribution used is a good description for the spread of the data points.

One can expect to find a probability of around 50 per cent (and $\chi^2/\nu \simeq 1$), since the calculated χ^2 -value from the data should be larger than the norm value in half of the set. However, this probability is either rather small or unreasonably large, giving in both cases confidence to its conclusion. Poor fits are characterized by $\chi^2/\nu \gg 1$ and the associated probability is very small. Concerning the EPIC pn spectrum the probability of obtaining a fit result with $\chi^2/\nu \gtrsim 1.2$ and 96 dof is calculated to be 10.8 per cent. This value is given within the fit results in XSPEC as the probability that the null hypothesis is true, *i.e.* that the model follows the distribution of the data. This value can be found in the following tables as the null hypothesis probability ("NHP"; see Table 4.2 on p. 91 and Table 4.3 on p. 94). The greater the NHP value, the more likely the applied model is an appropriate description of the data. In other words, recording many different data sets of Mrk 1014 independently this probability indicates that in $\simeq 11$ per cent of the

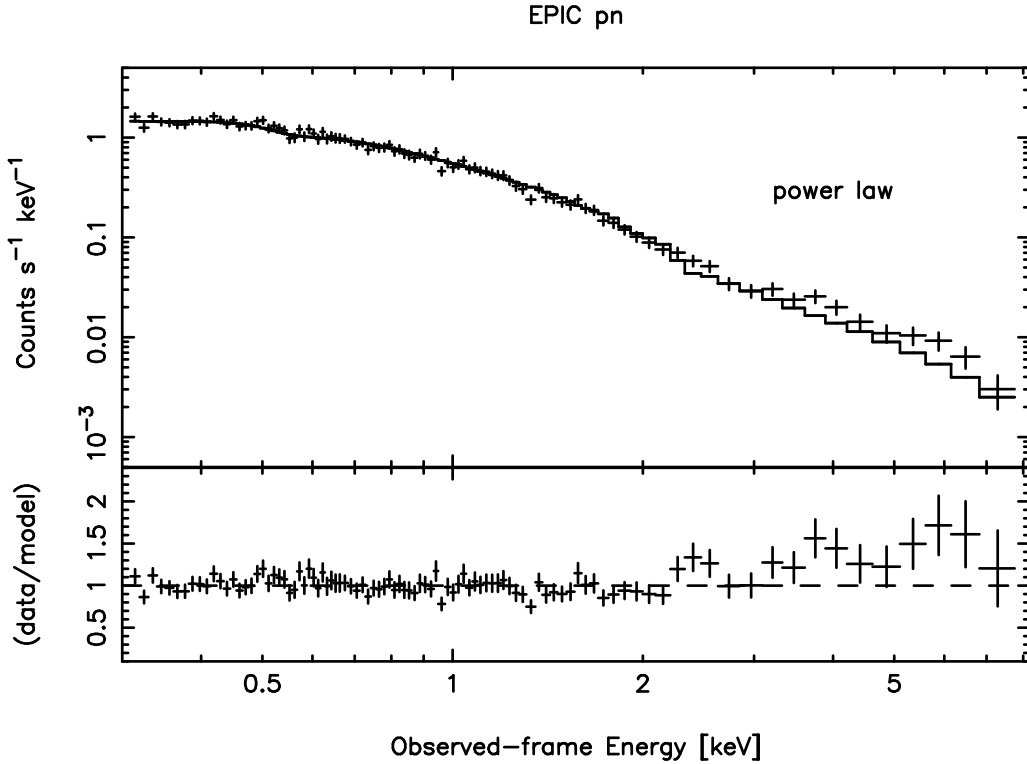


Figure 4.2: The (0.3 – 8.0) keV spectrum of Mrk 1014 from the EPIC pn data, plotted with the model component. The data set is fit with a power law component ($\Gamma = 2.51 \pm 0.03$; $\chi^2/\nu = 113.5/96 = 1.2$) marked by the solid line. The corresponding probability is ~ 11 per cent (\gtrsim CL defined in 3.1.1 on p. 46, see text for more information). The lower panel of the figure shows the residuals, *i.e.* the data/model ratio.

data sets the obtained fit results are worse than the parameter set listed in Table 4.2. Under the assumption of the correctness of the null hypothesis the deviations of the model from the data points is *significant* on a certain level, the level of confidence CL (see 3.1.1 on p. 46). A model fit can be regarded as acceptable if the NHP is larger than the CL. The CL is defined to be 10 per cent in this case, a value commonly quoted in the literature (e.g. Yuan et al. 2005). A simple comparison proves that the power law model is an appropriate description for the Mrk 1014 data set.

However, the residuals shown in the plot require a closer inspection of the spectrum. This has been done by adding a second model component to the power law. The physical nature of this component remains undefined in the sense that both thermal and non-thermal approaches have been applied, *i.e.* a second power law as well as two plasma model descriptions.

A combination of two power law components improves the fit of the EPIC pn data ($\chi^2/\nu = 0.95$ for 95 dof, *i.e.* NHP = 62.6 per cent). However, the model parameters of the second power law are poorly constrained. The data quality limits the possible model descriptions to a few model components (if not just one), in its simplest form to a power law. Any further attempt with more and/or advanced models is not unique, since the spectrum is not able to provide a quantitative improvement and reliability of their parameters and thus of the underlying physical conditions. For this reason the spectral analysis performed with other model assumptions as published by Boller et al. (2002) has to be regarded with some scepticism.

In order to demonstrate this conclusion, the EPIC pn data have been fit with the thermal model APEC, based on the physics of an optically-thin X-ray emitting gas (cf. subsection 3.2.3 on p. 56f). Combined with a power law the fit result of the EPIC pn data ($\chi^2/\nu = 97.5/94$, NHP = 38.2 per cent) is comparable to that of the double power law model, with a well constrained temperature $kT = (220 \pm 30)$ eV of the plasma. The NHPs in both cases are well above the 10 per cent threshold. Table 4.2 gives the fitting results of the EPIC pn data, together with the total (0.3 – 8.0) keV–flux values of each model component. The corresponding luminosities are listed in Table 4.5 on p. 97.

Table 4.2: Fitting parameters of attempted spectral models for the EPIC pn
EPIC pn ^{a)}

Model description		power law	(0.3 – 8.0) keV–flux ^{b)}		χ^2/ν	NHP ^{c)}
component	parameter ^{d)}	Γ	[10 ⁻¹² erg cm ⁻² s ⁻¹]			
			[parameter]	[power law]		
power law	–	2.51 ± 0.03	–	2.40 ± 0.04	1.18	10.8
double power law	$\Gamma_2 = 1.0 \pm 0.6$	2.6 ± 0.1	$0.4^{+1.2}_{-0.3}$	$2.2^{+0.2}_{-0.4}$	0.95	62.6
APEC	$kT = 0.23 \pm 0.04$	2.40 ± 0.06	0.13 ± 0.05	2.28 ± 0.07	1.04	38.2

a) The error numbers give the 90 per cent confidence interval uncertainties.

These are of statistical nature (without any contribution from systematic errors in the calibration),

b) the fluxes are corrected for Galactic absorption,

c) null hypothesis probability NHP, in per cent (see text for more information),

d) the temperatures kT are given in keV.

Considering pure statistical arguments, the simple power law approach can be regarded as an acceptable spectral model for describing the *XMM-Newton* data of Mrk 1014. As mentioned above, applying sophisticated models to the EPIC pn data set does not lead to a better understanding of the spectrum. Any additional model would cause an insufficient or wrong interpretation based on data of limited expressiveness. In order to quantify this behaviour the

NHP as an additional statistical value has been consulted. From this starting point the NHP determination reports the single power law model as an adequate approximation to the Mrk 1014 data. The NHP value for this model and for the other model approaches are included in Table 4.2 as well as in Table 4.3 (on p. 94) for the EPIC MOS devices and for the simultaneous fittings of the combined EPIC pn and MOS1/2 data. A comparison of the NHP values reveals the different results in terms of the significance of the power law model, and gives no preference to one of the models (EPIC pn: 10.8 per cent for the power law model, 62.6 per cent for the double power law, and 38.2 per cent for the APEC model). In other words, none of the presented models excel the others, and thus none of the model alternatives is closer than the others being a favourite model description of the *XMM-Newton* data of Mrk 1014. However, this statement does not take into account any physical consideration. As proposed by Boller et al., favouring the AGN-dominated spectral model to be the most realistic explanation for the X-ray features of Mrk 1014 are such a conclusion that is more far-reaching than the information within the spectrum can actually provide.

Given the EPIC MOS1 and MOS2 data sets, simultaneous spectral fitting procedures were performed applying the different models with common spectral parameters. The EPIC MOS1/2 data have lower photon statistics than the EPIC pn data. As a consequence, they can not help to improve the interpretation of the X-ray spectrum, *i.e.* constraining (or rejecting) putative model descriptions. Nevertheless, they can be used to obtain independent fit results of any spectral modelling and to compare them with the EPIC pn findings.

In general, the conclusions written for the EPIC pn data can be adopted to the discussion of the EPIC MOS1/2 data – despite of noticeable differences in the pure numbers (Table 4.3). The first attempt, one power law model, produces the statistical values $\chi^2/\nu = 169.8/123 = 1.4$, *i.e.* NHP = 0.3 per cent, whereas the approach with two power laws yields for both data sets fit results with $\chi^2/\nu = 1.1$ for 120 dof (NHP = 13.6 per cent). In this regard further fitting procedures using the APEC description are solely of statistical interest, but resembling the significance of the double power law model, albeit the NHPs of both models are below 10 per cent. Again, considering the NHP values the double power law description has the highest probability of representing the data compared to the other models. Nevertheless, it is of no exceptional importance for finding the true model description for the EPIC MOS1/2 data.

A simultaneous fit for both the EPIC pn and the EPIC MOS1/2 data has been performed for each model individually. The results of the fitting procedures are listed in Table 4.3 (lower part). The picture formed from the results of the independent fittings of EPIC pn and MOS1/2 is being resembled in this fit values. The simple power law gives $\chi^2/\nu = 280.18/221 = 1.27$ (NHP = 0.4 per cent). In the same sense, the thermal model shows comparable statistical values

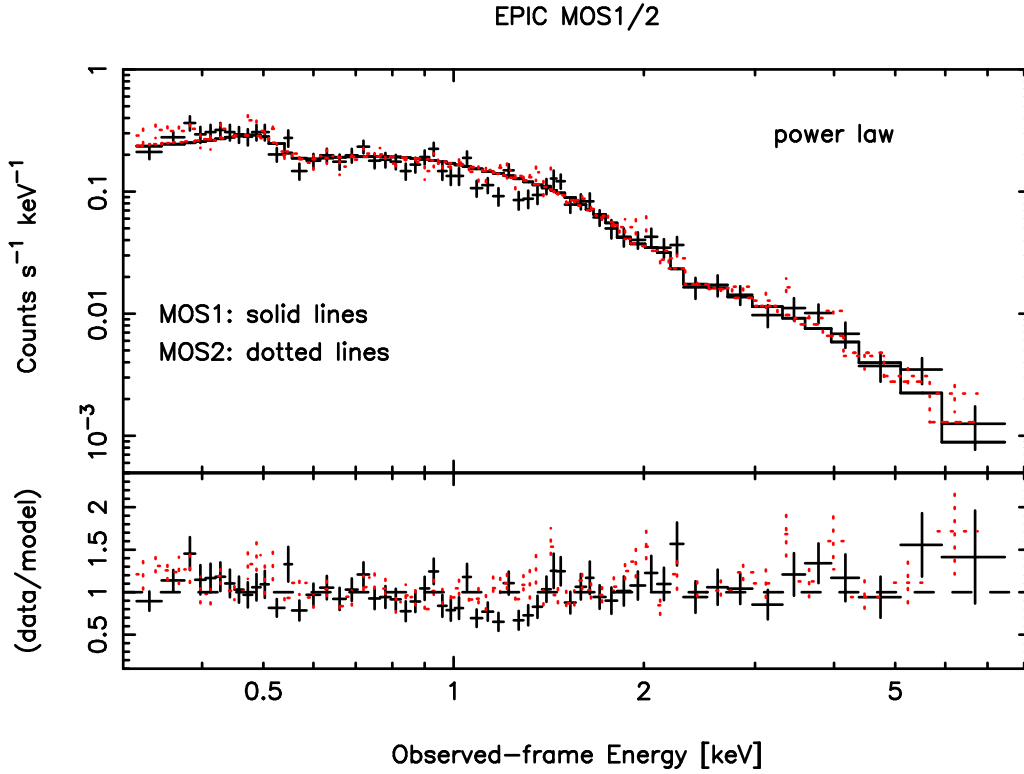


Figure 4.3: Power law fits to the EPIC MOS1/2 spectra of Mrk 1014 in the (0.3 – 8.0) keV range, as seen in the frame of the source. In each plot the upper panel shows the data and the model (thick solid line) as well as the model component. The lower panel displays the ratio of the data points to the model expectation at this points. A power law continuum model to the combined EPIC MOS1/2 data results in a fit with the statistical quantities $\chi^2/\nu = 1.38$ for 122 dof (NHP = 0.3 per cent).

($\chi^2/\nu = 266.93/219 = 1.22$) with a NHP significant below 10 per cent (NHP = 1.5 per cent). Even the model with two power laws ($\chi^2/\nu = 248.35/219 = 1.13$ with a NHP of 8.4 per cent) has the problem to find a suitable and stable parameter space (as confirmed by the corresponding contour plot). However, a physical interpretation can *not* be related to any of the models discussed (see below for the case of a soft and hard excess emission claimed by Boller et al., 2002). In particular, the APEC approach has been discussed here, because it was used for an estimation of the uncertainties due to the subtraction of the background signal (see subsection 3.3.1 on p. 78).

Finally, Boller et al. mentioned the presence of an excess emission above the power law slope at hard energies of > 5 keV. They have added a further power law to their model (with a negative gradient) to improve the fitting results. However, this procedure could only improve the results on a statistical basis, but is unable to provide additional information about the physical origin. Since the exposure time is too low to significantly detect a radiation excess and thus the number of data points above ~ 5 keV (but lower than 8 keV) is very limited, a deeper analysis of this

Table 4.3: Fitting parameters of attempted spectral models for the EPIC MOS1/2 and the combined EPIC pn and EPIC MOS1/2 devices

Simultaneous fits^{a)}

Model description		power law	(0.3 – 8.0) keV–flux ^{b)}		χ^2/ν	NHP ^{c)}
component	parameter ^{d)}	Γ	[10 ⁻¹² erg cm ⁻² s ⁻¹]			
			[parameter]	[power law]		
power law	–	2.41 ± 0.04	–	2.34 ± 0.06	1.38	0.3
double power law	$\Gamma_2 = 2.1 \pm 0.2$	3.9 ^{+1.2} _{-0.8}	1.9 ^{+0.4} _{-0.6}	0.6 ^{+1.2} _{-0.4}	1.14	13.6
APEC	kT = 0.12 ± 0.08	2.29 ± 0.06	0.02 ^{+4.6} _{-0.01}	2.26 ± 0.07	1.19	7.3

Model description		power law	(0.3 – 8.0) keV–flux ^{b)}		χ^2/ν	NHP ^{c)}
component	parameter ^{d)}	Γ	[10 ⁻¹² erg cm ⁻² s ⁻¹]			
			[parameter]	[power law]		
power law	–	2.44 ± 0.03	–	2.34 ± 0.04	1.27	0.4
double power law	$\Gamma_2 = 1.2 \pm 0.7$	2.6 ^{+0.3} _{-0.1}	0.4 ^{+1.4} _{-0.3}	2.1 ^{+0.1} _{-0.7}	1.13	8.4
APEC	kT = 0.24 ± 0.04	2.37 ± 0.04	0.09 ^{+0.05} _{-0.04}	2.30 ^{+0.04} _{-0.06}	1.22	1.5

a) The error numbers give the 90 per cent confidence interval uncertainties.

These are of statistical nature (without any contribution from systematic errors in the calibration),

b) the fluxes are corrected for Galactic absorption,

c) null hypothesis probability NHP, in per cent (see text for more information),

d) the temperatures kT are given in keV.

effect is not possible and will yield to unjustified statements. Concerning the claimed soft X–ray excess in the spectrum of Mrk 1014 the above consideration does not allow to give statements on any emission above the power law slope.

However, instead of trying to disentangle the various possible emission components in Mrk 1014, one can still use its overall emission properties for a comparison with the main target, NGC 6240.

4.3 Properties of the hard components

Studying the hard X-ray emission can help to deduce the presence of an AGN in the centre of ULIRGs. To address this issue one has to look at AGN-signatures in the hard X-ray data, and – if existing – to determine its contribution to the absorbed power law emission. This leads immediately to the question whether the obscured AGN dominates the bolometric luminosity. In combination with the analyzed Fe–K emission (see 4.3.3 on p. 117f) one is able to search for the energetically-important AGN engine.

4.3.1 Luminosities

In order to estimate the contribution for an AGN, the X-ray power law and the far-IR emission have to be determined. The computed $L_{\text{hard}}/L_{\text{FIR}}$ -ratio¹ can be compared to the ratio values typical for pure AGN and Starburst galaxies.

According to the analysis of the *Chandra* data of NGC 6240 (subsection 3.2.5 on p. 73) luminosities from the *XMM-Newton* data have been calculated in the bands (0.5 – 1.5) keV, (1.5 – 5.0) keV and (5.0 – 10.0) keV. They are listed in Table 4.4. All values are corrected for Galactic absorption. An additional correction for intrinsic absorption results in luminosities of a factor of about 7, 12, and 4.5 higher than the value in the table. In the softest band the emission from the 0.7 keV-plasma dominates the SED, with a contamination level of about 15 per cent from the (intrinsically absorbed) 1.4 keV-component. In the (1.5 – 5.0) keV band one has a mixture of all three plasma components, in which the 0.7 keV-plasma still contributes most of the emission, *i.e.* more than three times higher than the sum from the two other plasmas. Above 5 keV the absorbed 5.5 keV-plasma component dominates the spectrum, being more than 30 times more luminous than the 1.4 keV-plasma. Finally, the total (0.5 – 10.0) keV luminosity of NGC 6240 is $\log[L_{(0.5-10.0) \text{ keV}}] = 43.2 \pm 0.4$ and $\log[L_{(0.5-10.0) \text{ keV}}] = 44.0 \pm 0.4$ without any intrinsic absorption, resembling the luminosities in the whole *XMM-Newton* energy band.

In order to relate the X-ray luminosities of NGC 6240 and Mrk 1014 to the values of the far-IR-luminosity, Table 4.5 contains calculated luminosities in the bands (0.5 – 2.0) keV and (2.0 – 10.0) keV. These ranges were chosen for comparison with the results of other works on both objects, although they are not favourable for the analysis presented in this thesis, because *XMM-Newton* is able to measure their luminosities within a broader range. In the case of Mrk 1014 the single power law model has been used for all subsequent calculations. The fluxes and luminosities are determined from the results of simultaneous fitting processes of the EPIC pn and MOS1/2 data and are extrapolated to 10 keV. For NGC 6240 the values are listed for each model component with the same numbering for the APEC models as in Table 3.8 on p. 71.

¹note the footnote in subsection 1.1.3 on p. 11

Table 4.4: *Observed* luminosities and flux ratios of Mrk 1014 and NGC 6240 in selected energy regimes ^{a)}

Luminosity [erg s ⁻¹]	Mrk 1014 ^{b)}	NGC 6240	Reference ^{c)}
$\log[L_{(0.3-10.0) \text{ keV}}]$	44.6 ± 0.4	43.2 ± 0.4	this thesis
$\log[L_{(0.5-1.5) \text{ keV}}]$	44.2 ± 1.1	42.7 ± 0.4	this thesis
$\log[L_{(1.5-5.0) \text{ keV}}]$	44.0 ± 1.2	42.6 ± 0.4	this thesis
$\log[L_{(5.0-10.0) \text{ keV}}]$	43.6 ± 1.2	42.8 ± 0.4	this thesis
$\log[L_{(0.5-2.0) \text{ keV}}]$	44.2 ± 1.1	42.8 ± 0.4	this thesis
$\log[L_{(2.0-10.0) \text{ keV}}]$	44.1 ± 1.2	43.0 ± 0.4	this thesis
$\log[L_{(2.0-10.0) \text{ keV}}]_{\text{int}}$	–	43.8 ± 0.4	this thesis
$f_{25\mu\text{m}}/f_{60\mu\text{m}}$	0.3 ± 0.2	0.15 ± 0.05	I, II
$\log[L_{\text{FIR}}]$	46.3 ± 1.1	45.4 ± 1.7	III, IV
$\log\left[\frac{L_{(0.5-2.0) \text{ keV}}}{L_{\text{FIR}}}\right]$	$-(2.0 \pm 1.5)$	$-(2.6 \pm 1.7)$	
$\log\left[\frac{L_{(2.0-10.0) \text{ keV}}}{L_{\text{FIR}}}\right]$	$-(2.2 \pm 1.6)$	$-(2.4 \pm 1.7)$	
$\log\left[\frac{L_{(2.0-10.0) \text{ keV}}}{L_{\text{FIR}}}\right]_{\text{int}}$	–	–1.6	
$\log[L_{\text{Fe-K}}]$	–	41.9 ± 0.5	this thesis
$\log[L_{[\text{OIII}]}]_{\text{corr}}$	44.9	43.6	V, VI
$\log\left[\frac{L_{(2.0-10.0) \text{ keV}}}{L_{[\text{OIII}]}]_{\text{corr}}}\right]$	–0.83	–0.65	

a) Note: The values are corrected for Galactic absorption alone; the (2.0 – 10.0) keV–luminosity is *not* corrected for the measured intrinsic absorption in each source (as it was done in Table 4.5), exceptions:

$\log[L_{(2.0-10.0) \text{ keV}}]_{\text{int}}$ and $\log[L_{(2.0-10.0) \text{ keV}}/L_{\text{FIR}}]_{\text{int}}$ (see text),

b) calculated as the luminosities from the single power law model,

c) References: I Sanders et al. (1989), II Golombek et al. (1988), III f_{60} and f_{100} from Kim and Sanders (1998), IV f_{60} and f_{100} from Genzel et al. (1998), V Miller et al. (1992), VI Armus et al. (1989, 1990).

These values allow to determine the total (observed) X–ray continuum luminosities of Mrk 1014 and NGC 6240 within both bandpasses, as summarized in Table 4.4. They are listed with the $f_{25\mu\text{m}}/f_{60\mu\text{m}}$ –flux ratios and their luminosities in the far–IR. On account of the large absorbing column density to the power law component in the hard X–ray band, the table includes the absorption–corrected intrinsic luminosity $\log[L_{(2.0-10.0) \text{ keV}}]_{\text{int}}$ of NGC 6240 together with its corresponding luminosity–ratio $\log[L_{(2.0-10.0) \text{ keV}}/L_{\text{FIR}}]_{\text{int}}$. To support the claim of NGC 6240

Table 4.5: Absorption–corrected fluxes and luminosities of Mrk 1014 and NGC 6240 computed from the various model components within (0.5 – 2.0) keV and (2.0 – 10.0) keV ^{a)}

Mrk 1014				
Model		energy band	flux	luminosity
description	component	[keV]	[10^{-12} erg cm $^{-2}$ s $^{-1}$]	[10^{43} erg s $^{-1}$]
power law	power law	0.5 – 2.0	1.13 ± 0.03	17.5 ± 0.4
		2.0 – 10.0	0.68 ± 0.02	10.5 ± 0.2
NGC 6240				
Model		energy band	flux	luminosity
description	component	[keV]	[10^{-12} erg cm $^{-2}$ s $^{-1}$]	[10^{43} erg s $^{-1}$]
	vAPEC(1)	0.5 – 2.0	1.7 ± 0.3	0.5 ± 0.1
		2.0 – 10.0	0.13 ± 0.02	$(3.8 \pm 0.7) \cdot 10^{-2}$
	vAPEC(2)	0.5 – 2.0	$0.6^{+3.9}_{-0.5}$	$0.2^{+0.9}_{-0.1}$
		2.0 – 10.0	$0.3^{+1.6}_{-0.2}$	$0.1^{+0.5}_{-0.07}$
	APEC(3)	0.5 – 2.0	1.0 ± 0.3	0.3 ± 0.1
		2.0 – 10.0	1.8 ± 0.4	0.5 ± 0.1
	power law	0.5 – 2.0	13.3 ± 6.2	3.5 ± 1.7
		2.0 – 10.0	20.8 ± 9.8	5.6 ± 2.6
	Fe–K complex	0.5 – 2.0	–	–
		2.0 – 10.0	0.25 ± 0.07	0.07 ± 0.02

a) corrected for Galactic *and* intrinsic absorption.

being an AGN, the Fe–K complex luminosity is presented in the table as well (see subsection 4.3.3 on p. 117ff for further details). According to a work of Bassani et al. (1999) the flux ratio of the strongest optical line in the NLR, the [O III] λ 5007 emission–line, to the hard X–ray flux can be used as an indicator of quantifying the amount of X–ray absorbing material, even when the source is Compton–thick. To follow this idea the extinction–corrected [O III]–luminosity has been added to the table (q.v. p. 104).

Table 4.6 gives an overview of the fluxes and luminosities of Mrk 1014 and NGC 6240 as observed in the specified energy bands and gained with the satellites indicated. The values are measured or converted into the rest frame of the observer, except for the papers stated otherwise.

Table 4.6: *Observed X-ray fluxes and luminosities of Mrk 1014 and NGC 6240 within different energy regimes, taken from the literature (based on data of various observations/satellites)*

Reference	satellite	energy band	flux	luminosity
		[keV]	[10^{-12} erg cm $^{-2}$ s $^{-1}$]	[10^{43} erg s $^{-1}$]
Mrk 1014				
Wilkes et al. (1994)	<i>Einstein</i>	0.2 – 4.5	1.9 ± 0.4	23 ± 4
This thesis	<i>XMM-Newton</i>	0.2 – 4.5	2.1 ± 0.1	28.0 ± 1.4
Brinkmann et al. (2000) ^{a)}	<i>ROSAT</i>	0.1 – 2.4	3.8 ± 0.5	48 ± 6
This thesis ^{a)}	<i>XMM-Newton</i>	0.2 – 2.4	2.57 ± 0.06	37.2 ± 0.5
NGC 6240				
Schulz et al. (1998)	<i>ROSAT</i>	0.1 – 2.4	1.19	0.30
Turner et al. (1997a) ^{b), c)}	<i>ASCA</i>	0.5 – 2.0	0.71	0.18
Iwasawa & Comastri (1998)	<i>ASCA</i>	0.5 – 2.0	0.64	0.16
Vignati et al. (1999)	<i>BeppoSAX</i>	0.5 – 2.0	0.74	0.18
Ptak et al. (2003)	<i>Chandra</i>	0.5 – 2.0	0.72	0.18
This thesis	<i>XMM-Newton</i>	0.5 – 2.0	1.08 ± 0.07	0.27 ± 0.02
Turner et al. (1997a) ^{b)}	<i>ASCA</i>	2.0 – 10.0	1.17	0.29 ^{c)}
Iwasawa & Comastri (1998)	<i>ASCA</i>	2.0 – 10.0	1.9	0.47
Vignati et al. (1999)	<i>BeppoSAX</i>	2.0 – 10.0	3.2	0.79
Ikebe et al. (2000) ^{a), d)}	<i>ASCA + RXTE</i>	2.0 – 10.0	3.6 ± 1.5	0.9 ± 0.4
Ptak et al. (2003)	<i>Chandra</i>	2.0 – 10.0	2.6	0.65
This thesis	<i>XMM-Newton</i>	2.0 – 10.0	3.40 ± 0.20	0.85 ± 0.05
Komossa et al. (2003) ^{e)}	<i>Chandra</i>	0.2 – 10.0	1.03 ^{c)}	0.26
Ptak et al. (2003) ^{e)}	<i>Chandra</i>	0.2 – 10.0	1.88	0.47

a) corrected for Galactic absorption,

b) computed from the RAYMOND plus power law model,

c) corrected for intrinsic absorption,

d) the estimations are based on the favoured Ikebe et al. model applied to the *XMM-Newton* data,

e) the values are the sum of the fluxes and luminosities from both nuclei.

For the majority of the publications, the original published measurements are reported, even if a comparison between two numbers is problematic (see the results from Schulz et al. (1998) which have a different lower bound in the energy band or from Ikebe et al. (2000) with an intrinsic absorption correction). In addition, flux and luminosity measures from both nuclei of NGC 6240 were included, although *XMM-Newton* can only detect the superposed emission of both; thus their values were added up.

Concerning Mrk 1014, the results from the *Einstein* observation are in good agreement with the findings in this thesis. By looking at the flux measurements, one has to keep in mind that Mrk 1014 was observed during the survey phase of the *ROSAT* mission. Due to the short exposure time the *ROSAT*-flux was estimated via an indirect method, *i.e.* not by spectral modelling, but with the count rate in combination with an assumed power law slope of $\Gamma = 2.2$, in order to achieve a flux value. This was converted into a luminosity estimation of the presented value. Applying the model description and its associated parameters to the (0.2 – 2.4) keV band of the *XMM-Newton* data, the flux and luminosity are $f = (1.67 \pm 0.03) \cdot 10^{-12} \text{ erg cm}^{-2} \text{ s}^{-1}$ and $L = (20.5 \pm 0.4) \cdot 10^{43} \text{ erg s}^{-1}$, consistent with the other values (considering the different energy bands).

For NGC 6240, the results in the soft energy regime are in agreement with each other, although the values in this thesis are slightly higher than the others, but overlap with the *ROSAT* findings of Schulz et al. (1998) on a $\sim 1\sigma$ level (again, based on a different energy band). Boller (1999) computed the soft X-ray flux from the *PSPC* count rate under the assumption of a simple power law spectrum, resulting in a slightly higher flux value than that of Schulz et al.. The luminosity is $L_{(0.1-2.4) \text{ keV}} = 0.69 \cdot 10^{43} \text{ erg s}^{-1}$ (using eq. 7 of Schmidt & Green 1986), the observed value $L_{(0.1-2.4) \text{ keV, obs}} = 0.40 \cdot 10^{43} \text{ erg s}^{-1}$. The latter was calculated from the published Galactic-absorbed flux and converted to an observed measure (the same is valid for the Schulz et al. values). Turner et al. (1997a) analyzed the *ASCA* data with a large number of models, and came to the conclusion that the most promising model for the overall continuum shape is a more complex model description (in terms of absorption) or a two component model. Looking at the goodness of each fitting the RAYMOND plus power law model provides the best approximation to the data ($\chi^2_{\nu} = 1.43$ for 222 dof). Table 4.6 contains the fluxes and luminosities based on this model. Alternative model fits, e.g. a reflection continuum from neutral material or neutral/ionized partial covering descriptions, are checked, but suffer from worse statistical acceptance. Ptak et al. (2003) published fluxes for both band-passes from *ASCA* and *BeppoSAX* data using the model descriptions reported by Iwasawa & Comastri (1998) and Vignati et al. (1999). They are included in the table, although the original papers do not contain flux values explicitly. The difference of the values given by Turner et al. (1997a) with respect to the (2.0 – 10.0) keV results of Iwasawa & Comastri is mainly

caused by the diverse models used; whereas Turner et al. assume a one-temperature thermal component and found a steep power law shape ($\Gamma = 1.5 \pm 0.1$) without any constrain on an intrinsic absorption $N_{\text{H, intr}}$, Iwasawa & Comastri suggest a two-component thermal model plus a power law component of $\Gamma = 0.3_{-0.5}^{+0.6}$ as the best-fitting value, absorbed by a column of $N_{\text{H, intr}} = (1.3_{-1.3}^{+1.8}) \cdot 10^{22}$ atoms cm^{-2} . It is remarkable that – although both studies rely on data of the same observation – the values from the work of Turner et al. seem to be more precise than that by Iwasawa & Comastri, but the results from the latter investigation are likely more conservative and thus more reliable. The fluxes and luminosities published by Vignati et al. (1999) are comparable to the measures in this thesis, since both analyses make use of the excellent sensitivity of their detectors at high energies, thus allowing to determine an appropriate and stable emission measurement up to 10 keV (and beyond). In addition, the results of the *Chandra* data (concerning the "global" region defined in Ptak et al. 2003) are comparable to the *XMM-Newton* findings, despite of the slightly lower flux (and luminosity) value given in Table 4.6. According to Ikebe et al. (2000) the joined *ASCA* + *RXTE* data of NGC 6240 can be described by a combination of a reflection- and transmission model plus a two-temperature thermal component. The slope of the power law is consistent with the value from Turner et al. ($\Gamma = 1.6_{-0.3}^{+0.4}$), but with an intrinsic absorption of $N_{\text{H}} = (1.7_{-0.7}^{+1.0}) \cdot 10^{24}$ atoms cm^{-2} to the power law component. The resulting luminosity is $L_{(2.0-10.0) \text{ keV}} = (1.1_{-0.5}^{+4.5}) \cdot 10^{44}$ erg s^{-1} (compare with the luminosity in Table 4.4). Applying the Ikebe et al. model, eq. (4), to the *XMM-Newton* data, the fit is statistically acceptable ($\chi_{\nu}^2 = 1.06$ for 192 dof). Neglecting the contribution from the Fe lines, which is not more than about one per cent of the total (2.0 – 10.0) keV emission, the measurements of the (2.0 – 10.0) keV-flux and luminosity confirm the results of Ikebe et al., and thus allow – along the reversed line – to estimate the *observed* flux and luminosity of NGC 6240 in order to compare them with the values from other observations. Corrected for Galactic, but not for intrinsic absorption, both quantities are derived to $f_{(2.0-10.0) \text{ keV}} = (3.6 \pm 1.5) \cdot 10^{-12}$ erg $\text{cm}^{-2} \text{ s}^{-1}$ and $L_{(2.0-10.0) \text{ keV}} = (0.9 \pm 0.4) \cdot 10^{43}$ erg s^{-1} which are included in Table 4.6. Finally, the consistency of the fluxes and (independently determined) luminosities between the various observations/satellites is unambiguously demonstrated.

The analysis of the hard X-ray properties results in the luminosity $\log[L_{(2.0-10.0) \text{ keV}}] = 44.1 \pm 1.2$ for Mrk 1014. This is in the range of the ten lowest-luminous sources from a subsample of pure QSOs published by Elvis et al. (1994). Scaled to the IR-luminosity, the ratio of $\sim 4.6 \cdot 10^{-3}$ is about one order-of-magnitude below the typical value for QSOs ($\sim 3 \cdot 10^{-2}$ assuming $L_{\text{IR}} \approx L_{\text{bol}}$; see 3.2.1 on p. 49), which might be indicative for a low-luminous AGN contribution. Given the luminosities in a sample of Seyfert 1 galaxies (Nandra et al. 1997a; based on *ASCA* observations), Mrk 1014 is located at the high tail of the luminosity-distribution, comparable to four other sources (out of 18). Mrk 1014 is outside the luminosity distribution

built up by 25 Seyfert 2 galaxies (incl. NGC 6240) and analyzed by Turner et al. (1997a). The hard X-ray luminosity of NGC 6240 falls into the peak of the luminosity distribution of PG quasars (George et al. 2000). The median in the Sy-1 distribution by Nandra et al. is in good agreement to the value of NGC 6240, whereas the majority of the Seyfert 2 galaxies in the sample of Turner et al. has a lower luminosity. Concerning the NGC 6240 luminosity ratio of $L_{(2.0-10.0)\text{ keV}}/L_{\text{IR}} = 2.5 \cdot 10^{-2}$, this measure is close to the criterion for the presence of a dominant, *i.e.* luminous AGN, and supports and emphasizes the important role of the non-thermal source for the energy output not only in the IR regime but also for X-rays (cf. Ward et al. (1988) for comparative values of other Seyfert galaxies).

These results of two single sources can be compared with existing studies of LIGs/ULIRGs with larger sample statistics. The luminosity ratios published by Risaliti et al. (2000), Ptak et al. (2003) and Franceschini et al. (2003) coincide with the range of this ratio for sources being classified as ULIRGs, Starbursts and composite galaxies. All three author groups show that the range of this ratio in combination with other quantities can help to provide new insights into the physics of LIGs/ULIRGs.

Regarding the dominant activity mechanism the far-IR-flux ratio $f_{25\mu\text{m}}/f_{60\mu\text{m}}$ is an indication for the relative strength of an AGN activity compared to an enhanced star formation. According to de Grijp et al. (1987) it can be used to measure the (mean) temperature of the dust in a galaxy. The 25 μm -emission originates from warm dust that is more abundant in the centres of AGN than in Starburst galaxies, while the 60 μm -flux is the result of reprocesses of UV/optical radiation off dust at lower temperatures, as it appears both in the torus of an AGN and in star forming regions. Thus, the higher this ratio is the more dominant is the AGN as the main power engine. On the other hand, the hard X-ray luminosity, normalized to the far-IR-luminosity, allows to constrain the relative AGN and Starburst contribution to the source activity. Therefore, it is interesting to contrast both quantities with each other, illustrating the link between the Starburst phenomenon and the obscuration of the source due to a dense ISM on small distances around the centre. The larger the ISM-density is, the more obscuration occurs, and the more hard X-rays are blocked, leading to a decreasing hard X-ray luminosity and therefore to a smaller $L_{(2.0-10.0)\text{ keV}}/L_{\text{FIR}}$ -ratio. In addition, the far-IR-luminosity increases due to a larger reprocessing rate. Risaliti et al. (2000) found a strong correlation between both ratios for a sample of 78 LIGs and ULIRGs, based on *ASCA* and *BeppoSAX* data. Seyfert 1 galaxies, as defined by their optical classification, possess preferentially both a high luminosity ratio and a high far-IR-flux ratio, *i.e.* a warm infrared colour. For lower far-IR-flux ratios the luminosity ratios decrease, equivalent to the increasing strength of the obscured AGN contribution. Ptak et al. (2003) enlarged this study by using *Chandra* data of a sample of the nine nearest ULIRGs (including NGC 6240) in order to investigate the hard X-ray-IR-relation. They were compared

with a sample of pure Starbursts (e.g. Della Ceca et al. 1996, 1999; Dahlem et al. 1998; Ptak et al. 1999), a sample of composite Sy-2/Starburst galaxies, as well as for comparable samples of pure Seyfert 1 and Seyfert 2 galaxies (Levenson et al. 2001).

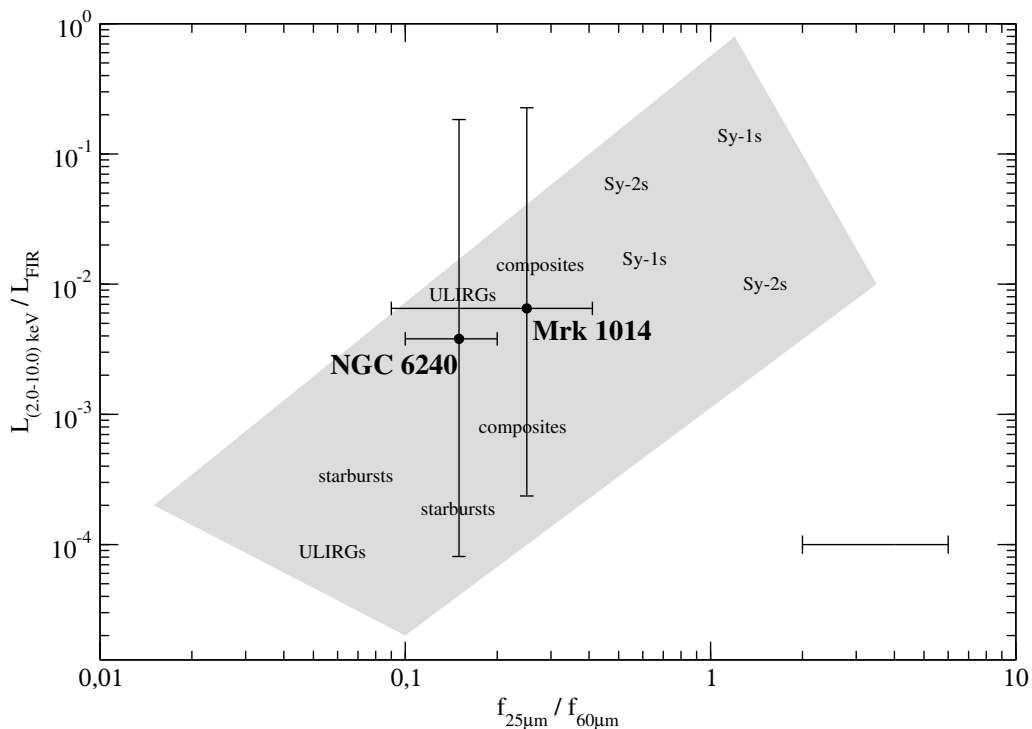


Figure 4.4: The (observed) luminosity ratio $L_{(2.0-10.0) \text{ keV}}/L_{\text{FIR}}$ as a function of the far-IR-flux ratio $f_{25\mu\text{m}}/f_{60\mu\text{m}}$ for various classes of objects. The former ratio decreases with increasing obscuration of the central source due to larger amounts of material around its nucleus. The larger the latter ratio, the more important is the AGN for the energy output. Mrk 1014 and NGC 6240 are more obscured than some pure Seyfert galaxies and show a balanced energy output from the AGN and the Starburst, respectively. However, the large errors in the luminosity ratio limit the validity of the link between both sources and the object class (plot adapted from Ptak et al. 2003).

Figure 4.4 shows the 2-dimensional parameter space, indicating where the samples are located. Although the $L_{(2.0-10.0) \text{ keV}}/L_{\text{FIR}}$ -ratio is a reciprocal function of the strength of obscuration, and therefore the areas of both Seyfert classes should be sufficiently separated from each other, their data points are mixed. The marking of the diverse classes in the plot is due to the presence of a few sources in the associated regions. Levenson et al. found out that the majority of the pure Sy-2s is Compton-thin, whereas the composite sources are considered to be Compton-thick (for a given $f_{25\mu\text{m}}/f_{60\mu\text{m}}$ -ratio).

Concerning the luminosity- and the far-IR-flux ratio values of Mrk 1014 and NGC 6240, it can be seen from Figure 4.4 that both sources are located in a region where the ULIRGs and the Compton-thick composite sources overlap each other. The plot points to the fact that sources,

such as NGC 6240 and Mrk 253, have generally the same properties as AGN/Starburst composite galaxies (both the far-IR-color and the relative strength of the hard X-ray emission). Note that for Mrk 253 the absorption-corrected hard X-ray luminosity shifts its position to the Compton-thin regime of Starburst galaxies. Basically, the properties of ULIRGs are more extreme than that of the composite objects. However, taking into account the large errors in the luminosity ratio of Mrk 1014 and NGC 6240, the link between observable quantities and the class of the sources can not be made unambiguously, since their 1σ error ranges to the region of pure Starbursts. This limits the usefulness of this plot. Based on a model, Risaliti et al. (2000) proposed an approach to quantify the contributions from an AGN and an Starburst in LIGs and ULIRGs by making use of the observed relation. Its shape leads to the suggestion that the absorption of the $25\ \mu\text{m}$ -flux is lower than the absorption of the hard X-ray emission, mainly caused by a particular viewing geometry. Following calculated tracks in the parameter space according to the measured ratios and the X-ray absorbing column density (Risaliti et al., Figure 5), the values of NGC 6240 are indicative for an AGN/Starburst composite galaxy. This lack of nuclear activity is likely due to the presence of a large column density absorbing the direct emission from the AGN. Levenson et al. (2001) pointed out that the larger absorption of LIGs/ULIRGs in the X-rays (compared to the far-IR) is not only due to an absorbing torus, but also to an additional absorber, interpreted as the Starburst component in this class.

Franceschini et al. (2003) published *XMM-Newton* spectra of ten ULIRGs and reported about X-ray AGN and Starburst signatures and quantified the emission of both components. Plotting the luminosity ratio of the (0.5 – 10.0) keV-thermal to the hard power law component within (2.0 – 10.0) keV as a function of the total observed (0.5 – 10.0) keV-luminosity reveals a fairly well-defined region that is covered by ULIRGs, suggesting a dominant AGN activity (parameter range: $L_{(0.5-10.0)\ \text{keV}} \approx 10^{42-43}\ \text{erg s}^{-1}$ and $L_{\text{thermal}}/L_{\text{po}} \lesssim 0.2$). Contrarily, all Starburst-dominated sources possess rather low X-ray luminosities ($L_{(0.5-10.0)\ \text{keV}} \lesssim 10^{42}\ \text{erg s}^{-1}$) and $L_{\text{thermal}}/L_{\text{po}} \gtrsim 0.2$. The best-fitting model to the NGC 6240 data results in the luminosity ratio of the thermal to the power law component of $L_{\text{thermal}}/L_{\text{po}} = 0.19$ (with all luminosities corrected for Galactic and intrinsic absorption). Combined with its total (0.5 – 10.0) keV-luminosity, NGC 6240 is close to the region of AGN-dominated sources (Franceschini et al., Fig. 6a) and can be clearly separated from the Starburst-driven objects. The comparison between the power law- and the far-IR-luminosity reveals a correlation for Starburst-driven ULIRGs. This is largely enhanced for AGN-dominated sources (at similar L_{FIR} values), caused by the excess in their power law emission. The calculated luminosity ratios for NGC 6240 put this source at the high part of the AGN-dominated ULIRGs. The range of values show that the X-ray luminosity is only a small fraction of the bolometric luminosity, from $\lesssim 0.01$ per cent for ULIRGs with an enhanced star formation (for both emission components) to \simeq

0.01 – 0.1 per cent (power law component) and $\lesssim 0.01$ per cent (thermal component) for AGN–dominated ULIRGs. Both luminosity ratios indicate that NGC 6240 ($L_{\text{thermal}}/L_{\text{FIR}} \simeq 4 \cdot 10^{-3}$ and $L_{\text{po}}/L_{\text{FIR}} \simeq 2 \cdot 10^{-2}$) is located in the AGN–dominated region.

In many studies of LIGs/ULIRGs the flux of the [OIII] λ 5007 emission–line serves as an alternative method to determine whether a Sey-2-like galaxy contains an obscured X–ray source. Mulchaey et al. (1994) examined a sample of 116 Seyfert galaxies and discovered a relationship between the (reddened) [O III]– and the (absorption–corrected) hard X–ray flux in 30 objects. An interesting implication of this result is the possibility to *independently* estimate the X–ray luminosity of Seyfert 2 galaxies. A comparison to the observed X–ray luminosity can give an indication of the amount of obscuration. If the observed luminosity is substantially less than the predicted value, then a small fraction of the total X–ray luminosity reaches the line–of–sight. Given the extinction–corrected [O III]–luminosity (Table 4.4 on p. 96), the predicted (2.0 – 10.0) keV–luminosity is determined to $L_{\text{X}, ([\text{OIII}])} = 1.5 \cdot 10^{46} \text{ erg s}^{-1}$ (NGC 6240; Turner et al. 1997b). This is more than two orders–of–magnitude higher than the directly measured value (Table 4.4). For Mrk 1014, the extrapolated luminosity is $L_{\text{X}, ([\text{OIII}])} = 2.3 \cdot 10^{46} \text{ erg s}^{-1}$, exceeding the observed (absorption–corrected) luminosity by roughly the same factor. These values were calculated by averaging the luminosity ratios of the measured to the predicted hard X–ray luminosity for all sources in the Seyfert 2 sample of Turner et al. (1997b). The results confirm the evidence for a hidden AGN continuum in NGC 6240.

Following Bassani et al. (1999) the $L_{(2.0-10.0) \text{ keV}}/L_{[\text{OIII}]}$ –luminosity ratio can serve as an indicator of the column density N_{H} to a Compton–thick source, as shown empirically for a sample of Seyfert 2 galaxies. In combination with the equivalent width of the Fe–K α line (see subsection 4.3.3.1 on p. 117ff), the strong reciprocal correlation (with N_{H} as a free parameter) can separate Compton–thick Seyfert 2 galaxies from Seyfert 1 galaxies. While the hard X–ray flux is decreased, the absorbing material has no direct effect on the [O III] flux. In other words, an increasing N_{H} leads to a diminished hard X–ray/[O III]–flux ratio. For large column densities ($N_{\text{H}} \gtrsim 10^{24} \text{ atoms cm}^{-2}$; the Compton–thick regime) the continuum flux is reduced with respect to the Fe–K line emission (Bassani et al., Figure 1; Levenson et al. 2001, Figure 7 with added composite galaxies). The upper graph of Figure 4.5 shows the Fe–K luminosity in dependency on the [O III]–luminosity. For Seyfert galaxies, both quantities show a relation with a positive slope and a rather large scatter. The Fe–K α line as well as the [OIII] λ 5007 emission–line indicate the presence of a hidden AGN. In order to determine the contribution of an AGN to the energy budget of the hard X–ray emission, the observed luminosity ratios $\log[L_{(2.0-10.0) \text{ keV}}/L_{\text{FIR}}]$ and $\log[L_{(2.0-10.0) \text{ keV}}/L_{[\text{OIII}]}]$ are plotted against each other (Figure 4.5, lower graph) for a sample of ULIRGs from Ptak et al. (2003) and Compton–thin Seyfert 2 galaxies from Panessa and Bassani (2002). Since the former sample contains NGC 6240, the

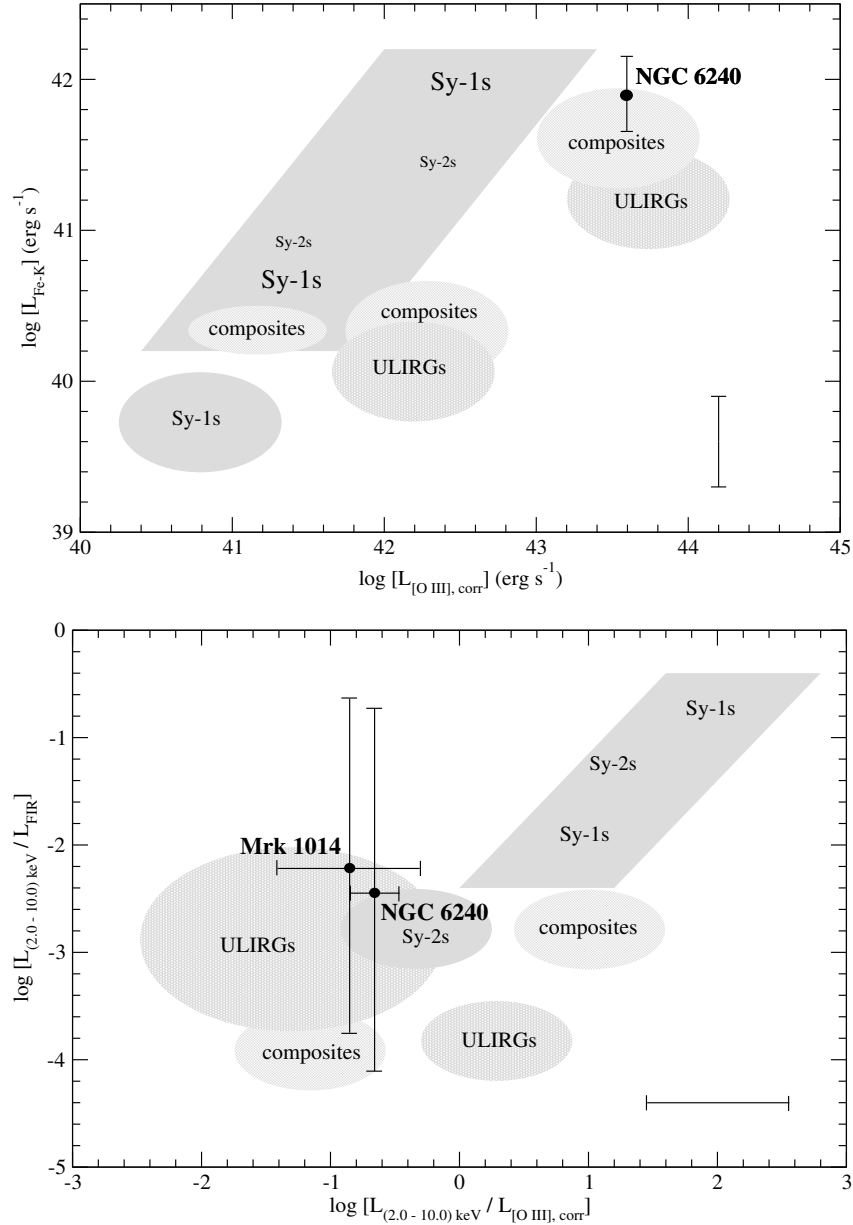


Figure 4.5: Luminosities and luminosity ratios of some observables for various classes of objects (adapted from Ptak et al. 2003). The error bar (lower right corner) represents a typical error estimate.

Upper plot: The Fe–K line luminosity $\log[L_{\text{Fe-K}}]$ as a function of the (extinction–corrected) [O III]–luminosity $L_{[\text{O III}], \text{corr}}$. The vertical solid line marks the error of the Fe–K measurement, whereas no error is given for the [O III]–luminosity.

Lower plot: The (observed) hard X–ray/FIR–luminosity ratio $\log[L_{(2.0-10.0) \text{ keV}}/L_{\text{FIR}}]$ as a function of the ratio $\log[L_{(2.0-10.0) \text{ keV}}/L_{[\text{O III}], \text{corr}}]$. The horizontal solid lines at NGC 6240 and Mrk 1014 show the error bars in the hard X–ray luminosity. The errors in the ordinate are comparably large and decrease the importance of the link between the luminosity ratio and the object classes. In the upper right corner Sy-1s and Compton–thin Sy-2s can be found.

values confirm the agreement between its *XMM-Newton* and *Chandra* data (as shown in Table 4.6 on p. 98 and stated on p. 100). In general, the ULIRGs overlap with the Compton–thick Seyfert 2 galaxies and with Starburst/Seyfert 2 composites. Mrk 1014 and NGC 6240 are at the upper part of the main ULIRG region, close to the Seyfert 2 galaxies. However, their positions are inaccurate due to the large errors of the ordinate of the graph, decreasing its importance of a classification. Compared to the former plot, ULIRGs can be easier localized and distinguished from the Seyfert 1 and (Compton–thin) Seyfert 2 galaxies.

The hard X–ray/far–IR–luminosity ratios of NGC 6240 and Mrk 1014 have intermediate values compared to other ULIRGs, and are similar to Starburst/Seyfert 2 composites. The Fe-K α line flux in NGC 6240 is brighter than in typical Seyfert galaxies, but comparable with the Starburst/Seyfert 2 composite galaxies. Scaled to the far–IR–luminosity, NGC 6240 and other ULIRGs have a luminosity ratio significantly smaller than the majority of the Seyfert galaxies and roughly one order–of–magnitude larger than the composite galaxies. Compared to other ULIRGs, NGC 6240 exhibits an extreme luminosity ratio. The scatter of the data points in the highlighted regions is rather large due to the low number of objects. This does not allow to make precise predictions of the AGN/Starburst emission rates.

It is of crucial importance for studying ULIRGs to estimate the X–ray flux contribution of Starburst activities to the total X–ray emission. The IR emission – mainly due to dust reprocessing of the radiation originating in stars – is associated with X–rays likely from emission from collisionally–ionized plasma.

According to a prescription of Turner et al. (1997a), the far–IR–luminosity (as given in Table 4.4 on p. 96) is used to compute the (Galactic) absorption–corrected (0.5 – 4.5) keV–luminosity following the correlation reported by David et al. (1992). The authors published a strong correlation between the far–IR– and the unabsorbed X–ray luminosities using *Einstein* data of a large sample of 71 normal and star forming galaxies. The best fitting relation is nearly linear

$$\log[L_{(0.5-4.5) \text{ keV}}] = (0.95^{+0.06}_{-0.05}) \cdot \log[L_{\text{far-IR}}] - (1.1^{+3.0}_{-2.6})$$

assuming a power law approximation, based on the maximum likelihood analysis (all luminosities in [erg s⁻¹]; see eq. (2) and the appendix of David et al.). Table 4.7 lists the predicted X–ray luminosities $\log[L_{(0.5-4.5) \text{ keV}}]_{\text{pred}}$ from Starbursts for Mrk 1014 and NGC 6240. The difference to the measured luminosity of each source helps to quantify the Starburst contribution to the total observed X–ray emission. This fraction is rather high for NGC 6240 (at least of the same order–of–magnitude as given by Turner et al.), and lower in case of Mrk 1014.

Table 4.7: Measured and predicted soft and hard X-ray luminosities from Starbursts applied to Mrk 1014 and NGC 6240 ^{a)}

Luminosity [erg s ⁻¹]	Mrk 1014 ^{b)}	NGC 6240	Reference ^{c)}
$\log[L_{(0.5-2.0) \text{ keV}}]_{\text{meas}}$	44.2 ± 1.1	42.8 ± 0.4	this thesis
$\log[L_{(2.0-10.0) \text{ keV}}]_{\text{meas}}$	44.1 ± 1.2	43.0 ± 0.4	this thesis
$\log[L_{(0.5-4.5) \text{ keV}}]_{\text{meas}}$	44.3 ± 1.1	42.7 ± 0.4	this thesis
$\log[L_{\text{FIR}}]$	46.3 ± 1.1	45.4 ± 1.7	I, II
$\log[L_{(0.5-2.0) \text{ keV}}]_{\text{pred}}$	42.7 ± 1.1	41.7 ± 1.7	III, eq. (8)
$\log[L_{(2.0-10.0) \text{ keV}}]_{\text{pred}}$	42.7 ± 1.1	41.7 ± 1.7	III, eq. (12)
$\log[L_{(0.5-4.5) \text{ keV}}]_{\text{pred}}$	43.0 ± 3.0	42.0 ± 3.1	IV, eq. (2)
$L_{\text{pred}}/L_{\text{meas}}^{\text{d)}$			
(0.5 – 2.0) keV	3.03	8.13	
(2.0 – 10.0) keV	4.78	5.50	
(0.5 – 4.5) keV	4.62	20.46	

a) Note: The values are corrected for Galactic absorption alone; the (2.0 – 10.0) keV–luminosity is *not* corrected for the measured intrinsic absorption in each source (as it was done in Table 4.5),

b) calculated as the luminosities from the single power law model,

c) References: I f_{60} and f_{100} from Kim and Sanders (1998), II f_{60} and f_{100} from Genzel et al. (1998), III Ranalli et al. (2003), IV David et al. (1992),

d) the percentage of the Starburst component to the luminosity of the host galaxy in the given bandpass.

Ranalli et al. (2003) published strong, linear correlations between the far-IR and X-ray emission using *ASCA* and *BeppoSAX* data of a well-defined sample of 17 nearby star forming galaxies. In agreement to David et al. the best fit relations are indicated in the soft (0.5 – 2.0) keV and extended to the hard bandpass (2.0 – 10.0) keV which is essentially not affected by the Galactic absorption. Computing the X-ray– from the far-IR–luminosities, the ratio $L_{\text{pred}}/L_{\text{meas}}$ is in good agreement with the value in the (0.5 – 4.5) keV regime of Mrk 1014. For NGC 6240, this estimation fails, *i.e.* it results in a too small ratio of only a few per cent. As Ranalli et al. pointed out, LLAGN like LINERs possess luminosity ratios in excess to star forming galaxies, making the hard X-ray/far-IR relation an inapplicable tool to predict the (2.0 – 10.0) keV–luminosity. This ratio underestimates the Starburst contribution compared with the hard X-ray flux (as can be seen in Table 4.7).

Franceschini et al. (2003) pointed out that the hot thermal plasma emission, indicative of a Starburst component, is not correlated with the far-IR-luminosity for ULIRGs. The mechanism to produce the observed plasma emission should depend not only on young and exploding stars forming a galactic wind, but also on other parameters, e.g. the density and the pressure of the adjacent ISM. Strickland and Stevens (2000) show that the soft X-rays cannot provide information about the gas responsible for the bulk of the energy output, its mass and its metal abundances, since this gas producing the soft emission via Starburst-driven galactic winds has a low filling factor (≤ 0.02) accounting only for a small mass (and energy) fraction of the wind ($\leq 10\%$). The number and complexity of the different parameters make it difficult to interpret the soft thermal emission as a reliable indicator of the SFR. This situation is valid for the *hard* X-ray emission of ULIRGs being dominated by an AGN, like in NGC 6240 and probably in Mrk 1014, as a strong correlation is missing (as shown in Figure 6 (d) of Franceschini et al. for a sample of four out of 10 sources). Starburst-dominated ULIRGs do show a correlation between the far-IR- and the power law-luminosity. For both types of ULIRGs the question arises, which fraction of the total hard X-ray emission is due to high-mass X-ray binaries ("HMXBs"). Although the HMXBs have never been modelled to the data and thus not seen in the spectra, their number is a good indicator for the current SFR in the X-ray- and the far-IR regime. A direct comparison of the SFR within both bandpasses reveals a coherence between the hard X-ray emission and the SFR in the ULIRGs. The number of HMXBs can be estimated by dividing the absorption-corrected (2.0 – 10.0) keV luminosity with the mean HMXB luminosity of $L_{(2.0-10.0) \text{ keV, HMXB}} = 5 \cdot 10^{37} \text{ erg s}^{-1}$ (e.g. White et al. 1983). In our Galaxy ~ 50 bright HMXBs (e.g. Iben et al. 1995) give a SFR of $\sim 3 M_{\odot} \text{ yr}^{-1}$ (e.g. Matteucci 2004). The HMXB number gives an estimation of the SFR in the X-rays,

$$\log[\text{SFR}_{\text{X-ray}} (M_{\odot} \text{ yr}^{-1})] \approx \log\left[\frac{L_{(2.0-10.0) \text{ keV, ULIRG}}}{L_{(2.0-10.0) \text{ keV, HMXB}}}\right] - 1.22 .$$

The $\text{SFR}_{\text{X-ray}}$ is $\log[\text{SFR}_{\text{X-ray}}] = 5.1 \pm 1.1$ for Mrk 1014 and $\log[\text{SFR}_{\text{X-ray}}] = 4.0 \pm 0.4$ for NGC 6240. Kennicutt (1998b) published a SFR estimation based on the far-IR-luminosity according to eq. (3),

$$\log[\text{SFR}_{\text{FIR}} (M_{\odot} \text{ yr}^{-1})] \approx \log[L_{\text{FIR}}] - 43.34 .$$

The values are $\log[\text{SFR}_{\text{FIR}}] = 3.1 \pm 1.1$ for Mrk 1014 and $\log[\text{SFR}_{\text{FIR}}] = 2.0 \pm 1.7$ for NGC 6240. The error in the SFR_{FIR} is correlated with the error in the far-IR-luminosity. Figure 4.6 displays both SFR quantities for a representative sample of 12 Starburst galaxies (taken from the literature; see Franceschini et al. 2003, subsection 6.1 for further details). The estimations based on the two bandpasses agree well between Starburst galaxies and ULIRGs in the

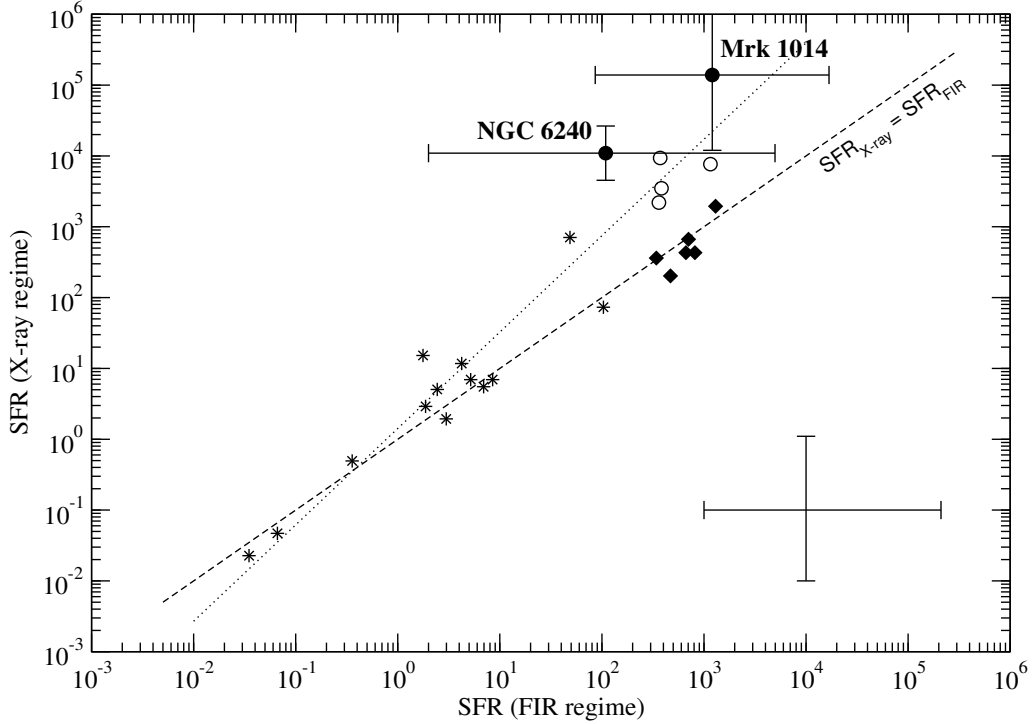


Figure 4.6: The SFR estimated from the hard X-ray emission versus the SFR calculated from the far-IR emission. Both values are calculated from the relations given in the text (incl. the SFR errors of Mrk 1014 and NGC 6240). The stars mark Starburst galaxies (found in the literature), the filled diamonds represent six Starburst-dominated ULIRGs from the Franceschini et al. sample, and the empty circles four AGN-dominated ULIRGs. Mrk 1014 and NGC 6240 are located very close to the locus of the latter sources, but significant above the dashed line $\text{SFR}_{\text{X-ray}} = \text{SFR}_{\text{FIR}}$. The dotted line is the regression line for the Starburst galaxies and the AGN-dominated ULIRGs, incl. Mrk 1014 and NGC 6240. (The plot is adapted from Franceschini et al. 2003).

sample of Franceschini et al., that show an enhanced Starburst activity. On the contrary, the $\text{SFR}_{\text{X-ray}}$ -values for the AGN-dominated ULIRGs are significantly above the values for the Starburst-ULIRGs for nearly the same range of SFR_{FIR} -values. Therefore, this consideration gives only a lower limit for the SFR in AGN-dominated ULIRGs. To make a quantitative statement about the discrepancy between the SFRs in both regimes the Starburst galaxies and the AGN-dominated ULIRGs together with the data points for Mrk 1014 and NGC 6240 have undergone a regression analysis, which results in a factor of ~ 1.4 for both sources exceeding the $\text{SFR}_{\text{X-ray}}$ from the 1-to-1 correlation. In the same sense that the Starburst-dominated AGN follow the $\text{SFR}_{\text{X-ray}} - L_{(2.0-10.0) \text{ keV}}$ -relation

$$\log [\text{SFR}_{\text{X-ray}} (\text{M}_{\odot} \text{ yr}^{-1})] \approx \log [L_{(2.0-10.0) \text{ keV}}] - 38.82,$$

(derived from the $L_{\text{FIR}} - L_{(2.0-10.0) \text{ keV}}$ -relation, with $L_{(2.0-10.0) \text{ keV}} \geq 10^{41} \text{ erg s}^{-1}$), a similar

approach can be made for AGN-dominated ULIRGs, resulting in the upper limit of

$$\log [\text{SFR}_{\text{X-ray}} (\text{M}_{\odot} \text{ yr}^{-1})] \leq 1.36 \cdot \log \left[400 \cdot \left(\frac{L_{(2.0-10.0) \text{ keV}}}{10^{44} \text{ erg s}^{-1}} \right) + 1 \right] + 2.53 ,$$

assuming that the power law-luminosity $L_{(2.0-10.0) \text{ keV}}$ of the AGN-ULIRGs is always above a certain limit, given by a linear approximation to the far-IR-luminosity as the independent variable.

Similar results are obtained by Ranalli et al. (2003), Grimm et al. (2003) and Gilfanov et al. (2004). They analyzed the contribution of low-mass X-ray binaries ("LMXBs") to the hard X-ray emission of low-luminous Starburst-ULIRGs and found a similar $\text{SFR}_{\text{X-ray}} - L_{(2.0-10.0) \text{ keV}}$ -relation. Since the stellar activity in these ULIRGs is very intense, visible through a rather large SFR-value of much more than $5 \text{ M}_{\odot} \text{ yr}^{-1}$, the main power for the hard X-ray flux originates from HMXBs. The LMXBs are playing a minor role in the energy budget of the Starburst-ULIRGs and a negligible role for AGN-dominated ULIRGs at high energies. In our Galaxy and in the Magellanic Clouds the typical HMXB-luminosity is found to be $L_{\text{HMXB}} \lesssim 10^{38-39} \text{ erg s}^{-1}$. Assuming that a large fraction of the hard X-ray component is due to HMXBs, it would require (up to) $10^3 - 10^4$ black hole candidates ("BHCs"), or correspondingly more luminous (and more massive) BHCs than normal BHCs. As they are modelled by a blackbody description, *i.e.* without any line emission, it would be impossible to explain the observed lines. However, Tanaka (1989) has shown that the spectra of BHCs are generally consistent with the measured hard continuum slope.

Franceschini et al. pointed out that in their sample at least four out of 10 ULIRGs show evidence for a buried AGN, based on the presence of a hard X-ray spectral slope and the emission of the Fe-K α line. These indications are superposed onto the thermal plasma emission, present in all ten sources.

4.3.2 The continuum slope

The continuum slope of the hard X-ray spectra in NGC 6240 and Mrk 1014 is remarkably flat. While previous studies point to the fact that the hardness of the continuum around the Fe-K line complex and the large EW of the 6.4 keV-line (cf. 4.3.3 on p. 117ff) favours a reflection model as the dominant emission mechanism (with or without an additional transmission component; see Table 4.8), this thesis indicates the presence of a hot thermal component at hard energies for NGC 6240, due to the ionized Fe-K emission lines.

Whereas Turner et al. (1997a) and Iwasawa & Comastri (1998) found no evidence for a transmission component, other authors state the presence of a highly obscured component, as it is indicated in Table 4.8.

Table 4.8: Diverse model approaches to the hard X–ray spectrum of NGC 6240 taken from the literature (based on data of various observations/satellites) ^{a)}

Reference	satellite	model	
		description	component
Turner et al. (1997a)	<i>ASCA</i>	unabsorbed power law, no transmission	power law
Iwasawa & Comastri (1998)	<i>ASCA</i>	cold reflection (from neutral material) no transmission component	power law
Vignati et al. (1999)	<i>BeppoSAX</i>	cold reflection + warm reflection, unabsorbed power law + transmission (highly absorbed)	PEXRAV power law power law
Ikebe et al. (2000)	<i>ASCA + RXTE</i>	cold reflection + transmission (highly absorbed)	PEXRAV power law
Komossa et al. (2003)	<i>Chandra</i>	intrinsically absorbed power law no transmission component	power law
Ptak et al. (2003)	<i>Chandra</i>	(highly absorbed) cold reflection + intrinsically scattered AGN emission no transmission component	PEXRAV power law
This thesis	<i>XMM-Newton</i>	hot thermal component + transmission (highly absorbed)	APEC power law

a) excluding the range of the Fe–K line complex, except for this thesis.

With this thesis, an alternative explanation for the hard X–ray continuum in NGC 6240 has been presented, using a collisionally–ionized plasma (APEC).

This has been worked out for the first time in this thesis, confirming the results from Boller, Keil, et al. (2003). Any model assumption using reflection would be in conflict with the *XMM-Newton* data.

While the presence of an AGN in NGC 6240 is evident, the origin of the remaining high–energy component is solved with this thesis and the paper (Boller et al. 2003). According to a study of Cappi et al. (1999) several classes of sources can account for the hard X–ray emission in pure Starburst galaxies, represented by NGC 253 and M 82, which opens the possibility to adopt this ideas for the hard X–ray emission of ULIRGs (after subtracting the AGN component). The detection of ionized Fe–K emission lines, as seen in the *XMM-Newton* data of NGC 6240, together with the observation of an extended high–energy gas (deduced from the *Chandra* data)

favours strongly the presence of a hot, (5 – 8) keV, thermal plasma responsible for the largest fraction of the total (thermal) hard X–ray emission, with $L_{(2.0-10.0) \text{ keV, thermal}} \simeq 6 \cdot 10^{42} \text{ erg s}^{-1}$ (Table 4.5 on p. 97).

A promising candidate explaining the direct thermal emission is the superwind scenario (cf. subsection 1.1.3 on p. 12) to account for the origin of the hard–energy component. In contrast to other ideas this model can explain *all* observational facts in a very natural way, and – what makes it even more attractive – it is independent from any tuning of spectral parameters. Moreover, the superwind–driven emission model is self–consistent concerning the energy balance of the various sources during a Starburst (e.g. SNe explosions, stellar winds, etc.). Assuming that the bulk of the hard X–ray emission is due to a superwind–driven hot, diffuse gas, then the spectral fit parameters (mainly the normalization of the hot thermal component) together with reasonable assumptions of spatial parameters can be directly related to interesting physical quantities. The best–fit model parameters allow to evaluate basic physical properties of the X–ray emitting gas like the temperature and the emission measure EM (see below). Table 4.9 on p. 114 summarizes the results for a number of different parameters. Since the spectral analysis reveals the presence of a hot gas only in NGC 6240 the calculated values in the table refer to the data of NGC 6240 alone. Nevertheless, the following should give an overview of the potential of computing various quantities from the hot thermal component in order to encourage the search for such a high–energy emission. To range and compare the results in the context of ULIRGs and pure Starburst galaxies, the table confronts the values of NGC 6240 to that of NGC 253.

Supposing the same spatial dependence for the electron and ion number densities, the estimated X–ray emitting volume of the gas is V_{gas} , which is typically less than the total volume of the X–ray emitting region V_{total} , parametrized by the filling factor $f := V_{\text{gas}}/V_{\text{total}} < 1$ as a measure for the “clumpiness” of the gas. The emission measure EM can be directly calculated from the fitting parameter of the hot plasma model,

$$\text{EM} = \frac{4\pi D^2}{10^{-14}} \cdot \text{Norm}_{\text{APEC}} \simeq 1.20 \cdot 10^{64} \cdot D_{\text{Mpc}}^2 \cdot \text{Norm}_{\text{APEC}} \text{ cm}^{-3},$$

where $D = D_A \cdot (1 + z)$ the source distance; $D = D_{\text{Mpc}} \cdot (1 \text{ Mpc/cm})$. Taking the EM definition with the simplification $\langle n_e n_H \rangle \approx \langle n_e \rangle \langle n_H \rangle \approx \langle n_e \rangle^2$, it can be written as

$$\text{EM} := \int n_e n_H dV \approx \langle n_e n_H \rangle \cdot V_{\text{gas}} \approx \langle n_e \rangle^2 \cdot f \cdot V_{\text{total}},$$

usable to calculate the mean density $\langle n_e \rangle$ of the gas to

$$\langle n_e \rangle \approx \sqrt{\frac{4\pi D^2}{10^{-14}} \cdot \frac{\text{Norm}_{\text{APEC}}}{f \cdot V_{\text{total}}}} \simeq 0.31 \cdot \sqrt{\frac{D_{\text{Mpc}}^2 \cdot \text{Norm}_{\text{APEC}}}{f \cdot R_{\text{kpc}}^3}} \text{ cm}^{-3},$$

where the X–ray emitting region is being modelled in a spherical geometry of radius $R = 3$ kpc, accounting for a volume of $V_{\text{total}} = 4\pi/3 \cdot (3 \text{ kpc})^3 = 4\pi/3 \cdot (3 R_{\text{kpc}})^3 (1 \text{ kpc}/\text{cm})^3$. This dimension corresponds on average to the extended X–ray emission in the (1.5 – 5.0) keV *Chandra* data of NGC 6240 (cf. Figure 3.4 on p. 51). The latter equation shows the sensitivity of the density estimation to the filling factor ($\propto f^{-1/2}$).

The mass of the X–ray emitting gas can be estimated from its density $\langle n_e \rangle$ in the volume V_{gas} , *i.e.*

$$\begin{aligned} M_{\text{gas}} &= m_{\text{H}} \int_{V_{\text{gas}}} \langle n_e \rangle dV_{\text{gas}} \approx m_{\text{p}} \langle n_e \rangle \cdot f \cdot V_{\text{total}} \\ &\simeq 3.23 \cdot 10^7 \sqrt{\text{Norm}_{\text{APEC}} \cdot D_{\text{Mpc}}^2 \cdot f \cdot R_{\text{kpc}}^3} M_{\odot}. \end{aligned}$$

The gas mass depends on the filling factor as $f^{1/2}$. In a similar way, the column density through the X–ray gas along the path length $\rho_{\text{gas}} \in [-R_{\text{kpc}}, R_{\text{kpc}}]$ is computed to

$$\begin{aligned} N_{\text{H, gas}} &= \int_{\rho_{\text{gas}}} \langle n_e \rangle d\rho_{\text{gas}} \approx \langle n_e \rangle \cdot f^{1/3} \cdot R_{\text{kpc}} \\ &\simeq 1.92 \cdot 10^{21} \cdot \sqrt{\frac{\text{Norm}_{\text{APEC}} \cdot D_{\text{Mpc}}^2}{f^{1/3} \cdot R_{\text{kpc}}}} \text{ atoms cm}^{-2}. \end{aligned}$$

Collisionless processes can be ignored, since Table 4.9 on p. 114 gives a conservative lower limit for the gas density of $\sim 10^{-2} \text{ cm}^{-3}$. Therefore, it is justified to describe the velocity distribution of the gas particles with a Maxwellian form. In this hydrostatic equilibrium the pressure P_{gas} and the thermal kinetic energy $E_{\text{thermal, kin}}$ of the gas can also be estimated. According to the equation of state, $P_{\text{gas}} = n_e kT_{\text{gas}}$, where kT_{gas} can be directly taken from the fitting results, the corresponding formula is

$$P_{\text{gas}} = \langle n_e \rangle kT_{\text{gas}} \simeq 5.00 \cdot 10^{-10} T_{\text{gas, keV}} \cdot \sqrt{\frac{\text{Norm}_{\text{APEC}} \cdot D_{\text{Mpc}}^2}{f \cdot R_{\text{kpc}}^3}} \text{ dyne cm}^{-2}$$

with $T_{\text{gas}} = T_{\text{gas, keV}} \cdot (1 \text{ keV}/k)$ and the thermal energy

$$\begin{aligned} E_{\text{thermal, kin}} &= \frac{3}{2} kT_{\text{gas}} \int_{V_{\text{gas}}} \langle n_e \rangle dV_{\text{gas}} \approx \frac{3}{2} kT_{\text{gas}} \cdot \langle n_e \rangle \cdot f \cdot V_{\text{total}} \\ &\simeq 9.22 \cdot 10^{55} T_{\text{gas, keV}} \cdot \sqrt{\text{Norm}_{\text{APEC}} \cdot D_{\text{Mpc}}^2 \cdot f \cdot R_{\text{kpc}}^3} \text{ erg}. \end{aligned}$$

The radiative cooling time τ_{cool} of the gas can be approximated from the equation in the subsection 1.3.1 on p. 25 assuming $L \approx E_{\text{thermal, kin}}/\tau_{\text{cool}}$ and $n_e \cdot n_{\text{ion}} \sim \langle n_e \rangle^2$, giving

$$\begin{aligned} \tau_{\text{cool}} &= \frac{3 kT_{\text{gas}}}{2 \Lambda \cdot n_e} \\ &\simeq 2.04 \cdot 10^7 T_{\text{gas, keV}} \cdot \sqrt{\frac{f \cdot R_{\text{kpc}}^3}{\text{Norm}_{\text{APEC}} \cdot D_{\text{Mpc}}^2}} \text{ yr}, \end{aligned}$$

Table 4.9: Derived physical parameters of the hot X–ray emitting gas in NGC 6240 averaged over an X–ray emitting volume of a sphere with radius $R = 3$ kpc and compared to the values for the Starburst galaxy NGC 253 ^{a)}.

Physical quantity		NGC 6240	NGC 253
distance D	[Mpc]	148	4.80
Norm _{APEC} ^{b)}	[10^{-3} cm^{-3}]	3.7 ± 1.3	4.50
Emission measure EM	[10^{63} cm^{-3}]	$1,000 \pm 300$	1.24
$\langle n_e \rangle \cdot f^{1/2}$	[10^{-1} cm^{-3}]	5.4 ± 0.9	0.19
$M_{\text{gas}} \cdot f^{-1/2}$	[$10^7 M_{\odot}$]	150 ± 30	5.40
$N_{\text{H, gas}} \cdot f^{1/6}$	[10^{20} cm^{-2}]	100 ± 20	3.58
kT_{gas}	[keV]	5.5 ± 1.5	5.8 ± 0.5
$P_{\text{gas}} \cdot f^{1/2}$	[$10^{-9} \text{ dyne cm}^{-2}$]	4.8 ± 0.8	0.18
$E_{\text{thermal, kin}} \cdot f^{-1/2}$	[10^{57} erg]	24 ± 4	0.89
$\tau_{\text{cool}} \cdot f^{-1/2}$ ^{c)}	[10^8 yr]	0.6 ± 0.1	18.9
v_{bulk} ^{d)}	[km s^{-1}]	1,000	1,050
$E_{\text{bulk, kin}} \cdot f^{-1/2}$	[10^{57} erg]	15 ± 3	0.59
$\dot{M}_{\text{bulk}} \cdot f^{1/2}$	[$M_{\odot} \text{ yr}^{-1}$]	600 ± 100	20

a) values are computed from the normalization Norm_{VAPEC} reported in Cappi et al. (1999),

b) the normalization of the hot APEC model follows the definition of N_{MEKAL} (see 3.2.3 on p. 56),

c) a more advanced formula is presented on the next page,

d) typical value of the bulk motion in Starburst galaxies and published value for NGC 253 (Cappi et al.).

where $\Lambda \approx 1.24 \cdot 10^{-23} \text{ erg cm}^3/\text{s}$ for a gas with $kT_{\text{gas}} = 5.5 \text{ keV}$ and normal abundances (and $\Lambda \approx 1.21 \cdot 10^{-23} \text{ erg cm}^3/\text{s}$ for $kT_{\text{gas}} = 5.75 \text{ keV}$; Emerson 1996).

Following Heckman et al. (1990), the outflow velocity of the hot gas is in the range of a few 1000 km s^{-1} for the superwind model. Is the gas moving with a bulk velocity v_{bulk} , the associated bulk kinetic energy $E_{\text{bulk, kin}}$ is

$$E_{\text{bulk, kin}} = \frac{1}{2} M_{\text{gas}} \cdot v_{\text{bulk}}^2 \simeq 3.21 \cdot 10^{56} v_{1000}^2 \cdot \sqrt{\text{Norm}_{\text{APEC}} \cdot D_{\text{Mpc}}^2 \cdot f \cdot R_{\text{kpc}}^3} \text{ erg},$$

with $v_{\text{bulk}} = v_{1000} \cdot (1000 \text{ km s}^{-1} / \text{cm s}^{-1})$. From the bulk velocity the mass outflow rate \dot{M}_{bulk} can be estimated to

$$\begin{aligned} \dot{M}_{\text{bulk}} &\sim 4\pi R_{\text{kpc}}^2 \cdot v_{\text{bulk}} \cdot \langle n_e, 3 \text{ kpc} \rangle \cdot m_{\text{H}} \\ &\simeq 36.67 v_{1000} \cdot \sqrt{\text{Norm}_{\text{APEC}} \cdot D_{\text{Mpc}}^2 \cdot R_{\text{kpc}} \cdot f^{-1}} M_{\odot} \text{ yr}^{-1}. \end{aligned}$$

In this expression $\langle n_{e,3 \text{ kpc}} \rangle$ gives the gas density at a radius of 3 kpc, calculated from a power law-like density profile to $\langle n_{e,3 \text{ kpc}} \rangle \approx \langle n_e \rangle / 2.7$. Note that many of the computed values listed in Table 4.9 represent upper limits, since their ranges are very sensitive to the spatial extend R_{kpc} .

Table 4.9 reveals that the X-ray column density of the gas is (at least) in the same order-of-magnitude as obtained from the spectral fitting (cf. Table 3.8 on p. 71). Concerning the gas pressure of a superwind in NGC 6240 and NGC 253, the values point to different conditions. Assuming Galactic values for various ISM phases, the gas pressure of the ambient ISM is typically below $P_{\text{gas, ISM}} \simeq 10^{-9} \text{ dyne/cm}^{-2}$ (e.g. Longair 1994), *i.e.* it is not sufficient to be in equilibrium with the gas pressure, causing clearly an outflow in NGC 6240 in the form of a superwind (likely originating in the overlapping superbubbles surrounding the galaxy's core). Given the uncertainties and the values being upper limits, it is plausible to presume the existence of an pressure equilibrium with the ambient ISM in the case of NGC 253. Moreover, the thermal energy $E_{\text{thermal, kin}}$ is a factor of 1.5 larger than the bulk energy $E_{\text{bulk, kin}}$ for NGC 253, and 1.6 for NGC 6240. Numerous SNe associated with an enhanced Starburst activity could heat the ISM to X-ray temperatures and play a major role in its energy budget. During a SN explosion, energy of the order of $\sim 10^{51}$ erg is being released, thus the ratio $E_{\text{thermal, kin}}/(10^{51} \text{ erg})$ is a rough estimate of the number of SNe. For NGC 6240, this number is $(2.4 \pm 0.4) \cdot 10^7$ and $8.9 \cdot 10^5$ for NGC 253. The radiative cooling time τ_{cool} of the gas is comparable to the lifetime of a Starburst, lasting in the order of 10^7 yrs (e.g. Satyapal et al. (1997), Engelbracht et al. 1998), with a slightly higher value for NGC 253. A more advanced formula – taken from the theory of X-ray emission from galaxy clusters (Sarazin 1988, eq. 5.23) – makes use of the thermal bremsstrahlung as the main emission mechanism. In dependence on the gas density $\langle n_e \rangle$ and the temperature $T_{\text{gas, keV}}$, τ_{cool} is

$$\tau_{\text{cool}} \approx 2.90 \cdot 10^7 \langle n_e \rangle^{-1} \cdot T_{\text{gas, keV}}^{1/2} \text{ yr}.$$

This relation leads to a gas lifetime of $\tau_{\text{cool}} = (1.3 \pm 0.2) \cdot 10^8$ yr for NGC 6240 and $3.7 \cdot 10^9$ yr in the case of NGC 253, slightly higher than the previous results, but at least roughly one order-of-magnitude larger than the Starburst lifetime. It seems that the X-ray emission exceeds the enhanced Starburst activity for heating the gas. However, SNe can produce some of the X-ray emission in a steady fashion, requiring a rate of $\sim L_{\text{X-ray}}/(10^{51} \text{ erg})$ events. For NGC 253, the measured luminosity $L_{(0.2-10.0) \text{ keV}} = 1.2 \cdot 10^{39} \text{ erg s}^{-1}$ (Pietsch et al. 2001) yields to an estimated SNe rate of $\sim 3.8 \cdot 10^{-4} \text{ yr}^{-1}$. The same authors assumed a SNe rate of 0.2 yr^{-1} within the nuclear Starburst to explain the ionized Fe-K line intensity, determined from the *XMM-Newton* data of NGC 253. Only a few per cent of the released SN energy in a Starburst would go into the heating of the X-ray gas to match both quantities. Taking the

luminosity $L_{(0.5-10.0)\text{ keV}} \approx 10^{43} \text{ erg s}^{-1}$ of NGC 6240, the rate is 0.3 SNe per year, of the same order as observed in pure Starburst galaxies like M 82.

The fraction of the X-ray emission due to direct emission of a SN-driven superwind can be estimated, *without* any geometrical assumptions. According to Suchkov et al. (1996) type-II-SNe dominate the ISM heating with an ejected mass of $10 M_{\odot}$ in connection with the kinetic energy of 10^{51} erg . The total energy release of a SN is the sum of the thermal energy $E_{\text{thermal, kin}}$ and the bulk energy $E_{\text{bulk, kin}}$

$$E_{\text{SN}} = \frac{3}{2} \langle n_e \rangle \cdot kT_{\text{gas}} \cdot V_{\text{total}} + \frac{1}{2} m_{\text{H}} \cdot \langle n_e \rangle \cdot v_{\text{bulk}}^2 \cdot V_{\text{total}},$$

and thus the fraction of the X-ray emitting gas from SN ejecta is the ratio of the SNe ejecta mass $M_{\text{SN ejecta mass}}$ to the total mass M_{total} of the hot gas,

$$\begin{aligned} \frac{M_{\text{SN ejecta mass}}}{M_{\text{total}}} &\sim \frac{E_{\text{SN}}}{10^{51}} \cdot \frac{M_{10}}{m_{\text{H}} \cdot \langle n_e \rangle \cdot V_{\text{total}}} \\ &= \frac{(\frac{3}{2} kT_{\text{gas}} + \frac{1}{2} m_{\text{H}} \cdot v_{\text{bulk}}^2)}{10^{51}} \cdot \frac{M_{10}}{m_{\text{H}}} \\ &= (2.86 \cdot 10^{-2} T_{\text{gas, keV}} + 9.95 \cdot 10^{-2} v_{1000}^2) \cdot M_{10}, \end{aligned}$$

with $M = M_{10} \cdot 10 M_{\odot}$ as the ejected mass from a standard SN, and m_{H} the atomic mass of a hydrogen atom. Using typical values of $M_{10} \sim 1$ and $v_{1000} \sim 1$, this ratio is roughly 0.26 for a plasma temperature of 5.5 keV. About 74 per cent of the gas expelled by the galaxy have to come from the "concentrated" ambient gas of the ISM collected by a superwind. Multiplying the mass outflow rate \dot{M}_{bulk} by the lifetime estimate of a Starburst the ejected mass would be $M_{\text{SB ejecta mass}} = (6 \pm 1) \cdot 10^9 M_{\odot}$ for NGC 6240 and $2 \cdot 10^8 M_{\odot}$ for NGC 253. For NGC 253, this is of the same order, but significantly larger for NGC 6240. To check for the self-consistency of the SNe-driven superwind model an assumed rate of 0.1 SNe/yr within a duration of 10^7 yr gives a total thermal energy output of $E_{\text{thermal SNe}} \sim 10^{57} \text{ erg}$. A comparison with the thermal (kinetic) energy within the superwind scenario shows that the emission from SNe dominates the total energy present in the superwind, at least in the case of NGC 253. The thermal energy loss $\dot{E}_{\text{thermal loss}}$ associated with the outflow rate points to a slight inconsistency of this scenario. With

$$\dot{E}_{\text{thermal loss}} \sim kT_{\text{gas}} \cdot \frac{\dot{M}_{\text{bulk}}}{m_{\text{H}}} \simeq 6.99 \cdot 10^{49} v_{1000} \cdot \sqrt{\frac{\text{Norm}_{\text{APEC}} \cdot D_{\text{Mpc}}^2 \cdot R_{\text{kpc}}}{f^2}} \text{ erg/yr},$$

this loss is $(1.1 \pm 0.2) \cdot 10^{51} \cdot f^{-1} \text{ erg/yr}$ (NGC 6240) and $4.09 \cdot 10^{49} \cdot f^{-1} \text{ erg/yr}$ (NGC 253), respectively. In order to refill this loss, the SNe typically produce $\sim 10^{50} \text{ erg/yr}$, sufficient for NGC 253, but an order-of-magnitude too low for NGC 6240. Basically, three different

models may explain this inconsistency. Firstly, intense winds from stars on the main sequence combined with the intense UV emission of young stars and/or a higher SNe rate; secondly, a rather small filling factor $f \lesssim 0.1$; thirdly, the gas could be gravitationally bound in the galaxy by e.g. an unusual high interstellar pressure.

4.3.3 Fe–K line diagnostics

One of the striking features in the X–ray spectra is the Fe–K emission. Its strength can serve as a diagnostic tool for the presence of obscuring material. In the cases of a direct view of the X–ray continuum from an AGN, theoretical considerations predict EWs of the Fe–K α line of the order of a few hundred eV (see below), expected from Compton–thin sources and common in Seyfert 1 galaxies. NGC 6240 is one prominent example for a highly absorbed and Compton–thick object, whereas the neutral Fe 6.4 keV–line is generally not detected in Starburst galaxies (e.g. Ptak et al. 1997, Persic et al. 1998, Pietsch et al. 2001), thus providing a clear relation to the presence of an AGN in the source.

4.3.3.1 Equivalent widths

The amount of absorbing material can be determined by one of the following three parameters, the cut–off in photoelectric absorption, the luminosity ratio $L_{(2.0-10.0) \text{ keV}}/L_{[\text{OIII}]_{\text{corr}}}$ (see 4.3.1 on p. 104), and the EW of the Fe–K emission line, respectively.

Table 4.10 contains the centroid energy and the line width together with the EW of the neutral Fe–K α line. In addition, the equivalent widths of the whole Fe–K line complex from other observations/satellites have been listed, where it could not be resolved. The EW of the narrow 6.4 keV–line taken from this thesis (Table 3.8 on p. 71) is in good agreement with the values found with *ASCA*, and provides a better constrain on its value. Concerning the recent *Chandra* data the measurement of the Fe–K line complex has been performed by using a plasma model plus an absorbed power law and a Gaussian line (Ptak et al. 2003), and a single power law plus two Gaussian lines (Komossa et al. 2003), respectively. Whereas no EW was presented from the latter model, the former approach covers the whole Fe–K complex emission. The authors reported a large $\text{EW} = (2.4_{-0.7}^{+0.8}) \text{ keV}$. However, this upper limit should be considered as not very restrictive, since hot gas producing the 6.7 keV–Fe–K α line contributes to the EW of the Fe–K line complex in a non–negligible way, dependent on the temperature and the abundances in the gas.

Turner et al. (1997a) plotted the measured EW of the Fe–K α line as a function of the intrinsic absorbing column density $N_{\text{H, int}}$ for a sample of 18 Seyfert 2 galaxies, including NGC 6240. Compared to the pure Sy-2s NGC 6240 has an EW of the 6.4 keV–Fe–K α line, comparable

Table 4.10: X-ray parameters of the lines in the Fe–K complex of NGC 6240 distinguished between the neutral Fe–K α line and the line complex as a whole, taken from the literature (based on data of various observations/satellites) ^{a)}

Reference	satellite	line energy E_C	line width σ	EW
		[keV]	[keV]	[eV]
Turner et al. (1997a) ^{b)}	<i>ASCA</i>	6.4 (fixed)	0 (fixed)	710^{+660}_{-400}
Ikebe et al. (2000) ^{c)}	<i>ASCA + RXTE</i>	$6.44^{+0.04}_{-0.05}$	0 (fixed)	~ 950
Komossa et al. (2003)	<i>Chandra</i>	6.42 ± 0.03	–	–
This thesis	<i>XMM-Newton</i>	6.41 ± 0.01	0 (fixed)	600 ± 200
Turner et al. (1997a) ^{b)}	<i>ASCA</i>	$6.4^{+0.5}_{-0.2}$	0.2 ± 0.2	$600^{+6,000}_{-400}$
Iwasawa & Comastri (1998)	<i>ASCA</i>	6.44 ± 0.04	0.11 ± 0.05	$1,600 \pm 400$
– ” –	<i>ASCA</i>	6.57 ± 0.07	0.25 ± 0.10	$2,200 \pm 500$
Vignati et al. (1999)	<i>BeppoSAX</i>	6.4 (fixed)	–	$\sim 1,800$ ^{d)}
Ptak et al. (2003)	<i>Chandra</i>	6.5 ± 0.1	$0.20^{+0.16}_{-0.10}$	$2,400^{+800}_{-700}$

a) the ”–” sign symbolizes a missing value,

b) derived from the partial covering model,

c) the numbers are based on the favoured reflected– and transmitted AGN model,

d) *i.e.* the sum of the EWs of the ionized lines to the whole Fe–K line complex.

with sources (in particular NGC 1068) that are thought to be dominated by reprocessed X-rays. However, Figure 4.7 shows that the amount of absorbing matter along the line-of-sight towards NGC 6240 is by far much higher than that of the other sources. The graphic shows the results of Monte–Carlo simulations performed by Leahy & Creighton (1993) and Ghisellini et al. (1994) on calculations of EWs as a function of the X-ray intervening column density N_H . Since these simulations require an assumption of the geometrical structure of the material, the plot can help to provide possible geometries (e.g. Inoue 1985). While Leahy & Creighton prefer a spherical geometry in form of a uniform shell of material, surrounding the central source (with a continuum power law slope $\Gamma = 1.0$), Ghisellini et al. favour a toroidal structure and $\Gamma = 1.9$. Both models assume a fluorescence yield of $Y_{26}^K \approx 0.3$ (see 1.2.2 on p. 17), but differ in the absolute Fe abundances and in the threshold cross sections for the Fe–K edge. Figure 4.7 reveals differences between both models for very large column densities, exceeding $N_H \approx 2 \cdot 10^{24}$ atoms cm^{-2} and for low densities, $N_H \approx 3 \cdot 10^{23}$ atoms cm^{-2} . In the former

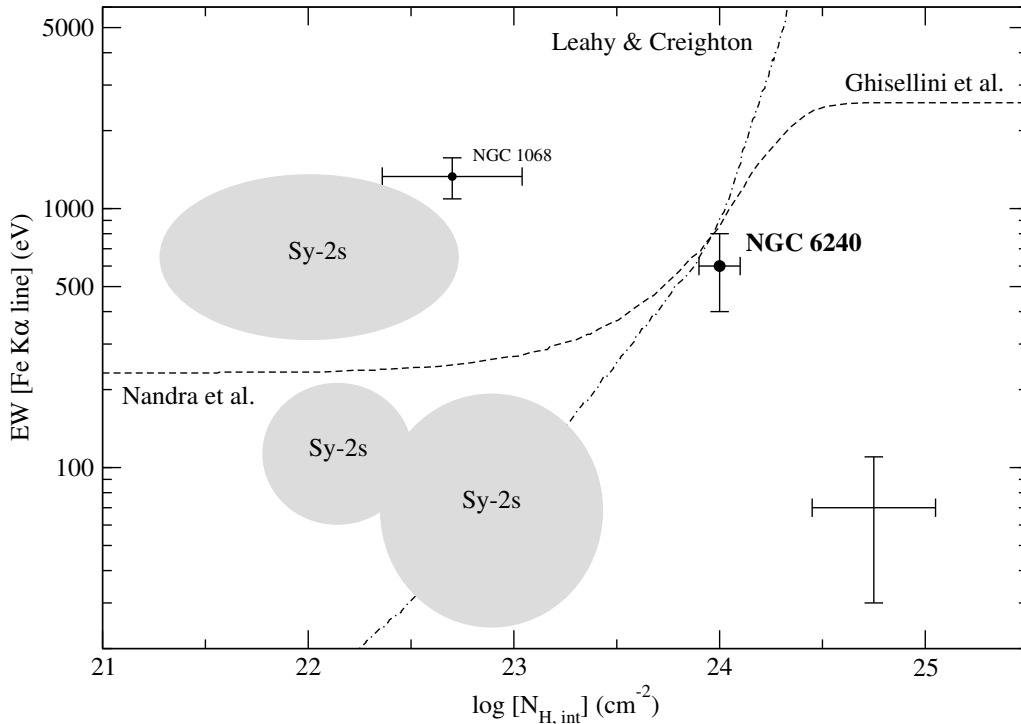


Figure 4.7: The EW of the 6.4 keV–Fe–K α line in dependence on the (intrinsic) column density N_{H} of the X–ray intervening gas along the line–of–sight according to the results of Turner et al. (1997a). Their sources are located and displayed in the highlighted regions, with an emphasize on NGC 1068 and on own measurements for NGC 6240 (note the error bars in the lower right corner which represent the derived uncertainties). The lines mark various geometrical configurations (assuming an isotropically emitting central source) based on Monte–Carlo simulations. Leahy & Creighton (1993) propose a spherical, shell–like geometry of the absorbing material, whereas Ghisellini et al. (1994) prefer a toroidal geometry. For moderate densities, $10^{23} \lesssim N_{\text{H}} \lesssim 10^{24}$ atoms cm^{-2} , the calculations agree well with theoretical predictions by Krolik and Kallman (1987). Nandra et al. (1997a) determine a mean EW in Seyfert 1 galaxies of (230 ± 60) eV, hence giving a reference value for sources with a small amount of obscuring material in a toroidal structure. (See the text for further details.)

case, the EW prediction from the Leahy model diverges, while the EWs in the Ghisellini model remain nearly constant in the range of several keV, assuming the presence of reflected line- and continuum emission.

The localization of NGC 6240 in Figure 4.7 suggests that both the spherical and the toroidal model can explain the measured EW value, since they coincide at a column density of $N_{\text{H}} \approx 10^{24}$ atoms cm^{-2} . According to Leahy & Creighton the strength of the Fe–K α line–EW originates in a uniform shell of neutral material with solar abundances subtending a 4π solid angle around the central source. The measured column density is higher than the mean column density of the sources in the sample of Turner et al. (1997a). The continuum flux at 6.4 keV is reduced

and therefore the EW of the Fe-K α line is enhanced (compared to the sources in the lower left corner of the plot). The reflection-oriented Ghisellini et al. model assumes that only the power law emission of the source is absorbed without any change in the reflection emission. At the position of NGC 6240 this model predicts a dominant role of the reflection component, since the direct continuum emission at high energies is heavily suppressed. This thesis shows that the idea of a reflection component in the X-ray spectrum of NGC 6240 – as proposed by several research groups – can be dismissed in support of a collisionally-ionized plasma accounting for most of the continuum radiation and the ionized Fe-K emission lines. In the mid-1980's Inoue (1985) and Makishima (1986) published results of Monte-Carlo simulations on the fluorescent Fe-K line emission in order to relate the measured EW to geometrical requirements of the line emitting material. They studied the effects of geometrical configurations on the EW of the Fe-K α line based on decomposed calculations for the Thomson-scattered continuum and the line emission. Both components on their part depend on the geometry of the system. Makishima used available X-ray data of a few AGN to estimate the EW of the 6.4 keV-Fe-K α line for various configurations of the source. The measured EW of NGC 6240 can be related to a model, in which the (uniformly distributed) material causes heavy absorption along the line-of-sight in combination with fluorescence processes.

Applying the simplistic case $E_{c, \text{line}} \gg \text{EW}$ (certainly true for a centroid line energy of $E_{c, \text{line}} = (6.4 - 6.9)$ keV and $\text{EW} \lesssim 1$ keV), the EW can be well approximated by the ratio of the line intensity I_{line} to the continuum emission $L(E)$ at energy E , hence $\text{EW}_{\text{line}} \sim I_{\text{line}}/L(E)$. Consider an *optically-thin* gas along the line-of-sight that produces the Fe-K photons when illuminated by a power law continuum $L(E) = L_0(E/E_{K_0})^{-\alpha}$; $[L] = \text{erg s}^{-1} \text{keV}^{-1}$ and $\Gamma = \alpha + 1$. The Fe-K line emission originates in fluorescence processes with an intensity of

$$I_{\text{Fe-K line}} = \frac{E_{c, \text{line}}}{3 + \alpha} \cdot \langle Y \rangle \cdot \frac{\Delta\Omega}{4\pi} \cdot L_0 \cdot \langle \tau_{K_0} \rangle$$

(in erg s^{-1} ; Krolik & Kallman 1987, eq. 3), where $\langle Y \rangle := \sum_i X_i Y_i$ is the mean Fe fluorescence yield in the gas (X_i is the relative abundance of the i^{th} ionization state) and $\langle \tau_{K_0} \rangle$ is the mean optical depth at the Fe edge, averaged over the ionization state and the solid angle $\Delta\Omega$. Along the line-of-sight the EW of a line in transmission is

$$\text{EW}_{\text{trans, line}} = \frac{E_{c, \text{line}}}{3 + \alpha} \cdot \langle Y \rangle \cdot \frac{\Delta\Omega}{4\pi} \cdot \left(\frac{E_0}{E_{K_0}} \right)^\alpha \cdot \langle \tau_{K_0} \rangle$$

For the neutral Fe-K α line ($E_{c, \text{line}} = 6.4$ keV, $E_{K_0} = 7.1$ keV, $\langle Y \rangle \approx 0.3$ and assuming $\alpha \approx 0.8$ and $\Delta\Omega \approx 1$), $\text{EW}_{\text{trans, Fe-K}\alpha \text{ line}} \approx 470 \cdot N_{\text{H}} / (10^{24} \text{ atoms cm}^{-2})$ eV. Given the NGC 6240 column density of $N_{\text{H}} = (1 \pm 0.2) \cdot 10^{24} \text{ atoms cm}^{-2}$, the predicted EW from transmitted emission is $\text{EW}_{\text{trans, Fe-K}\alpha \text{ line}} \approx (500 \pm 50)$ eV. This value is in good agreement with the measured Fe-K α line-EW in NGC 6240.

4.3.3.2 Ionized iron

The analysis of the hard X-ray spectrum from NGC 6240 reveals clearly that a fraction of the total emission of the Fe–K line complex can be attributed to ionized Fe, *i.e.* He– and H–like. A first idea to explain their presence is reflection from an ionized accretion disk (Terashima et al. 1998). However, the disk is obscured by large amounts of material, thus it is not attainable for investigations.

A more convincing interpretation of the ionized Fe–K line emission is the presence of an optically–thin hot plasma, in which the Fe atoms are collisionally excited. In the energy range (6–7) keV the thermal plasma produces the significant Fe–K line emission, but the absorbed power law emission contributes only to the total continuum. This results in a reduced observed EW value compared to the expected value from plasma theory. A 5.5 keV–plasma is able to generate an Fe–K emission line with an $EW \approx 650$ eV (Fe XXV), and $EW \approx 250$ eV (Fe XXVI) assuming solar abundances (Rothenflug & Arnaud 1985; cf. Inoue 1985 for the 6.7 keV–line). Naming $I_{\text{thermal, line}}$ and $F_{\text{thermal, cont}}$ the thermal line and continuum intensity, and $F_{\text{po, cont}}$ the power law continuum intensity, respectively, the measured EW is given by

$$EW_{\text{meas}} = \frac{I_{\text{thermal, line}}}{F_{\text{thermal, cont}} + F_{\text{po, cont}}} = \frac{EW_{\text{thermal, line}}}{1 + F_{\text{po, cont}}/F_{\text{thermal, cont}}},$$

where $EW_{\text{thermal, line}}$ is the thermal line EW (determined relative to the thermal continuum) that can be written as $EW_{\text{thermal, line}} = I_{\text{thermal, line}}/F_{\text{thermal, cont}} \approx 650$ eV $\cdot [\text{Fe}/\text{H}]/[\text{Fe}/\text{H}]_{\odot}$ (Fe XXV) and $EW_{\text{thermal, line}} \approx 250$ eV $\cdot [\text{Fe}/\text{H}]/[\text{Fe}/\text{H}]_{\odot}$ (Fe XXVI). By measuring the continuum fluxes the intensity ratio is determined to $F_{\text{po, cont}}/F_{\text{thermal, cont}} \approx 0.5$, and ≈ 1.63 , respectively. The corresponding measured EW would be $EW_{\text{meas}} \approx 430$ eV for Fe XXV, and $EW_{\text{meas}} \approx 100$ eV in the case of Fe XXVI. Since both values are within the 1σ error level of the observed EWs (see Table 3.8 on p. 71), a thermal origin for the ionized Fe–K lines in combination with some power law contribution can give a plausible explanation.

A second idea is to relate the line emission to the fluorescence emission from a photoionized plasma that is illuminated by the X-ray radiation of the source (Inoue 1985). The atomic physics to understand the fluorescence process in an Fe ion is slightly different from that for neutral Fe (see paragraph 1.2.2 on p. 17ff). After a photoionization in the K-shell the recombination of a free electron takes place in a level higher than the ground state, followed by cascades to the ground state and accompanied by the fluorescent line emission. The corresponding probability to generate the line emission can be estimated from the recombination probability in the states higher than the ground state. For the He–like Fe–K line this probability is about 82 per cent. In analogy to the case of the neutral Fe–K α line this consideration has been investigated by Monte–Carlo simulations in order to calculate EWs of the 6.7 keV–line as a function of the obscuring matter thickness for various geometries. The results show a similar behaviour

of the expected EW to the absorbing material compared to the findings for the 6.4 keV–line, whereas the EW values for a massive line–of–sight absorption and an entirely blocking material are closer to each other than for the neutral Fe line (for $N_{\text{H}} \gtrsim 2 \cdot 10^{23}$ atoms cm^{-2}). This results from the influence of self–absorption processes that are reduced in ionized atoms, since other abundant and lighter elements are fully ionized and therefore, the EW values are higher than in the case of neutral Fe. On the other hand, the estimates of the 6.7 keV–EWs are significantly lower than the EWs of the 6.4 keV–line for a given geometrical case. The expected EW of the 6.7 keV–line is roughly (500 – 650) eV when assuming a spherically distributed gas with a column density of $N_{\text{H}} \approx 10^{24}$ atoms cm^{-2} (Inoue 1985, Figure 13). This is in accordance with the measured Fe XXV–EW from the NGC 6240 spectrum under the assumption of a full–angle coverage of the central source with an X–ray illuminating plasma.

4.4 The soft components

While the analysis of the hard X–ray emission meets the expectation to find a (highly–absorbed) AGN in NGC 6240, investigating the soft X–ray spectrum reveals that hot collisionally–ionized gas with one or more low keV–temperature components can explain the continuum emission in LIGs/ULIRGs. Against this background, they show a great similarity to pure Starburst galaxies (e.g. Lira et al. 2002; Martin et al. 2002; Strickland et al. 2002).

4.4.1 X–ray to IR flux ratios

The observed luminosity ratio $L_{(2.0-10.0) \text{ keV}}/L_{\text{FIR}}$ is greater than 0.01 for Seyfert galaxies (without any contribution from Starburst activities), but this ratio seems to be much lower for Starburst galaxies and LIGs/ULIRGs (Levenson et al. 2001, Ptak et al. 2003; cf. Figure 4.4 on p. 102 and Figure 4.5 on p. 105). In continuation of the discussion about the X–ray luminosities given in subsection 4.3.1 on p. 95ff, this subsection throws light on the implications of the measured luminosity values in the soft X–ray regime. Analogous to the measured hard X–ray luminosity ratios, the observed $L_{(0.5-2.0) \text{ keV}}/L_{\text{FIR}}$ values are $6.6 \cdot 10^{-3}$ for Mrk 1014 (roughly 1.5 times higher than the corresponding value for hard X–rays) and $2.5 \cdot 10^{-3}$ for NGC 6240 (~ 1.5 times smaller), however, comparable with each other and with the values from the hard bandpass. Considering only the thermal contribution from the collisionally–ionized plasmas, this ratio is $L_{(0.5-2.0) \text{ keV}}/L_{\text{FIR}} = 4.2 \cdot 10^{-3}$ for NGC 6240, almost in perfect accordance with the hard X–ray value. In the case of Mrk 1014 the soft X–ray luminosity of the power law model results in a ratio of $5.3 \cdot 10^{-4}$, eight per cent of the total soft value, and roughly one order–of–magnitude smaller than the hard X–ray value. In comparison with the

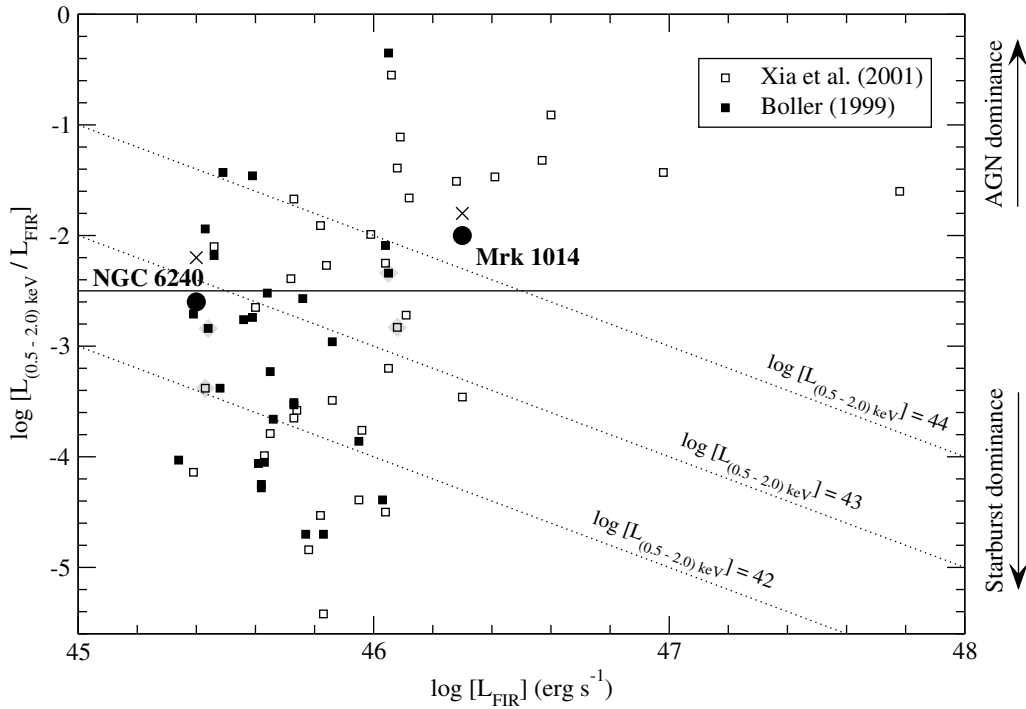


Figure 4.8: The observed luminosity ratio $L_{(0.5-2.0) \text{ keV}}/L_{\text{FIR}}$ versus the far-IR-luminosity L_{FIR} for NGC 6240 and Mrk 1014 (filled circles), compared to a sample of *ROSAT*-detected ULIRGs from Xia et al. (2001) (open squares) and 22 ULIRGs from the RASS-BSC and six ULIRGs from *ROSAT* pointed observations analysed by Boller (1999; filled squares). 20 sources are included in both samples. The solid line indicates that ULIRGs with $\log[L_{(0.5-2.0) \text{ keV}}/L_{\text{FIR}}] < -2.5$ are supposed to be related to an enhanced Starburst activity (Boller and Bertoldi 1996). NGC 6240, Mrk 1014 and other ULIRGs, lying close to this line, seem to possess AGN and Starburst contributions to a comparable fraction. Although the region of an AGN dominance is shown, *ROSAT* was not able to detect the AGN in NGC 6240. The grey diamonds represent the locations of NGC 6240 and Mrk 1014 in the samples of Xia et al. and Boller. In addition, the $L_{(0.3-10.0) \text{ keV}}/L_{\text{FIR}}$ ratio from the *XMM-Newton* data for both objects have been included (marked with crosses). One can see a shift in their locations to larger ratios. (For illustrating purposes the error bars are not shown.)

empirically determined luminosity ratio of a local sample of Starburst galaxies analysed by Ranalli et al. (2003), these values are significantly higher than the Starburst average. Pure Starburst galaxies as M 82 and NGC 253 are along a relation with $L_{(0.5-2.0) \text{ keV}}/L_{\text{FIR}} \approx 2 \cdot 10^{-4}$. This difference may be caused by an overestimation of the inferred X-ray emission due to Starburst activities, since the far-IR emission from the torus(-like geometry) could account for a considerable fraction of the total far-IR-luminosity.

Figure 4.8 displays the observed luminosity ratio $L_{(0.5-2.0) \text{ keV}}/L_{\text{FIR}}$ against the far-IR-luminosity L_{FIR} of a *ROSAT*-selected sample of 35 ULIRGs (Xia et al. 2001; cf. subsection 1.1.3 on p. 11). This ratio spreads over a wide range of measured values, spanning over more

than four orders-of-magnitude. It was calculated from the published (0.1 – 2.4) keV luminosity under the assumption of a power law slope with $\Gamma \neq 2$ (as given in Xia et al.) according to

$$\log [L_{(0.5-2.0) \text{ keV}}] = \log [L_{(0.1-2.4) \text{ keV}}] + \log \left[\frac{E_2^{2-\Gamma} - E_1^{2-\Gamma}}{E_{\text{ref,u}}^{2-\Gamma} - E_{\text{ref,d}}^{2-\Gamma}} \right],$$

where all energies are given in keV and $E_1 = 0.5 \text{ keV}$, $E_2 = 2.0 \text{ keV}$, $E_{\text{ref,d}} = 0.1 \text{ keV}$ and $E_{\text{ref,u}} = 2.4 \text{ keV}$. In the case of $\Gamma = 2$, the relation

$$\begin{aligned} \log [L_{(0.5-2.0) \text{ keV}}] &= \log [L_{(0.1-2.4) \text{ keV}}] + \log \left[\frac{\ln(E_2/E_1)}{\ln(E_{\text{ref,u}}/E_{\text{ref,d}})} \right] \\ &= \log [L_{(0.1-2.4) \text{ keV}}] - 0.36, \end{aligned}$$

has been used. Where available, the (0.1 – 2.4) keV luminosities were taken from the pointed observations due to a better photon statistics. As a comparison, Boller (1999) published the soft X-ray properties of a sample of 28 ULIRGs observed within the RASS and the *ROSAT* pointings out of a database of 323 ULIRGs. 20 sources are detected and analyzed in both studies and their luminosities agree well with each other within the given 1σ uncertainties. For the remaining 15 sources in the sample of Xia et al. and eight sources from Boller the soft X-ray luminosity was computed with the presented power law slope and assumed to $\Gamma = 2.3$, respectively, where no Γ value has been published, being the typical value for extragalactic objects when observed with *ROSAT*. Both samples contain NGC 6240 and Mrk 1014 (grey diamonds in Figure 4.8). Theoretical considerations based on population synthesis models for Starburst galaxies assuming a time-averaged SFR indicate that the luminosity ratio is roughly given by $\sim 10^{-2.5}$ in the soft X-ray bandpass (Boller and Bertoldi 1996). Values above this threshold should represent sources with a dominant accretion mechanism, hence if they have $L_{(0.5-2.0) \text{ keV}}/L_{\text{FIR}} \gtrsim 10^{-2}$, their energy output appears to be powered by an AGN. In the sample of Xia et al. 12 sources have a soft X-ray luminosity of $L_{(0.5-2.0) \text{ keV}} \gtrsim 10^{44} \text{ erg s}^{-1}$ and a luminosity ratio greater than 10^{-2} . All these sources are classified as QSOs/Seyfert 1 galaxies with two BL Lacs. On the contrary, sources with $L_{(0.5-2.0) \text{ keV}}/L_{\text{FIR}} \lesssim 10^{-3}$ show an enhanced Starburst activity responsible for the huge emission power. The graphic illustrates that all sources below this value have a soft X-ray luminosity smaller than $\sim 10^{43} \text{ erg s}^{-1}$. According to their optical classification (taken from the NED) these 14 objects are Seyfert 2 galaxies, LINERs and H II regions, except for two sources close to the latter threshold with the use of the typical Γ value which might be improper in both cases.

A problem arises for NGC 6240, when comparing its location in the plot based on the three different luminosity values. Although the hard X-ray regime favours an AGN contribution comparable (if not even stronger) to the Starburst energy output, as it is confirmed by the hard X-ray data from *XMM-Newton*, the values presented in Xia et al. seem to indicate an enhanced

Starburst phenomenon in NGC 6240. Looking at the results from other observations/satellites the Xia et al. numbers are at the lower end of reasonable soft X-ray luminosity values (~ 1.5 smaller than the lowest (0.5 – 2.0) keV–luminosity value in Table 4.6 on p. 98, equivalent to ~ 0.2 dex) and thus leading to a lower luminosity ratio than found by others.

4.4.2 Plasma properties

The X-ray emission of NGC 6240 requires the presence of thermal emission in form of three optically–thin, collisionally–ionized plasmas with different temperatures.

This is in contrast to previous papers and shows that *XMM-Newton* allows more precise measurements of the plasmas than other satellites due to its high throughput and collecting area. In addition to the work of Kii et al. (1997) and Turner et al. (1997a) on *ASCA* data of NGC 6240, Iwasawa & Comastri (1998) published a more detailed analysis of its spectrum. Their model for the soft X-ray spectrum included a two-temperature thermal emission (using two MEKAL components), suggesting a combination of an absorbed high-temperature gas and a low-temperature, spatially more extended gas as the origin of a Starburst activity. This is in contrast to the findings of Schulz et al. (1998) and Netzer et al. (1998) who investigated *ASCA* and *ROSAT* data and attributed more than 80 per cent of the soft X-ray emission to scattered AGN radiation. Nevertheless, the *ROSAT-HRI* image reveals that more than 70 per cent of the soft X-ray emission is extended beyond the PSF of the *HRI* (*i.e.* with a radius of ~ 2.4 kpc at the distance of NGC 6240). Ptak et al. (2003) applied a two-temperature model (2x MEKAL) to the low energy range of the *Chandra* data of NGC 6240, revealing a rather cold plasma of $kT_1 = (0.30 \pm 0.03)$ keV and a warmer component with $kT_2 = (0.67 \pm 0.05)$ keV. The latter seems to be present in most of the nuclei of ULIRGs, which makes them seen as a related class to the pure Starburst galaxies (e.g. Lira et al. 2002, Martin et al. 2002). Significantly higher values are reported by Komossa et al. (2003). A single-component MEKAL approach gives the temperature $kT_1 = (0.81 \pm 0.05)$ keV for the extended X-ray emission, but for a ”blob”-like emission southwest of the southern nuclei a second MEKAL model with $kT_2 = (2.8 \pm 0.8)$ keV was used. However, all these facts favour the Starburst interpretation for the soft X-ray emission in NGC 6240.

As described in subsection 4.2.3 on p. 88ff (in particular on p. 91), the X-ray emission from Mrk 1014 can be preferentially described by a power law. Therefore, a study of the physical quantities based on a *thermal* model approach is not recommendable and even counterproductive. Consequently, putative model approximations to the low-energy part of the X-ray spectrum with a thermal origin are neglected and not considered for the spectrum of Mrk 1014.

Table 4.11: Derived physical parameters of the X–ray emitting gas using all three APEC components (for NGC 6240), averaged over an X–ray emitting volume of a sphere with radius $R = 3 \text{ kpc}$ ^{a)}.

Physical quantity		NGC 6240		
		cool	medium	hot
Norm _{APEC} ^{b)}	$[10^{-3} \text{ cm}^{-3}]$	5.8 ± 1.0	2.4 ± 1.5	3.7 ± 1.3
Emission measure EM	$[10^{63} \text{ cm}^{-3}]$	$1,500 \pm 300$	600 ± 400	$1,000 \pm 300$
$\langle n_e \rangle \cdot f^{1/2}$	$[10^{-1} \text{ cm}^{-3}]$	6.8 ± 0.6	4.4 ± 1.4	5.4 ± 0.9
$M_{\text{gas}} \cdot f^{-1/2}$	$[10^7 M_{\odot}]$	200 ± 20	120 ± 40	150 ± 30
$N_{\text{H, gas}} \cdot f^{1/6}$	$[10^{20} \text{ cm}^{-2}]$	130 ± 10	80 ± 30	100 ± 20
kT_{gas}	[keV]	0.66 ± 0.03	1.4 ± 0.2	5.5 ± 1.5
$P_{\text{gas}} \cdot f^{-1/2}$	$[10^{-9} \text{ dyne cm}^{-2}]$	0.72 ± 0.06	1.0 ± 0.3	4.8 ± 0.8
$E_{\text{thermal, kin}} \cdot f^{-1/2}$	$[10^{57} \text{ erg}]$	3.6 ± 0.3	4.9 ± 1.5	24 ± 4
$\tau_{\text{cool}} \cdot f^{-1/2}$	$[10^6 \text{ yr}]$	1.7 ± 0.1	8.7 ± 2.7	60 ± 10
v_{bulk}	$[\text{km s}^{-1}]$	1,000	1,000	1,000
$E_{\text{bulk, kin}} \cdot f^{-1/2}$	$[10^{57} \text{ erg}]$	19 ± 2	12 ± 4	15 ± 3
$\dot{M}_{\text{bulk}} \cdot f^{1/2}$	$[M_{\odot} \text{ yr}^{-1}]$	700 ± 100	500 ± 100	600 ± 100

a) for the definition of the quantities see subsection 4.3.2 on p. 112ff,

b) the normalization of the cool and the medium APEC model follows the definition of the MEKAL normalization N_{MEKAL} (see the subsection 3.2.3 on p. 56).

Table 4.11 lists the results of the calculations of diverse physical quantities described in subsection 4.3.2 on p. 112ff. They are based on the APEC normalization Norm_{APEC} of the cool and the medium plasma component in the NGC 6240 spectrum. With this value, the (mean) gas density $\langle n_e \rangle$ in NGC 6240, its mass M_{gas} and column density $N_{\text{H, gas}}$ were computed along with the explicit dependence on the filling factor f . The results are in excellent agreement with the values presented for the hot APEC component (last column of Table 4.11 and Table 4.9 on p. 114), since they all are related to the square–root of the normalizations and the latter are of the same order–of–magnitude. Table 4.11 shows the thermodynamic properties of the gas, the temperature $kT_{(\text{cool|medium}) \text{ gas}}$, pressure $P_{(\text{cool|medium}) \text{ gas}}$, and thermal kinetic energy $E_{\text{thermal, kin}}$. The temperatures of the diverse plasmas cause different values, obviously resulting in larger values for the pressure and the thermal energy for the higher–temperature plasmas. The pressure values are similar to the ISM–induced gas pressure so that they could balance each

other (cf. subsection 4.3.2 on p. 115f). According to previous observations the luminosity of the low energy component is similar in all data sets (see Table 4.6 on p. 98).

Several line features are present in the spectrum of NGC 6240. They can be attributed to an enhanced Starburst activity when interpreted in terms of three optically–thin multi–temperature plasmas. These can be compared to similar findings in the prototype Seyfert 2 galaxy NGC 1068. The (0.5 – 2.0) keV luminosity of NGC 6240 is consistent with a powerful Starburst, if the entire emission below 2 keV is due to the Starburst. NGC 6240 and NGC 1068 show similar luminosity ratios of the soft X–ray to the far–IR–luminosity. Despite of this corresponding finding the soft X–ray spectrum of NGC 1068 reveals a huge excess emission and thus the slope of the spectrum below ~ 2 keV is much steeper than that of NGC 6240. Ueno et al. (1994) applied a two–temperature thermal model to the *ASCA* data of NGC 1068 assuming a Galactic absorption component alone, whereas the temperature components for NGC 6240 require an additional absorbing contribution of typically more than $2 \cdot 10^{21}$ atoms cm^{-2} . The detected absorption by cold gas attenuates the soft X–ray emission in NGC 6240. Correcting for this effect results in a large X–ray excess comparable to that of NGC 1068. This similarity would be at the expense of a significantly higher soft X–ray luminosity than the expected value from Starburst models. Concerning the spectral line features a detailed discussion will be given in the next subsection.

4.4.3 Emission lines at low energies

The measured plasma temperature kT and the degree of ionization determine the centroid energy of an atomic line. Whereas the former is obtained from the fitting process, the latter depends on the product of the gas density $\langle n_e \rangle$ and the time scale t of the relevant process. In the case of an external disturbance in form of a mechanical impact, e.g. by shock heating, electrons are thermalized by collisions with ions. The associated time scale $t_{e \rightarrow i}$ for electron–ion collisions (Masai 1984) – multiplied by $\langle n_e \rangle$ – is given by

$$\langle n_e \rangle \cdot t_{e \rightarrow i} = 9.8 \cdot 10^{12} \langle A_i \rangle \langle z \rangle^{-2} T_{\text{gas, keV}}^{3/2} / (|\ln[\Lambda]|) \text{ s},$$

where $\langle A_i \rangle$ is the average ion mass (in atomic units) and $\langle z \rangle$ is the average ion charge. Following the argumentation of Kaneda et al. (1997) to use the kT – $\langle n_e \rangle \cdot t_{e \rightarrow i}$ –plot (cf. Figure 2b) as a diagnostic for allowable pair values, this tool indicates the number of plasma components required.

Table 4.12 lists the properties of three selected prominent emission lines at soft X–rays (cf. Figure 3.15 on p. 67). On top of an assumed power law–like continuum slope a Gaussian line has been used to determine the diverse line parameters. Comparing the centroid line energies with the permitted kT – $\langle n_e \rangle \cdot t_{e \rightarrow i}$ –regions the Kaneda–plot shows a discrepancy

Table 4.12: Selected emission lines in the soft X-ray spectrum of NGC 6240
with fixed width ($\sigma = 0$), EPIC MOS1/2, revolution 0144 ^{a)}

Element identification ^{d)}	E_C [keV]	EW [eV]	I ^{b)}	f ^{c)}
Ne IX/X (incl. Fe-L)	1.02 ± 0.02	40^{+10}_{-20}	2.5 ± 1.3	4.0 ± 2.0
Si XIV	1.99 ± 0.02	80^{+40}_{-20}	1.1 ± 0.5	3.4 ± 1.6
S XV	2.44 ± 0.04	80^{+60}_{-40}	0.8 ± 0.5	2.9 ± 2.0

a) measured by a Gaussian line fit on top of a power law-like continuum slope,

b) the emission line intensity, in [10^{-5} photons cm^{-2} s^{-1}],

c) the emission line flux, in [10^{-14} erg cm^{-2} s^{-1}],

d) nearest $K\alpha$ line of H- and He-like ions: $E(\text{Ne IX/X}) = 0.92/1.02$ keV, $E(\text{Fe-L}) \approx (0.8 - 1.1)$ keV, $E(\text{Si XIV}) = 1.99$ keV, and $E(\text{S XV}) = 2.46$ keV.

for a single-temperature plasma. Considering (at least) two plasma components with different ionization states can overcome this difficulty.

5

Conclusion and future prospects

A detailed spectral analysis has been performed on the basis of X-ray data of NGC 6240 received from the *XMM-Newton* observatory (Boller, Keil, Hasinger et al., 2003, *A&A*, 411, 63), while the data on Mrk 1014 have been re-examined and contrasted to the findings of Boller et al. (2002).

5.1 Summary

The observational results for the ULIRG NGC 6240 studied in this thesis have been summarized in section 4.1 on p. 85f. The *XMM-Newton* observation of Mrk 1014 confirms the dominant role of a power law at high energies with no evidence for any Fe-K line emission. In the case of NGC 6240 the observations allowed to give strong constraints on the spectral properties and on model parameters that were only assumed but could not directly detected by previous missions. Based on these results the conclusions can be summarized as follows.

- The total (0.3 – 10.0) keV emission of NGC 6240 is modelled by three optically-thin, collisionally-ionized plasmas, together with a highly absorbed power law;
- In NGC 6240 the X-ray emission above ~ 8 keV is almost due to a predominant AGN. Supposing NGC 6240 as a representative of the ULIRG class, this supports the idea that many, if not most, LIGs/ULIRGs contain a significant AGN contribution in form of super-massive black holes in their nuclei;
- The detection of the neutral Fe-K α line at 6.4 keV in the spectrum of NGC 6240 indicates the presence of an AGN;

- Resolving the ionized Fe-K emission lines within the Fe-K line complex of NGC 6240 hints to a hot thermal plasma ($kT_{\text{hot}} \approx 5.5$ keV). Starburst galaxies like NGC 253 show a comparable thermal contribution to the hard X-ray emission;
- The three plasma emission processes are probably originating in SN explosions which provide the energy to heat up the ambient ISM to X-ray temperatures;
- (At least) in NGC 6240 the heating mechanism is probably due to a shock-heating process from a "superwind". This direct emission, *i.e.* the collective ejecta of numerous SNe, comprises not more than ~ 12 per cent to the total emission;
- The (0.3 – 10.0) keV spectrum of Mrk 1014 can be sufficiently modelled with a single power law. This is in contrast to the results presented by Boller et al. (2002);
- The presence of a soft X-ray excess could not be confirmed. The mentioned hard X-ray excess emission above 5 keV is far lower than stated in the paper.

5.2 Future prospects

The *XMM-Newton* observatory with its broad X-ray bandpass, its effective area which is more than 10 times larger than that of *ASCA* and the high throughput, complementary to *Chandra* with its high spatial resolution, are able to resolve the nuclear emission from the AGN and Starburst activity in great detail. In combination with a high sensitivity for detecting point sources, both observatories provide a better understanding of the physics of X-ray sources in general, and LIGs/ULIRGs in particular.

The future X-ray missions, namely *XEUS* and *Constellation-X*, will establish a new generation of observatories to address the issue of thermal and non-thermal sources comprising the energy release of a large number of active galaxies. These facilities will be able to resolve all or at least most of the nuclear emission from both activity centres – from an enhanced Starburst activity, of nuclear and extended size, and from discrete point sources in the galaxies' nuclei. The conceptions of this missions in the framework of LIG/ULIRG research are aimed at the isolation of any AGN activity. Moreover, they should allow to determine the contributing fraction, from the hot plasma emission mechanism to the hard power law component, or should hint at signatures originating from other, yet unknown physical processes. In this context, *XEUS* could be able to fully resolve the cosmic X-ray background radiation between (10 – 40) keV into discrete sources. This would increase the number of highly obscured, nearby ($z \lesssim 1$) AGN together with an increased number of highly obscured, distant ($z > 1$) AGN, leading to a complete survey of highly obscured AGN. At the same time, *XEUS* can provide detailed observations of SNRs,

galaxies and galaxy clusters, studying their thermal and non-thermal contribution. *Suzaku* (formerly *Astro-E2*), which was launched on July 10th, 2005, carried a new type of X-ray micro-calorimeter device that was supposed to have an energy resolution of less than ~ 10 eV within the range of (0.3 – 12.0) keV, the *XRS* instrument. Unfortunately, the *XRS* lost all its cryogen in early August 2005 before routine scientific observations could begin. Even though *Suzaku* hosts a second X-ray spectrometer, the X-ray Imaging Spectrometer *XIS*, sensitive between (0.2 – 12.0) keV, this instrument with a spectral resolution of 50 eV at 1 keV is unlikely to achieve major discoveries in the X-ray domain. A second instrument (the hard X-ray detector *HXD*) is fully operational with an energy bandpass in the range of (10 – 600) keV with suitable energy resolution to search directly for highly absorbed AGN, although the *HXD* has no spatial resolution. Both the *XEUS*– as well as the *Constellation-X* mission, planned for years after 2015, are far more ambitious projects. NASA’s concept for the *Constellation-X* mission, as part of its scientific programme for the next decades, will place an array of four X-ray telescopes into orbit in order to increase the sensitivity of the observations. All spacecrafts will work in unison to shed light on – among other things – the research of heavily absorbed AGN in combination with studies of the X-ray background radiation. Presently, there is an ongoing discussion, whether a joined single mission by ESA and NASA can be achieved. The surveys by *XMM-Newton* and *Chandra* to look at highly obscured sources are limited to energies below ~ 12 keV, thus they can only probe absorbing column densities of not more than a few times 10^{24} atoms cm^{-2} . Due to the higher sensitivity the hard X-ray telescopes (*HXTs*) of *Constellation-X* can survey IR-selected AGN in the local and distant universe to analyse the X-ray properties of these populations. The *XEUS* project by ESA pursues a different design concept, but will also be built in view of a maximum collecting area as one of the main key parameters. *XEUS* will be a permanent space-borne X-ray observatory with a sensitivity comparable to the most advanced planned future observatories in other energy ranges, such as *JWST*, *ALMA* and *HERSCHEL*. *XEUS* will be around 220 times more sensitive than *XMM-Newton*, possessing a few square meters of collecting area at 1 keV, an imaging resolution of 5'' HEW and a spectral resolution between 1 eV and 10 eV in the energy range of (0.05 – 30) keV, attainable by a new technology generation of X-ray detectors (Superconducting Tunnel Junctions STJs, and Transition Edge Sensor arrays TESs).

The scientific goals include the study of local AGN and Starburst galaxies in unprecedented detail and compare their properties with those at redshifts of $z \gtrsim 1$. The high sensitivity of the *XEUS* mission for spectroscopic observations will allow to investigate high-redshift AGN as well as AGN/Starburst hybrid galaxies. The ability of the final *XEUS* configuration for discriminating both activity mechanisms can be seen in Figure 5.2 (left plot) which shows a simulated spectrum of a composite galaxy at redshift $z = 4$ consisting of a Starburst with a nuclear hidden

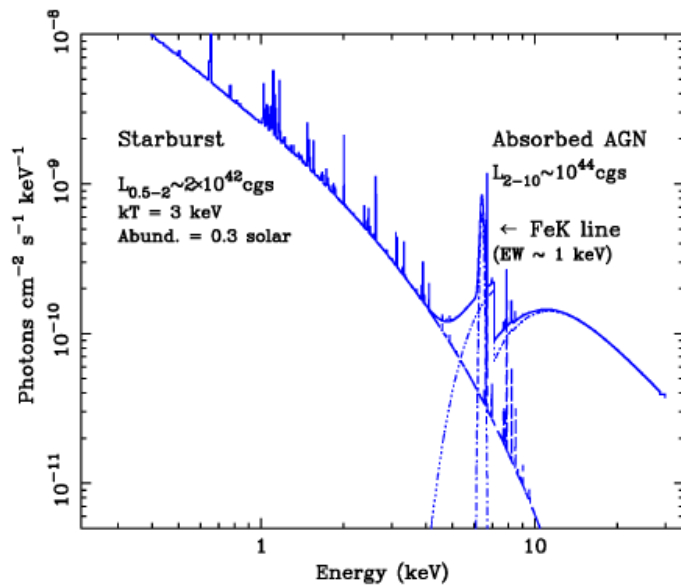


Figure 5.1: X-ray model spectrum with its components of a composite galaxy consisting of a heavily absorbed AGN and a Starburst. The intrinsic luminosities of both components (as indicated in the plot) are due to the values of NGC 6240. Accounting the Starburst for the entire emission at lower energies, it has been modelled by a thermal gas with $kT_{\text{gas}} = 3 \text{ keV}$ and sub-solar abundances ($Z = 0.3 Z_{\odot}$). In the high-energy regime a deeply suppressed power law and a strong Fe-K α line ($\text{EW} = 1 \text{ keV}$) indicates an absorbed AGN with a column density of $N_{\text{H}} = 10^{24} \text{ atoms cm}^{-2}$.

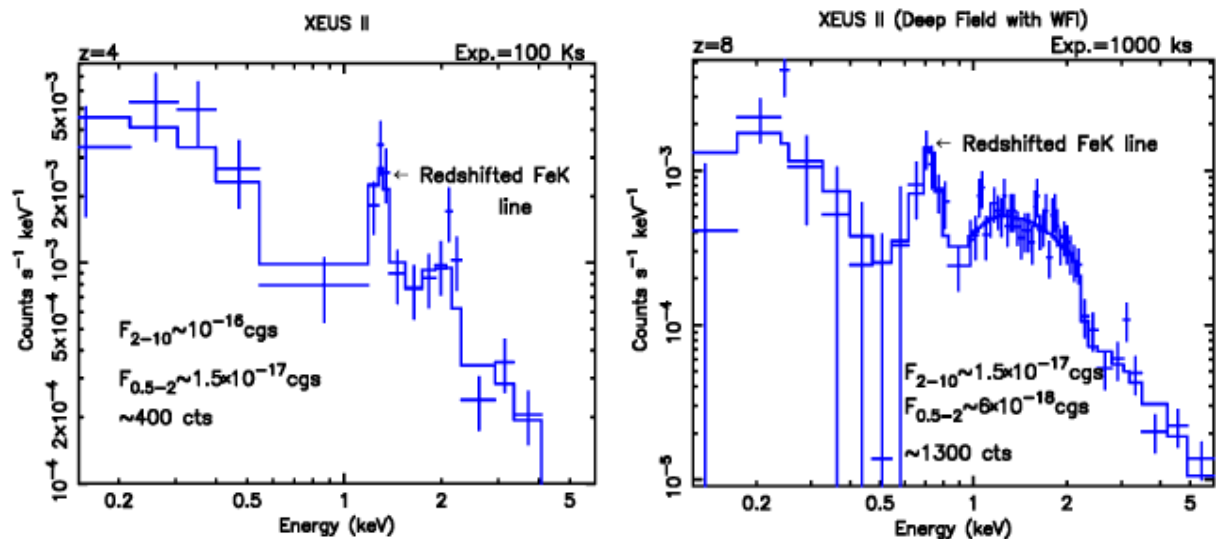


Figure 5.2: Simulated X-ray spectrum of a composite galaxy of a heavily absorbed AGN and a Starburst as seen by *XEUS*. The **left plot** shows the *XEUS* spectrum of a source at redshift $z = 4$ for the given band fluxes. The exposure time was chosen to be 100 ks for the final *XEUS* configuration (*XEUS* II). The **right plot** demonstrates the capabilities of *XEUS* to obtain an X-ray spectrum of the same object at $z \gg 1$ (here: $z = 8$) around the Fe-K α line. This simulation was calculated for an exposure time of 1 Ms (reproduced from *The XEUS Science Case*, ESA SP-1238).

AGN, based on the input model from Figure 5.1. In this plot each model component is included, together with their superposed slope. The mid-temperature thermal model ($kT_{\text{gas}} = 3 \text{ keV}$ and $Z_{\text{gas}} = 0.3 Z_{\odot}$) represents the Starburst contribution to the flux and is solely responsible for the low-energy emission. Plasma diagnostics of the soft X-ray emission lines will distinguish between collisionally-ionized and photoionized plasma, which is a direct evidence for the origin of the soft component. At higher energies the AGN dominates. Its presence can be deduced from a strong Fe-K α line (with $\text{EW} = 1 \text{ keV}$), measurable out to redshifts $z \gg 1$ (for an AGN with $10^{44} \text{ erg s}^{-1}$; cf. Figure 5.2; right plot) and from a non-thermal component, even with an absorbing material of $N_{\text{H}} \gtrsim 10^{24} \text{ atoms cm}^{-2}$. The intensity of the Fe-K α line will discriminate the origin of the hard X-ray emission and will give constraints on the contribution of the direct and the scattered/reflected light. Hence, these kind of spectra represent the only way to tackle the problem of finding a dust-enshrouded AGN at high redshifts in a *direct* way. In the case of an unambiguous detection, an analysis would disentangle the AGN and the Starburst contribution to the total X-ray emission. In the other case, *XEUS* would give strong constraints on an AGN contribution to the detected emission. The implications would be substantial for the star forming processes in galaxies and for the radiation history of the universe at large.

The new generation of X-ray missions promise to extend our knowledge of AGN and Starburst activity considerably. Moreover, they can help to answer the fundamental question, whether or not all galaxies harbour a super-massive black hole in their centre.

References

- Anders, E. and Grevesse, N.: 1989, *Geochim. Cosmochim. Acta* **53**, 197
- Antonucci, R.: 1993, *Ann. Rev. Astron. Astrophys.* **31**, 473
- Antonucci, R. R. J. and Miller, J. S.: 1985, *Astrophys. J.* **297**, 621
- Armus, L., Heckman, T. M., and Miley, G. K.: 1989, *Astrophys. J.* **347**, 727
- Armus, L., Heckman, T. M., and Miley, G. K.: 1990, *Astrophys. J.* **364**, 471
- Armus, L., Neugebauer, G., Soifer, B. T., and Matthews, K.: 1995a, *Astron. J.* **110**, 2610
- Armus, L., Shupe, D. L., Matthews, K., Soifer, B. T., and Neugebauer, G.: 1995b, *Astrophys. J.* **440**, 200
- Arnaud, K. A.: 1996, in *ASP Conf. Ser. 101: Astronomical Data Analysis Software and Systems V*, p. 17
- Arnaud, K. A.: 1999, *Bulletin of the American Astronomical Society* **31**, 734
- Aschenbach, B.: 1985, *Reports of Progress in Physics* **48**, 579
- Aschenbach, B.: 2002, in *Proc. SPIE Vol. 4496, p. 8-22, X-Ray Optics for Astronomy: Telescopes, Multilayers, Spectrometers, and Missions*, Paul Gorenstein; Richard B. Hoover; Eds., p. 8
- Awaki, H., Koyama, K., Kunieda, H., and Tawara, Y.: 1990, *Nature* **346**, 544
- Babu, G. J. and Feigelson, E. D.: 1996, *Astrostatistics*, London: Chapman and Hall.
- Bagnasco, G., Eggel, H., Giannini, F., and Thürey, S.: 1999, in *ESA-Bulletin No. 100, "XMM-Newton Special issue"*, ESA Publications Division, Noordwijk, The Netherlands, p. 21
- Balbus, S. A. and Hawley, J. F.: 1991, *Astrophys. J.* **376**, 214
- Ballantyne, D. R., Iwasawa, K., and Fabian, A. C.: 2001, *Mon. Not. R. Astron. Soc.* **323**, 506

- Balucinska-Church, M. and McCammon, D.: 1992, *Astrophys. J.* **400**, 699
- Bambynek, W., Crasemann, B., Fink, R. W., Freund, H.-U., Mark, H., Swift, C. D., Price, R. E., and Rao, P. V.: 1972, *Rev. Mod. Phys.* **44**, 716
- Barré, H., Nye, H., and Janin, G.: 1999, in *ESA-Bulletin No. 100, "XMM-Newton Special issue"*, ESA Publications Division, Noordwijk, The Netherlands, p. 15
- Bassani, L., Dadina, M., Maiolino, R., Salvati, M., Risaliti, G., Della Ceca, R., Matt, G., and Zamorani, G.: 1999, *Astrophys. J., Suppl. Ser.* **121**, 473
- Bevington, P. R. and Robinson, D. K.: 2003, *Data reduction and error analysis for the physical sciences*, 3rd ed., Boston, MA: McGraw-Hill
- Blackburn, J. K.: 1995, in *ASP Conf. Ser. 77: Astronomical Data Analysis Software and Systems IV*; eds. R. A. Shaw, H. E. Payne, and J. J. E. Hayes (San Francisco: ASP), p. 367
- Blandford, R. D., Netzer, H., Woltjer, L., Courvoisier, T. J.-L., and Mayor, M.: 1990, *Active Galactic Nuclei*, Saas-Fee Advanced Course 20. Lecture Notes 1990. Swiss Society for Astrophysics and Astronomy, XII, Springer-Verlag Berlin Heidelberg New York
- Boller, T.: 1999, *Astrophys. Space. Sci.* **266**, 49
- Boller, T. and Bertoldi, F.: 1996, in *ASP Conf. Ser. 103: The Physics of Liners in View of Recent Observations*, p. 159
- Boller, T., Fabian, A. C., Brandt, W. N., and Freyberg, M. J.: 2000, *Mon. Not. R. Astron. Soc.* **315**, 23
- Boller, T., Gallo, L. C., Lutz, D., and Sturm, E.: 2002, *Mon. Not. R. Astron. Soc.* **336**, 1143
- Boller, T., Keil, R., Hasinger, G., Costantini, E., Fujimoto, R., Anabuki, N., Lehmann, I., and Gallo, L.: 2003, *Astron. Astrophys.* **411**, 63
- Borkowski, K. J., Lyerly, W. J., and Reynolds, S. P.: 2001, *Astrophys. J.* **548**, 820
- Braitto, V., Franceschini, A., Della Ceca, R., Severgnini, P., Bassani, L., Cappi, M., Malaguti, G., Palumbo, G. G. C., Persic, M., Risaliti, G., and Salvati, M.: 2003, *Astron. Astrophys.* **398**, 107
- Brandt, W. N., Fabian, A. C., Takahashi, K., Fujimoto, R., Yamashita, A., Inoue, H., and Ogasaka, Y.: 1997, *Mon. Not. R. Astron. Soc.* **290**, 617
- Bregman, J. N., Schulman, E., and Tomisaka, K.: 1995, *Astrophys. J.* **439**, 155

- Brickhouse, N. S., Smith, R. K., Raymond, J. C., and Liedahl, D. A.: 2000, *Bulletin of the American Astronomical Society* **32**, 1227
- Brinkmann, W., Laurent-Muehleisen, S. A., Voges, W., Siebert, J., Becker, R. H., Brotherton, M. S., White, R. L., and Gregg, M. D.: 2000, *Astron. Astrophys.* **356**, 445
- Brunner, H., Müller, C., Friedrich, P., Dörrer, T., Staubert, R., and Riffert, H.: 1997, *Astron. Astrophys.* **326**, 885
- Burrows, D. N., Michael, E., Hwang, U., McCray, R., Chevalier, R. A., Petre, R., Garmire, G. P., Holt, S. S., and Nousek, J. A.: 2000, *Astrophys. J., Lett.* **543**, 149
- Cappi, M., Persic, M., Bassani, L., Franceschini, A., Hunt, L. K., Molendi, S., Palazzi, E., Palumbo, G. G. C., Rephaeli, Y., and Salucci, P.: 1999, *Astron. Astrophys.* **350**, 777
- Christian, D. J. and Swank, J. H.: 1997, *Astrophys. J., Suppl. Ser.* **109**, 177
- Clements, D. L., van der Werf, P. P., Krabbe, A., Blietz, M., Genzel, R., and Ward, M. J.: 1993, *Mon. Not. R. Astron. Soc.* **262**, 23
- Colbert, E. J. M., Weaver, K. A., Krolik, J. H., Mulchaey, J. S., and Mushotzky, R. F.: 2002, *Astrophys. J.* **581**, 182
- Colbert, E. J. M., Wilson, A. S., and Bland-Hawthorn, J.: 1994, *Astrophys. J.* **436**, 89
- Condon, J. J., Anderson, M. L., and Helou, G.: 1991, *Astrophys. J.* **376**, 95
- Dahlem, M., Weaver, K. A., and Heckman, T. M.: 1998, *Astrophys. J., Suppl. Ser.* **118**, 401
- David, L. P., Jones, C., and Forman, W.: 1992, *Astrophys. J.* **388**, 82
- de Chambure, D., Lainé, R., van Katwijk, K., and Kletzkine, P.: 1999, in *ESA-Bulletin No. 100, "XMM-Newton Special issue"*, ESA Publications Division, Noordwijk, The Netherlands, p. 30
- de Grijp, M. H. K., Lub, J., and Miley, G. K.: 1987, *Astron. Astrophys. Suppl. Ser.* **70**, 95
- Decourchelle, A., Ellison, D. C., and Ballet, J.: 2000, *Astrophys. J., Lett.* **543**, 57
- Della Ceca, R., Griffiths, R. E., Heckman, T. M., Lehnert, M. D., and Weaver, K. A.: 1999, *Astrophys. J.* **514**, 772
- Della Ceca, R., Griffiths, R. E., Heckman, T. M., and MacKenty, J. W.: 1996, *Astrophys. J.* **469**, 662

- den Herder, J. W., Brinkman, A. C., Kahn, S. M., Branduardi-Raymont, G., Thomsen, K., Aarts, H., Audard, M., Bixler, J. V., den Boggende, A. J., Cottam, J., Decker, T., Dubbeldam, L., Erd, C., Goulooze, H., Güdel, M., Guttridge, P., Hailey, C. J., Janabi, K. A., Kaastra, J. S., de Korte, P. A. J., van Leeuwen, B. J., Mauche, C., McCalden, A. J., Mewe, R., Naber, A., Paerels, F. B., Peterson, J. R., Rasmussen, A. P., Rees, K., Sakelliou, I., Sako, M., Spodek, J., Stern, M., Tamura, T., Tandy, J., de Vries, C. P., Welch, S., and Zehnder, A.: 2001, *Astron. Astrophys. Lett.* **365**, 7
- Dickey, J. M. and Lockman, F. J.: 1990, *Ann. Rev. Astron. Astrophys.* **28**, 215
- Dickey, J. M. and Salpeter, E. E.: 1984, *Astrophys. J.* **284**, 461
- Dopita, M. A. and Sutherland, R. S.: 2003, *Astrophysics of the diffuse universe*, Berlin, New York: Springer, 2003. Astronomy and astrophysics library.
- Eales, S. A., Wynn-Williams, C. G., and Duncan, W. D.: 1989, *Astrophys. J.* **339**, 859
- Ebisawa, K., Day, C. S. R., Kallman, T. R., Nagase, F., Kotani, T., Kawashima, K., Kitamoto, S., and Woo, J. W.: 1996, *Publ. Astron. Soc. Jpn.* **48**, 425
- Ehle, M., Breittellner, M., González Riestra, R., Guainazzi, M., Loiseau, N., Rodríguez, P., Santos-Lleó, M., Schartel, N., Tomás, L., Verdugo, E., and Dahlem, M.: 2004, in *XMM-Newton Users' Handbook*, v2.2
- Elvis, M., Wilkes, B. J., McDowell, J. C., Green, R. F., Bechtold, J., Willner, S. P., Oey, M. S., Polonski, E., and Cutri, R.: 1994, *Astrophys. J., Suppl. Ser.* **95**, 1
- Emerson, D.: 1996, *Interpreting astronomical spectra*, Chichester, UK: Wiley
- Emerson, J. P., Clegg, P. E., Gee, G., Griffin, M. J., Cunningham, C. T., Brown, L. M. J., Robson, E. I., and Longmore, A. J.: 1984, *Nature* **311**, 237
- Engelbracht, C. W., Rieke, M. J., Rieke, G. H., Kelly, D. M., and Achtermann, J. M.: 1998, *Astrophys. J.* **505**, 639
- Fabian, A. C.: 1998, in *Theory of Black Hole Accretion Disks*, p. 123
- Fabian, A. C.: 2004, in *Coevolution of Black Holes and Galaxies*, p. 447
- Fabian, A. C., Iwasawa, K., Reynolds, C. S., and Young, A. J.: 2000, *Publ. Astron. Soc. Pac.* **112**, 1145

- Fabian, A. C., Nandra, K., Reynolds, C. S., Brandt, W. N., Otani, C., Tanaka, Y., Inoue, H., and Iwasawa, K.: 1995, *Mon. Not. R. Astron. Soc.* **277**, 11
- Fabian, A. C. and Vaughan, S.: 2003, *Mon. Not. R. Astron. Soc.* **340**, 28
- Fisher, K. B., Huchra, J. P., Strauss, M. A., Davis, M., Yahil, A., and Schlegel, D.: 1995, *Astrophys. J., Suppl. Ser.* **100**, 69
- Fosbury, R. A. E. and Wall, J. V.: 1979, *Mon. Not. R. Astron. Soc.* **189**, 79
- Franceschini, A., Braitto, V., Persic, M., Della Ceca, R., Bassani, L., Cappi, M., Malaguti, P., Palumbo, G. G. C., Risaliti, G., Salvati, M., and Severgnini, P.: 2003, *Mon. Not. R. Astron. Soc.* **343**, 1181
- Fried, J. W. and Schulz, H.: 1983, *Astron. Astrophys.* **118**, 166
- Gehrels, N.: 1986, *Astrophys. J.* **303**, 336
- Genzel, R., Lutz, D., Sturm, E., Egami, E., Kunze, D., Moorwood, A. F. M., Rigopoulou, D., Spoon, H. W. W., Sternberg, A., Tacconi-Garman, L. E., Tacconi, L., and Thatte, N.: 1998, *Astrophys. J.* **498**, 579
- George, I. M. and Fabian, A. C.: 1991, *Mon. Not. R. Astron. Soc.* **249**, 352
- George, I. M., Fabian, A. C., and Nandra, K.: 1990, *Mon. Not. R. Astron. Soc.* **242**, 28
- George, I. M., Turner, T. J., Yaqoob, T., Netzer, H., Laor, A., Mushotzky, R. F., Nandra, K., and Takahashi, T.: 2000, *Astrophys. J.* **531**, 52
- Ghisellini, G., Haardt, F., and Matt, G.: 1994, *Mon. Not. R. Astron. Soc.* **267**, 743
- Giacconi, R. and Rossi, B.: 1960, *J. Geophys. Res.* **65**, 773
- Gilfanov, M., Grimm, H.-J., and Sunyaev, R.: 2004, *Mon. Not. R. Astron. Soc. Lett.* **347**, 57
- Goldader, J. D., Joseph, R. D., Doyon, R., and Sanders, D. B.: 1995, *Astrophys. J.* **444**, 97
- Golombek, D., Miley, G. K., and Neugebauer, G.: 1988, *Astron. J.* **95**, 26
- Greenhill, L. J., Jiang, D. R., Moran, J. M., Reid, M. J., Lo, K. Y., and Claussen, M. J.: 1995, *Astrophys. J.* **440**, 619
- Griffiths, R. E. and Padovani, P.: 1990, *Astrophys. J.* **360**, 483

- Griffiths, R. E., Ptak, A., Feigelson, E. D., Garmire, G., Townsley, L., Brandt, W. N., Sambruna, R., and Bregman, J. N.: 2000, *Science* **290**, 1325
- Grimm, H.-J., Gilfanov, M., and Sunyaev, R.: 2003, *Mon. Not. R. Astron. Soc.* **339**, 793
- Guainazzi, M. and Santos-Lleó: 2002, in *XMM-Newton Documentation: XMM-Newton Data Files Handbook (XMM-SOC-DFHB-2.3), Issue 2.3*
- Guilbert, P. W. and Rees, M. J.: 1988, *Mon. Not. R. Astron. Soc.* **233**, 475
- Gursky, H. and Schwartz, D.: 1974, in *ASSL Vol. 43: X-ray Astronomy*, p. 25
- Haardt, F. and Maraschi, L.: 1991, *Astrophys. J., Lett.* **380**, 51
- Hagiwara, K. e.: 2002, *Review of Particle Physics*, Vol. 66, <http://pdg.lbl.gov>
- Hanisch, R. J., Farris, A., Greisen, E. W., Pence, W. D., Schlesinger, B. M., Teuben, P. J., Thompson, R. W., and Warnock, A.: 2001, *Astron. Astrophys. Lett.* **376**, 359
- Hasinger, G.: 2000, *Lecture Notes in Physics, Berlin Springer Verlag* **548**, 423
- Hasinger, G.: 2001, in *ASP Conf. Ser. 251: New Century of X-ray Astronomy*, p. 172
- Hasinger, G.: 2002, *Royal Society of London Philosophical Transactions Series A* **360**, 2077
- Heckman, T. M., Armus, L., and Miley, G. K.: 1987, *Astron. J.* **93**, 276
- Heckman, T. M., Armus, L., and Miley, G. K.: 1990, *Astrophys. J., Suppl. Ser.* **74**, 833
- Heckman, T. M., Dahlem, M., Eales, S. A., Fabbiano, G., and Weaver, K.: 1996, *Astrophys. J.* **457**, 616
- Helou, G.: 1986, *Astrophys. J., Lett.* **311**, 33
- Helou, G., Soifer, B. T., and Rowan-Robinson, M.: 1985, *Astrophys. J., Lett.* **298**, 7
- Houck, J. R., Soifer, B. T., Neugebauer, G., Beichman, C. A., Aumann, H. H., Clegg, P. E., Gillett, F. C., Habing, H. J., Hauser, M. G., Low, F. J., Miley, G., Rowan-Robinson, M., and Walker, R. G.: 1984, *Astrophys. J., Lett.* **278**, 63
- Huchra, J. P.: 1977, *Astrophys. J., Suppl. Ser.* **35**, 171
- Hummer, D. G., Berrington, K. A., Eissner, W., Pradhan, A. K., Saraph, H. E., and Tully, J. A.: 1993, *Astron. Astrophys.* **279**, 298
- Iben, I. J., Tutukov, A. V., and Yungelson, L. R.: 1995, *Astrophys. J., Suppl. Ser.* **100**, 217

- Ikebe, Y., Leighly, K., Tanaka, Y., Nakagawa, T., Terashima, Y., and Komossa, S.: 2000, *Mon. Not. R. Astron. Soc.* **316**, 433
- Inoue, H.: 1985, *Space Science Reviews* **40**, 317
- Isobe, T. and Feigelson, E. D.: 1992, *Astrophys. J., Suppl. Ser.* **79**, 197
- Iwasawa, K.: 1999, *Mon. Not. R. Astron. Soc.* **302**, 96
- Iwasawa, K. and Comastri, A.: 1998, *Mon. Not. R. Astron. Soc.* **297**, 1219
- Iwasawa, K., Fabian, A. C., Mushotzky, R. F., Brandt, W. N., Awaki, H., and Kunieda, H.: 1996a, *Mon. Not. R. Astron. Soc.* **279**, 837
- Iwasawa, K., Fabian, A. C., Reynolds, C. S., Nandra, K., Otani, C., Inoue, H., Hayashida, K., Brandt, W. N., Dotani, T., Kunieda, H., Matsuoka, M., and Tanaka, Y.: 1996b, *Mon. Not. R. Astron. Soc.* **282**, 1038
- Jansen, F., Lumb, D., Altieri, B., Clavel, J., Ehle, M., Erd, C., Gabriel, C., Guainazzi, M., Gondoin, P., Much, R., Munoz, R., Santos, M., Schartel, N., Texier, D., and Vacanti, G.: 2001, *Astron. Astrophys.* **365**, 1
- Jansen, F. A.: 1999, in *ESA-Bulletin No. 100, "XMM-Newton Special issue"*, ESA Publications Division, Noordwijk, The Netherlands, p. 9
- Joseph, R. D.: 1999, *Astrophys. Space. Sci.* **266**, 321
- Joseph, R. D. and Wright, G. S.: 1985, *Mon. Not. R. Astron. Soc.* **214**, 87
- Kaastra, J. S.: 1992, in *Internal SRON-Leiden Report (updated version 2.0)*, Koyama, K., Kitamoto, S., Itoh, M., eds, *Proc. IAU Symp. 188, The Hot Universe*. Kluwer Academic, Dordrecht, p. 43
- Kaastra, J. S. and Mewe, R.: 1993, *Astron. Astrophys. Suppl. Ser.* **97**, 443
- Kaastra, J. S., Mewe, R., and Nieuwenhuijzen, H.: 1996, in *UV and X-ray Spectroscopy of Astrophysical and Laboratory Plasmas: Proceedings of the Eleventh Colloquium on UV and X-ray ... held on May 29-June 2, 1995, Nagoya, Japan*. Edited by K. Yamashita and T. Watanabe. Tokyo : Universal Academy Press (Frontiers science series; no. 15), p. 411
- Kaneda, H., Makishima, K., Yamauchi, S., Koyama, K., Matsuzaki, K., and Yamasaki, N. Y.: 1997, *Astrophys. J.* **491**, 638

- Kembhavi, A. K. and Narlikar, J. V.: 1999, *Quasars and active galactic nuclei : an introduction*, Cambridge University Press, Cambridge, U.K.
- Kennicutt, R. C.: 1998a, *Ann. Rev. Astron. Astrophys.* **36**, 189
- Kennicutt, R. C.: 1998b, *Astrophys. J.* **498**, 541
- Kennicutt, R. C., Röttiger, K. A., Keel, W. C., van der Hulst, J. M., and Hummel, E.: 1987, *Astron. J.* **93**, 1011
- Kii, T., Nakagawa, T., Fujimoto, R., Ogasaka, Y., Miyazaki, T., Kawabe, R., and Terashima, Y.: 1997, in *X-Ray Imaging and Spectroscopy of Cosmic Hot Plasmas*, p. 161
- Kim, D.-C.: 1995, *Ph.D. Thesis*
- Kim, D.-C. and Sanders, D. B.: 1998, *Astrophys. J., Suppl. Ser.* **119**, 41
- Kirsch, M. G. F.: 2003, *Ph.D. thesis*, University of Tübingen
- Klaas, U., Haas, M., Heinrichsen, I., and Schulz, B.: 1997, *Astron. Astrophys.* **325**, 21
- Kleinmann, D. E. and Low, F. J.: 1970a, *Astrophys. J., Lett.* **161**, 203
- Kleinmann, D. E. and Low, F. J.: 1970b, *Astrophys. J., Lett.* **159**, 165
- Komossa, S., Burwitz, V., Hasinger, G., Predehl, P., Kaastra, J. S., and Ikebe, Y.: 2003, *Astrophys. J., Lett.* **582**, 15
- Komossa, S., Schulz, H., and Greiner, J.: 1998, *Astron. Astrophys.* **334**, 110
- Koyama, K.: 1992, in *X-ray emission from Active Galactic Nuclei and the Cosmic X-ray Background*, eds. W. Brinkmann and J. Trümper, MPE-Report 235, p. 74
- Koyama, K., Inoue, H., Tanaka, Y., Awaki, H., Takano, S., Ohashi, T., and Matsuoka, M.: 1989, *Publ. Astron. Soc. Jpn.* **41**, 731
- Krolik, J. H. and Kallman, T. R.: 1987, *Astrophys. J., Lett.* **320**, 5
- Kuijpers, J.: 1995, in *Coronal Magnetic Energy Releases*, p. 135
- Larson, R. B. and Tinsley, B. M.: 1978, *Astrophys. J.* **219**, 46
- Leahy, D. A. and Creighton, J.: 1993, *Mon. Not. R. Astron. Soc.* **263**, 314
- Leech, K. J., Rowan-Robinson, M., Lawrence, A., and Hughes, J. D.: 1994, *Mon. Not. R. Astron. Soc.* **267**, 253

- Lehmann, I., Hasinger, G., Murray, S. S., and Schmidt, M.: 2002, in *ASP Conf. Ser. 262: The High Energy Universe at Sharp Focus: Chandra Science*, p. 105
- Levenson, N. A., Weaver, K. A., and Heckman, T. M.: 2001, *Astrophys. J.* **550**, 230
- Liedahl, D. A., Osterheld, A. L., and Goldstein, W. H.: 1995, *Astrophys. J., Lett.* **438**, 115
- Lightman, A. P. and White, T. R.: 1988, *Astrophys. J.* **335**, 57
- Lira, P., Ward, M. J., Zezas, A., and Murray, S. S.: 2002, *Mon. Not. R. Astron. Soc.* **333**, 709
- Lisenfeld, U., Isaak, K. G., and Hills, R.: 2000, *Mon. Not. R. Astron. Soc.* **312**, 433
- Lisenfeld, U., Völk, H. J., and Xu, C.: 1996, *Astron. Astrophys.* **306**, 677
- Liu, C. T. and Kennicutt, R. C.: 1995, *Astrophys. J.* **450**, 547
- Loiseau, N., e. a.: 2004, in *XMM-Newton Proposer's Info and Manuals: User's Guide to the XMM-Newton Science Analysis System*
- Longair, M. S.: 1994, *High energy astrophysics. Vol.2: Stars, the galaxy and the interstellar medium*, 2nd ed., Cambridge University Press, Cambridge, U.K.
- Lonsdale, C. J., Smith, H. J., and Lonsdale, C. J.: 1993, *Astrophys. J., Lett.* **405**, 9
- Low, J. and Kleinmann, D. E.: 1968, *Astron. J.* **73**, 868
- Lumb, D. H., Eggel, H., Laine, R., and Peacock, A. J.: 1996, in *Proc. SPIE Vol. 2808, p. 326-337, EUV, X-Ray, and Gamma-Ray Instrumentation for Astronomy VII, Oswald H. Siegmund; Mark A. Gummin; Eds.*, p. 326
- Lutz, D., Genzel, R., Sternberg, A., Netzer, H., Kunze, D., Rigopoulou, D., Sturm, E., Egami, E., Feuchtgruber, H., Moorwood, A. F. M., and de Graauw, T.: 1996, *Astron. Astrophys.* **315**, 137
- Magdziarz, P. and Zdziarski, A. A.: 1995, *Mon. Not. R. Astron. Soc.* **273**, 837
- Makishima, K.: 1986, *Lecture Notes in Physics: The Physics of Accretion onto Compact Objects, Berlin Springer Verlag* **266**, 249
- Marshall, H. L., Harris, D. E., Grimes, J. P., Drake, J. J., Fruscione, A., Juda, M., Kraft, R. P., Mathur, S., Murray, S. S., Ogle, P. M., Pease, D. O., Schwartz, D. A., Siemiginowska, A. L., Vrtilik, S. D., and Wargelin, B. J.: 2001, *Astrophys. J., Lett.* **549**, 167
- Martin, C. L., Kobulnicky, H. A., and Heckman, T. M.: 2002, *Astrophys. J.* **574**, 663

- Masai, K.: 1984, *Astrophys. Space. Sci.* **98**, 367
- Matsuoka, M., Piro, L., Yamauchi, M., and Murakami, T.: 1990, *Astrophys. J.* **361**, 440
- Matt, G.: 2000, *Astron. Astrophys.* **355**, 31
- Matt, G.: 2002, *Royal Society of London Philosophical Transactions Series A* **360**, 2045
- Matt, G., Perola, G. C., Piro, L., and Stella, L.: 1992, *Astron. Astrophys.* **257**, 63
- Matteucci, F.: 2004, in *Cosmochemistry. The melting pot of the elements*, p. 217
- Mazzotta, P., Mazzitelli, G., Colafrancesco, S., and Vittorio, N.: 1998, *Astron. Astrophys. Suppl. Ser.* **133**, 403
- Mewe, R., Gronenschild, E. H. B. M., and van den Oord, G. H. J.: 1985, *Astron. Astrophys. Suppl. Ser.* **62**, 197
- Mewe, R., Kaastra, J. S., and Liedahl, D. A.: 1995, *Legacy* **6**, 16
- Mewe, R., Lemen, J. R., and van den Oord, G. H. J.: 1986, *Astron. Astrophys. Suppl. Ser.* **65**, 511
- Miller, J. S. and Goodrich, R. W.: 1990, *Astrophys. J.* **355**, 456
- Miller, P., Rawlings, S., Saunders, R., and Eales, S.: 1992, *Mon. Not. R. Astron. Soc.* **254**, 93
- Mirabel, I. F.: 1992, in *Collected Works*, p. 479
- Mitsuda, K.: 1995, in *Seventeenth Texas Symposium on Relativistic Astrophysics and Cosmology*, p. 213
- Moorwood, A. F. M.: 1996, *Space Science Reviews* **77**, 303
- Moran, E. C., Lehnert, M. D., and Helfand, D. J.: 1999, *Astrophys. J.* **526**, 649
- Morrison, R. and McCammon, D.: 1983, *Astrophys. J.* **270**, 119
- Mulchaey, J. S., Koratkar, A., Ward, M. J., Wilson, A. S., Whittle, M., Antonucci, R. R. J., Kinney, A. L., and Hurt, T.: 1994, *Astrophys. J.* **436**, 586
- Mushotzky, R. and Ferland, G. J.: 1984, *Astrophys. J.* **278**, 558
- Mushotzky, R. F., Done, C., and Pounds, K. A.: 1993, *Ann. Rev. Astron. Astrophys.* **31**, 717

- Mushotzky, R. F., Serlemitsos, P. J., Boldt, E. A., Holt, S. S., and Becker, R. H.: 1978, *Astrophys. J.* **220**, 790
- Nandra, K., George, I. M., Mushotzky, R. F., Turner, T. J., and Yaqoob, T.: 1997a, *Astrophys. J.* **476**, 70
- Nandra, K., George, I. M., Mushotzky, R. F., Turner, T. J., and Yaqoob, T.: 1997b, *Astrophys. J.* **477**, 602
- Nandra, K. and Pounds, K. A.: 1994, *Mon. Not. R. Astron. Soc.* **268**, 405
- Netzer, H.: 2004, *Astrophys. J.* **604**, 551
- Netzer, H., Turner, T. J., and George, I. M.: 1998, *Astrophys. J.* **504**, 680
- Neugebauer, G., Habing, H. J., van Duinen, R., Aumann, H. H., Baud, B., Beichman, C. A., Beintema, D. A., Boggess, N., Clegg, P. E., de Jong, T., Emerson, J. P., Gautier, T. N., Gillett, F. C., Harris, S., Hauser, M. G., Houck, J. R., Jennings, R. E., Low, F. J., Marsden, P. L., Miley, G., Olon, F. M., Pottasch, S. R., Raimond, E., Rowan-Robinson, M., Soifer, B. T., Walker, R. G., Wesselius, P. R., and Young, E.: 1984, *Astrophys. J., Lett.* **278**, 1
- Norris, R. P., Kesteven, M. J., Troup, E. R., Allen, D. A., and Sramek, R. A.: 1990, *Astrophys. J.* **359**, 291
- Osterbrock, D. E.: 1989, *Astrophysics of gaseous nebulae and active galactic nuclei*, University of Minnesota et al.; Mill Valley, CA, University Science Books
- Panessa, F. and Bassani, L.: 2002, *Astron. Astrophys.* **394**, 435
- Persic, M., Mariani, S., Cappi, M., Bassani, L., Danese, L., Dean, A. J., di Cocco, G., Franceschini, A., Hunt, L. K., Matteucci, F., Palazzi, E., Palumbo, G. G. C., Rephaeli, Y., Salucci, P., and Spizzichino, A.: 1998, *Astron. Astrophys. Lett.* **339**, 33
- Persic, M. and Rephaeli, Y.: 2002, *Astron. Astrophys.* **382**, 843
- Peterson, B. M. (ed.): 1997, *An introduction to active galactic nuclei*, Cambridge University Press, Cambridge, New York
- Petre, R.: 1992, in *Contributions to the Madrid conference on the nearest active galaxies*, p. 117

- Pietsch, W., Roberts, T. P., Sako, M., Freyberg, M. J., Read, A. M., Borozdin, K. N., Branduardi-Raymont, G., Cappi, M., Ehle, M., Ferrando, P., Kahn, S. M., Ponman, T. J., Ptak, A., Shirey, R. E., and Ward, M.: 2001, *Astron. Astrophys. Lett.* **365**, 174
- Pogge, R. W. and Eskridge, P. B.: 1993, *Astron. J.* **106**, 1405
- Pounds, K. A., Nandra, K., Stewart, G. C., George, I. M., and Fabian, A. C.: 1990, *Nature* **344**, 132
- Pradhan, A.: 1995, in *The Analysis of Emission Lines: Atomic Data for the Analysis of Emission Lines*, p. 8
- Pradhan, A. K.: 2000, in *Atomic Data Needs for X-ray Astronomy: The Iron Project*, p. 69
- Ptak, A., Heckman, T., Levenson, N. A., Weaver, K., and Strickland, D.: 2003, *Astrophys. J.* **592**, 782
- Ptak, A., Serlemitsos, P., Yaqoob, T., and Mushotzky, R.: 1999, *Astrophys. J., Suppl. Ser.* **120**, 179
- Ptak, A., Serlemitsos, P., Yaqoob, T., Mushotzky, R., and Tsuru, T.: 1997, *Astron. J.* **113**, 1286
- Ranalli, P., Comastri, A., and Setti, G.: 2003, *Astron. Astrophys.* **399**, 39
- Raymond, J. C. and Smith, B. W.: 1977, *Astrophys. J., Suppl. Ser.* **35**, 419
- Reynolds, C. S. and Nowak, M. A.: 2003, *Physics Reports* **377**, 389
- Reynolds, S. P.: 1998, *Astrophys. J.* **493**, 375
- Rieke, G. H.: 1988, *Astrophys. J., Lett.* **331**, 5
- Rieke, G. H., Cutri, R. M., Black, J. H., Kailey, W. F., McAlary, C. W., Lebofsky, M. J., and Elston, R.: 1985, *Astrophys. J.* **290**, 116
- Rieke, G. H. and Low, F. J.: 1972, *Astrophys. J., Lett.* **176**, 95
- Rigopoulou, D., Lawrence, A., and Rowan-Robinson, M.: 1996, *Mon. Not. R. Astron. Soc.* **278**, 1049
- Risaliti, G., Gilli, R., Maiolino, R., and Salvati, M.: 2000, *Astron. Astrophys.* **357**, 13
- Ross, R. R. and Fabian, A. C.: 1993, *Mon. Not. R. Astron. Soc.* **261**, 74
- Rothenflug, R. and Arnaud, M.: 1985, *Astron. Astrophys.* **144**, 431

- Rowan-Robinson, M., Clegg, P. E., Beichman, C. A., Neugebauer, G., Soifer, B. T., Aumann, H. H., Beintema, D. A., Boggess, N., Emerson, J. P., Gautier, T. N., Gillett, F. C., Hauser, M. G., Houck, J. R., Low, F. J., and Walker, R. G.: 1984, *Astrophys. J., Lett.* **278**, 7
- Rowan-Robinson, M. and Efstathiou, A.: 1993, *Mon. Not. R. Astron. Soc.* **263**, 675
- Roy, A.: 1994, *Ph.D. thesis*, School of Physics, University of Sidney
- Sako, M., Kahn, S. M., Behar, E., Kaastra, J. S., Brinkman, A. C., Boller, T., Puchnarewicz, E. M., Starling, R., Liedahl, D. A., Clavel, J., and Santos-Lleo, M.: 2001, *Astron. Astrophys. Lett.* **365**, 168
- Sanders, D. B.: 1992, in *ASP Conf. Ser. 31: Relationships Between Active Galactic Nuclei and Starburst Galaxies*, p. 303
- Sanders, D. B.: 1999, *Astrophys. Space. Sci.* **266**, 331
- Sanders, D. B., Egami, E., Lipari, S., Mirabel, I. F., and Soifer, B. T.: 1995, *Astron. J.* **110**, 1993
- Sanders, D. B. and Mirabel, I. F.: 1985, *Astrophys. J., Lett.* **298**, 31
- Sanders, D. B. and Mirabel, I. F.: 1996, *Ann. Rev. Astron. Astrophys.* **34**, 749
- Sanders, D. B., Phinney, E. S., Neugebauer, G., Soifer, B. T., and Matthews, K.: 1989, *Astrophys. J.* **347**, 29
- Sanders, D. B., Soifer, B. T., Elias, J. H., Madore, B. F., Matthews, K., Neugebauer, G., and Scoville, N. Z.: 1988a, *Astrophys. J.* **325**, 74
- Sanders, D. B., Soifer, B. T., Elias, J. H., Neugebauer, G., and Matthews, K.: 1988b, *Astrophys. J., Lett.* **328**, 35
- Sanders, D. B., Surace, J. A., and Ishida, C. M.: 1999, in *IAU Symp. 186: Galaxy Interactions at Low and High Redshift*, p. 289
- Sarazin, C. L.: 1988, *X-ray emission from clusters of galaxies*, Cambridge Astrophysics Series, Cambridge: Cambridge University Press
- Satyapal, S., Watson, D. M., Pipher, J. L., Forrest, W. J., Greenhouse, M. A., Smith, H. A., Fischer, J., and Woodward, C. E.: 1997, *Astrophys. J.* **483**, 148

- Saunders, W., Rowan-Robinson, M., Lawrence, A., Efstathiou, G., Kaiser, N., Ellis, R. S., and Frenk, C. S.: 1990, *Mon. Not. R. Astron. Soc.* **242**, 318
- Saunders, W., Sutherland, W. J., Maddox, S. J., Keeble, O., Oliver, S. J., Rowan-Robinson, M., McMahon, R. G., Efstathiou, G. P., Tadros, H., White, S. D. M., Frenk, C. S., Carramiñana, A., and Hawkins, M. R. S.: 2000, *Mon. Not. R. Astron. Soc.* **317**, 55
- Schechter, P.: 1976, *Astrophys. J.* **203**, 297
- Schmidt, M. and Green, R. F.: 1983, *Astrophys. J.* **269**, 352
- Schmidt, M. and Green, R. F.: 1986, *Astrophys. J.* **305**, 68
- Schmitt, H. R., Kinney, A. L., Calzetti, D., and Storchi Bergmann, T.: 1997, *Astron. J.* **114**, 592
- Schramkowski, G. P. and Torkelsson, U.: 1996, *Astron. Astrophys. Rev.* **7**, 55
- Schreier, E. J., Gorenstein, P., and Feigelson, E. D.: 1982, *Astrophys. J.* **261**, 42
- Schulz, H., Komossa, S., Berghofer, T. W., and Boer, B.: 1998, *Astron. Astrophys.* **330**, 823
- Scoville, N. Z., Evans, A. S., Thompson, R., Rieke, M., Hines, D. C., Low, F. J., Dinshaw, N., Surace, J. A., and Armus, L.: 2000, *Astron. J.* **119**, 991
- Scoville, N. Z., Hibbard, J. E., Yun, M. S., and van Gorkom, J. H.: 1994, in *Mass-Transfer Induced Activity in Galaxies*, p. 191
- Sekiguchi, K. and Anderson, K. S.: 1987, *Astron. J.* **94**, 644
- Seyfert, C. K.: 1943, *Astrophys. J.* **97**, 28
- Shakura, N. I. and Sunyaev, R. A.: 1973, *Astron. Astrophys.* **24**, 337
- Slane, P., Gaensler, B. M., Dame, T. M., Hughes, J. P., Plucinsky, P. P., and Green, A.: 1999, *Astrophys. J.* **525**, 357
- Smith, R. K., Brickhouse, N. S., Liedahl, D. A., and Raymond, J. C.: 2001, *Astrophys. J., Lett.* **556**, 91
- Soifer, B. T. and Neugebauer, G.: 1991, *Astron. J.* **101**, 354
- Soifer, B. T., Neugebauer, G., and Houck, J. R.: 1987a, *Ann. Rev. Astron. Astrophys.* **25**, 187
- Soifer, B. T., Neugebauer, G., Matthews, K., Egami, E., Weinberger, A. J., Ressler, M., Scoville, N. Z., Stolovy, S. R., Condon, J. J., and Becklin, E. E.: 2001, *Astron. J.* **122**, 1213

- Soifer, B. T., Rowan-Robinson, M., Houck, J. R., de Jong, T., Neugebauer, G., Aumann, H. H., Beichman, C. A., Boggess, N., Clegg, P. E., Emerson, J. P., Gillett, F. C., Habing, H. J., Hauser, M. G., Low, F. J., Miley, G., and Young, E.: 1984, *Astrophys. J., Lett.* **278**, 71
- Soifer, B. T., Sanders, D. B., Madore, B. F., Neugebauer, G., Danielson, G. E., Elias, J. H., Lonsdale, C. J., and Rice, W. L.: 1987b, *Astrophys. J.* **320**, 238
- Soifer, B. T., Sanders, D. B., Neugebauer, G., Danielson, G. E., Lonsdale, C. J., Madore, B. F., and Persson, S. E.: 1986, *Astrophys. J., Lett.* **303**, 41
- Strickland, D. K., Heckman, T. M., Weaver, K. A., and Dahlem, M.: 2000, *Astron. J.* **120**, 2965
- Strickland, D. K., Heckman, T. M., Weaver, K. A., Hoopes, C. G., and Dahlem, M.: 2002, *Astrophys. J.* **568**, 689
- Strickland, D. K. and Stevens, I. R.: 2000, *Mon. Not. R. Astron. Soc.* **314**, 511
- Strüder, L., Briel, U., Dennerl, K., Hartmann, R., Kendziorra, E., Meidinger, N., Pfeffermann, E., Reppin, C., Aschenbach, B., Bornemann, W., Bräuninger, H., Burkert, W., Elender, M., Freyberg, M., Haberl, F., Hartner, G., Heuschmann, F., Hippmann, H., Kastelic, E., Kemmer, S., Kettenring, G., Kink, W., Krause, N., Müller, S., Oppitz, A., Pietsch, W., Popp, M., Predehl, P., Read, A., Stephan, K. H., Stötter, D., Trümper, J., Holl, P., Kemmer, J., Soltau, H., Stötter, R., Weber, U., Weichert, U., von Zanthier, C., Carathanassis, D., Lutz, G., Richter, R. H., Solc, P., Böttcher, H., Kuster, M., Staubert, R., Abbey, A., Holland, A., Turner, M., Balasini, M., Bignami, G. F., La Palombara, N., Villa, G., Buttler, W., Gianini, F., Lainé, R., Lumb, D., and Dhez, P.: 2001, *Astron. Astrophys. Lett.* **365**, 18
- Strüder, L., Meidinger, N., Pfeffermann, E., Hartmann, R., Bräuninger, H. W., Reppin, C., Briel, U. G., Hippmann, H., Kink, W., Hauff, D., Krause, N., Aschenbach, B., Hartner, G. D., Dennerl, K., Haberl, F., Stötter, D., Kemmer, S., Trümper, J. E., Lutz, G., Richter, R. H., Solc, P., Eckhardt, R., Kendziorra, E., Kuster, M., von Zanthier, C., Holl, P., Viehl, A., Krisch, S., Kemmer, J., and Soltau, H.: 2000, in *Proc. SPIE Vol. 4012, X-Ray Optics, Instruments, and Missions III*; eds. J. E. Trümper; B. Aschenbach, p. 342
- Suchkov, A. A., Berman, V. G., Heckman, T. M., and Balsara, D. S.: 1996, *Astrophys. J.* **463**, 528
- Sulentic, J. W.: 1989, *Astron. J.* **98**, 2066
- Svensson, R. and Zdziarski, A. A.: 1994, *Astrophys. J.* **436**, 599

- Tacconi, L. J., Genzel, R., Tecza, M., Gallimore, J. F., Downes, D., and Scoville, N. Z.: 1999, *Astrophys. J.* **524**, 732
- Tanaka, Y.: 1989, in *ESA SP-296: Two Topics in X-Ray Astronomy, Volume 1: X Ray Binaries. Volume 2: AGN and the X Ray Background*, p. 3
- Tanaka, Y., Nandra, K., Fabian, A. C., Inoue, H., Otani, C., Dotani, T., Hayashida, K., Iwasawa, K., Kii, T., Kunieda, H., Makino, F., and Matsuoka, M.: 1995, *Nature* **375**, 659
- Tecza, M., Genzel, R., Tacconi, L. J., Anders, S., Tacconi-Garman, L. E., and Thatte, N.: 2000, *Astrophys. J.* **537**, 178
- Telesco, C. M.: 1988, *Ann. Rev. Astron. Astrophys.* **26**, 343
- Terashima, Y., Kunieda, H., Misaki, K., Mushotzky, R. F., Ptak, A. F., and Reichert, G. A.: 1998, *Astrophys. J.* **503**, 212
- Terlevich, R., Tenorio-Tagle, G., Franco, J., and Melnick, J.: 1992, *Mon. Not. R. Astron. Soc.* **255**, 713
- Thompson, A. C., Attwood, D. T., Gullikson, E. M., Howells, M. R., Kortright, J. B., Robinson, A. L., Underwood, J. H., Attwood, D. T., Kim, K.-J., Kirz, J., Attwood, D. T., Lindau, I., Pianetta, P., Winick, H., Williams, G. P., Scofield, J. H., and D., V.: 2001, *X-ray Data Booklet*, <http://xdg.lbl.gov>
- Trümper, J.: 1990, in *IAU Colloq. 115: High Resolution X-ray Spectroscopy of Cosmic Plasmas*, p. 291
- Turner, M. J. L., Abbey, A., Arnaud, M., Balasini, M., Barbera, M., Belsole, E., Bennie, P. J., Bernard, J. P., Bignami, G. F., Boer, M., Briel, U., Butler, I., Cara, C., Chabaud, C., Cole, R., Collura, A., Conte, M., Cros, A., Denby, M., Dhez, P., Di Coco, G., Dowson, J., Ferrando, P., Ghizzardi, S., Gianotti, F., Goodall, C. V., Gretton, L., Griffiths, R. G., Hainaut, O., Hochedez, J. F., Holland, A. D., Jourdain, E., Kendziorra, E., Lagostina, A., Laine, R., La Palombara, N., Lortholary, M., Lumb, D., Marty, P., Molendi, S., Pigot, C., Poindron, E., Pounds, K. A., Reeves, J. N., Reppin, C., Rothenflug, R., Salvétat, P., Sauvageot, J. L., Schmitt, D., Sembay, S., Short, A. D. T., Spragg, J., Stephen, J., Strüder, L., Tiengo, A., Trifoglio, M., Trümper, J., Vercellone, S., Vigroux, L., Villa, G., Ward, M. J., Whitehead, S., and Zonca, E.: 2001, *Astron. Astrophys. Lett.* **365**, 27
- Turner, T. J., George, I. M., Nandra, K., and Mushotzky, R. F.: 1997a, *Astrophys. J., Suppl. Ser.* **113**, 23

- Turner, T. J., George, I. M., Nandra, K., and Mushotzky, R. F.: 1997b, *Astrophys. J.* **488**, 164
- Ueno, S., Mushotzky, R. F., Koyama, K., Iwasawa, K., Awaki, H., and Hayashi, I.: 1994, *Publ. Astron. Soc. Jpn. Lett.* **46**, 71
- van den Broek, A. C.: 1993, *Astron. Astrophys.* **269**, 96
- van der Kruit, P. C.: 1971, *Astron. Astrophys.* **15**, 110
- Veilleux, S., Kim, D.-C., Sanders, D. B., Mazzarella, J. M., and Soifer, B. T.: 1995, *Astrophys. J., Suppl. Ser.* **98**, 171
- Veilleux, S., Sanders, D. B., and Kim, D.-C.: 1997, *Astrophys. J.* **484**, 92
- Veilleux, S., Sanders, D. B., and Kim, D.-C.: 1999, *Astrophys. J.* **522**, 139
- Vignati, P., Molendi, S., Matt, G., Guainazzi, M., Antonelli, L. A., Bassani, L., Brandt, W. N., Fabian, A. C., Iwasawa, K., Maiolino, R., Malaguti, G., Marconi, A., and Perola, G. C.: 1999, *Astron. Astrophys.* **349**, 57
- Voges, W., Aschenbach, B., Boller, T., Bräuninger, H., Briel, U., Burkert, W., Dennerl, K., Englhauser, J., Gruber, R., Haberl, F., Hartner, G., Hasinger, G., Kürster, M., Pfeffermann, E., Pietsch, W., Predehl, P., Rosso, C., Schmitt, J. H. M. M., Trümper, J., and Zimmermann, H. U.: 1999, *Astron. Astrophys.* **349**, 389
- Wall, J. V.: 1996, *Q. J. R. Astron. Soc.* **37**, 519
- Wang, T., Brinkmann, W., and Bergeron, J.: 1996, *Astron. Astrophys.* **309**, 81
- Ward, M. J., Done, C., Fabian, A. C., Tennant, A. F., and Shafer, R. A.: 1988, *Astrophys. J.* **324**, 767
- Weedman, D. W.: 1986, *Quasar astronomy*, Cambridge and New York, Cambridge University Press
- Weedman, D. W., Feldman, F. R., Balzano, V. A., Ramsey, L. W., Sramek, R. A., and Wu, C.-C.: 1981, *Astrophys. J.* **248**, 105
- White, N. E., Swank, J. H., and Holt, S. S.: 1983, *Astrophys. J.* **270**, 711
- Wilkes, B. J., Tananbaum, H., Worrall, D. M., Avni, Y., Oey, M. S., and Flanagan, J.: 1994, *Astrophys. J., Suppl. Ser.* **92**, 53
- Wilms, J.: 1996, *Master's thesis*, Eberhard-Karls-Universität Tübingen

- Wilson, A. S. and Raymond, J. C.: 1999, *Astrophys. J., Lett.* **513**, 115
- Wilson, C. K. and Rothschild, R. E.: 1983, *Astrophys. J.* **274**, 717
- Wolter, H.: 1952a, *Annalen der Physik* **10**, 286
- Wolter, H.: 1952b, *Annalen der Physik* **10**, 94
- Wunderlich, E., Wielebinski, R., and Klein, U.: 1987, *Astron. Astrophys. Suppl. Ser.* **69**, 487
- Xia, X., Boller, T., Deng, Z., and Börner, G.: 2001, *Chinese Journal of Astronomy and Astrophysics* **1**, 221
- Yaqoob, T.: 1992, *Mon. Not. R. Astron. Soc.* **258**, 198
- Yaqoob, T., Edelson, R., Weaver, K. A., Warwick, R. S., Mushotzky, R. F., Serlemitsos, P. J., and Holt, S. S.: 1995, *Astrophys. J., Lett.* **453**, 81
- Yuan, W., Fabian, A. C., Celotti, A., McMahon, R. G., and Matsuoka, M.: 2005, *Mon. Not. R. Astron. Soc.* **358**, 432
- Yun, M. S., Reddy, N. A., and Condon, J. J.: 2001, *Astrophys. J.* **554**, 803
- Zdziarski, A. A., Ghisellini, G., George, I. M., Fabian, A. C., Svensson, R., and Done, C.: 1990, *Astrophys. J., Lett.* **363**, 1
- Zhou, Y. Y., Yu, K. N., Young, E. C. M., Wang, J. M., and Ma, E.: 1997, *Astrophys. J., Lett.* **475**, 9
- Zombeck, M. V.: 1990, *Handbook of space astronomy and astrophysics*, 2nd ed., Cambridge University Press, Cambridge U.K., <http://ads.harvard.edu/books/hsaa/toc.html>

Acronyms

This list is a synopsis of acronyms and abbreviations used in this thesis.

Technical terms

<i>ACIS</i>	Advanced CCD Imaging Spectrometer (detector on <i>Chandra</i>)
<i>ACIS-S</i>	<i>ACIS</i> Spectroscopic array
<i>ALMA</i>	Atacama Large Millimeter Array (ESO; submm to mm antennae array)
<i>ASCA</i>	Advanced Satellite for Cosmology and Astrophysics; Japanese X-ray Astronomy satellite – also known as Asuka (formerly Astro-D), (ISAS, launched 1993)
<i>AXAF</i>	Advanced X-ray Astrophysics Facility, → <i>Chandra</i>
<i>BeppoSAX</i>	<i>BeppoSAX</i> X-ray satellite (Italy, launched 1996)
<i>BBXRT</i>	Broad-Band X-ray Telescope (1990, on the Space Shuttle Columbia as part of the Astro-1 mission)
BG	BackGround spectrum
BI	Back-Illuminated
CCD	Charge Coupled Device
CCF	Current Calibration File
<i>Chandra</i>	<i>Chandra</i> X-ray Observatory (CXO, NASA, launched 1999)
CL	Confidence Level
CTE	Charge Transfer Efficiency
CTI	Charge Transfer Inefficiency
dof	degree(s) of freedom
<i>Einstein</i>	<i>Einstein</i> Observatory (HEAO-2), X-ray Astronomy satellite (NASA, launched 1978)
EPCE	EPIC pn Control Electronics unit
EPCH	EPIC pn Focal Camera Head unit

EPIC	European Photon Imaging Camera (detectors on <i>XMM-Newton</i>)
EPVC	EPIC pn low Voltage Converter unit
ERMS	EPIC Radiation Monitor System
ESA	European Space Agency
ESO	European Southern Observatory
<i>EXOSAT</i>	European X-ray Observatory SATellite (ESA, launched 1983)
FI	Focal plane Instrumentation / Front-Illuminated
FITS	Flexible Image Transport System
FOV	Field Of View
FTOOLS	FITS-based software utilities developed at GSFC
FWHM	Full Width Half Maximum
<i>Ginga</i>	Japanese X-ray astronomy mission, known as Astro-C (ISAS, launched 1987)
GO	Guest Observer
GUI	Graphical User Interface
GSFC	Goddard Space Flight Center (NASA centre, USA)
GTI	Good Time Interval
<i>HEAO-1</i>	High Energy Astrophysics Observatory No. 1, X-ray Astronomy Mission (NASA, launched 1977)
HEASARC	High Energy Astrophysics Science Archive Research Center (at GSFC, NASA) (http://heasarc.gsfc.nasa.gov/)
<i>HERSCHEL</i>	Herschel space observatory (ESA; far-IR and submm mission; to be launched in early 2007)
HEW	Half Energy Width
HLL	Semi-conductor laboratory (Halbleiter-Laboratorium) of the MPIs for Extraterrestrial physics (Garching, Germany) and for Physics (Munich, Germany)
<i>HRC-I</i>	High Resolution Camera - Imager (detector on <i>Chandra</i>)
<i>HRI</i>	High Resolution Imager (detector on <i>ROSAT</i>)
<i>HST</i>	Hubble Space Telescope (NASA+ESA, launched 1990)
IAAT	Institut für Astronomie und Astrophysik Tübingen (Germany)
IAU	International Astronomical Union
IDL	Interactive Data Language (developed by Research Systems Inc.)
IPC	Imaging Proportional Counter (detector on <i>Einstein</i>)
<i>IRAS</i>	Infra-Red Astronomical Satellite (ESA/Netherlands, launched 1983)

<i>IRAS-BGS</i>	<i>IRAS</i> - Bright Galaxy Survey
<i>IRAS-PSC</i>	<i>IRAS</i> - Point Source Catalogue
<i>IRAS-PSCz</i>	<i>IRAS</i> - Point Source Catalogue redshift survey (modified and enlarged <i>IRAS-PSC</i> in terms of completeness and uniformity)
<i>ISO</i>	Infrared Space Observatory (ESA, launched 1995)
ISOPHOT	<i>ISO</i> - PHOTometer (detector on <i>ISO</i>)
ISOPHOT-S	<i>ISO</i> - SpectroPHOTometer (detector on <i>ISO</i>)
<i>ISO-SWS</i>	<i>ISO</i> - Short Wavelength Spectrometer (detector on <i>ISO</i>)
<i>JWST</i>	James Webb Space Telescope (NASA+ESA; near- and mid-IR telescope; to be launched in the mid 2010s)
Jy	Jansky ($= 10^{-26} \text{ W/m}^2/\text{Hz} = 10^{-23} \text{ erg/cm}^2/\text{Hz}$)
MCP	Micro-Channel Plate (or Multi Channel Plate)
MOS	Metal Oxide Semi-conductor (a type of CCD used on <i>XMM-Newton</i>)
MPE	Max-Planck-Institute for Extraterrestrial physics, Garching (Germany)
MPI	Max-Planck-Institute
MSSL	Mullard Space Science Laboratory (College London, Great Britain)
NASA	National Aeronautics and Space Administration (USA)
NED	NASA/IPAC Extragalactic Database (http://nedwww.ipac.caltech.edu/)
<i>Newton</i>	→ <i>XMM-Newton</i>
<i>NICMOS</i>	Near-Infrared Camera and Multi-Object Spectrometer (detector on <i>HST</i>)
NHP	Null Hypothesis Probability
ODF	Observation Data File
ODS	Observation Data System
OM	Optical Monitor
PHA	Pulse Height Amplitude (or Analyser/Amplifier)
PI	Pulse Invariant
Pixel	Picture Element
PMS	Payload Monitoring System
PN	P-type/N-type semi-conductor (EPIC) (PN junction CCD, a type of CCD used on <i>XMM-Newton</i>)
PPS	<i>XMM-Newton</i> Pipeline Processing Subsystem
PSF	Point Spread Function

PSPC	Position Sensitive Proportional Counter (detector on <i>ROSAT</i>)
QE	Quantum Efficiency
RASS-BSC	<i>ROSAT</i> All-Sky Survey - Bright Source Catalogue
RFC	RGS Focal Camera
RGA	RGS Grating Array (or Assembly)
RGS	Reflection Grating Spectrometer (detector on <i>XMM-Newton</i>)
RMF	Response Matrix Function (or File); also: Redistribution Matrix Function (or File)
<i>ROSAT</i>	ROentgen SATellit, X-ray mission (Germany/USA/UK, launched 1990)
<i>RXTE</i>	Rossi X-ray Timing (or Transient) Explorer (launched 1995)
SAS	→ XMM-SAS
<i>SCUBA</i>	Submm Common User Bolometer Array (on the James Clerk Maxwell Telescope)
SDF	Slew Data File
SIS	Solid state Imaging Spectrometer (detector on <i>ASCA</i>)
SOC	(<i>XMM-Newton</i>) Science Operations Centre (VILSPA, Spain)
SRC	SouRCe spectrum (see the footnote on p. 46)
SSC	(<i>XMM-Newton</i>) Survey Science Centre (Leicester, Great Britain)
<i>Suzaku</i>	Japanese X-ray Astronomy Satellite – formerly Astro-E2 (ISAS/NASA, launched 2005)
UHB	→ <i>XMM-Newton</i> UHB
VILSPA	<i>XMM-Newton</i> ground station (VILlafranca del Castillo, SPain)
<i>WFPC2</i>	Wide-Field-Planetary-Camera 2 (detector on <i>HST</i>)
<i>XEUS</i>	X-ray Evolving Universe Spectroscopy mission (or Spectrometer; ESA; to be launched in the mid 2010s)
<i>XMM-Newton</i>	X-ray Multi Mirror mission or <i>XMM-Newton</i> observatory (ESA, launched 1999)
XMM-SAS	(<i>XMM-Newton</i>) Science Analysis Software (or Subsystem)
<i>XMM-Newton</i> UHB	<i>XMM-Newton</i> Users' HandBook
XSA	<i>XMM-Newton</i> Science Archive (http://xmm.vilspa.esa.es/external/xmm_data_acc/xsa/index.shtml)
XSPEC	X-ray SPECtral fitting (software) package

Scientific terms

AGN	Active Galactic Nucleus (or Nuclei)
APEC	Astrophysical Plasma Emission Code (http://cxc.harvard.edu/atomdb/)
APED	Astrophysical Plasma Emission Database, → APEC
BB	BlackBody (spectral) model
BBB	Big Blue Bump
BH	Black Hole
BHC	Black Hole Candidate
BL Lac	BL Lacertae object
BLR	Broad Line Region
BLS1	Broad-Line Seyfert 1 galaxy
CIE	Collisional Ionization Equilibrium
DEC	DEClination (here: J2000.0)
ELF	Extremely Luminous Far–infrared galaxy (old for LIG/ULIRG)
EUV	Extreme UV
EW	Equivalent Width
FIR	Far–InfraRed
HMXB	High–Mass X–ray Binary
IC	Inverse Compton
IR	InfraRed
ISM	InterStellar Medium
LIG	Luminous Infrared Galaxy
LINER	Low Ionization Nuclear Emission–line Region
LLAGN	Low–Luminous AGN
LMXB	Low–Mass X–ray Binary
M	Messier catalogue number
MEKAL	MEwe–KAastra–Liedahl (spectral) model (for a hot diffuse plasma, with new data on Fe-L lines)
mid-IR	mid–InfraRed
NGC	New General Catalog
NIR	Near–InfraRed
NLR	Narrow Line Region

NLS1	Narrow-Line Seyfert 1 galaxy
PAH	Polycyclic Aromatic Hydrocarbon
PEXRAV	simulated model for a reflection spectrum from a neutral accretion disk
PEXRIV	simulated model for a reflection spectrum from an ionized accretion disk
PHABS	PHoto–electric ABSorption (spectral) model
QSO	Quasi-Stellar Object, quasar
R.A.	Right Ascension (here: J2000.0)
RAYMOND	RAYMOND & Smith (spectral) model (for a hot diffuse plasma)
SED	Spectral Energy Distribution
SFR	Star Formation Rate
SN	SuperNova (pl. SNe)
SNR	SuperNova Remnant
Sy	Seyfert galaxy
Sy-1	Seyfert 1 galaxy
Sy-2	Seyfert 2 galaxy
ULIRG	UltraLuminous InfraRed Galaxy
UTA	Unresolved Transition Array
UV	UltraViolet

Appendix

A Combining spectral files within XSPEC

In the case of the ultraluminous infrared galaxy NGC 6240 data sets from two time-separated observations were available for analysing. In order to gain the best possible statistics in the number of photons the analysis was based on the combination of different spectral FITS-files using XSPEC.

A data set is defined mainly by the spectral files of the (background-contaminated) source and the background. Calling the two spectral files

- SRC ,
with the EXPOSURE value $(EXP)_{SRC}$,
and the BACKSCAL keyword $(BS)_{SRC}$,

and the corresponding background file is

- BG ,
which have the EXPOSURE value $(EXP)_{BG}$,
and the BACKSCAL value $(BS)_{BG}$,

these files contain the number of detected counts in the unit COUNTS (*not* in COUNTS/sec), as being produced with the standard XMM-SAS and the HEASARC software packages.

By considering two different data sets to be combined, for each pair of the source and background spectral files, *i.e.* $(SRC_i, BG_i)_{i=1,2}$, XSPEC calculates the quantities

$$\frac{1}{(EXP)_{SRC_i}} \cdot SRC_i - \frac{(BS)_{SRC_i}}{(BS)_{BG_i} (EXP)_{BG_i}} \cdot BG_i$$

as the starting point of the fitting procedure.

Multiplying these quantities in pairs with

$$\frac{(EXP)_{SRC_i}}{(EXP)_{SRC_1} + (EXP)_{SRC_2}},$$

the summing up gives

$$\frac{SRC_1 + SRC_2}{(EXP)_{SRC_1} + (EXP)_{SRC_2}} - \frac{1}{(EXP)_{SRC_1} + (EXP)_{SRC_2}} \left\{ \frac{(EXP)_{SRC_1} (BS)_{SRC_1}}{(EXP)_{BG_1} (BS)_{BG_1}} \cdot BG_1 + \frac{(EXP)_{SRC_2} (BS)_{SRC_2}}{(EXP)_{BG_2} (BS)_{BG_2}} \cdot BG_2 \right\}. \quad (A.1)$$

This quantity is being used when fitted with models.

The easiest way to add the source files SRC_1 and SRC_2 is to use the FTOOL `mathpha` (with the options "exposure=CALC" and "backscal=NONE" or "backscal=1"). The combined spectrum has the EXPOSURE value $(EXP)_{SRC} = (EXP)_{SRC_1} + (EXP)_{SRC_2}$ and the BACKSCAL value $(BS)_{SRC}$ is unity.

Naming w_1 and w_2 as the weight constants for the background spectra to combine, the EXPOSURE value of the combined background spectrum (with the option "exposure=CALC") is then

$$w_1 \cdot (EXP)_{BG_1} + w_2 \cdot (EXP)_{BG_2}.$$

This should *formally* be equated with the desirable EXPOSURE value

$$(EXP)_{BG_1} + (EXP)_{BG_2},$$

if the constants are chosen properly (see below). This leads to the (symbolic) equation

$$w_1 \cdot (EXP)_{BG_1} + w_2 \cdot (EXP)_{BG_2} = (EXP)_{BG_1} + (EXP)_{BG_2}. \quad (A.2)$$

which is the first of three equations to solve for the weight constants and the BACKSCAL value for the combined background spectrum, $(BS)_{BG}$.

The combined background spectrum made according to this description is subtracted from the combined source spectrum – in XSPEC this is realized by calculating the quantity

$$\frac{SRC_1 + SRC_2}{(EXP)_{SRC_1} + (EXP)_{SRC_2}} - \frac{1}{(EXP)_{BG_1} + (EXP)_{BG_2}} \frac{1}{(BS)_{BG}} \{w_1 \cdot BG_1 + w_2 \cdot BG_2\}. \quad (A.3)$$

The equations (A.1) and (A.3) represent the same quantity. Hence the weight constants as a function of $(BS)_{BG}$ are

$$w_i = (BS)_{BG} \left\{ \frac{(BS)_{SRC_i}}{(BS)_{BG_i}} \right\} \cdot (EXP)_{net,i} \quad (\text{A.4})$$

with

$$(EXP)_{net,i} := \left\{ \frac{(EXP)_{BG_1} + (EXP)_{BG_2}}{(EXP)_{SRC_1} + (EXP)_{SRC_2}} \right\} \left\{ \frac{(EXP)_{SRC_i}}{(EXP)_{BG_i}} \right\}.$$

Solving the system of the equations (A.2) and (A.4) for $(BS)_{BG}$ and w_1, w_2 , one gets

$$(BS)_{BG} = \frac{(EXP)_{SRC_1} + (EXP)_{SRC_2}}{(EXP)_{SRC_1} \left\{ \frac{(BS)_{SRC_1}}{(BS)_{BG_1}} \right\} + (EXP)_{SRC_2} \left\{ \frac{(BS)_{SRC_2}}{(BS)_{BG_2}} \right\}}$$

and

$$w_i = f[(EXP)_{SRC_{1,2}, BG_{1,2}}, (BS)_{SRC_{1,2}, BG_{1,2}}] \cdot \left\{ \frac{(EXP)_{SRC_i}}{(EXP)_{BG_i}} \right\} \left\{ \frac{(BS)_{SRC_i}}{(BS)_{BG_i}} \right\},$$

where

$$f[(EXP)_{SRC_{1,2}, BG_{1,2}}, (BS)_{SRC_{1,2}, BG_{1,2}}] := \frac{(EXP)_{BG_1} + (EXP)_{BG_2}}{(EXP)_{SRC_1} \left\{ \frac{(BS)_{SRC_1}}{(BS)_{BG_1}} \right\} + (EXP)_{SRC_2} \left\{ \frac{(BS)_{SRC_2}}{(BS)_{BG_2}} \right\}}.$$

These values are the corrected amounts of the combined background subtraction from the combined source spectrum.

The equations presented here can be easily generalized for any number of data sets.

Acknowledgement

The *XMM-Newton* observatory was developed, launched, and operated successfully with great efforts by the *XMM-Newton* team members, including colleagues at the Max-Planck-Institut für Extraterrestrische Physik, Garching, Germany.

Participating in the astronomical world, I met interesting people and honourable persons, traversed beautiful countries, and made wonderful friends. These friends supported me and made it all look worth while.

Prof. Dr. Thomas Boller was the person who stood next to me from the beginning of my PhD time not only as my advisor, but – above all – as a colleague and collaborator. Without his successful proposals and his kindness to leave all the data to my person, the research work would not have been realized at all. The working time we shared was a recurrent source of close teamwork and familiarity. Without his ideas and support, the thesis would not have been feasible. Without him, a PhD at the MPE would not have been an option at all. His continuous encouragement and strong belief in me and his devoted friendship are invaluable ingredients for the success of this thesis. I am grateful to **Prof. Dr. J. Trümper** for allowing me to perform my thesis at the MPE, **Prof. Dr. G. Hasinger** for his hospitality during the last phase of this work and **Prof. Dr. D. Reimers** for his readiness to get my person under into the university facility of the observatory of Hamburg.

Moreover, my gratitude goes to **Frank Pfefferkorn**, with whom I had interesting specialist and non–specialist discussions and with whom I shared much more than an office.

Daniel Schaudel for his unique manner to set in always amusing discussions, **Helmut Dannerbauer** for giving insights into wavelength bands other than the X–rays, **Elisa Costantini** for providing me the *Chandra* images and the radial profile of NGC 6240 and all the others I forgot to mention, granted me with their undoubted cooperativeness and friendliness making work and life in Munich more enjoyable.

I don't wish to cease without thanking **my family**, who lead and supported me continuously through the good and the hard times, believes in me and encouraged me to give birth to this thesis.

Declaration

The research described in this thesis were performed in the X-ray group at the Max-Planck-Institut for Extraterrestrial physics (MPE), Garching near Munich between July 2000 and June 2003 under the supervision of Dr. Thomas Boller.

Herewith I declare that this thesis has been composed by myself and that only the mentioned sources and tools have been used. Furthermore, this thesis has not, nor any similar dissertation, submitted in any previous application for a degree.

Garching, 22.11.2005